Acta Pharmacologica Sinica (2011) 32: 415–416
 1671-4083/11 $32.00
www.nature.com/aps

Research Highlight

A molecular switch of "Yin and Yang": S-glutathionylation of eNOS turns off NO synthesis and turns on superoxide generation

Dayue Darrel DUAN[1, *], Chiu-yin KWAN[2]

Acta Pharmacologica Sinica (2011) 32: 415–416; doi: 10.1038/aps.2011.21; published online 28 Mar 2011

Nitric oxide (NO) is a short-lived free radical produced endogenously in biological tissues by nitric oxide synthases (NOSs)[1, 2]. Three NOS isoforms, namely NOS1 or neuronal NOS (nNOS), NOS2 or inducible NOS (iNOS), and NOS3 or endothelial NOS (eNOS) are present in most cell types, including cardiac myocytes and vascular endothelial cells. Vascular relaxation to mediators such as acetylcholine or increased blood flow depends on NO produced by the eNOS. The discovery of NO as the endothelium-derived relaxing factor (EDRF) and its crucial function as a signaling molecule in cardiovascular system was awarded the Nobel Prize in Physiology or Medicine in 1998[1].

Under normal circumstances the main function of eNOS is to produce NO. It catalyzes the conversion of *L*-arginine (*L*-Arg) to *L*-citrulline and NO via electron transfer from the reduced form of nicotinamide adenine dinucleotide phosphate (NADPH) through a flavin containing reductase domain to oxygen bound at the heme of an oxygenase domain containing tetrahydrobiopterin (BH_4) and *L*-Arg binding sites (Figure 1). The eNOS-derived NO activates the guanylate cyclase/cGMP/protein kinase G (PKG) pathway and modulates protein properties and function through nitrosylation of tyrosine and thiol-groups of cysteine in proteins, which are usually effective protection mechanisms against oxidative stress.

Under pathophysiological conditions such as hypertension, diabetes, septic shock and atherosclerosis, oxidative stress alters many functions of the endothelium and leads to endothelial dysfunction when the endothelium fails to serve its normal physiologic and protective mechanisms. A common feature of endothelial dysfunction is the reduced bioavailability of NO and increased production of superoxide ($\cdot O^{2-}$) and other

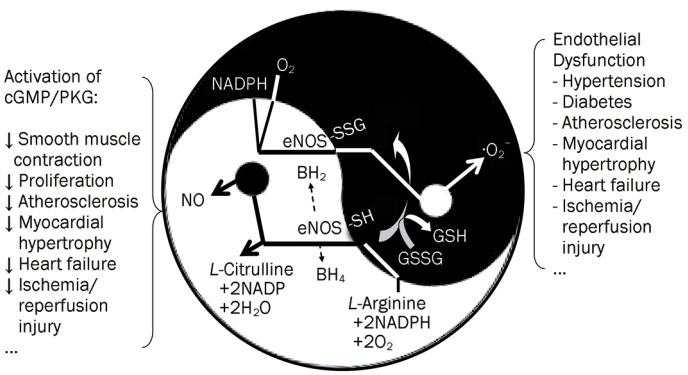

Figure 1. Schematic representation of S-glutathionylation of eNOS as a molecular switch of eNOS function from generation of NO to production of superoxide anion. The endothelial NO synthase (eNOS) uses *L*-arginine to generate NO. NO activates the guanylate cyclase/cyclic GMP (cGMP)/protein kinase G (PKG) pathway and modulates protein properties and function through nitrosylation of tyrosine and thiol-groups of cysteine in proteins, which are effective protection mechanisms against oxidative stress. Under pathological conditions NO production and bioavailability could be attenuated due to decreased supply of *L*-arginine or oxidation of the cofactor tetrahydrobiopterin (BH_4) of eNOS, leading to eNOS uncoupling and superoxide anion ($\cdot O^{2-}$) formation. Under oxidative stress, eNOS is S-glutathionylated through reversible thiol-disulfide exchange with oxidized glutathione (GSSG) or reaction of oxidant-induced protein thiolyl radicals with reduced glutathione (GSH). S-Glutathionylation of eNOS in endothelial cells switch off NO synthesis and turns on $\cdot O^{2-}$ generation, which is a pivotal mechanism for many diseases associated with epithelial dysfunction.

[1] *The Laboratory of Cardiovascular Phenomics, Center of Biomedical Research Excellence, and the Department of Pharmacology, University of Nevada School of Medicine, Reno, Nevada 89557, USA;* [2]*Vascular Biology Research Group, Research Institute of Basic Medical Sciences and Center for Faculty Development, China Medical University, Taichung, Taiwan, China*
Correspondence: Dayue Darrel DUAN, MD, PhD, FAHA
(dduan@medicine.nevada.edu)

reactive oxygen species (ROS) in the vasculature[3]. Multiple mechanisms may underlie the impaired NO availability[4]. These include a reduction in the expression level of eNOS mRNA or protein, changes in subcellular compartmentalization of eNOS activity, and compromised availability of the substrates and/or enzymatic cofactors for eNOS[5, 6]. Depletion of the substrate *L*-arginine, accumulation of methylarginines, and oxidation of the cofactor BH_4 of eNOS can uncouple the electron transfer reactions and revert eNOS to function as an NADPH oxidase, thus producing $\cdot O^{2-}$ instead of NO (Figure 1). The rapid reaction of NO with $\cdot O^{2-}$ can form the most potent oxidant peroxynitrite anion ($OONO^-$) and causes cellular injury associated with many pathophysiologic conditions, such as hypertension, atherosclerosis, diabetes, myocardial hypertrophy, heart failure, and ischemia/reperfusion injury[7]. The precise molecular mechanisms underlying the "switch" of the eNOS function from NO synthesis to $\cdot O^{2-}$ production under oxidative stress conditions, however, are still not fully understood.

Recently, Chen *et al* reported that *S*-glutathionylation of eNOS may be a unique mechanism for the redox regulation of eNOS[8]. It has been demonstrated previously that cysteine residues are critical for the maintenance of normal eNOS function[9]. Protein *S*-glutathionylation has been known as a specific post-translational modification of protein cysteine residues by adding the tripeptide glutathione through reversible thiol-disulfide exchange with oxidized glutathione (GSSG) or reaction of oxidant-induced protein thiyl radicals with reduced glutathione (GSH). Under oxidative stress, therefore, protein *S*-glutathionylation can serve to prevent irreversible oxidation of protein thiols[10]. *S*-glutathionylation has now emerged as a potential mechanism for dynamic, post-translational regulation of a variety of regulatory, structural, and metabolic proteins. Increasing lines of evidence point to the important role of S-glutathionylation in the regulation of signaling and metabolic pathways in intact cellular systems. Indeed, Chen *et al* found that GSSG induced dose-dependent *S*-glutathionylation of human eNOS that was reversed by reducing agents β-mercaptoethanol or dithiothreitol[8]. *S*-glutathionylation of eNOS reversibly decreases NOS activity with a concomitant increase in $\cdot O^{2-}$ generation primarily from the reductase domain. Two highly conserved cysteine residuals are identified as sites of *S*-glutathionylation and found to be critical for redox-regulation of eNOS function. They further demonstrated that *S*-glutathionylation of eNOS in endothelial cells turned off NO synthesis and turned on $\cdot O^{2-}$ generation (Figure 1). This conversion of eNOS function by *S*-glutathionylation is closely associated with impaired endothelium-dependent vasodilatation. In hypertensive vessels, *S*-glutathionylation of eNOS is increased with impaired endothelium-dependent vasodilatation. Thio-specific reducing agents that reverse the *S*-glutathionylation of eNOS are able to restore the endothelium-dependent vasodilatation of the hypertensive vessels. Thus, *S*-glutathionylation of eNOS may represent a novel and pivotal molecular switch providing redox regulation of cellular signaling and endothelial function. Control of this molecular switch will perhaps provide new therapeutic targets and specific strategy to correct endothelial dysfunction under pathophysiological conditions. Importantly, it may also shed new mechanistic light on the action of some antihypertensive herbal extracts that elicit potent antioxidant properties and relax blood vessels in an endothelium-dependent and NO-mediated manner. It can be speculated that herbs with varying degrees of redox potential may exert different, or even opposite, vascular effects by flipping the switch to preferentially cause the formation of NO or $\cdot O^2$ [11], thus lending scientific support for the Yin-Yang temperaments emphasized in the theory of traditional Chinese medicine.

1 Furchgott RF. Endothelium-derived relaxing factor: discovery, early studies, and identification as nitric oxide. Biosci Rep 1999; 19: 235–51.
2 Murad F. Nitric oxide signaling: would you believe that a simple free radical could be a second messenger, autacoid, paracrine substance, neurotransmitter, and hormone? Recent Prog Horm Res 1998; 53: 43–59.
3 Cai H, Harrison DG. Endothelial dysfunction in cardiovascular diseases: the role of oxidant stress. Circ Res 2000; 87: 840–4.
4 Wang Y, Marsden PA. Nitric oxide synthases: gene structure and regulation. Adv Pharmacol 1995; 34: 71–90.
5 Xia Y, Dawson VL, Dawson TM, Snyder SH, Zweier JL. Nitric oxide synthase generates superoxide and nitric oxide in arginine-depleted cells leading to peroxynitrite-mediated cellular injury. Proc Natl Acad Sci U S A 1996; 93: 6770–4.
6 Vasquez-Vivar J. Tetrahydrobiopterin, superoxide, and vascular dysfunction. Free Radic Biol Med 2009; 47: 1108–19.
7 Pacher P, Beckman JS, Liaudet L. Nitric oxide and peroxynitrite in health and disease. Physiol Rev 2007; 87: 315–424.
8 Chen CA, Wang TY, Varadharaj S, Reyes LA, Hemann, C Talukder MA, *et al*. S-glutathionylation uncouples eNOS and regulates its cellular and vascular function. Nature 2010; 468: 1115–8.
9 Chen PF, Tsai AL, Wu KK. Cysteine 184 of endothelial nitric oxide synthase is involved in heme coordination and catalytic activity. J Biol Chem 1994; 269: 25062–6.
10 Mieyal JJ, Gallogly MM, Qanungo S, Sabens EA, Shelton MD. Molecular mechanisms and clinical implications of reversible protein S-glutathionylation. Antioxid Redox Signal 2008; 10: 1941–88.
11 Achike FI, Kwan CY. Nitric oxide, human diseases and the herbal products that affect the nitric oxide signalling pathway. Clin Exp Pharmacol Physiol 2003; 30: 605–15.

Acta Pharmacologica Sinica (2011) 32: 417–424
 1671-4083/11 $32.00
www.nature.com/aps

Perspective

Erythrocyte Duffy antigen receptor for chemokines (DARC): diagnostic and therapeutic implications in atherosclerotic cardiovascular disease

Stavros APOSTOLAKIS, Georgios K CHALIKIAS, Dimitrios N TZIAKAS*, Stavros KONSTANTINIDES

Department of Cardiology, Medical School, Democritus University of Thrace, Alexandroupolis, Greece

Atherosclerosis is an inflammatory disease. The last three decades efforts have been made to elucidate the biochemical pathways that are implicated in the process of atherogenesis and plaque development. Chemokines are crucial mediators in every step of this process. Additionally, cellular components of the peripheral blood have been proved important mediators in the formation and progression of atherosclerotic lesions. However, until recently data were mostly focusing on leukocytes and platelets. Erythrocytes were considered unreceptive bystanders and limited data supported their importance in the progression and destabilization of the atherosclerotic plaque. Recently erythrocytes, through their Duffy antigen receptor for chemokines (DARC), have been proposed as appealing regulators of chemokine-induced pathways. Dissimilar to every other chemokine receptor DARC possesses high affinity for several ligands from both CC and CXC chemokine sub-families. Moreover, DARC is not coupled to a G-protein or any other intracellular signalling system; thus it is incapable of generating second messages. The exact biochemical role of erythrocyte DARC remains to be determined. It is however challenging the fact that DARC is a regulator of almost every CC and CXC chemokine ligand and therefore DARC antagonism could effectively block the complex pre-inflammatory chemokine network. In the present review we intent to provide recent evidence supporting the role of erythrocytes in atherosclerosis focusing on the erythrocyte-chemokine interaction through the Duffy antigen system.

Keywords: erythrocytes; chemokines; Duffy antigen receptors for chemokines; atherosclerosis

Acta Pharmacologica Sinica (2011) 32: 417–424; doi: 10.1038/aps.2011.13; published online 28 Mar 2011

Introduction

The Duffy blood group system was first reported by Cutbush and Mollison in 1950[1]. The authors reported an alloantibody against an antigen denoted as Fy^a in a multiple transfused patient with haemophilia. The antigen was named after the patient. The antithetical antigen, Fy^b, was described one year later. Three phenotypes were identified in Caucasians: Fy^{a+b-}, Fy^{a-b+}, and Fy^{a+b+}. These phenotypes are the products of co-dominant alleles comprising genotypes FY*A/FY*A, FY*B/FY*B, and FY*A/FY*B, respectively. The Fy^{a-b-} phenotype, is extremely rare in Caucasians and occurs primarily as a result of GATA promoter region mutation upstream of the FY allele. This mutation prevents expression of Duffy glycoprotein on erythrocytes only, while permitting expression of nonerythroid cells. Most West Africans and 68% of African Americans do not express Duffy antigens on their erythrocytes[2, 3]. Interestingly recent data suggest that reduced neutrophil count in people of African descent is due to a regulatory variant in the Duffy antigen receptor gene[4].

Soon, the Duffy blood group antigen was identified as a potent multi-ligand chemokine receptor and was therefore renamed to Duffy antigen receptor for chemokines (DARC)[5].

DARC belongs to the family of rhodopsin-like seven-helix transmembrane proteins[5, 6]. Besides erythrocytes DARC is expressed in postcapillary venular endothelial cells, which are the primary site of leukocyte transmigration in most tissues. The Duffy antigen has emerged as a highly specific binding site for both CC and CXC chemokines. The Duffy antigen possesses higher affinity for ELR motif CXC chemokines, which are neutrophil chemoattractants and presumably proangiogenic. The best studied interaction between DARC and CXCL8 has demonstrated a dissociation constant (K_d) of 5 nmol/L and receptor binding sites estimated at 1000–9000 per erythrocyte[7]. Unlike all other seven-transmembrane chemokine receptors, DARC lacks the highly conserved G protein-coupling motif located in the second cytoplasmic loop[6–8]. Thus DARC is not G-protein coupled and has no known alternative signalling mechanism. The biological role of a

* To whom correspondence should be addressed.
E-mail dtziakas@med.duth.gr
Received 2010-11-28 Accepted 2011-02-14

chemokine receptor that is unable to generate a second message and promote chemotaxis became a challenging field of investigation[6–8].

In the present review we intent to provide recent evidence supporting the role of erythrocytes in atherosclerosis focusing on the erythrocyte-chemokine interaction through the Duffy antigen system; a novel and challenging regulatory mechanism with potential implications in the management of atherosclerotic cardiovascular disease.

Erythrocytes and atherosclerosis

Erythrocytes: new players in the atherosclerotic cascade

Despite that knowledge on the pathophysiological background of atherosclerosis is exponentially growing, several aspects of the natural history of the disease remain unclear[9]. Cellular components of the peripheral blood have been proved important mediators in the genesis and progression of atherosclerotic lesions. However, until recently data were mostly focusing on leukocytes and platelets. Erythrocytes were considered unreceptive bystanders and limited data supported their importance in the progression and destabilization of the atherosclerotic plaque[10].

Roberts and Virmani were the first to report the presence of extravasated erythrocytes and iron within coronary atherosclerotic plaques[11]. The authors further demonstrated that the amount of intraplaque extravasated erythrocytes and iron was proportional to the extent of coronary atherosclerotic plaque[11]. Accordingly, Arbustini *et al*, identified erythrocyte membranes in atherosclerotic plaques outside the coronary circulation and suggested that cholesterol contained in their membranes may contribute significantly to the formation of the atheromatous core[12]. Kolodgie *et al*, reported that erythrocyte membranes were present in the necrotic core of advanced coronary atheromas and that their presence was correlated with the size of the necrotic core[13]. Subsequently a theory was raised suggesting that erythrocyte membranes contributed significantly to the growth of the plaque's core and subsequently contribute to its vulnerability[14].

Erythrocytes: mediators of plaque vulnerability

The erythrocyte membrane is a simple plasma membrane comprised mainly of cholesterol and phospholipids[15]. The erythrocyte membranes are 1.5–2.0 times richer in cholesterol than any other membrane in the body and approximately 40% of its weight is composed of lipids[16]. The volume of cholesterol in the membrane of a single erythrocyte is estimated to be 0.378 μm^3 whilst the majority of its cholesterol is considered to be free[16]. Only 50 μL erythrocytes are needed to produce a ≥0.2 mm^3 necrotic core[17]. Therefore, breakdown of the erythrocytes within advanced atheromatous lesions can result in substantial cholesterol accumulation. We have previously demonstrated that–in the clinical setting–cholesterol content of erythrocyte membranes is higher in patients with acute coronary syndromes compared to those with stable coronary artery disease[18, 19]. At the same time, degradation of erythrocytes inside the atheromas may lead to haemoglobin and iron release which is known to promote inflammation, further oxidation of lipids, free radicals production and activation of apoptotic pathways[13, 20].

Erythrocytes: a sink for pro-inflammatory molecules

Erythrocytes can also regulate inflammation within the plaque. Through the Duffy antigen receptor for chemokines (DARC) erythrocytes can bind and curry without deactivating a wide range of CXC and CC chemokines[8, 21]. The accumulation of erythrocytes within the plaques is the natural consequence of intraplaque haemorrhage. Thus it is reasonable to hypothesize that erythrocytes entering the necrotic lipid core can release within the plaque a substantial amount of their pro-inflammatory load. Therefore, erythrocyte emerges as a non-inflammatory cellular regulator of the local inflammatory processes acting as a bidirectional sink for chemokines[22].

Moreover erythrocytes are a major source of microparticles[23]. Microparticles or microvesicles are circulating, phospholipid rich, submicron elements released from the membranes of endothelial cells, platelets, leucocytes and erythrocytes[23]. Microvesicles play a role in intercellular communication and can deliver mRNA, miRNA, and proteins between cells[23]. These actions are mediated through their phospholipid rich surfaces and the expression of cell surface molecules which reflect their cell of origin and its state of activation. Investigation into their biological activity has also revealed diverse actions in coagulation[23]. Their procoagulant properties rely on the exposure of phosphatidylserine and on the possible presence of tissue factor, the main initiator of blood coagulation. Microparticles constitute the main reservoir of blood-borne tissue factor[23]. Elevated levels of microparticles have been encountered in systemic inflammatory disease, especially diseases with vascular involvement including acute coronary syndromes, where they appear indicative of a poor clinical outcome[23–26]. In the context of atherothrombosis both intact erythrocytes and erythrocyte derived microparticles could be acted as vehicles transferring DARC-bound chemokine ligands in sites of vascular damage. The chemokine content of erythrocyte microvesicles *in vivo* has not been assessed yet. Nevertheless, erythrocyte microparticles express DARK[24]. Moreover, *in vitro* and *ex vivo* data suggest that erythrocyte microvesicles have altered membrane properties compared to intact erythrocyte membranes and under stimulation they can increase chemokine bioavailability[25].

Atherosclerosis can also affect the morphology and function of erythrocytes. It has been proposed that reactive oxygen species produced in the course of atherosclerosis, lead to excessive cytoskeletal protein modification of erythrocytes. The modified erythrocytes are abnormally prone to vesiculation during mechanical stress *in vitro* and apparently *in vivo*. Although these data were originally obtained from sickle cell anaemia models this abnormality was successfully reproduced in normal erythrocytes by causing stress conditions using phenazine methosulfate (PMS)-induced stimulation of intracellular superoxide generation, a process similar to that occurring in sickle erythrocytes. Thus it could be that the genera-

tion of reactive oxygen species in atherosclerosis activates red blood cells, and microvesicles of red blood cells are formed, enhancing the activation of the vascular endothelium and leading to vascular inflammation and atherogenesis[26].

CXC chemokines and their receptors in atherosclerosis

Chemokine network in atherosclerosis

Chemokines are small secreted chemoattractant proteins (approximately 8–17 kDa) that serve as regulatory molecules in cellular trafficking and activation. Chemokines share considerable homology and most importantly, a conserved tetracysteine motif. They are classified into four sub-families based on the number and structural arrangement of conserved cysteine residues within their amino-terminal polypeptide sequence (Table 1)[27–29]. Chemokines induce cell activation by binding to specific seven-transmembrane G-protein coupled cell-surface receptors on target cells. Chemokines interact with their receptors on the cell surface leading to the generation of an intracellular signal via the G-protein complex, and subsequently to cell chemotaxis towards a chemokine gradient[27–29]. Cell movement and migration is driven by the dynamic assemblies of the actin cytoskeleton. In chemotaxis, chemokine gradients strongly bias this actin assembly to the cell's leading edge and, hence modify the direction of cell movement[30]. Decoy receptors–also known as interceptors (internalizing receptors)–, which bind chemokine ligands with high affinity but do not elicit signal transduction, include D6, DARC, and CCX-CKR[31]. Chemokine receptor CCX-CKR is a scavenger of CCR7 ligand chemokines while D6 is thought to act as a chemokine scavenger for pro-inflammatory CC chemokines. DARC is considered a decoy receptor for both CC and CXC motif chemokines while no data exist on its affinity for CX3C and XC chemokines (Table 1).

In the context of atherosclerotic cardiovascular disease the role of chemokine signalling is complex and not fully elucidated. In fact it seems that each stage of atherosclerosis is characterized by different chemokine-signalling[32]. In the early stages of atherosclerosis, oxLDL induces the expression of CCL2 (or monocyte chemoattractant protein 1) and CX3CL1, by vascular smooth muscle cells (SMCs) and endothelial cells (ECs)[32, 33]. CX3CL1 is a structurally unique chemokine that acts both as a chemoattractant and as a potent adhesion molecule through a non-integrin-dependent mechanism[34–36]. CCL2, secreted by ECs and SMCs, promotes structural changes in the cytoskeleton of CCR2-positive monocytes, potentiating transendothelial migration[34–36]. The interaction of CCL5 (or regulated on activation normal T cell expressed and secreted), with its receptor CCR1 is also considered an early pathway leading to the firm adhesion of rolling monocytes to stimulated ECs. Concurrently, CXC chemokines induced by interferon gamma, such as CXCL9, CXCL10, and CXCL11 expressed predominantly by ECs interact with CXCR3-positive T cells, inducing their accumulation and migration, and subsequently increasing the vascular inflammatory response[34-36]. Recruitment of neutrophils and vascular progenitor cells in atherosclerotic lesions is controlled by CXCR2 and CXCR4, and their ligands CXCL8 (or interleukin 8) and CXCL1 (or growth related oncogene-alpha). CXCL8 is highly expressed by lesion macrophages, as well as by ECs and SMCs. CXCL8 also promotes angiogenesis in advanced stages of plague development[33]. It is obvious that in the course of atherosclerosis, chemokines form a complicated network. Different chemokines promote different pathways. Moreover, the interaction of the same chemokine ligand with different receptors results in a different outcome. In such a complex system the consequences of a single pathway blockade cannot be predicted.

CXC chemokines in atherosclerosis

The CXC chemokines are the second largest class (Table 1)[33]. Since CXC chemokines are mainly neutrophil chemoattractants, they have received less attention concerning their role in the pathogenesis of atherosclerosis. However accumulating evidence–focusing mostly on CXCL8–supports a crucial role of CXC chemokines in vascular pathology. In 1996, Rus *et al* first reported high levels of CXCL8 in the human arterial atherosclerotic wall, as cellular and extracellular deposit in the connective tissue matrix[37]. Similarly, Apostolopoulos *et al* demonstrated the expression of CXCL8 in human atherosclerotic plaques by *in situ* hybridization and also identified the macrophages as the main source of CXCL8 in atherosclerotic plaques[38]. CXCL8 has been further shown to promote firm adhesion of rolling monocytes to endothelial monolayers expressing E-selectin while it was proposed to contribute in SMC proliferation and migration in more advance stages of atherogenesis[39, 40]. Boisvert *et al* provided direct evidence on the role of CXCL8 in atherosclerosis, demonstrating that LDL receptor knockout mice which were irradiated and repopulated with bone marrow cells lacking the murine homologue of CXCL8 receptor CXCR2 had less extensive lesions and fewer macrophages than those mice receiving bone marrow cells expressing the receptor[41]. Schwartz *et al* reported that CXCL1 an alternative ligand of CXCR2, contribute to the adhesion of monocytes to minimally modified-LDL stimulated ECs[42]. Similarly, Huo *et al*, using isolated carotid arteries from ApoE knockout mice demonstrated that CXCL1 but not CCL2 promotes monocyte arrest on the endothelium of atherosclerosis-prone vessels[43]. CXCL8 is not the only CXC chemokine that has been implicated in the pathways of atherogenesis. The chemokine receptor, CXCR3, has multiple high-affinity ligands including CXCL9 (or monokine induced by IFN-gamma), CXCL10 (or 10-kDa IFN-gamma-inducible protein) and CXCL11 (IFN-gamma-inducible T cell –chemoattrac–ant). Mach *et al* demonstrated different levels of expression of CXCL9, CXCL10, and CXCL11 by atheroma-associated cells and suggested a potential role for these 3 interferon gamma-inducible CXC chemokines in the recruitment and retention of activated T lymphocytes in atherosclerotic lesions[44]. Platelets represent both a source and a target of CXC chemokines[45]. Abi-Younes *et al* reported that, of the 16 chemokines tested, only CXCL12 (or stromal cell derived factor-alpha) induced platelet aggregation and proposed an involvement of

Table 1. Chemokine ligands and receptors.

Family	Chemo-kine	Chemokine receptor	Main cellular sources	Comments	Ref
CC	CCL1	CCR8	Tc, Ec	CC (or β) chemokines have no amino acid separating the amino-terminal cysteines. Twenty seven ligands have been identified up to now. (CCL9 is the same as CCL10). They mainly induce the migration of Mc, Tc, and NK cells.	28–33
	CCL2	CCR2	Ec, Mc/Mp, NK, SMc, Dc, F		
	CCL3	CCR1, CCR5	Ec, NK, T, Mc/Mp, N, Dc, mast cells		
	CCL4	CCR5	Ec, Tc, Mc/Mp, N, NK, Dc		
	CCL5	CCR1, CCR3, CCR5	Tc, Ec, Mc/Mp, SMc, N, Dc, P		
	CCL6	CCR1	Mc/Mp, F		
	CCL7	CCR1, CCR2, CCR3	Tc, Ec, Mc/Mp, F		
	CCL8	CCR1, CCR2, CCR3	F		
	CCL9	CCR1	Mc/Mp, DC		
	CCL10	CCR1	Mc/Mp, DC		
	CCL11	CCR3	SMc		
	CCL12	CCR2	Mast cells		
	CCL13	CCR1, CCR2, CCR3	Mc/Mp, Ec, Tc		
	CCL14	CCR1	Eepithelial cells		
	CCL15	CCR1, CCR3	Mc/Mp, Dc		
	CCL16	CCR1, CCR2, CCR5	Mc/Mp, Dc		
	CCL17	CCR4	Mc/Mp, Dc		
	CCL18	Unknown	Mc/Mp, Dc		
	CCL19	CCR7, CCR10	Mc/Mp, SMc, Dc		
	CCL20	CCR6	N, Mc/Mp, Dc		
	CCL21	CCR7, CCR10	Dc		
	CCL22	CCR4	Mc/Mp, Dc		
	CCL23	CCR1	EC, Mc/Mp		
	CCL24	CCR3	Eepithelial cells		
	CCL25	CCR9	Dc		
	CCL26	CCR3	Ec, F		
	CCL27	CCR10	K		
	CCL28	CCR3, CCR10	K, epithelial cells, Mc/Mp		
CXC	CXCL1	CXCR1	Ec, Mc/Mp, NK, F	CXC (or α) chemokines have a single amino acid separating the two amino-terminal cysteine residues of the protein. They are further distinguished by the presence or absence of an amino acid sequence, glutamic acid-leucine arginine (ELR motif), which precedes the CXC sequence. ELR motif CXC chemokines are chemotactic *in vitro* for neutrophils but not for mononuclear cells. ELR negative CXC chemokines exhibit chemotactic activity toward monocytes and lymphocytes.	28–33
	CXCL2	CXCR2	Ec		
	CXCL3	CXCR2	Mc/Mp		
	CXCL4	CXCR2	Tc, P, Mc/Mp		
	CXCL5	CXCR3	N		
	CXCL6	CXCR1, CXCR2	Ec		
	CXCL7	CXCR2	Megakaryocytes		
	CXCL8	CXCR1, CXCR2	Tc, Mc/Mp, Ec, Dc, N, SMc, F		
	CXCL9	CXCR3	Ec, Mc/Mp, N, SMc, F		
	CXCL10	CXCR3	Tc, Ec, Mc/Mp, DC		
	CXCL11	CXCR3, CXCR7	Ec, Mc/Mp, SMc, mast cells, F		
	CXCL12	CXCR4, CXCR7	Ec, SMc, Mc/Mp, Dc,		
	CXCL13	CXCR5	Mc/Mp, Dc		
	CXCL14	Unknown	F		
	CXCL15	Unknown	Epithelial cells		
	CXCL16	CXCR6	Mc/Mp, Dc		
	CXCL17	Unknown	Dc		
C	XCL1	XCR1	NK, Tc	C chemokines lack two of the four conserved cysteines in the mature protein. They recruit Tc and NK cells.	28
	XCL2	XCR1	NK, Tc		
CX3C	CX3CL1	CX3CR1	Ec, Mc/Mp, SMc, Dc	Include an amino-terminal domain with a novel arrangement of three amino acids separating their first two cysteines. It exists as membrane-bound and in soluble form acting both as a chemoattractant and as an adhesion molecule mainly for Mc/Mp and Tc.	28, 33

(Continued)

Table 1. Chemokine ligands and receptors.

Family	Chemo-kine	Chemokine receptor	Main cellular sources	Comments	Ref
Interceptors		D6		A chemokine scavenger for pro-inflammatory CC chemokines.	31
		DARC		Decoy receptor for both CC and CXC motif chemokines.	21, 22
		CCX-CKR		A scavenger of CCR7 ligand chemokines.	31

Tc, T lymphocytes; NK, natural killer cells; Ec, endothelial cells; N, neutrophils; Mc/Mp, monocytes/macrophages; P, platelets; F, fibroblasts; Dc, dendritic cells; K, keratinocyte; DARC, Duffy antigen receptor for chemokines.

CXCL12 in the pathogenesis of atherosclerosis and thrombo-occlusive disease[46]. Additionally, Schober *et al* assessed the role of CXCL12 in neointimal formation after vascular injury. CXCL12 was detected in the carotid arteries of ApoE knock-out mice after wire-induced injury and was mostly located at sites of SMCs accumulation. Treatment of ApoE knockout mice after carotid injury with a neutralizing CXCL12 monoclonal antibody reduced neointimal lesion area, and decreased neointimal SMC content without influencing the relative content of neointimal macrophages. Thus, the authors concluded that CXCL12 played an active role in neointimal formation after vascular injury[47]. CXCL4 (or platelet factor 4) a CXC-chemokine member secreted by platelets, induces monocyte activation, firm adherence of neutrophils on shear stressed ECs, and release of neutrophil granule components[48, 49]. Pitsilos *et al* detected CXCL4 in the cytoplasm of luminal and neovascular endothelium, in macrophages and in regions of plaque calcification[50]. Yu *et al* demonstrated that E-selectin, is up-regulated in human umbilical vein endothelial cells exposed to CXCL4[51]. Finally, Nassar *et al* showed that CXCL4 bound to oxidized LDL directly, and also increased oxidized LDL binding to vascular cells and macrophages, thus demonstrating an alternative mechanism by which platelet activation at sites of vascular injury may promote the accumulation of lipoproteins[52].

Erythrocytes as reservoirs/regulators of CXC chemokines

DARC receptors on erythrocytes

The current theory on erythrocytic DARC suggests that it acts as a regulator of chemokine activity. Since DARC is unable to initiate intracellular signals it is considered a negative regulator of chemokine signalling. However, current experimental data are unclear and sometimes conflicting and the exact role of erythrocyte DARC *in vivo* remains unclear. The function of this chemokine reservoir on the erythrocyte surface, and the fate of these chemokines at the end of the erythrocyte lifespan are essential pathways that still need to be elucidated. Increasing experimental evidence suggests that DARC on venular endothelium mediates chemokine internalization at the abluminal surface followed by transcytosis and transport of the chemokine load onto the luminal surface. DARC expressed on the erythrocyte membrane binds plasma chemokines resulting in neutralization of chemokines in the blood. This leads to leukocyte protection from unintended "desensitization" and enhancement of leukocyte recruitment[53]. The current concept on Duffy antigen's biological role is summarized in Figure 1.

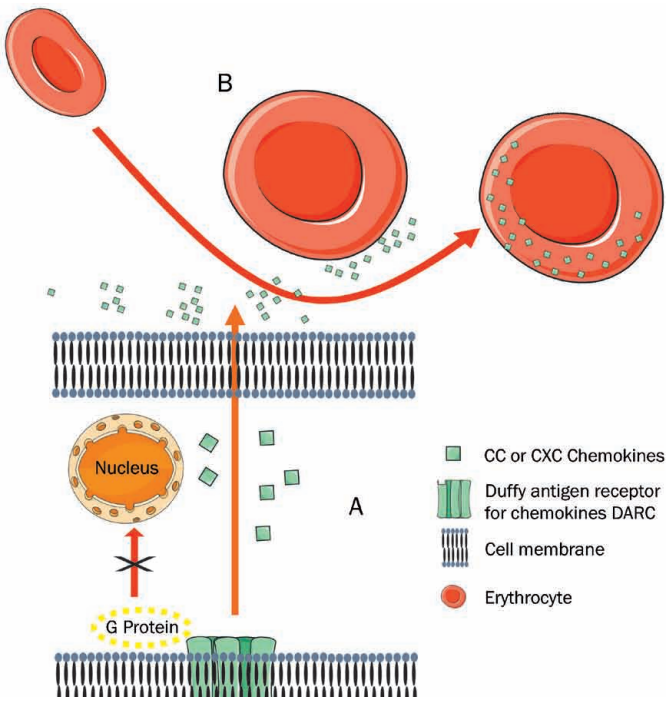

Figure 1. Schematic presentation of Duffy antigen's presumed biological action: Duffy antigen expressed on endothelial cells binds and internalizes chemokine ligands creating a transendothelial chemokine gradient (A), while Duffy antigen expressed on erythrocytes binds excess circulating chemokines. Despite structural homology with G-coupled chemokine receptors Duffy antigen cannot create a secondary message.

An important issue that had to be addressed early in DARC research was the impact of Duffy antigen activity on levels of circulating chemokines. If DARC positive erythrocytes serve as a reservoir for circulating chemokines then individuals carrying the DARC negative genotype or DARC loss of function polymorphisms should have higher levels of chemokines following an inflammatory stimulus. Dawson *et al* assessed indirectly this matter in a model of DARC negative mice. The authors demonstrated an increased number of neutrophils in organs of DARC deficient mice following intraperitoneal

injection of lipopolysaccharide (LPS)[54]. Similarly in a model of human disease Nebor *et al* reported higher plasma levels of CXCL8 and CCL5 in Duffy negative patients with sickle cell anaemia[55]. Accordingly, in a genome wide analysis to identify the genetic basis of variance in circulating concentrations of CCL2, Schnabel *et al* concluded that the stronger predictor of CCL2 levels was a nonsynonymous polymorphism, (rs12075) in DARC gene[56]. Similarly, Lee *et al* utilized an in vitro model based on whole blood derived from humans currying "loss-of-function" genotypes of the DARC gene. The authors reported that plasma CXCL8 and CCL2 concentrations from humans homozygous for a "loss of function" DARC polymorphism were higher than in heterozygotes following LPS stimulation of their whole blood *in vitro*[57]. Finally, direct evidence of the impact of DARC phenotype on chemokine activity came from a pharmacokinetic study. Mayr *et al* assessed the impact of DARC phenotype on the pharmacokinetics of infused recombinant human CCL2. In a randomized, double-blinded, placebo-controlled dose escalation trial the authors demonstrated that DARC negative individuals reached maximal plasma levels significantly earlier. Despite the fact that overall plasma concentration profiles were not altered the investigators provided direct evidence that DARC influences the kinetics of chemokines *in vivo*[58]. Moreover, the latter observation implies the presence of alternative pathways of chemokine homeostasis and disserves further investigation.

DARC and atherosclerosis: *In vitro* and *in vivo* derived evidence

Chemokine signalling has been a critical part of vascular inflammation and a leading field of investigation the last three decades. A regulatory point in the early stages of atherogenesis is accumulation and migration of circulating leukocytes into the intima of the vessel wall[33]. Chemokines promote this stage of atherogenesis by creating a chemotactic gradient that mobilizes the inflammatory cells towards the area of increased chemokine concentration[33]. Endothelial DARC has been proved essential in creating and preserving a transcellular chemokine gradient that promotes intercellular or transcellular leukocyte migration. Pruenster *et al* demonstrating that DARC, like other silent receptors, internalized chemokines but did not effectively scavenge them. Instead, DARC mediated chemokine transcytosis, which led to apical retention of intact chemokines. Subsequently, a constant transcellular chemokine gradient led to more leukocyte migration across monolayers expressing DARC[59]. Despite the fact that the endothelial DARC activity fits perfectly in the inflammatory model underlying plaque formation there is no direct evidence linking DARC mediated pathways and atherosclerosis. In fact the only available data in the field of cardiovascular disease refer to the erythrocyte DARC and its ability to bind CXCL8. de Winter *et al* investigated whether rapid clearance of CXCL8 from plasma through binding to the erythrocyte DARC may be responsible for failure to detect CXCL8 consistently after acute myocardial infarction. The investigators measured plasma concentrations of CXCL8 and erythrocyte bound CXCL8 post myocardial infarction and concluded that CXCL8 was released in plasma after acute myocardial infarction and subsequently bound to red blood cells; resulting in only a transient rise of plasma CXCL8 and a more prolonged increase of erythrocyte bound CXCL8[60].

Erythrocytes have been also implicated in atherosclerotic plaque destabilization. Histopathology studies support this hypothesis since they have identified erythrocyte membranes in the atherosclerotic plaque and also have shown an association between the presence of erythrocytes and plaque vulnerability[12, 13, 61]. Haemorrhages within the plaque (intraplaque haemorrhage), arising from rupture of intraplaque micro-vessels and "healed" erosions of the atherosclerotic plaque have been proposed as major mechanisms by which erythrocytes can reach the atherosclerotic plaque[17, 20]. Since erythrocytes carry on their surface DARC-bound pro-inflammatory chemokines it is possible that they release their pro-inflammatory load –including CXCL8–, when extravasated in lesion area. The latter phenomenon could initiate an inflammatory cascade that would lead to plaque rupture. We have recently reported an association between CXCL8 concentrations on erythrocyte membranes and clinical instability in coronary artery disease that further supports the above hypothesis[10, 62]. However, the exact biochemical pathways following the extravasation of erythrocytes in the atherosclerotic milieu, the kinetics and activity of their membrane chemokines and the associated ligands has not been studied in detail and deserves further investigation.

Future perspectives

Erythrocytes as regulators of inflammation in atherosclerosis

Published data have shown that erythrocyte membranes are characterized by a multispecific cell surface receptor that has the capacity to bind a wide variety of inflammatory peptides of both major chemokine families[21, 22]. The main characteristics of the DARC receptor may be summarized as follows: a) it is multi-specific; b) it is unable to initiate intracellular signals, and c) chemokines bound to erythrocyte surface are inaccessible to their normal target inflammatory cells[21, 22]. DARC presence on erythrocytes' membranes and its unique functional features suggest a crucial role for these cells in the regulation of inflammatory processes.

In general cytokines are presumed to be circulating soluble plasma proteins[22]. No other cell type –apart from erythrocytes– is known to act as a reservoir for signal transduction peptides[22]. Furthermore, the 1000-fold greater abundance of erythrocytes over immune-related circulating cells in blood accounts for the significance of their role in chemokine homeostasis in sites of vascular inflammation[22].

More importantly, atherosclerotic vasa vasorum are characterized by compromised structural integrity[63]. The aforementioned leaky and fragile morphology of plaque neovessels may lead to extensive erythrocyte infiltration or to intraplaque haemorrhage[63]. Erythrocytes and their membranes' inflammatory arsenal could thus reach the atherosclerotic plaque and exert their regulatory role at local lesional level. A wide variety of inflammation-related modulator roles may be attributed

to erythrocytes. Although not proven till today, erythrocytes can possibly release their chemokine load within the plaque thus fuelling the inflammatory process. Conversely, erythrocytes might scavenge locally produced chemokines with their uncoupled receptors therefore cooling the inflammatory cascade.

From bench to bedside

The role of erythrocytes as a sink for chemokines could inspire numerous diagnostic and therapeutic applications. The chemokine content of circulating erythrocyte membranes could be used as a prognostic marker of future acute ischemic events, since the augmentation of atherosclerotic lesion inflammation is well associated with plaque's instability. The density of uncoupled DARC receptors on erythrocyte membranes could on the other hand be used as a protective marker regarding clinical instability in coronary artery disease. Finally, the use of DARC receptors as vehicles for local delivery of inflammatory regulators –ie, CXC receptors blocking peptides reflects another therapeutic potential that deserves further investigation.

In conclusion, the key points of the present article can be summarised as follows:

Erythrocytes carry multispecific receptors on their membrane that can bind a wide array of chemokines. CXC chemokines –high affinity ligands for DARC receptors– have been shown to modulate the inflammatory cascade within the atherosclerotic plaque.

Erythrocytes have been identified within atherosclerotic plaques and their role in promoting plaque growth and instability has also been established.

Considerable more data will be needed to elucidate the role of erythrocyte DARC in atherosclerosis and establish its role as a novel diagnostic and therapeutic target.

References

1 Cutbush M, Mollison PL, The Duffy blood group system. Heredity 1950; 4: 383–9.
2 Lewis M, Kaita H, Chown B. The Duffy blood group in caucasians: A further population sample. Vox Sang 1972; 23: 523–7.
3 Pogo AO, Chaudhuri A. The Duffy protein: a malarial and chemokine receptor. Semin Hematol 2000; 37: 122–9.
4 Reich D, Nalls MA, Kao WH, Akylbekova EL, Tandon A, Patterson N, *et al*. Reduced neutrophil count in people of African descent is due to a regulatory variant in the Duffy antigen receptor for chemokines gene. PLoS Genet 2009; 5: e1000360.
5 Pruenster M, Rot A. Throwing light on DARC. Biochem Soc Trans 2006; 34: 1005–8.
6 Meny GM. The Duffy blood group system: a review. Immunohematology 2010; 26: 51–6.
7 Hadley TJ, Peiper SC. From malaria to chemokine receptor: the emerging physiologic role of the Duffy blood group antigen. Blood 1997; 89: 3077–91.
8 Neote K, Malk JY, Kolakowski LF, Schall TJ. Functional and biochemical analysis of the cloned Duffy antigen: identity with the red blood cell chemokine receptor. Blood 1994; 84: 44–52.
9 Hellings WE, Peeters W, Moll FL, Pasterkamp G. From vulnerable plaque to vulnerable patient: the search for biomarkers of plaque destabilization. Trends Cardiovasc Med 2007; 17: 162–71.
10 Tziakas DN, Chalikias GK, Stakos D, Boudoulas H. The role of red blood cells in the progression and instability of atherosclerotic plaque. Int J Cardiol 2010; 142: 2–7.
11 Virmani R, Roberts WC. Extravasated erythrocytes, iron, and fibrin in atherosclerotic plaques of coronary arteries in fatal coronary heart disease and their relation to luminal thrombus: frequency and significance in 57 necropsy patients and in 2958 five mm segments of 224 major epicardial coronary arteries. Am Heart J 1983; 105: 788–97.
12 Arbustini E, Morbini P, D'Armini AM, Repetto A, Minzioni G, Piovella F, *et al*. Plaque composition in plexogenic and thromboembolic pulmonary hypertension: the critical role of the thrombotic material in pultaceous core formation. Heart 2002; 88: 177–82.
13 Kolodgie FD, Gold HK, Burke AP, Fowler DR, Kruth HS, Weber DK, *et al*. Intraplaque hemorrhage and progression of coronary atheroma. N Engl J Med 2003; 349: 2316–25.
14 Minetti M, Agati L, Malorni W. An emerging concept in cardiovascular disease is the role of the erythrocyte as a "barometer" of overall cardiovascular health. The microenvironment can shift erythrocytes from a friendly to harmful behavior: pathogenic implications for vascular diseases. Cardiovasc Res 2007; 75: 21–8.
15 Yeagle PL. Cholesterol and the cell membrane. Biochim Biophys Acta 1985; 822: 267–87.
16 Yuan XM, Brunk UT, Olsson AG. Effects of iron- and hemoglobin-loaded human monocyte-derived macrophages on oxidation and uptake of LDL. Arterioscler Thromb Vasc Biol 1995; 15: 1345–51.
17 Virmani R, Kolodgie FD, Burke AP, Finn AV, Gold HK, Tulenko TN, *et al*. Atherosclerotic plaque progression and vulnerability to rupture: Angiogenesis as a source of intraplaque hemorrhage. Arterioscler Thromb Vasc Biol 2005; 25: 2054–61.
18 Tziakas DN, Kaski JC, Chalikias GK, Romero C, Fredericks S, Tentes IK, *et al*. Total cholesterol content of erythrocyte membranes is increased in patients with acute coronary syndrome. J Am Coll Cardiol 2007; 49: 2081–9.
19 Tziakas DN, Chalikias GK, Stakos D, Tentes IK, Chatzikyriakou SV, Mitrousi K, *et al*. Cholesterol composition of erythrocyte membranes and its association with clinical presentation of coronary artery disease. Coron Artery Dis 2008; 19: 583–90.
20 Moreno P, Purushothaman KR, Sirol M, Levy AP, Fuster V. Neovascularization in human atherosclerosis. Circulation 2006; 113: 2245–52.
21 Neote K, Darbonne W, Ogez J, Horuk R, Schall TJ. Identification of a promiscuous inflammatory peptide receptor on the surface of red blood cells. J Biol Chem 1993; 268: 12247–9.
22 Darbonne WC, Rice GC, Mohler MA, Apple T, Hebert CA, Valente AJ, *et al*. Red blood cells are a sink for interleukin-8, a leukocyte chemotaxin. J Clin Invest 1991; 88: 1362–9.
23 Rubin O, Crettaz D, Tissot JD, Lion N. Microparticles in stored red blood cells: submicron clotting bombs? Blood Transfus 2010; 8: s31–s8.
24 Oreskovic RT, Dumaswala UJ, Greenwalt TJ. Expression of blood group antigens on red cell microvesicles. Transfusion 1992; 32: 848–9.
25 Xiong Z, Cavaretta J, Qu L, Stolz DB, Triulzi D, Lee JS. Red blood cell microparticles show altered inflammatory chemokine binding and release ligand upon interaction with platelets. Transfusion 2011; 51: 610–21.
26 Blum A. The possible role of red blood cell microvesicles in atherosclerosis. Eur J Intern Med 2009; 20: 101–5.
27 Luster AD. Chemokines - chemotactic cytokines that mediate inflammation. N Engl J Med 1998; 338: 436–45.
28 Apostolakis S, Papadakis EG, Krambovitis E, Spandidos DA. Chem-

okines in vascular pathology (review). Int J Mol Med 2006; 17: 691–701.
29 Shimizu K, Mitchell RN. The role of chemokines in transplant graft arterial disease. Arterioscler Thromb Vasc Biol 2008; 28; 1937–49.
30 Jin T, Xu X, Hereld D. Chemotaxis, chemokine receptors and human disease. Cytokine 2008; 44: 1–8.
31 Comerford I, Nibbs RJ. Post-translational control of chemokines: a role for decoy receptors? Immunol Lett 2005; 96: 163–74.
32 Zernecke A, Shagdarsuren E, Weber C. Chemokines in atherosclerosis: an update. Arterioscler Thromb Vasc Biol 2008; 28: 1897–908.
33 Apostolakis S, Vogiatzi K, Amanatidou V, Spandidos DA. Interleukin 8 and cardiovascular disease. Cardiovasc Res 2009; 84: 353–60.
34 Weber C, Schober A, Zernecke A. Chemokines: key regulators of mononuclear cell recruitment in atherosclerotic vascular disease. Arterioscler Thromb Vasc Biol 2004; 24: 1997–2008.
35 Barlic J, Murphy PM. Chemokine regulation of atherosclerosis. J Leukoc Biol 2007; 82: 226–36.
36 Weber KS, von Hundelshausen P, Clark-Lewis I, Weber PC, Weber C. Differential immobilization and hierarchical involvement of chemokines in monocyte arrest and transmigration on inflamed endothelium in shear flow. Eur J Immunol 1999; 29: 700–12.
37 Rus HG, Vlaicu R, Niculescu F. Interleukin-6 and interleukin-8 protein and gene expression in human arterial atherosclerotic wall. Atherosclerosis 1996; 127: 263–71.
38 Apostolopoulos J, Davenport P, Tipping PG. Interleukin-8 production by macrophages from atheromatous plaques. Arterioscler Thromb Vasc Biol 1996; 16: 1007–12.
39 Yue TL, Wang X, Sung CP, Olson B, McKenna PJ, Gu JL, *et al*. Interleukin-8. A mitogen and chemoattractant for vascular smooth muscle cells. Circ Res 1994; 75: 1–7.
40 Gerszten RE, Garcia-Zepeda EA, Lim YC, Yoshida M, Ding HA, Gimbrone MA Jr, *et al*. MCP-1 and IL-8 trigger firm adhesion of monocytes to vascular endothelium under flow conditions. Nature 1999; 398: 718–23.
41 Boisvert WA, Santiago R, Curtiss LK, Terkeltaub RA. A leukocyte homologue of the IL-8 receptor CXCR-2 mediates the accumulation of macrophages in atherosclerotic lesions of LDL receptor-deficient mice. J Clin Invest 1998; 101: 353–63.
42 Schwartz D, Andalibi A, Chaverri-Almada L, Berliner JA, Kirchgessner T, Fang ZT, *et al*. Role of the GRO family of chemokines in monocyte adhesion to MM-LDL-stimulated endothelium. J Clin Invest 1994; 94: 1968–73.
43 Huo Y, Weber C, Forlow SB, Sperandio M, Thatte J, Mack M, *et al*. The chemokine KC, but not monocyte chemoattractant protein-1, triggers monocyte arrest on early atherosclerotic endothelium. J Clin Invest 2001; 108: 1307–14.
44 Mach F, Sauty A, Iarossi AS, Sukhova GK, Neote K, Libby P, *et al*. Differential expression of three T lymphocyteactivating CXC chemokines by human atheroma-associated cells. J Clin Invest 1999; 104: 1041–50.
45 Gear AR, Camerini D. Platelet chemokines and chemokine receptors: linking hemostasis, inflammation, and host defense. Microcirculation 2003; 10: 335–46.
46 Abi-Younes S, Sauty A, Mach F, Sukhova GK, Libby P, Luster AD. The stromal cell-derived factor-1 chemokine is a potent platelet agonist highly expressed in atherosclerotic plaques. Circ Res 2000; 86: 131–8.
47 Schober A, Knarren S, Lietz M, Lin EA, Weber C. Crucial role of stromal cell-derived factor-1alpha in neointima formation after vascular injury in apolipoprotein E-deficient mice. Circulation 2003; 108: 2491–7.
48 Petersen F, Bock L, Flad HD, Brandt E. Platelet factor 4-induced neutrophil-endothelial cell interaction: involvement of mechanisms and functional consequences different from those elicited by interleukin-8. Blood 1999; 94: 4020–8.
49 Engstad CS, Lia K, Rekdal O, Olsen JO, Osterud B. A novel biological effect of platelet factor 4 (PF4): enhancement of LPS induced tissue factor activity in monocytes. J Leukoc Biol 1995; 58: 575–81.
50 Pitsilos S, Hunt J, Mohler ER, Prabhakar AM, Poncz M, Dawicki J, *et al*. Platelet factor 4 localization in carotid atherosclerotic plaques: correlation with clinical parameters. Thromb Haemost 2003; 90: 1112–20.
51 Yu G, Rux AH, Ma P, Bdeir K, Sachais BS. Endothelial expression of E-selectin is induced by the plateletspecific chemokine platelet factor 4 through LRP in an NF-kappaB dependent manner. Blood 2005; 105: 3545–51.
52 Nassar T, Sachais BS, Akkawi S, Kowalska MA, Bdeir K, Leitersdorf E, *et al*. Platelet factor 4 enhances the binding of oxidized low-density lipoprotein to vascular wall cells. J Biol Chem 2003; 278: 6187–93.
53 Rot A. Contribution of Duffy antigen to chemokine function. Cytokine Growth Factor Rev 2005; 16: 687–94.
54 Dawson TC, Lentsch AB, Wang Z, Cowhig JE, Rot A, Maeda N, *et al*. Exaggerated response to endotoxin in mice lacking the Duffy antigen/receptor for chemokines (DARC). Blood 2000; 96: 1681–4.
55 Nebor D, Durpes MC, Mougenel D, Mukisi-Mukaza M, Elion J, Hardy-Dessources MD, *et al*. Association between Duffy antigen receptor for chemokines expression and levels of inflammation markers in sickle cell anemia patients. Clin Immunol 2010; 136: 116–22.
56 Schnabel RB, Baumert J, Barbalic M, Dupuis J, Ellinor PT, Durda P, *et al*. Duffy antigen receptor for chemokines (Darc) polymorphism regulates circulating concentrations of monocyte chemoattractant protein-1 and other inflammatory mediators. Blood 2010; 115: 5289–99.
57 Lee JS, Frevert CW, Wurfel MM, Peiper SC, Wong VA, Ballman KK, *et al*. Duffy antigen facilitates movement of chemokine across the endothelium *in vitro* and promotes neutrophil transmigration *in vitro* and *in vivo*. J Immunol 2003; 170; 5244–51.
58 Mayr FB, Spiel AO, Leitner JM, Firbas C, Schnee J, Hilbert J, *et al*. Influence of the Duffy antigen on pharmacokinetics and pharmacodynamics of recombinant monocyte chemoattractant protein (MCP-1, CCL-2) *in vivo*. Int J Immunopathol Pharmacol 2009; 22: 615–25.
59 Pruenster M, Mudde L, Bombosi P, Dimitrova S, Zsak M, Middleton J, *et al*. The Duffy antigen receptor for chemokines transports chemokines and supports their promigratory activity. Nat Immunol 2009; 10: 101–8.
60 de Winter RJ, Manten A, de Jong YP, Adams R, van Deventer SJ, Lie KI. Interleukin 8 released after acute myocardial infarction is mainly bound to erythrocytes. Heart 1997; 78: 598–602.
61 Lin HL, Xu XS, Lu HX, Zhang L, Li CJ, Tang MX, *et al*. Pathological mechanisms and dose dependency of erythrocyte-induced vulnerability of atherosclerotic plaques. J Mol Cell Cardiol 2007; 43: 272–80.
62 Tziakas DN, Chalikias GK, Tentes IK, Stakos D, Chatzikyriakou SV, Mitrousi K, *et al*. Interleukin-8 is increased in the membrane of circulating erythrocytes in patients with acute coronary syndrome. Eur Heart J 2008; 29: 2713–22.
63 Sluimer JC, Kolodgie FD, Bijnens AP, Maxfield K, Pacheco E, Kutys B, *et al*. Thin-walled microvessels in human coronary atherosclerotic plaques show incomplete endothelial junctions relevance of compromised structural integrity for intraplaque microvascular leakage. J Am Coll Cardiol 2009; 53: 1517–27.

Acta Pharmacologica Sinica (2011) 32: 425–432
 1671-4083/11 $32.00
www.nature.com/aps

Original Article

Promoting effects of isobavachin on neurogenesis of mouse embryonic stem cells were associated with protein prenylation

Dan-yin WANG[1], Yu-zhe HU[1, #], Si-si KONG[1, #], Yong-ping YU[2], Dan-yan ZHU[1, *], Yi-jia LOU[1, *]

[1]*Division of Cardio-Cerebral Vascular and Hepatic Pharmacology, College of Pharmaceutical Sciences, Zhejiang University;* [2]*Institute of Materia Medica, Zhejiang University, Hangzhou 310058, China*

Aim: Some small molecules can induce mouse embryonic stem (ES) cells to differentiate into neuronal cells. Here, we explored the effect of isobavachin (IBA), a compound with a prenyl group at position 8 of ring A, on promoting neuronal differentiation and the potential role of its protein prenylation.
Methods: The hanging drop method was employed for embryonic body (EB) formation to mimic embryo development *in vivo*. The EBs were treated with IBA at a final concentration of 10^{-7} mol/L from EB stage (d 4) to d 8+10. Geranylgeranyltransferase I inhibitor GGTI-298 was subsequently used to disrupt protein prenylation. Neuronal subtypes, including neurons and astrocytes, were observed by fluorescence microscopy. Gene and protein expression levels were detected using RT-PCR and Western blot analysis, respectively.
Results: With IBA treatment, nestin was highly expressed in the neural progenitors generated from EBs (d 4, d 8+0). EBs then further differentiated into neurons (marked by β-tubulin III) and astrocytes (marked by GFAP), which were both up-regulated in a time-dependent manner on d 8+5 and d 8+10. Co-treatment with GGTI-298 selectively abolished the IBA-induced neuronal differentiation. Moreover, in the MAPK pathway, p38 and JNK phosphorylation were down-regulated, while ERK phosphorylation was up-regulated after IBA treatment at different neuronal differentiation passages.
Conclusion: IBA can facilitate mouse ES cells differentiating into neuronal cells. The mechanism involved protein prenylation and, subsequently, phos-ERK activation and the phos-p38 off pathway.

Keywords: mouse embryonic stem cells; isobavachin; neurogenesis; protein prenylation; ERK; MAPK; p38

Acta Pharmacologica Sinica (2011) 32: 425–432; doi: 10.1038/aps.2011.5; published online 28 Mar 2011

Introduction

Embryonic stem (ES) cells are pluripotent cells that have the capacity to continuously proliferate while retaining the potential to differentiate into three germ cells (cells derived from the end-, mes-, and ectoderm).

Mouse ES cells or their derivatives have been widely studied in the field of developmental biology, drug discovery and regenerative medicine[1–3]. Small molecules offer distinct advantages for the differentiation of mouse ES cells and are useful tools to facilitate therapeutic applications. Moreover, small molecules can provide temporal control over protein functions, inducing rapid activation or inhibition, and the effects are often reversible and can be adjusted by varying the concentrations of small molecules[3, 4]. Furthermore, a single small molecule can simultaneously regulate multiple specific targets within a protein family or across various protein families[5]. Small molecules for neuronal differentiation from mouse ES cells have received increasing attention as potential treatments for neurodegenerative diseases, such as Alzheimer's and Parkinson's diseases[6, 7]. However, there still remains a question about how small molecules direct and control the neuronal differentiation of mouse ES cells[8]. Recently, several small molecules have been reported to have neuronal differentiation ability. We have previously demonstrated that prenylflavonid compounds, such as icaritin[9], can promote neuronal differentiation of ES cells in an estrogen receptor-independent manner *in vitro*[9]. However, the structure-related neuronal differentiation mechanisms are still poorly understood. It is, therefore, important to identify the intrinsic or extrinsic factors that regulate the underlying molecular mechanisms involved in ES cell self-renewal, proliferation and neuronal differentiation[8]. Thus, isobavachin (IBA, Figure 1),

Undergraduate students in Research Training Project at Zhejiang University.
* To whom correspondence should be addressed.
E-mail zdyzxb@zju.edu.cn (Dan-yan ZHU);
yijialou@zju.edu.cn (Yi-jia LOU)
Received 2010-09-29 Accepted 2011-01-12

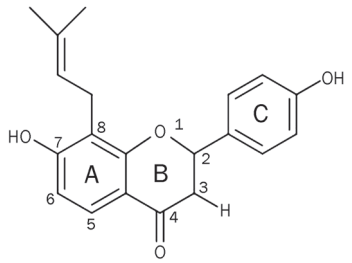

Figure 1. Chemical structure of isobavachin (IBA).

a prenylflavonid compound with a prenyl group at position 8 of ring A, was used to evaluate the possible differentiation effects and potential mechanisms.

Protein prenylation is a process of posttranslational modification present in a great number of proteins[10]. It has been proposed to be responsible for membrane association and protein-protein interactions, which contribute to its role in signal transduction pathways[11, 12]. Geranylgeranyltransferase I (GGTase I) is necessary for protein prenylation and is involved in cell survival, proliferation, and migration[12, 13]. GGTase I is also associated with the mitogen-activated protein kinase (MAPK) pathway[10]. The MAPK pathway regulates cell survival, proliferation, differentiation and motility[14, 15], such as the case of differentiation of mouse ES cells[15–17]. In the MAPK pathway, sustained activation or phosphorylation of extracellular signal-regulated kinase (ERK) is a specific requirement for the neural lineage commitment[8] and is associated with neuritis formation and neuron survival during ES cells differentiation[16]. In addition to ERK, p38MAPK phosphorylation is also activated during early mouse ES cell differentiation[8, 15]. This was proved to be a trigger in determining the ES cell differentiation fate[15]. The control of p38MAPK activity constitutes an early switch in ES cell commitment into cardiomyocytes and neurons[18]. Moreover, JNK MAPK phosphorylation has neuronal protective effects[19]. Thus, distinct mouse ES cell lineage commitment programs are likely regulated by the integrated action of multiple signaling mechanisms[20]. However, whether prenylflavonid compounds are prenylated by GGTase I catalysis and whether prenylflavonid compounds can in turn activate the MAPK signaling pathway associated with neuronal differentiation has not been reported. Here, we explore the protein prenylation effect of IBA and the subsequent MAPK pathway.

Our data demonstrated that IBA can promote neuronal differentiation from mouse ES cells. The mechanism involved protein prenylation and, subsequently, phos-ERK activation and the phos-P38/JNK off pathway.

Materials and methods

Materials

IBA was prepared according to the existing protocol[21]. Retinoic acid (RA), dimethylsulfoxide (DMSO), 4,6-diamidino-2-phenylindole (DAPI), and β-mercaptoethanol (β-ME) were purchased from Sigma-Aldrich (St Louis, MO, USA). DMEM medium, neural basal medium, B27 supplement, fetal bovine serum (FBS) and GGTI-298 were obtained from Gibco BRL (Burlington, Ontario, Canada). Non-essential amino acid (NEAA) stock solution was purchased from Hyclon (Logan, UT, USA). Recombinant mouse leukemia inhibitory factor (LIF), primary antibodies against neural specific markers β-tubulin III, neurofilament (NEFM), and JNK were purchased from Chemicon (CA, USA). ERK (Cat #9102) primary antibodies against GFAP, p38, phos-p38, phos-ERK, phos-JNK, and GAPDH were purchased from Cell Signaling. The HRP conjugated secondary antibodies (bovine anti-goat IgG-HRP, sc-2350, bovine anti-rabbit IgG-HRP, sc-2370, goat anti-mouse IgG-HRP, sc-2005) were purchased from Santa Cruz, Inc (CA, USA).

Cell culture and differentiation scheme

Mouse ES cells (D3 line, American Type Culture Collection, CRL-1934)[22] were routinely cultured on primary cultured mouse embryonic fibroblasts (MEF) cells in DMEM, supplemented with 10% FBS, 0.1 mmol/L β-mercaptoethanol (β-ME), 1×NEAA and 1×10^6 U/L LIF[23]. The experiment conformed to the Guide for the Care and Use of Laboratory Animals published by the United States National Institutes of Health, and approval was granted by Ethics Review Board of Zhejiang University. A hanging drop method[24–26] was used to initiate embryonic body (EB) formation in differentiation medium. A typical 4-/4+ protocol was used to induce neuronal differentiation[27]. Briefly, drops (30 μL) containing approximately 900 ES cells were gently dropped on the lids of Petri dishes and were cultured for 2 d in hanging drops. After EB formation, they were transferred to agar-coated Petri dishes and cultured in suspension for another 2 d. On d 4, IBA (10^{-7} mol/L) was added to the medium, and EBs were cultured in suspension for another 4 d. As indicated, GGTase I inhibitor GGTI-298 (10^{-6} mol/L) was added into the medium with IBA during differentiation. On d 8+0, EBs were planted on poly-*D*-lysine-coated culture plates in differentiation medium (neural basal medium and 1% B27 supplement) with IBA to induce neuronal differentiation. A culture treated with 10^{-7} mol/L RA was used as a positive control, and 0.1% DMSO was used as a solvent control.

Morphological evaluation

To evaluate the morphological changes during differentiation, an inverted microscope with a phase-contrast optic lens was used. Images were captured by a Leica DFC300 FX camera device, and the images were processed using Image-Pro Plus version 5.1 software (Media Cybernetics, MA, USA). Morphological evaluation was performed according to the existing protocol[28] with some modification. The cells with axons at least three times longer than the size of their cell bodies were considered to be neuron-like cells.

Immunocytochemistry analysis

Immunostaining with cell markers was used to confirm the

cell subtypes[29]. Cultures were washed with PBS solution and then fixed for 15 min in ice-cold methanol containing 0.3% hydrogen peroxide. Fixed cultures were then washed three times with PBS and incubated in blocking solution (10% FBS in PBS) for 1 h. After washing three times with PBS, the cultures were incubated with primary antibodies at a dilution of 1:50 in buffer (0.5% triton X-100 in PBS) overnight at 4 °C. Subsequently, the cultures were washed with PBS and incubated with the corresponding fluorescent secondary antibodies at a dilution of 1:200 for 2 h, avoiding light. Then, the culture was incubated in 2 μg/mL DAPI solution in PBS for 1 min to label the nuclei. In the experiment, β-tubulin III was used as a neuron marker, and GFAP was used as an astrocyte marker. The immunostaining results were visualized by microscopic examination using a Leica inverted microscope equipped with a fluorescence system.

Western blot analysis

The cells were harvested and were lysed at 4 °C in extraction buffer containing Tris–HCl (pH 7.5, 20 mmol/L), NaCl (150 mmol/L), EDTA (1 mmol/L), Triton X-100 (1%), sodium deoxycholate (0.5%), PMSF (1 mmol/L), leupeptin (10 μg/mL), and aprotinin (30 μg/mL). The lysates were centrifuged at 14 000×*g* for 30 min at 4 °C. The protein concentration was quantified by modified Lowry assay (DC protein assay; Bio-Rad, Hercules, CA, USA). SDS-PAGE, Western blotting, and the optical density measurements of the films were performed according to existing protocols. Briefly, 40 μg of protein was loaded on each lane, and the proteins were transferred to a nitrocellulose membrane after running SDS-PAGE. Transferred membranes were blocked for 1 h in 5% nonfat milk in Tris buffer containing 0.1% Tween-20 (TBS/T). The specific dilutions of the primary antibodies were as follows: NEFM (1:500); β-tubulin III (1:1000); GFAP (1:1000); p38 (1:500); phos-p38 (1:500); ERK (1:1000); phos-ERK (1:500); JNK (1:500); phos-JNK (1:500); and GAPDH (1:10000). Primary antibodies were diluted in 5% milk, and the blots were incubated overnight at 4 °C. The blots were washed three times (15 min each) with 10 mL TBS/T and were incubated with secondary antibody (1:5000) with gentle agitation for 1 h at room temperature. Then, the blots were washed three times with TBS/T and were exposed to a chemiluminescencent detection system using the Super Signal West Pico Substrate (Pierce, Rockford, IL, USA). Digital images of appropriate films were captured and quantified using the bio-imaging system (Bio-Rad, USA).

Semi-quantitative RT-PCR analysis

The total RNA was extracted with Trizol reagent according to the manufacturer's instructions. To synthesize first strand cDNA, 7 μL total RNA was incubated with 0.5 μg of oligo (dT) 6 primer and 5 μL water at 65 °C for 15 min. Reverse transcription reactions were performed using 200 units of M-MuLV reverse transcriptase (Gibco BRL) in 5×reaction buffer (250 mmol/L Tris–HCl; pH 8.3 at 25 °C, 375 mmol/L KCl, 15 mmol/L $MgCl_2$, 50 mmol/L dithiothreitol) and 1 mmol/L dNTP (deoxynucleotide triphosphate) mixture containing 10×PCR buffer (100 mmol/L Tris–HCl; pH 8.3 at 25 °C, 500 mmol/L KCl, 15 mmol/L $MgCl_2$), 25 units Taq polymerase (Sangon, China), 1 μL of 10 mmol/L dNTP mixture, and 30 pmol of each primer. The final volume was adjusted to 50 μL. The PCR reactions were initiated by denaturation at 94 °C, followed by annealing at a certain temperature (Table 1) for 45 s and amplification at 72 °C for 45 s using mastercycler gradient PCR amplifier (Eppendorf, Germany). The specific primer pairs and PCR reaction conditions are described in detail in Table 1.

The PCR products were analyzed by 1.5% agarose gel electrophoresis, visualized with ethidium bromide staining, and quantified by a bio-imaging analyzer (Bio-Rad, USA). The quantification analysis of the optical density of the products was performed using Quantity One software (Bio-Rad, USA).

Results

Neuronal differentiation effect

The morphological changes during the course of neuronal differentiation were observed. There was apparent difference between the IBA treatment group and the solvent control group. At the terminal of cultivation d 8+10 in our

Table 1. Primer sequences and reaction conditions for RT-PCR.

Gene	Primer sequence	Size (bp)	Mg^{2+} concentration (mmol/L)	Annealing temperature Tm (°C)	Cycle
GAPDH	S: 5′-TGACGGGGTCACCCACACTGTGCCCATCTA-3′ A: 5′-CTAGAAGCATTTGCGGTGGACGATGGAGGG-3′	660	3	69	28
β-tubulin III	S: 5′-CTCCCTTCGATTCCCTGGTC-3′ A: 5′-TGCTCCGAGATGCGTTTGA-3′	438	3	59	35
GFAP	S: 5′-GACTATCGCCGCCAACTGC-3′ A: 5′-CGCCTTGTGCTCCTGCTTC-3′	448	3	61	35
OCT3/4	S: 5′-AGGGATGGCATACTGTGGAC-3′ A: 5′-CCTGGGAAAGGTGTCCTGTA-3′	702	3	60	35
Nestin	S: 5′-CTGGGACTGAAGCACTGGG-3′ A: 5′-CGGACACCTCTTTGGGAAC-3′	384	3	59	35

study, RA (10^{-7} mol/L) and IBA (10^{-7} mol/L) significantly increased the population of neuron-like cells, which have axons more than three times longer than the length of their cell bodies[9] (Figure 2A). Neurons expressing β-tubulin III and astrocytes expressing GFAP induced by IBA were more obvious than those in solvent control (Figure 2B). The neural progenitor cell marker nestin is highly expressed in EBs (d 4 or d 8+0) with or without IBA treatments, and expression decreases gradually during neuronal differentiation. Oct3/4, a marker of pluripotency, was highly expressed in ES cells and disappeared at terminal differentiation. The mRNA and protein levels of β-tubulin III were both expressed from the EB stage to terminal differentiation. However, only a small amount of GFAP was expressed at the early stage, and GFAP expression was up-regulated in a time-dependent manner (Figure 2C). NEFM, a neurofilament marker that can reveal the fates of axons, was up-regulated by IBA treatment (Figure 2D).

Involvement of protein prenylation in IBA-promoted pneuronal differentiation

GGTase I inhibitor GGTI-298[11] was used to explore whether protein prenylation was involved in neuronal differentiation of mouse ES cells in this study. After the treatment with IBA accompanied with 10^{-6} mol/L GGTI-298 (no cytotoxicity to EBs, data not shown), the promoting effect in neuron and astrocyte differentiation was remarkably reduced as demonstrated by immunocytochemistry and Western blot analysis. Interestingly, GGTI-298 has no effect on RA-induced differentiation, which means that the promoting effects of IBA and RA on neuronal differentiation act via completely different pathways (Figure 3).

Involvement of MAPK pathway in IBA promoted neuronal differentiation

To explore the further possible mechanisms of the neuronal differentiation promoted by IBA, proteins related with the MAPK pathway were assessed by Western blot analysis. The samples were collected at multiple time points up to and including terminal differentiation. It was observed that p38 and JNK phosphorylation was detected during the ES and EB (d 4, d 8+0) passages and then was down-regulated on d 8+5 and d 8+10. Moreover, little p38 phosphorylation was detected during the entire differentiation course. In contrast, ERK phosphorylation was detected in ES cells, little was seen in EBs (d 4, d 8+0), and then it appeared to be up-regulated during the neuronal differentiation (Figure 4).

Discussion

Mouse ES cells as a model system can be used to investigate the effects of small molecules on differentiation and cell function in pharmacology[30]. Although numerous studies on the neuronal differentiation of mouse ES cells have been reported, the underlying molecular mechanism is probably a complex process and is still largely unknown. Recent studies have indicated that protein prenylation may play some role in the neuropharmacology of Alzheimer's disease[10]. Thus, we speculated that the process of protein prenylation may be associated with the neuronal differentiation induced by prenylflavonid compound IBA. IBA with prenyl group at position 8 of ring A may be activated by GGTase I, which can further regulate the ERK MAPK pathway and induce ES cell differentiation[11]. Moreover, mouse ES cell-derived neurons and astrocytes are regulated via the MAPK signaling pathway[11]. Pathways including ERK MAPK, and protein prenylation conceivably converge to alter the expression of cytoskeletal protein neurofilaments (NEFM) to modulate neurite outgrowth[31, 32] and promote neuronal differentiation from mouse ES cells. However, whether prenylflavonid compounds are capable of protein prenylation and other elements in the MAPK pathway are related to protein prenylation is still unknown.

In our study, at the early stages of the first two days in hanging drops and extra two days in suspension, mouse ES cells were allowed to form aggregated EBs, which resemble 5- to 6-day-old mouse embryos *in vivo*[33] and express the *Oct*3/4 gene. As shown in Figure 2, OCT3/4 was rapidly degraded following IBA treatment, while both β-tubulin III and GFAP were gradually expressed, representing neuron and astrocyte differentiation. Nestin, a well-known marker of neural progenitor cells in EBs, which was highly expressed in EBs (d 4, d 8+0 culture), was remarkably down-regulated in the period of neuronal differentiation (d 8+5, d 8+10 culture) after IBA treatment, indicating that IBA can further promote neural progenitor cells to differentiate into terminal neuronal cells. More interestingly, a significantly increased number of neurons was observed in the IBA-treated cultures accompanied by astrocytes compared with solvent control.

IBA with a prenyl group at position 8 of ring A was found to possess neurogenesis stimulatory activity in our work, but whether prenylflavonoid compounds can play a role in protein prenylation in mouse ES cells and whether protein prenylation is necessary for neurogenesis has not yet been confirmed. To explore the possible role of protein prenylation in inducing neuronal differentiation, pure GGTase I inhibitor GGTI-298 was used. GGTI-298 co-treatment with IBA could obviously affect the fates of mouse ES-cell-derived neurons and astrocytes. Surprisingly, GGTI-298 co-treatment with RA had no effect on the differentiation of either neurons or astrocytes, suggesting that GGTI-298 has no effect on RA-induced neuronal cell generation. Therefore, GGTI-298 might block IBA-induced protein prenylation and influence the neuronal differentiation. These data demonstrate that a prenyl group at position 8 of ring A of IBA is capable of protein prenylation during neurogenesis of mouse ES cells. These effects make IBA and its derivatives promising candidates for developing an efficient method to derive more neuronal or neural progenitor cells for cell replacement therapy.

Protein prenylation has been reported to activate the ERK MAPK pathway[13, 34]. It has also been reported that the sustained activation or phosphorylation of ERK is associated with differentiation[35]. In our study, the level of ERK phosphorylation was high in ES cells and was low in the early periods

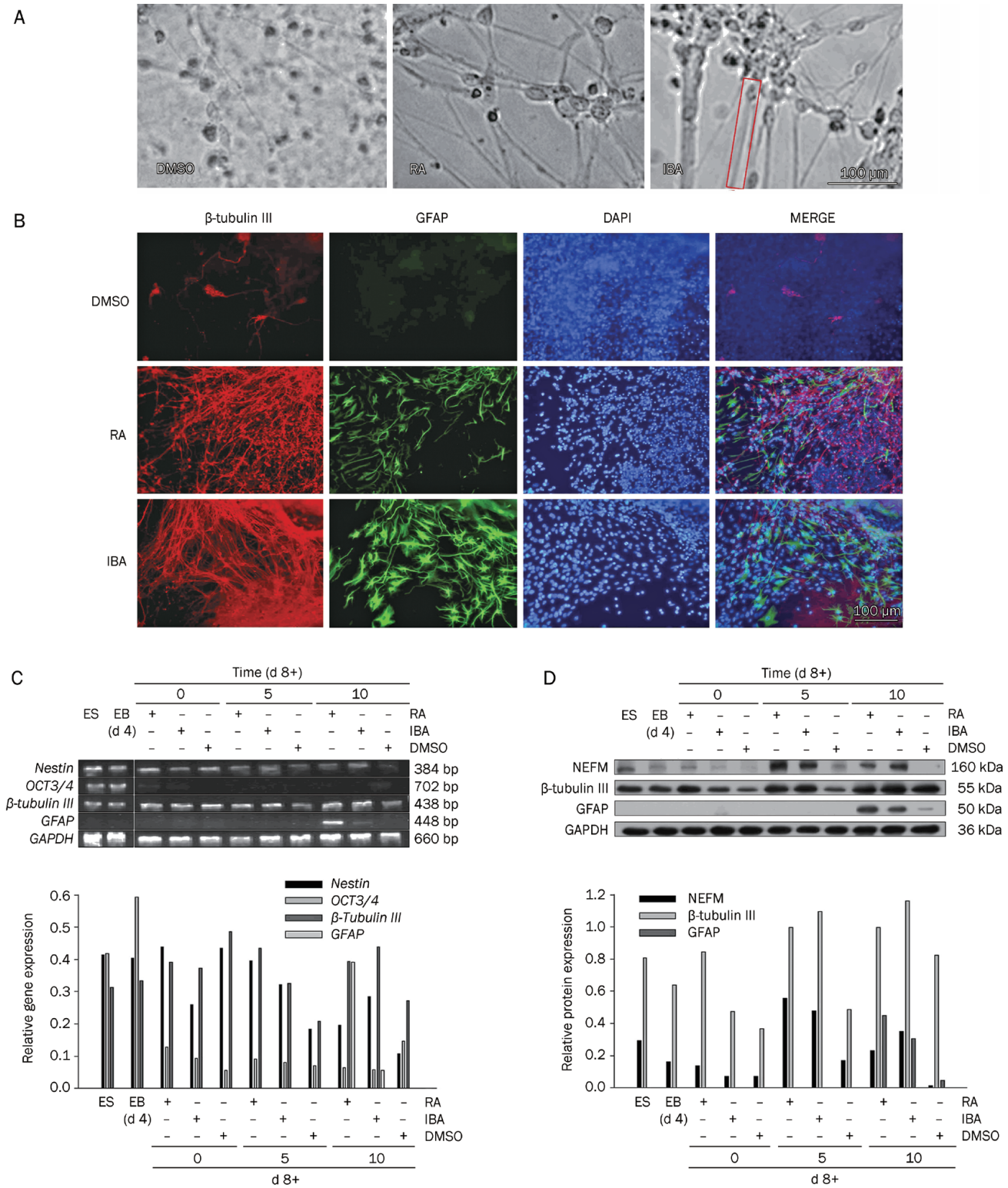

Figure 2. Differentiation potential of mouse ES cells into neurons and astrocytes after IBA treatment. All the morphological images were taken on d 8+10 EBs culture. DMSO: vehicle control; RA: 10^{-7} mol/L; IBA: 10^{-7} mol/L. (A) Morphological evaluation of neurongenesis of mouse ES cells induced by IBA. A typical axon with three times longer than the size of neuronal body (indicated with square) by phase contrast microscope. (B) Immunostaining with β-tubulin III (neuronal marker in red) or GFAP (astrocytes marker in green). DAPI staining (in blue) shows nuclear morphology. (C) RT-PCR analysis at different passages of mouse ES cells by IBA treatment. Stem cell marker gene (*OCT3/4*), neuronal genes (*nestin* for early differentiation, *β-tubulin III* and *GFAP* for late differentiation). The expression levels of genes were normalized with those of *GAPDH* gene. (D) Western blot analysis at different passages of mouse ES cells differentiation induced by IBA. β-tubulin III, NEFM for neurons, GFAP for astrocytes. The expression levels of proteins were normalized with those of GAPDH protein.

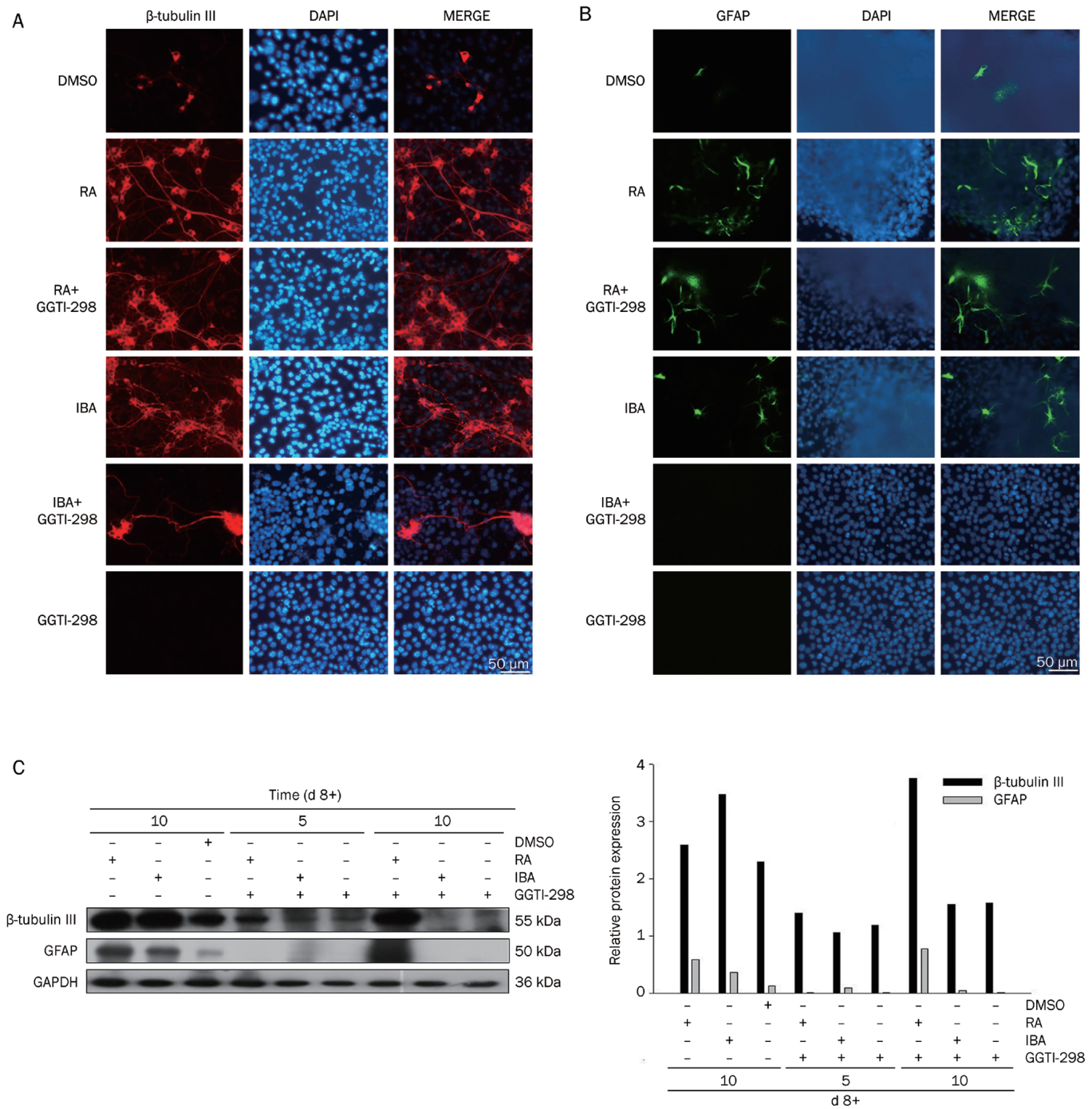

Figure 3. GGTI-298 decreased mouse ES cell derived neurons and astrocytes promoted by IBA. (A) Immunofluorescent staining of neurons co-localization with nuclei (DAPI staining) differentiated from mouse ES cells with or without GGTI-298 treatment. The morphological images were taken on day 8+10; 0.1% DMSO: (vehicle control), RA: 10^{-7} mol/L, IBA: 10^{-7} mol/L, GGTI-298: 10^{-6} mol/L. (B) Immunofluorescent staining for astrocytes with or without GGTI-298, and co-localization with nuclei (DAPI staining). (C) Neuronal marker proteins expressions in various stages during neurogenesis with or without GGTI-298. Neuronal proteins (β-tubulin III for neurons and GFAP for astrocytes) were examined by Western blot analysis. Results are presented as the ratio of the target protein compared with GAPDH. The treatments were the same as (A).

of d 4 and d 8+0 EB culture, while it increased greatly during late neuronal differentiation at d 8+5 and d 8+10 culture. These data indicate that ERK phosphorylation is a key event required for the survival of ES cells and for neurite formation and neuron survival during mouse ES cell differentiation[16]. At d 4 and d 8+0 culture, nestin was highly expressed in EBs, while ERK phosphorylation was inhibited, suggesting that the inhibition of ERK phosphorylation is associated with neural

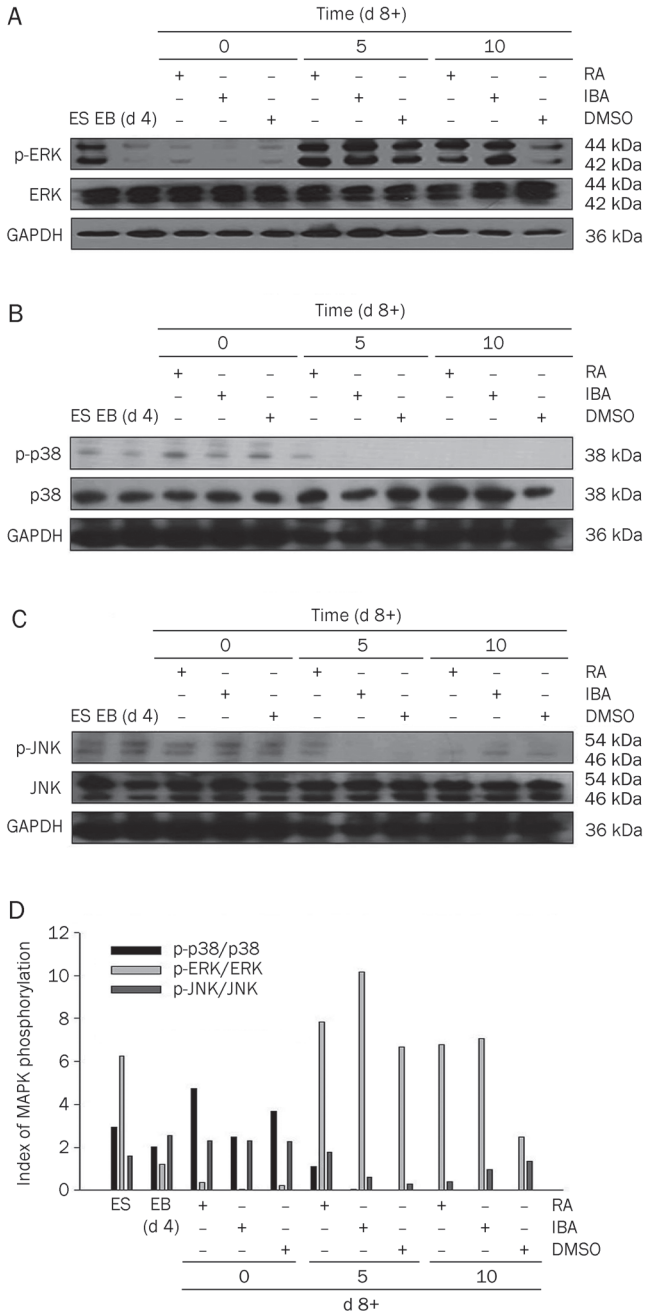

Figure 4. Effects of IBA on phosphorylation of MAPK pathway in ES cells-derive neurons and astrocytes by Western blot analysis. Samples were harvested at ES, EB, d 8+0, d 8+5, d 8+10 incubation with the treatment of various compounds. 0.1% DMSO: (vehicle control); RA: 10^{-7} mol/L; IBA: 10^{-7} mol/L. (A) Phos-ERK; (B) phos-p38; (C) Phos-JNK; (D) The semi-quantified levels of phos-ERK, phos-JNK and phos-p38 ratio were represented by histograms.

progenitor formation in mouse ES cells. p38 MAPK phosphorylation was shown to be a trigger in determining whether ES cells differentiated into neuronal cells or cardiomyocytes[15]. The control of p38 MAPK activity constitutes an early switch in ES cell commitment into cardiomyocytes (phos-p38 on) and neurons (phos-p38 off)[18]. In our study, p38 phosphorylation was expressed in the period of ES and EBs (d 4, d 8+0 culture), suggesting that p38 phosphorylation plays a critical role in maintaining mouse ES cell pluripotency and appears to promote neuroectoderm formation, while IBA can prevent p38 phosphorylation and subsequently promote neuronal differentiation. In the late period of neuronal differentiation, p38 phosphorylation was rare, indicating that p38 phosphorylation is associated with the trigger of mouse ES-cell differentiation and that its inhibition is important to neuronal differentiation. JNK phosphorylation was inhibited during neuronal differentiation compared with early stages of ES and EBs. It is noteworthy that the inhibitory effect of IBA on p38 is larger than on JNK phosphorylation. These results suggest that the regulation of the p38 and JNK MAPK signaling cascade may involve two mechanisms underlying the promoting effect of IBA on mouse ES cell neuronal differentiation[19]. Thus, a phosphatase-mediated crosstalk may exist between protein prenylation and the MAPK pathway in the regulation of neuronal differentiation from mouse ES cells promoted by IBA. Moreover, there may be a negative feedback regulation of their phosphorylation[17, 36]. Otherwise, ERK, p38, and JNK may be downstream targets of protein prenylation. However, how IBA regulates the ERK/JNK/p38 MAPK pathways and the specific relationship with protein prenylation needs to be further investigated.

In conclusion, this study suggests that IBA (prenyl group at position 8 of ring A) can facilitate the differentiation of mouse ES cells into multiple kinds of neuronal cell subtypes, such as neurons and astrocytes. The mechanism involved protein prenylation and, subsequently, phos-ERK activation and the phos-p38 off pathway.

Acknowledgements

This work was supported by the National Natural Science Foundation of China (NSFC No 30973600, No 90813026).

Author contribution

Yi-jia LOU: Conception and design, financial support, final approval of manuscript; Dan-yin WANG: Provision of study material, acquisition of data and data analysis, manuscript writing; Yu-zhe HU and Si-si KONG: Partial acquisition of data; Yong-ping YU: Partial provision of study molecule; Dan-yan ZHU: Partial conception and new skills; all authors have read and approved the final manuscript.

References

1 MacLaren RE, Pearson RA. Stem cell therapy and the retina. Eye (Lond) 2007; 21: 1352–9.
2 Xing F, Fang Z, Qin B, Li Y, Hou J, Chen X. Parthenogenetic embryonic stem cells derived from cryopreserved newborn mouse ovaries: a new approach to autologous stem cell therapy. Fertil Steril 2009; 91: 1238–44.
3 Emre N, Coleman R, Ding S. A chemical approach to stem cell biology. Curr Opin Chem Biol 2007; 11: 252–8.
4 Trompouki E, Zon LI. Small molecule screen in zebrafish and HSC expansion. Methods Mol Biol 2010; 636: 301–16.
5 Xu Y, Shi Y, Ding S. A chemical approach to stem-cell biology and

regenerative medicine. Nature 2008; 453: 338–44.
6 Dantuma E, Merchant S, Sugaya K. Stem cells for the treatment of neurodegenerative diseases. Stem Cell Res Ther 2010; 1: 37.
7 Ding S, Schultz PG. Small molecules and future regenerative medicine. Curr Top Med Chem 2005; 5: 383–95.
8 Tavakoli-Nezhad M, Arbogast LA. Mu and kappa opioid receptor expression in the mediobasal hypothalamus and effectiveness of selective antagonists on prolactin release during lactation. Neuroscience 2010; 166: 359–67.
9 Wang Z, Wang H, Wu J, Zhu D, Zhang X, Ou L, *et al*. Enhanced co-expression of beta-tubulin III and choline acetyltransferase in neurons from mouse embryonic stem cells promoted by icaritin in an estrogen receptor-independent manner. Chem Biol Interact 2009; 179: 375–85.
10 Ochocki JD, Igbavboa U, Gibson Wood W, Wattenberg EV, Distefano MD. Enlarging the scope of cell-penetrating prenylated peptides to include farnesylated 'CAAX' box sequences and diverse cell types. Chem Biol Drug Des 2010; 76: 107–15.
11 Chen S, Fu L, Raja SM, Yue P, Khuri FR, Sun SY. Dissecting the roles of DR4, DR5 and c-FLIP in the regulation of geranylgeranyltransferase I inhibition-mediated augmentation of TRAIL-induced apoptosis. Mol Cancer 2010; 9: 23.
12 Seabra MC. Membrane association and targeting of prenylated Ras-like GTPases. Cell Signal 1998; 10: 167–72.
13 Kim HS, Kim JW, Gang J, Wen J, Koh SS, Koh JS, *et al*. The farnesyltransferase inhibitor, LB42708, inhibits growth and induces apoptosis irreversibly in H-ras and K-ras-transformed rat intestinal epithelial cells. Toxicol Appl Pharmacol 2006; 215: 317–29.
14 Binetruy B, Heasley L, Bost F, Caron L, Aouadi M. Concise review: regulation of embryonic stem cell lineage commitment by mitogen-activated protein kinases. Stem Cells 2007; 25: 1090–5.
15 Roux PP, Blenis J. ERK and p38 MAPK-activated protein kinases: a family of protein kinases with diverse biological functions. Microbiol Mol Biol Rev 2004; 68: 320–44.
16 Li Z, Theus MH, Wei L. Role of ERK 1/2 signaling in neuronal differentiation of cultured embryonic stem cells. Dev Growth Differ 2006; 48: 513–23.
17 Wang Z, Yang H, Tachado SD, Capo-Aponte JE, Bildin VN, Koziel H, *et al*. Phosphatase-mediated crosstalk control of ERK and p38 MAPK signaling in corneal epithelial cells. Invest Ophthalmol Vis Sci 2006; 47: 5267–75.
18 Aouadi M, Bost F, Caron L, Laurent K, Le Marchand Brustel Y, Binetruy B. p38 mitogen-activated protein kinase activity commits embryonic stem cells to either neurogenesis or cardiomyogenesis. Stem Cells 2006; 24: 1399–406.
19 Zeng KW, Fu H, Liu GX, Wang XM. Icariin attenuates lipopolysaccharide-induced microglial activation and resultant death of neurons by inhibiting TAK1/IKK/NF-kappaB and JNK/p38 MAPK pathways. Int Immunopharmacol 2010; 10: 668–78.
20 Rajan P, McKay RD. Multiple routes to astrocytic differentiation in the CNS. J Neurosci 1998; 18: 3620–9.
21 Liu J, Ye H, Lou Y. Determination of rat urinary metabolites of icariin *in vivo* and estrogenic activities of its metabolites on MCF-7 cells. Pharmazie 2005; 60: 120–5.
22 Doetschman TC, Eistetter H, Katz M, Schmidt W, Kemler R. The *in vitro* development of blastocyst-derived embryonic stem cell lines: formation of visceral yolk sac, blood islands and myocardium. J Embryol Exp Morphol 1985; 87: 27–45.
23 Stewart R, Stojkovic M, Lako M. Mechanisms of self-renewal in human embryonic stem cells. Eur J Cancer 2006; 42: 1257–72.
24 Zhu DY, Lou YJ. Inducible effects of icariin, icaritin, and desmethylicaritin on directional differentiation of embryonic stem cells into cardiomyocytes *in vitro*. Acta Pharmacol Sin 2005; 26: 477–85.
25 Metzger JM, Lin WI, Johnston RA, Westfall MV, Samuelson LC. Myosin heavy chain expression in contracting myocytes isolated during embryonic stem cell cardiogenesis. Circ Res 1995; 76: 710–9.
26 Scholz G, Pohl I, Genschow E, Klemm M, Spielmann H. Embryotoxicity screening using embryonic stem cells *in vitro*: correlation to *in vivo* teratogenicity. Cells Tissues Organs 1999; 165: 203–11.
27 Bain G, Kitchens D, Yao M, Huettner JE, Gottlieb DI. Embryonic stem cells express neuronal properties *in vitro*. Dev Biol 1995; 168: 342–57.
28 Murashov AK, Pak ES, Hendricks WA, Tatko LM. 17beta-Estradiol enhances neuronal differentiation of mouse embryonic stem cells. FEBS Lett 2004; 569: 165–8.
29 Zhang SC, Wernig M, Duncan ID, Brustle O, Thomson JA. *In vitro* differentiation of transplantable neural precursors from human embryonic stem cells. Nat Biotechnol 2001; 19: 1129–33.
30 Wobus AM. Potential of embryonic stem cells. Mol Aspects Med 2001; 22: 149–64.
31 Canals M, Angulo E, Casado V, Canela EI, Mallol J, Vinals F, *et al*. Molecular mechanisms involved in the adenosine A and A receptor-induced neuronal differentiation in neuroblastoma cells and striatal primary cultures. J Neurochem 2005; 92: 337–48.
32 Li BS, Zhang L, Gu J, Amin ND, Pant HC. Integrin alpha(1) beta(1)-mediated activation of cyclin-dependent kinase 5 activity is involved in neurite outgrowth and human neurofilament protein H Lys-Ser-Pro tail domain phosphorylation. J Neurosci 2000; 20: 6055–62.
33 Martin GR, Evans MJ. Differentiation of clonal lines of teratocarcinoma cells: formation of embryoid bodies *in vitro*. Proc Natl Acad Sci U S A 1975; 72: 1441–5.
34 Solomon CS, Goalstone ML. Dominant negative alpha-subunit of FTase inhibits effects of insulin and IGF-I in MCF-7 cells. Biochem Biophys Res Commun 2002; 291: 458–65.
35 Marshall CJ. Specificity of receptor tyrosine kinase signaling: transient versus sustained extracellular signal-regulated kinase activation. Cell 1995; 80: 179–85.
36 Estrada Y, Dong J, Ossowski L. Positive crosstalk between ERK and p38 in melanoma stimulates migration and *in vivo* proliferation. Pigment Cell Melanoma Res 2009; 22: 66–76.

Acta Pharmacologica Sinica (2011) 32: 433–440

www.nature.com/aps

Original Article

Involvement of estrogen receptor-β in farrerol inhibition of rat thoracic aorta vascular smooth muscle cell proliferation

Qun-yi LI[1, #, §], Li CHEN[2, #, ¶], Yan-hui ZHU[1], Meng ZHANG[1], Yi-ping WANG[2], Ming-wei WANG[1, 2, *]

[1]*The National Center for Drug Screening and* [2]*the State Key Laboratory of New Drug Research, Shanghai Institute of Materia Medica, Chinese Academy of Sciences, Shanghai 201203, China*

Aim: To investigate the effect of farrerol, a major active component isolated from a traditional Chinese herb "Man-shan-hong" (the dried leaves of *Rhododendron dauricum* L) on fetal bovine serum (FBS)-induced proliferation of cultured vascular smooth muscle cells (VSMCs) of rat thoracic aorta.

Methods: VSMCs proliferation, DNA synthesis and cell cycle progression were studied using the MTT assay, bromodeoxyuridine (BrdU) incorporation and flow cytometry, respectively. The mRNA levels of cell cycle proteins were quantified using real-time RT-PCR, and the phosphorylation of ERK1/2 was determined using Western blotting. Reporter gene and receptor binding assays were employed to study the interaction between farrerol and estrogen receptors (ERs).

Results: Farrerol (0.3–10 μmol/L) inhibited VSMC proliferation and DNA synthesis induced by 5% FBS in a concentration-dependent manner. The effects were associated with G_1 cell cycle arrest, down-regulation of cell cycle proteins and reduction in FBS-induced ERK1/2 phosphorylation. Using a reporter gene, it was found that farrerol (3 μmol/L) induced 2.1-fold transcription of ER. In receptor binding assays, farrerol inhibited the binding of [^{3}H]estradiol for ERα and ERβ with IC_{50} values of 57 μmol/L and 2.7 μmol/L, respectively, implying that farrerol had a higher affinity for ERβ. Finally, the inhibition of VSMC proliferation by farrerol (3 μmol/L) was abolished by the specific ERβ antagonist PHTPP (5 μmol/L).

Conclusion: Farrerol acts as a functional phytoestrogen to inhibit FBS-induced VSMC proliferation, mainly via interaction with ERβ, which may be helpful in the treatment of cardiovascular diseases related to abnormal VSMCs proliferation.

Keywords: farrerol; phytoestrogen; estrogen receptor; vascular smooth muscle cells; cell proliferation; cell cycle; ERK1/2; receptor binding assay

Acta Pharmacologica Sinica (2011) 32: 433–440; doi: 10.1038/aps.2011.1; published online 14 Mar 2011

Introduction

Abnormal proliferation of vascular smooth muscle cells (VSMCs) plays a critical role in intimal formation in the early stage of atherosclerosis and restenosis[1]. Several reports have indicated that reduction of VSMC proliferation using therapeutic agents (*eg*, estrogen) would give rise to vasoprotective effects[2]. Estrogen exhibits a variety of actions on the vascular wall that could be implicated in its athero-protective properties[3]. These include, but are not limited to, the inhibition of VSMC proliferation[4, 5].

As we know, earlier studies supported the widespread belief in the hypothesis of cardiovascular benefit of hormone replacement therapy (HRT) in postmenopausal women, but recent Women's Health Initiative (WHI) trials found no coronary heart disease (CHD) benefit among women aged 50 to 79 and HRT increased risk of stroke[6, 7]. However, WHI also provided evidence that CHD risks are reasonably low for short-term use by younger postmenopausal women[8, 9]. Although "timing hypothesis" and "critical window theory" for estrogen intervention in preventing atherosclerosis were developed, there is still a need to better understand the relationship between circulating estrogen levels and aging of the cardiovascular system.

It has been suggested that steroidal hormones used in HRT may lead to unacceptable adverse effects such as carcinogenicity in the endometrium[10]. Tamoxifen and raloxifene[11, 12], the

# These two authors contributed equally to this work.
§ Now in *Clinical Pharmacy Laboratory, Huashan Hospital, Fudan University, Shanghai 200040, China*.
¶ Now in *Department of Preventive Medicine, Tongji University School of Medicine, Shanghai 200092, China*.
*To whom correspondence should be addressed.
E-mail wangmw@mail.shcnc.ac.cn
Received 2010-09-02 Accepted 2011-01-05

nonsteroidal and selective estrogen receptor modulators, have shown cardioprotective benefits with reduced side effects, indicating that alternative estrogen-like agents may possess better therapeutic index. Therefore, interests have been directed to phytoestrogens derived from natural products, especially isoflavones present in soya beans[13]. An increasing number of studies suggest that some phytoestrogens could be promising substitutes for estrogen in preventing cardiovascular diseases through inhibiting VSMC proliferation and migration[14-16].

The flavonoid farrerol (Figure 1) is abundant in a traditional Chinese herb "Man-shan-hong", the dried leaves of *Rhododendron dauricum* L. It is considered to be the main bioactive ingredient of this plant and has been used as an antibechic in China[17]. In recent years, farrerol has attracted considerable interests due to its anti-inflammatory, antibacterial, and antioxidant activities exerted via scavenging radicals and inhibiting a variety of enzymes[18, 19]. However, to our knowledge, the effects of farrerol on cardiovascular system have not been reported to date. In view of the structural similarities between farrerol and estrogenic isoflavones (*eg*, genistein and daidzein), it would be tempting to learn if farrerol could act as a phytoestrogen in VSMCs. Thus, this study was designed and carried out to investigate the impact of farrerol on VSMC proliferation and its interaction with estrogen receptors.

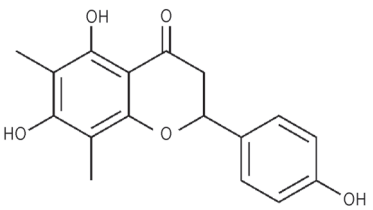

Figure 1. Chemical structure of farrerol.

Materials and methods

Reagents

Farrerol is a reference compound (purity ≥99.0%) supplied by the Division of Chinese Materia Medica and Natural Products, National Institute for the Control of Pharmaceutical and Biological Products (NICPBP), Ministry of Health, China. β-Estradiol 17-acetate (E_2), methyl-piperidino-pyrazole (MPP), 4-[2-[phenyl-5,7-*bis*(trifluoromethyl)pyrazolo[1,5-a]pyrimidin-3-yl]phenol (PHTPP), ICI182,780, BrdU, and 2,3-*bis*(4-hydroxyphenyl)-propionitrile (DPN) were obtained from Sigma (St Louis, MO, USA). Polyclonal anti-β-actin, monoclonal anti-phospho-ERK1/2 and polyclonal anti-ERK1/2 antibodies were purchased from Santa Cruz Biotechnology (Santa Cruz, CA, USA). Polyclonal antibodies to ERα and ERβ were procured from Abcam Inc (Cambridge, MA, USA).

Cell culture

Primary VSMCs were obtained from the thoracic aorta of 3-month old female Sprague-Dawley rats using the tissue explant method described elsewhere[20]. More than 98% of the cells were positive for staining with smooth muscle-specific α-actin, and exhibited the typical hill-and-valley morphology of VSMCs. Cells between passages 2 and 5 were used in this study to ensure the genetic stability of the culture. Cells grown to 80%−95% confluence were made quiescent by starvation (0.1% FBS) for 24 h.

Cell proliferation

The cell proliferation assay was performed using the MTT [3-(4,5-dimethylthiazol-2-yl)-2,5-diphenyltetrazolium bromide] method. Briefly, growth-arrested VSMCs were incubated with or without farrerol for 2 h prior to stimulation with 5% FBS for 48 h. They were then incubated with 0.5 mg/mL MTT for 4 h at 37 °C. Finally, the culture medium was removed and the formazan salt crystals was dissolved with 200 μL dimethylsulfoxide (DMSO) followed by shaking at room temperature for 10 min. The absorbance was read at a wavelength of 570 nm using a Spectramax M2 microplate reader (Molecular Devices, Sunnyvale, CA, USA).

BrdU incorporation

DNA synthesis in VSMCs was examined using the BrdU incorporation assay previously described[21]. Quiescent VSMCs were treated with or without farrerol for 2 h prior to stimulation with 5% FBS for 24 h. For inhibition experiments, cells were pretreated with MPP or PHTPP for 30 min before addition of farrerol or DMSO.

Subsequently, 10 μmol/L BrdU was added to the cells and incubated for additional 24 h. To immunostain BrdU, the cells were washed with PBS, fixed in 4% polyformaldehyde and permeabilized with 0.1% Triton X-100. After DNA denaturation with 4 mol/L HCl, non-specific binding sites were blocked with 5% non-fat milk. The cells were then stained with an antibody to BrdU (Invitrogen, Carlsbad, CA, USA) followed by incubation with Alexa Flour 568 labeled goat anti-mouse IgG (Invitrogen) secondary antibodies. The cell nuclei were stained with Hoechst 33342 and evaluated by fluorescence microscopy with appropriate fluorescent filters. Results are presented as mitotic index, and defined as the percentage of BrdU-positive nuclei observed in a cell population.

Flow cytometry

Quiescent VSMCs were preincubated with or without farrerol for 2 h, followed by 5% FBS treatment for 24 h. They were then trypsinized, collected, and washed twice with cold PBS. Cell pellets were fixed in 70% ethanol and stored at 4 °C until use. The fixed cells were reacted with RNase A (10 μg/mL), DNA was stained with propidium iodide (50 μg/mL) for 30 min at 37 °C, and 1×10^4 cells were analyzed by flow cytometry. The rates of G_0/G_1, S, and G_2/M phases were determined using the software program ModiFit LT (BD, Franklin Lakes, NJ, USA).

Quantitative real-time PCR

Total RNA from VSMCs was extracted with the TRIzol reagent

(Invitrogen) and reverse transcribed (RT) using Superscript II First-strand Synthesis SuperMix (Invitrogen). Primers and real-time PCR conditions were described previously[22, 23]: β-actin: 5′-ATG GAT GAC GAT ATC GCT GCG-3′ (forward) and 5′-CAG GGT CAG GAT GCC TCT CTT-3′ (reverse); cyclin D1: 5′-TGC ATC TAC ACT GAC AAC TCT AT-3′ (forward) and 5′-GCA TTT TGG AGA GGA AGT GTT C-3′ (reverse); cyclin E: 5′-TGA AAT TGG TGT CGG TGC CTA T-3′ (forward) and 5′-TGC TCC TCC ATT AGG AAC TCT CAC-3′ (reverse); cyclin-dependent kinase 2 (CDK2): 5′-CTT AAG AAA ATC CGG CTC GAC-3′ (forward) and 5′-ATC CAG CAG CTT GAC GAT GTT A-3′ (reverse); CDK4: 5′-GAC TCC CAC AAC ATC CAG ACC-3′ (forward) and 5′-ACT CGG AGG AGG AGA AAT CCT-3′ (reverse); ERα: 5′-CTA AGA AGA ATA GCC CCG CC-3′ (forward) and 5′-CAG ACC AGA CCA ATC ATC AGG-3′ (reverse); ERβ: 5′-CGA CTG AGC ACA AGC CCA AAT G-3′ (forward) and 5′-ACG CCG TAA TGA TAC CCA GAT G-3′ (reverse). For RT-PCR, SYBR® Premix Ex Taq™ (Takara Bio Inc, Dalian, China) was used. Final PCR products were subjected to graded temperature-dependent dissociation to verify that only one product was amplified. Reactions with no RT sample and no template were included as negative controls. Relative quantitative evaluation of target gene levels was performed by the comparative CT (cycle threshold) method[24] and performed in triplicates.

Western blotting

VSMCs were lysed and equal amounts of protein from each sample were subjected to SDS-PAGE and blotted on PVDF membrane, which was incubated for 2 h at room temperature with blocking buffer (5% non-fat milk, 0.1% Tween 20, in TBS, pH 7.6) and then probed with primary antibodies overnight at 4 °C. After incubation with the appropriate secondary antibodies, the immunoreactive band was detected by an ECL Western blotting detection system (GE Healthcare, Bucks, UK) and subsequently photographed by a LAS-3000 luminescent image system (Fujifilm, Tokyo, Japan).

Receptor binding assays

For ER binding assay, an appropriate amount of estrogen receptor α/β (ERα/β) was loaded into each well of an Isoplate™ (PerkinElmer, Boston, MA, USA) containing the assay buffer [10% glycerol (*v/v*), NaH_2PO_4 25 mmol/L, $MgCl_2$ 0.5 mmol/L, DTT 1 mmol/L, edetic acid 1 mmol/L, CHAPS 5 mmol/L, aprotinin 2 mg/L and leupeptin 100 μmol/L] followed by addition of [^{3}H]estradiol (140 Ci/mmol, 5 nmol/L; PerkinElmer). Various concentrations of E_2 were added thereafter and incubated overnight at 4 °C. Twenty-five μL of hydroxyapatite (25%, *v/v*) was added to each well the next morning and the plates were gently agitated twice for 5 min each. Following centrifugation for 3 min at 2500 r/min (4 °C), the supernatant was decanted and 100 μL of assay buffer was added to each well. This washing procedure was repeated twice before the addition of 150 μL scintillation liquid (PerkinElmer), gentle agitation of the plates to resuspend hydroxyapatite and measurement of radioactivity with a MicroBeta counter (PerkinElmer).

For peroxisome proliferator-activated receptor γ (PPARγ) binding assay, biotinylated PPRE was mixed with the assay buffer containing fish sperm DNA (Shanghai Sangon Biotechnology, Shanghai, China) and 4 mg streptavidin-coated microbeads (GE Healthcare) in a conical polypropylene centrifuge tube, and incubated overnight at 4 °C. The mixture was centrifuged for 10 min at 2500 r/min. The supernatant was then removed followed by washing three times with 10 mL assay buffer. Reaction solution (10 mL) containing 700 μg PPARγ extract protein, 47 μg retinoid X receptor α (RXRα) extract protein, 10 nmol/L [^{3}H]BRL49653 (American Radiolabeled Chemicals, Inc, St Louis, MO, USA), and various concentrations of BRL49653 or farrerol were distributed to each well of an Isoplate™ (PerkinElmer) and incubated at 4 °C for 4 h before counting by a MicroBeta counter (PerkinElmer).

Reporter gene assay

pERE-Luc reporter (0.5 μg/well of 24-well plate) or pGL3-Luc (negative control) plasmids were transfected into VSMCs with Lipofectamine™ (Invitrogen) and the procedure was carried out as directed by the manufacturer. pERE-Luc contains tandems of ERE linked to a downstream luciferase reporter gene. pGL3-Luc is an identical plasmid but without the ERE. The pSV-β-galactosidase plasmid (pCH110) was co-transfected as an internal control. After transfection for 24 h, cells were treated in conditioned medium and harvested following further 24 h incubation. Luciferase activity was assayed according to the manufacturer's protocol using the luciferase assay system (Promega, Madison, WI, USA). Relative luciferase units (RLU) normalized to transfection efficiency were calculated as the ratio of luciferase activity to β-galactosidase.

Gal-ERα and Gal-ERβ were constructed by transferring the coding sequences for the ligand-binding domain (LBD) of ERα (amino acids 282–595) or ERβ (amino acids 234–530) to yeast transcription activator protein Gal4, respectively. Gal-ERα or Gal-ERβ, together with the 5×UAS-Luc reporter and pSV-β-galactosidase plasmids, were co-transfected into HEK293 cells according to the manufacturer's instructions. Luciferase activity and β-galactosidase activity were determined as described above.

Statistical analysis

Results are expressed as mean±SEM. Statistical analysis was performed using one-way analysis of variance (ANOVA). The inter-group comparisons (*post hoc* analysis) among the data with equal variances were made by the LSD method, while Tamhane's T2 method was used for the data with unequal variances. A P value of less than 0.05 is considered significant.

Results

Farrerol inhibits FBS-induced VSMC proliferation and DNA synthesis

In this study, we first investigated the effect of farrerol on the proliferation of VSMCs using the MTT assay. When growth-arrested cells were treated with farrerol (0.3, 1, 3, and

10 μmol/L) in the presence of 0.1% FBS, no significant difference was observed in cell viability (Figure 2A, left panel), suggesting that farrerol did not show significant cytotoxicity up to 10 μmol/L. The absence of cytotoxicity was further confirmed with a trypan blue exclusion assay (data not shown). However, we found that 5% FBS treatment led to a 2.65-fold increase in VSMC proliferation, while incubation of the cells with farrerol for 2 h prior to FBS stimulation reduced cell proliferation in a dose-dependent manner (Figure 2A, right panel). The influence of farrerol on DNA synthesis was also studied: BrdU incorporation was markedly increased in VSMCs following exposure to 5% FBS for 48 h, indicative of elevated DNA synthesis; this effect was abolished by pretreatment of VSMCs with farrerol in a dose-dependent manner and the complete blocking was achieved at the highest concentration (10 μmol/L) used (Figure 2B).

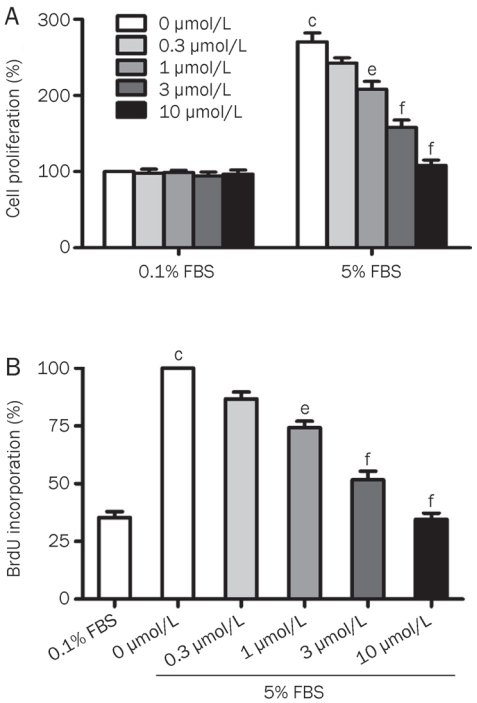

Figure 2. Effects of farrerol on FBS-induced proliferation and DNA synthesis in VSMCs. A, proliferation was measured by the MTT assay in the absence (left) or presence (right) of 5% FBS. Relative proliferation (%) was displayed using untreated control cells as a standard (n=6). B, DNA synthesis was measured by BrdU incorporation. The left part shows BrdU incorporation of quiescent and FBS-stimulated VSMCs. On the right side, a concentration-dependent decrease of BrdU incorporation in farrerol-treated VSMCs is shown (n=6). Values are presented as mean±SEM. ^{c}P<0.01 *vs* control; ^{e}P<0.05, ^{f}P<0.01 *vs* FBS induction.

Farrerol arrests FBS-stimulated VSMCs in G_1 phase and abrogates cell cycle protein transcription

Proliferative cells pass through several cell cycle checkpoints, mainly the G_1 to S and G_2 to M transitions. The former checkpoint is considered to be the most important step in DNA replication. Accordingly, flow cytometric assessment was performed to determine the effect of farrerol on cell cycle progression. As shown in Figure 3, the percentage of G_0/G_1 or S phase cells in the 5% FBS-stimulated group were 59.32%±2.73% and 18.30%±2.62%, respectively. Farrerol at concentrations of 3 and 10 μmol/L effectively increased the proportion of cells in the G_0/G_1 phase and simultaneously decreased the S phase cell population.

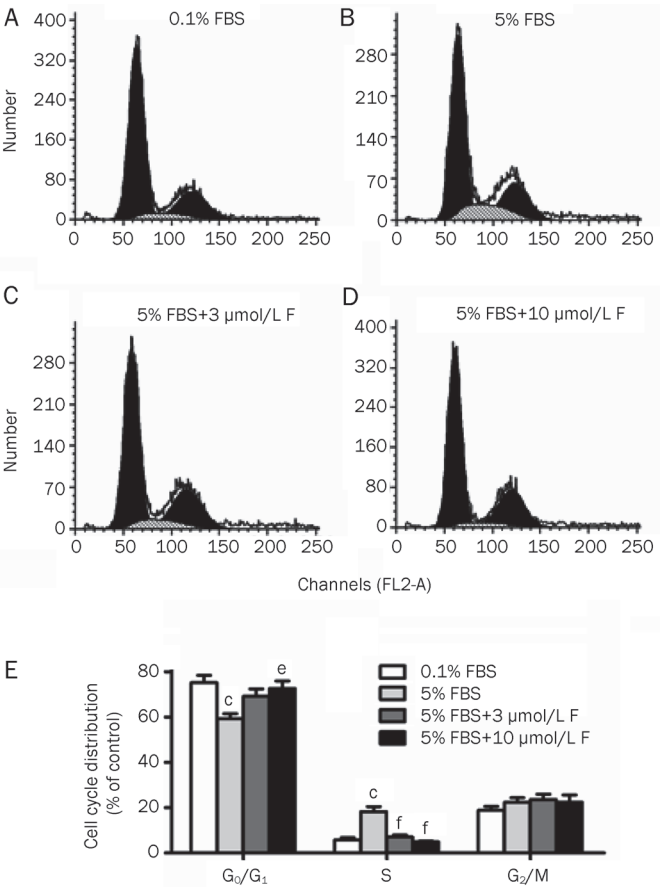

Figure 3. Cell cycle distribution of (A) quiescent and (B) FBS-stimulated VSMCs. C and D show VSMCs treated with 3 μmol/L and 10 μmol/L farrerol (F), respectively, in the presence of FBS. It demonstrates farrerol-induced cell cycle arrest at the G_0/G_1 phase. G_0/G_1 phase is represented by the first peak, S phase in diagonal and G_2/M by the second peak. E, results are expressed as a percentage of the total number of cells in G_0/G_1, S, or G_2/M phases of the cell cycle. Values are presented as mean±SEM. ^{c}P<0.01 *vs* control; ^{e}P<0.05, ^{f}P<0.01 vs FBS induction.

Then, we examined the mRNA levels of cell cycle-related proteins using real-time PCR to determine whether farrerol induced changes in this pathway. The results were analyzed by the comparative CT method. Treatment with farrerol not only produced a significant down-regulation in cyclin D1 and E gene transcription, but also markedly decreased the expression of CDK2 and CDK4 genes (Figure 4A).

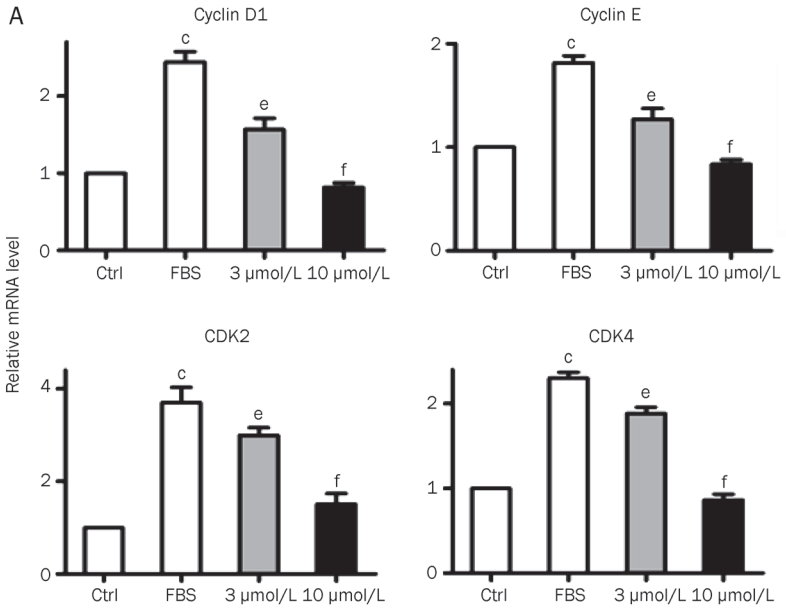

Figure 4. Effects of farrerol on FBS-induced cell cycle protein transcription and ERK1/2 activation in VSMCs. (A) The mRNA levels of cyclin D1, cyclin E, CDK2 and CDK4 were measured by real-time RT-PCR. β-actin was used as an internal control (n=4). Values are presented as mean±SEM. ^{c}P<0.01 *vs* control (Ctrl); ^{e}P<0.05, ^{f}P<0.01 *vs* FBS induction. (B) VSMCs were treated with farrerol for 2 h prior to FBS (5%) stimulation for 15 min. Whole cell lysates were prepared and subsequently used for detection of p-ERK1/2 and ERK1/2 by Western blot.

Farrerol suppresses FBS-induced ERK1/2 phosphorylation in VSMCs

It was reported that ERK1/2 activation plays a critical role in the proliferation of VSMCs[21]. Inhibition of this signaling protein proved to be a useful method for preventing intimal hyperplasia[25]. Therefore, we examined the effect of farrerol on ERK1/2 activation and the results indicate that exposure of VSMCs to FBS for 15 min enhanced ERK1/2 phosphorylation considerably. Conversely, addition of farrerol dose-dependently abrogated ERK1/2 activation in FBS-stimulated VSMCs: at a concentration of 10 μmol/L, farrerol completely blocked the phosphorylation of ERK1/2 (Figure 4B).

Farrerol is a functional ERβ ligand in VSMCs

To evaluate the possible role of ER in farrerol-induced antimitogenic activity, we first evaluated the expression of ERα and ERβ by both Western blot analysis and real-time PCR in VSMCs. Figure 5A depicts that protein and mRNA of both ER subtypes were present in the VSMCs derived from female Sprague-Dawley rats, as reported previously[26].

Thereafter, an ERE-luciferase reporter gene assay was performed to study whether farrerol acts as a phytoestrogen in VSMCs. As shown in Figure 5B, farrerol was able to activate ER transcription from a luciferase reporter gene (pERE-luc) under the control of a promoter containing two copies of the ERE in VSMCs, showing a 2.1-fold induction over control and the efficacy was comparable to that of E_2. The ERE-driven luciferase activity induced by farrerol was completely blocked by the ERα/β antagonist ICI182,780, but not by the specific ERα antagonist MPP, implying that farrerol may exert its phytoestrogen action via ERβ.

To obtain further evidence that farrerol activates ERβ directly, a heterologous system was employed. Chimeric protein consisting of the DNA binding domain of Gal4 and ERβ LBD, but not ERα LBD, responded to farrerol in a transient expression assay in HEK293 cells (Figures 5C and 5D), thereby pointing to a mechanism of direct interaction between farrerol and ERβ signaling.

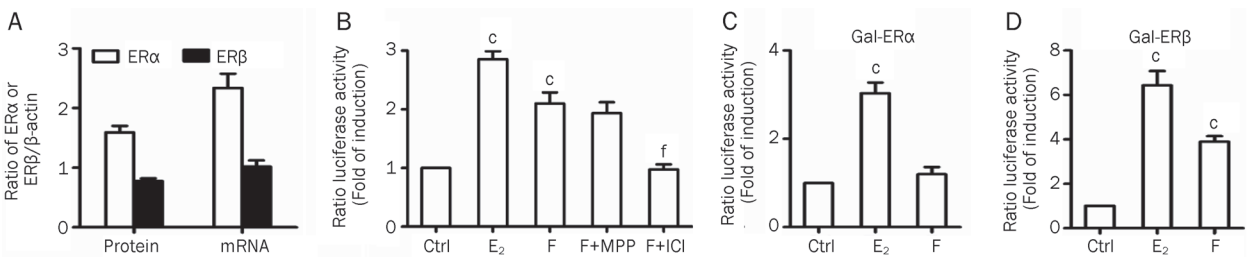

Figure 5. Activation of ERβ-mediated transcription by farrerol in reporter gene assays. A, expression of ERα and ERβ in VSMCs. Western blot and real-time PCR were performed on VSMCs for ERα and ERβ protein expression and mRNA quantification. β-actin was used as an internal control (n=3). B, farrerol activates ERE-mediated transcription in VSMCs. Cells cotransfected with pERE-luc and β-gal expression plasmids were treated with 3 μmol/L farrerol (F) with or without MPP (10 μmol/L) or ICI182,780 (ICI, 10 μmol/L). E_2 (100 nmol/L) was used as a positive control. Relative luciferase units (RLU) normalized to transfection efficiency were calculated as the ratio of luciferase activity to β-galactosidase (n=3). C, fusion protein consisting of ERβ and Gal4 DBD was activated by farrerol in transfected HEK293 cells (n=3). Values are presented as mean±SEM. ^{c}P<0.01 *vs* control (Ctrl); ^{f}P<0.01 *vs* farrerol treatment.

Next, a competitive receptor-binding assay was employed to study binding specificities of farrerol for ERα and ERβ. As shown in Figure 6, the IC_{50} values of farrerol for ERα and ERβ were 57 μmol/L and 2.7 μmol/L, respectively, implying that farrerol has a higher binding specificity for ERβ than ERα. Moreover, cross-reactivity check revealed that the binding affinity of farrerol to PPARγ is rather weak (IC_{50}=238 μmol/L; Figure 6). These data suggest that farrerol appears to be a selective ERβ agonist.

Farrerol exerts its action on DNA synthesis mainly via ERβ in VSMCs

Previous work has suggested the involvement of ERβ in the inhibitory effects of estrogen on VSMCs[27]. Our results also showed that the selective ERβ agonist 2,3-*bis*(4-hydroxyphenyl)-propionitrile (DPN, 1 μmol/L) closely resembled E_2 in significantly reducing DNA synthesis in VSMCs (data not shown).

Having established that farrerol is an ERβ agonist, PHTPP, a specific ERβ antagonist was chosen to characterize the role of ERβ in farrerol-mediated effects. Figure 7 shows that blockade of ERβ signaling by PHTPP noticeably attenuated the inhibitory effect of farrerol on VSMC proliferation while MPP, a specific ERα antagonist was ineffective. Furthermore, neither PPARγ antagonist GW9662 nor PPARα antagonist GW6471 was able to reverse the inhibitory effects of farrerol on VSMCs (data not shown). Taken together, the results indicate that ERβ is involved in farrerol-mediated inhibition on VSMC proliferation.

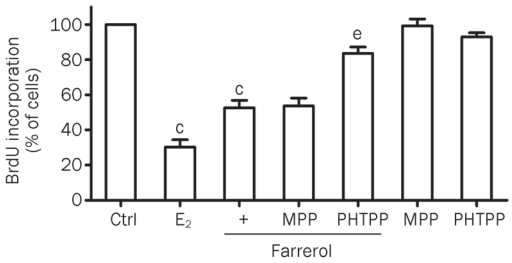

Figure 7. Inhibition on VSMC DNA synthesis by farrerol was reversed by a specific ERβ antagonist, PHTPP. Cells were treated with or without 3 μmol/L farrerol, in the absence or presence of PHTPP (5 μmol/L) or MPP (10 μmol/L). E_2 (100 nmol/L) was used as a positive control (n=3). Values are presented as mean±SEM. ^cP<0.01 *vs* control (Ctrl); ^eP<0.05 *vs* farrerol treatment.

Discussion

The development of advanced lesions associated with atherosclerosis and restenosis is highly dependent on VSMC proliferation. Thus, inhibition of VSMC proliferation has become one of the focal points in the prevention of atherosclerosis[3]. Farrerol, a naturally occurring flavonoid derivative, is found in various plants and more abundantly in *Rhododendron dauricum* L. Here we show that farrerol possesses estrogenic properties and could mimic E_2 to suppress VSMC proliferation *in vitro*. We also demonstrate that the effect exerted by farrerol on cell cycle involves the participation of ERβ, but not ERα. Our data thus provide a potential molecular target through which farrerol manifests itself as an anti-mitogenic agent.

In this study, we replaced a single growth factor with 5% FBS to induce cell proliferation. FBS contains a range of growth factors, including platelet-derived growth factor (PDGF), fibroblast growth factor (FGF), transforming growth factor, serotonin, and thrombin[18]. It was hoped that this would simulate the multiple factors environment *in vivo*. Indeed, addition of 5% FBS to the culture medium resulted in a 2.65-fold increase in VSMC proliferation that was blocked by farrerol in a concentration-dependent manner (Figure 2).

Cell cycle is a highly regulated process that involves a complex cascade of events. Modulation of expression and function of cell cycle regulatory proteins provides an important approach to the control of cell growth. According to the flow cytometry analysis, farrerol profoundly decreased FBS-induced transition to the S phase (Figure 3). It is known that the move from G_1 to S phase is closely linked to the activation of cell cycle regulatory proteins such as CDKs[28]. In particular, the cyclin D1/CDK4 and cyclin E/CDK2 complexes are essential for entering the S phase[28]. As shown in Figure 4A, farrerol displayed a potent inhibitory effect on the expression of a number of cell cycle regulatory proteins (cyclin D1, cyclin

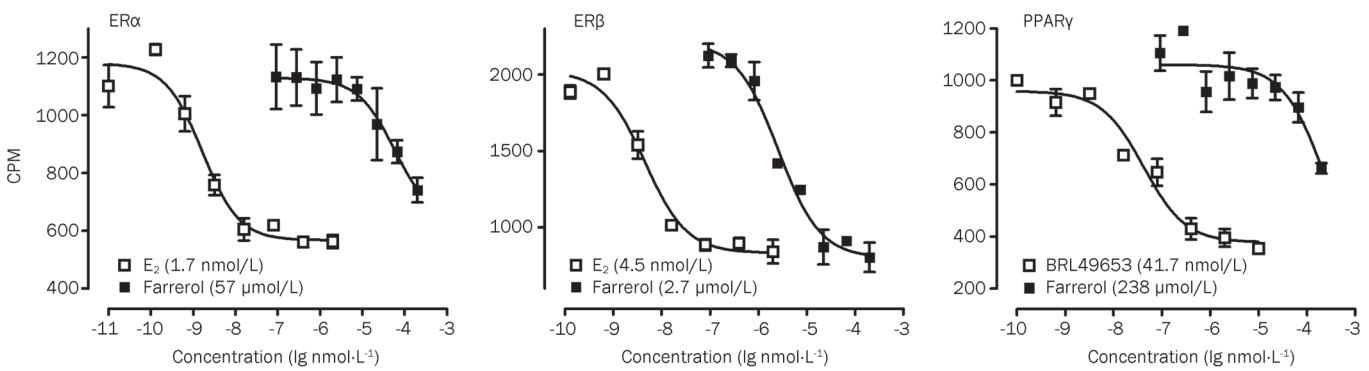

Figure 6. Specificity of farrerol for ERβ. Competitive receptor-binding assay was conducted to assess interaction between radiolabeled ligands and recombinant human ERα, ERβ, and PPARγ. Values in parentheses indicate respective IC_{50} (μmol/L) of farrerol for each receptor. Data are presented as mean±SEM.

E, CDK2, and CDK4). It appears that farrerol exerts its action through down-regulation of positive regulators in the cell cycle.

Cell cycle modulators such as cyclin D1 and cyclin E are regulated by ERK1/2 pathway, which plays a crucial role in serum-induced VSMC proliferation[28]. After mitogenic stimulation, ERK1/2 is phosphorylated by MEK kinase and enters the nucleus, where it regulates the expression of cell cycle regulators and subsequent DNA synthesis in VSMCs[29]. In our study, farrerol significantly decreased FBS-induced phosphorylation of ERK1/2 thereby suggesting that farrerol is a negative effecter for ERK1/2 activation leading to suppression on the expression of cell cycle regulators and eventual growth arrest.

An interesting observation relates to the fact that farrerol interacts directly with ERβ, rather than ERα, in VSMCs. In the ERE-reporter gene assay, farrerol was able to activate transcription from the consensus ERE motifs, while specific induction of Gal-ERβ-mediated transactivation and direct binding to ERβ confirmed the relationship between this phytoestrogen and ERβ signaling machinery.

The mechanism by which of estrogens exert inhibitory actions on VSMCs has been intensely investigated following the discovery of a second ER subtype, ERβ. Earlier studies in mice showed that estrogen inhibited VSMC proliferation in the medial area in response to vascular injury in both ERα[30] and ERβ knockout mice[31], indicating that both subtypes are responsible for the anti-mitogenic effect observed. Moreover, it was documented that ERβ was more potent than ERα in inhibiting VSMC proliferation[23, 32]. Taken together, it seems that ERβ behaves like a key mediator for estrogen-related vascular protection. Since isoflavones are capable of preferentially inducing ERβ expression, their beneficial effects on the cardiovascular system of postmenopausal women may be mediated via this pathway[33, 34].

In conclusion, our study provides new experimental evidence supporting the postulated property of farrerol as a functional phytoestrogen capable of inhibiting FBS-induced VSMC proliferation. The effects exerted by farrerol are cell cycle related and ERβ specific. Elucidation of underlying mechanisms of action may offer insights into a possible molecular target relevant to the therapeutic use of this class of natural products, represented by farrerol, in certain cardiovascular diseases, where excess proliferation plays a pivotal pathological role.

Acknowledgements

We are indebted to Drs Tao HE and Dale E MAIS for valuable comments on this manuscript. The study was supported in part by grants from the Ministry of Science and Technology of China (No 2009ZX09302-001) and Shanghai Municipality Government (No 08DZ2291300 and 09DZ2291200).

Author contribution

Qun-yi LI, Li CHEN, and Meng ZHANG performed experiments; Qun-yi LI, Li CHEN, Yan-hui ZHU, Yi-ping WANG, and Ming-wei WANG analyzed the data; Qun-yi LI, Li CHEN, and Ming-wei WANG wrote the paper.

References

1 Rivard A, Andres V. Vascular smooth muscle cell proliferation in the pathogenesis of atherosclerotic cardiovascular diseases. Histol Histopathol 2000; 15: 557–71.
2 Andres V, Castro C. Antiproliferative strategies for the treatment of vascular proliferative disease. Curr Vasc Pharmacol 2003; 1: 85–98.
3 Grodstein F, Stampfer MJ, Manson JE, Colditz GA, Willett WC, Rosner B, *et al*. Postmenopausal estrogen and progestin use and the risk of cardiovascular disease. N Engl J Med 1996; 335: 453–61.
4 Dubey RK, Gillespie DG, Mi Z, Rosselli M, Keller PJ, Jackson EK. Estradiol inhibits smooth muscle cell growth in part by activating the cAMP-adenosine pathway. Hypertension 2000; 35: 262–6.
5 Akishita M, Ouchi Y, Miyoshi H, Kozaki K, Inoue S, Ishikawa M, *et al*. Estrogen inhibits cuff-induced intimal thickening of rat femoral artery: effects on migration and proliferation of vascular smooth muscle cells. Atherosclerosis 1997; 130: 1–10.
6 Rossouw JE, Anderson GL, Prentice RL, LaCroix AZ, Kooperberg C, Stefanick ML, *et al*. Risks and benefits of estrogen plus progestin in healthy postmenopausal women: principal results from the Women's Health Initiative randomized controlled trial. JAMA 2002; 288: 321–33.
7 Anderson GL, Limacher M, Assaf AR, Bassford T, Beresford SA, Black H, *et al*. Effects of conjugated equine estrogen in postmenopausal women with hysterectomy: the Women's Health Initiative randomized controlled trial. JAMA 2004; 291: 1701–12.
8 Hsia J, Langer RD, Manson JE, Kuller L, Johnson KC, Hendrix SL, *et al*. Conjugated equine estrogens and coronary heart disease: the Women's Health Initiative. Arch Intern Med 2006; 166: 357–65.
9 Manson JE, Allison MA, Rossouw JE, Carr JJ, Langer RD, Hsia J, *et al*. Estrogen therapy and coronary-artery calcification. N Engl J Med 2007; 356: 2591–602.
10 Dubey RK, Gillespie DG, Imthurn B, Rosselli M, Jackson EK, Keller PJ. Phytoestrogens inhibit growth and MAP kinase activity in human aortic smooth muscle cells. Hypertension 1999; 33: 177–82.
11 Grainger DJ, Metcalfe JC. Tamoxifen: teaching an old drug new tricks? Nat Med 1996; 2: 381–5.
12 Cerquetani E, Vitale C, Mercuro G, Fini M, Zoncu S, Rosano GM. Comparative vascular effects of hormone replacement therapy and raloxifene in women at increased cardiovascular risk. Gynecol Endocrinol 2004; 18: 291–8.
13 Sacks FM, Lichtenstein A, Van Horn L, Harris W, Kris-Etherton P, Winston M. Soy protein, isoflavones, and cardiovascular health: an American Heart Association Science Advisory for professionals from the Nutrition Committee. Circulation 2006; 113: 1034–44.
14 Cassidy A, Hooper L. Phytoestrogens and cardiovascular disease. J Br Menopause Soc 2006; 12: 49–56.
15 Kim SY, Jin YR, Lim Y, Kim JH, Cho MR, Hong JT, *et al*. Inhibition of PDGFβ-receptor tyrosine phosphorylation and its downstream intracellular signal transduction in rat aortic vascular smooth muscle cells by kaempferol. Planta Med 2005; 71: 599–603.
16 Ibarra M, Perez-Vizcaino F, Cogolludo A, Duarte J, Zaragoza-Arnaez F, Lopez-Lopez JG, *et al*. Cardiovascular effects of isorhamnetin and quercetin in isolated rat and porcine vascular smooth muscle and isolated rat atria. Planta Med 2002; 68: 307–10.
17 Cao Y, Lou C, Fang Y, Ye J. Determination of active ingredients of *Rhododendron dauricum* L by capillary electrophoresis with electrochemical detection. J Chromatogr A 2002; 943: 153–7.
18 Peng YY, Liu FH, Ye JN. Determination of bioactive flavonoids

in *Rhododendron dauricum* L by capillary electrophoresis with electrochemical detection. Chromatographia 2004; 60: 597–602.
19 Cao Y, Chu Q, Ye J. Chromatographic and electrophoretic methods for pharmaceutically active compounds in *Rhododendron dauricum*. J Chromatogr B Analyt Technol Biomed Life Sci 2004; 812: 231–40.
20 Rodriguez A, Fortuno A, Gomez-Ambrosi J, Zalba G, Diez J, Fruhbeck G. The inhibitory effect of leptin on angiotensin II-induced vasoconstriction in vascular smooth muscle cells is mediated via a nitric oxide-dependent mechanism. Endocrinology 2007; 148: 324–31.
21 Sasu S, LaVerda D, Qureshi N, Golenbock DT, Beasley D. *Chlamydia pneumoniae* and chlamydial heat shock protein 60 stimulate proliferation of human vascular smooth muscle cells via toll-like receptor 4 and p44/p42 mitogen-activated protein kinase activation. Circ Res 2001; 89: 244–50.
22 Pizarro JG, Yeste-Velasco M, Esparza JL, Verdaguer E, Pallas M, Camins A, *et al*. The antiproliferative activity of melatonin in B65 rat dopaminergic neuroblastoma cells is related to the downregulation of cell cycle-related genes. J Pineal Res 2008; 45: 8–16.
23 Watanabe T, Akishita M, Nakaoka T, Kozaki K, Miyahara Y, He H, *et al*. Estrogen receptor β mediates the inhibitory effect of estradiol on vascular smooth muscle cell proliferation. Cardiovasc Res 2003; 59: 734–44.
24 Livak KJ, Schmittgen TD. Analysis of relative gene expression data using real-time quantitative PCR and the $2^{-\Delta\Delta CT}$ method. Methods 2001; 25: 402–8.
25 Nelson PR, Yamamura S, Mureebe L, Itoh H, Kent KC. Smooth muscle cell migration and proliferation are mediated by distinct phases of activation of the intracellular messenger mitogen-activated protein kinase. J Vasc Surg 1998; 27: 117–25.
26 Yoon BK, Oh WJ, Kessel B, Roh CR, Choi D, Lee JH, *et al*. 17β-Estradiol inhibits proliferation of cultured vascular smooth muscle cells induced by lysophosphatidylcholine via a nongenomic antioxidant mechanism. Menopause 2001; 8: 58–64.
27 Geraldes P, Sirois MG, Tanguay JF. Specific contribution of estrogen receptors on mitogen-activated protein kinase pathways and vascular cell activation. Circ Res 2003; 93: 399–405.
28 Wei GL, Krasinski K, Kearney M, Isner JM, Walsh K, Andres V. Temporally and spatially coordinated expression of cell cycle regulatory factors after angioplasty. Circ Res 1997; 80: 418–26.
29 Adam RM, Borer JG, Williams J, Eastham JA, Loughlin KR, Freeman MR. Amphiregulin is coordinately expressed with heparin-binding epidermal growth factor-like growth factor in the interstitial smooth muscle of the human prostate. Endocrinology 1999; 140: 5866–75.
30 Iafrati MD, Karas RH, Aronovitz M, Kim S, Sullivan TR Jr, Lubahn DB, *et al*. Estrogen inhibits the vascular injury response in estrogen receptor α-deficient mice. Nat Med 1997; 3: 545–8.
31 Karas RH, Hodgin JB, Kwoun M, Krege JH, Aronovitz M, Mackey W, *et al*. Estrogen inhibits the vascular injury response in estrogen receptor β-deficient female mice. Proc Natl Acad Sci U S A 1999; 96: 15133–6.
32 Lindner V, Kim SK, Karas RH, Kuiper GG, Gustafsson JA, Mendelsohn ME. Increased expression of estrogen receptor-β mRNA in male blood vessels after vascular injury. Circ Res 1998; 83: 224–9.
33 Crisafulli A, Altavilla D, Marini H, Bitto A, Cucinotta D, Frisina N, *et al*. Effects of the phytoestrogen genistein on cardiovascular risk factors in postmenopausal women. Menopause 2005; 12: 186–92.
34 Goodman-Gruen D, Kritz-Silverstein D. Usual dietary isoflavone intake is associated with cardiovascular disease risk factors in postmenopausal women. J Nutr 2001; 131: 1202–6.

Acta Pharmacologica Sinica (2011) 32: 441–448
 1671-4083/11 $32.00
www.nature.com/aps

Original Article

Sildenafil and FDP-Sr attenuate diabetic cardiomyopathy by suppressing abnormal expression of myocardial CASQ2, FKBP12.6, and SERCA2a in rats

Yu-si CHENG[1], De-zai DAI[1, *], Hui JI[1, *], Qi ZHANG[2], Yin DAI[1]

[1]The Faculty of Pharmacy, China Pharmaceutical University, Nanjing 210009, China; [2]The Bioengineering and Pharmaceutical Faculty, Nanjing University of Technology, Nanjing 210009, China

Aim: To study whether calcium-modulating proteins CASQ2, FKBP12.6 and SERCA2a participate in diabetic cardiomyopathy, and whether the beneficial actions of testosterone, sildenafil or fructose diphosphate Sr (FDP-Sr) in the treatment of diabetic cardiomyopathy result from suppressing these molecules.

Methods: Fifty male Sprague-Dawley (SD) rats were divided into five groups. Except for the normal group (non-diabetic), the other four groups were injected with streptozotocin (STZ, 60 mg/kg, ip) to induce diabetes. Four weeks after STZ injection, the four groups received sildenafil (12 mg·kg^{-1}·d^{-1}, ig, for 4 week), FDP-Sr (200 mg/kg, ig, for 4 week), testosterone propionate (4 mg·kg^{-1}·d^{-1}, sc, for 4 week), or no treatment, respectively.

Results: In the diabetic rats, blood glucose, free fatty acids, triglycerides, total cholesterol, and low-density lipoprotein cholesterol (LDL-C) were significantly increased, while high-density lipoprotein cholesterol (HDL-C) was significantly reduced, as compared to the non-diabetic rats. Cardiac dysfunction and myocardial hypertrophy of the diabetic rats were associated with increased mRNA and protein expression of iNOS, OBRb, and PKCε, while expression of CASQ2, SERCA2a, and FKBP12.6 was significantly down-regulated. Sildenafil and FDP-Sr, but not testosterone, significantly attenuated the biomarker abnormalities, without changing the metabolic abnormalities.

Conclusion: CASQ2, FKBP12.6 and SERCA2a were down-regulated in diabetic cardiomyopathy. Sildenafil and FDP-Sr, but not testosterone, attenuated the cardiac dysfunction in diabetic cardiomyopathy, without changing the metabolic abnormalities, which may results from inhibiting oxidative and inflammatory cytokines and improving calcium homeostasis.

.

Keywords: diabetic cardiomyopathy; CASQ2; FKBP12.6; SERCA2a; sildenafil; FDP-Sr; testosterone; calcium homeostasis

Acta Pharmacologica Sinica (2011) 32: 441–448; doi: 10.1038/aps.2010.226; published online 28 Mar 2011

Introduction

By 2025, there will be an estimated 300 million people worldwide suffering from diabetes mellitus (DM)[1]. Up to 80% of morbidity and mortality in diabetic patients is due to cardiovascular disease (CVD). Initially, cardiac changes are asymptomatic. Later, left ventricular hypertrophy as well as diastolic and systolic dysfunction develops, and finally, symptomatic heart failure occurs. This unique pathological process is referred to as diabetic cardiomyopathy[2, 3].

The main cause of diabetic cardiomyopathy is metabolic changes characterized by a sustained elevation of blood glucose and lipids, which promotes the formation of advance glycation end products (AGEs) over time[4, 5]. AGE excess stimulates glycosylation, which adversely affects cardiac contractility, likely through calcium-modulating proteins in the sarcoplasmic reticulum (SR). Sarcoplasmic reticulum calcium pump 2a (SERCA2a) is responsible for the uptake of intracellular calcium back into the SR and is essential for cardiac function. SERCA2a is very sensitive to posttranslational modification, and glycosylation of SERCA2a leads to cardiac dysfunction[6, 7]. The systolic function of myocardial cells relies mainly on ryanodine receptor type 2 (RyR2), FOK binding protein/calstabin 2 (FKBP12.6), SERCA2a, and troponin C, whereas diastolic function is dependent on SERCA2a and sodium calcium exchangers (NCX). Calcium homeostasis, the basis of cardiac function, relies on the release (RyR2 and FKBP12.6), uptake (SERCA2a and phospholamban, PLB), and storage (calsequestin 2, CASQ2) of Ca^{2+} in the SR. RyR2, FKBP12.6, SERCA2a, and PLB were found to be downregulated in failing hearts and diabetic cardiomyopathy, but these changes can be

* To whom correspondence should be addressed.
E-mail dezaidai@vip.sina.com; huijicpu@163.com
Received 2010-08-24 Accepted 2010-12-17

alleviated by drug intervention[8, 9]. Furthermore, SERCA2a overexpression is protective against STZ-induced cardiotoxicity in rats[10]. CASQ2 holds Ca^{2+} in the ER lumen and affects calcium release during the cardiac cycle. CASQ2 or RyR2 mutations may lead to a dangerous arrhythmia called catecholaminergic polymorphic ventricular tachycardia (CPVT)[11]. Additionally, abnormal CASQ2 expression can be caused by isoproterenol and relieved by CPU0213, an endothelin receptor antagonist[11, 12]. We aimed to explore if downregulation of CASQ2 disrupts calcium homeostasis in diabetic cardiomyopathy. Currently, no studies have investigated how changes in CASQ2 expression affect diabetic cardiomyopathy.

Recent evidence has suggested that low serum testosterone, as seen in male hypogonadism, is an independent risk factor for cardiovascular disease (CVD) due to increased inflammatory factors and cytokines in the myocardium[13]. Testosterone replacement therapy (TRT) has become an attractive intervention that may relieve the cardiac dysfunction associated with late-onset hypogonadism, a potential oxidative stress, through its antioxidant activity[14–16].

Sildenafil, a phosphodiesterase type 5 (PDE5) selective inhibitor, has been shown to improve heart failure by correcting vascular dysfunction through increasing vascular cyclic guanosine monophosphate (cGMP), endogenous NO, and free radical-scavenging activity[17, 18]. However, the efficacy of sildenafil in attenuating diabetic cardiomyopathy has not been shown. FDP-Sr, a derivative of FDP that contains three extra adenosine triphosphates (ATPs) in the moiety, has been shown to be effective in attenuating diabetic cardiomyopathy[19, 20] (Figure 1).

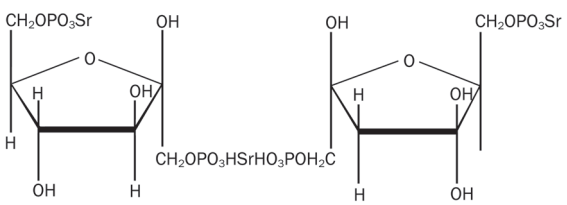

Figure 1. The chemical structure of FDP-Sr.

We hypothesized that diabetic cardiomyopathy was a unique disorder characterized by cardiac dysfunction associated with low serum testosterone and downregulated calcium-handling proteins at the SR, including CASQ2, FKBP12.6, and SERCA2a. In this study, the effects of FDP-Sr, sildenafil, and testosterone on diabetic cardiomyopathy were tested in terms of relieving oxidative stress and normalizing calcium homeostasis in the myocardium.

Materials and methods

Animals

Adult male Sprague-Dawley (SD) rats weighing 200–220 g were used. They were housed in a controlled environment and allowed free access to water and food. Animal handling and experimental procedures were in accordance with the regulations of the Jiangsu Provincial Government and the Principles of Laboratory Animal Care published by the US National Institutes of Health (NIH Publication No 85-23, revised 1996).

Experimental protocol

Fifty SD male rats were randomly divided into five groups. Except for the non-diabetic group, rats were injected with STZ (60 mg/kg, intraperitoneal) once. On days 7, 14, 21, and 28 after STZ administration, blood glucose was measured. Blood glucose consistently greater than 16.7 mmol/L was considered to be indicative of diabetes. During weeks 5 to 8 after STZ injection, animals were treated with sildenafil (12 mg/kg, ig), FDP-Sr (200 mg/kg, ig), or testosterone propionate (4 mg/kg, subcutaneous). Rats in the non-diabetic or STZ untreated groups were given an equal amount of citric acid buffer.

Hemodynamic changes

On day 57, the rats were anesthetized with urethane (1.5 g/kg, intraperitoneal). A catheter (PE 50, ID 0.58 mm, *OD* 0.965 mm, Becton Dickinson, San Jose, CA, USA) was inserted into the left ventricular (LV) chamber through the right carotid artery to measure LV systolic blood pressure (LVSP), LV end diastolic blood pressure (LVEDP), maximum rising rate of LV pressure (LV+dp/dt_{max}), and minimum declining rate of LV pressure (LV-dp/dt_{min}), as described previously[21].

LV weight index

After hemodynamic measurements, the rats' hearts were excised and dissected into the LV free wall plus septum (LV) and right ventricle (RV). The LV weight index was assessed as the weight of the LV divided by body weight (LVW/BW).

Cell culture

Cardiomyocytes isolated from neonatal rats (1–3 d old) were cultured for 72 h in DMEM medium containing 20% fetal bovine serum and 0.1 mmol/L bromodeoxyuridine. The adherent cell density was 0.5×10^6/mL. Then the cardiomyocytes were incubated for 24 h with testosterone (10^{-5}, 10^{-6}, or 10^{-7} mol/L), FDP-Sr (10^{-5}, 10^{-6}, or 10^{-7} mol/L), or sildenafil (10^{-5}, 10^{-6}, or 10^{-7} mol/L). The control cells were treated with DMSO. CASQ2 mRNA and protein expression were measured to investigate if changes in CASQ2 could be induced by testosterone, FDP-Sr, or sildenafil in the absence of high-glucose medium.

RT-PCR

Total RNA was extracted using Trizol reagent (Biouniquer Technology Company, Nanjing, China) according to the manufacturer's instructions. Five milligrams of RNA was used to synthesize cDNA using SUPERSCRIPT II RNase H-Reverse Transcriptase (Biouniquer Technology Company, Nanjing, China) according to the manufacturer's protocol. This cDNA was used as a template for the PCR reactions[22]. PCR primers specific for iNOS, OBRb, PKCε, CASQ2, FKBP12.6, SER-

CA2a, and GAPDH were designed as indicated in previous reports[12, 21].

Western blotting

For quantitative analysis of myocardial phosphorylated PKCε (pPKCε), CASQ2, FKBP12.6, and SERCA2a protein levels, 100 mg of heart tissue was homogenized in 1 mL of extraction buffer and centrifuged at 10 000×*g* for 10 min as previously described[21]. After determining protein concentration, the supernatants were stored at -20 °C. An aliquot was heated to 100 °C for 10 min and size fractionated using 10% sodium dodecyl sulfate-polyacrylamide gel electrophoresis (SDS-PAGE). The extracted protein was transferred to a nitrocellulose membrane and blocked with nonfat milk (5% *w/v*) followed by incubation with primary antibody for another 1–2 h at 37 °C. After three washes, the blot was incubated with horseradish peroxidase-conjugated goat secondary antibody IgG (Affinity Bioreagents; 1:500) for an additional 1 h at 37 °C[22]. Antigen was detected with a DAB kit. The density of the bands was analyzed using Labworks imaging acquisition and analysis software (GDS8000, Syngene, UK).

Statistical analysis

SPSS 11.5 (SPSS company, Chicago, USA) was used to analyze the results. Data were presented as the mean±SD. For statistical evaluation, one-way analysis of variance was used followed by Dunnett's test. The Student Newman Keuls test was performed when the variance was equal, and the Games-Howell test was performed when the variance was not equal. A *P*-value of less than 0.05 was considered statistically significant.

Results

Serum glucose, lipids, and androgens

In the diabetic group, blood glucose, free fatty acids, triglycerides, total cholesterol, and LDL-C were significantly increased, and HDL-C was significantly decreased, indicating that the STZ-injected rats had marked metabolic changes ($P<0.01$). Single treatment with testosterone, Sildenafil, and FDP-Sr had no effects on the metabolic changes (Figure 2). Serum androgens (nmol/L) were sharply reduced in the STZ-injected rats (4.6±1.9, $P<0.01$) compared to the non-diabetic group (15.6±4.1). Serum androgens were significantly elevated in the testosterone group compared to the diabetic untreated group (12.9±2.1, $P<0.01$). There was no difference compared to the non-diabetic rats. The FDP-Sr group had a moderate increase in serum androgen compared to the diabetic untreated group (10.6±2.6, $P<0.01$). Sildenafil did not raise serum androgen (5.8±2.1).

Cardiac performance

In the diabetic group, LVSP and LV plus dp/dt_{max} decreased significantly, while LVEDP and LV-dp/dt_{min} significantly increased compared to the non-diabetic group ($P<0.01$). Sildenafil and FDP-Sr led to a significant recovery in cardiac dysfunction ($P<0.01$). Additionally, the diabetic untreated group had a significantly increased LV mass index compared to the normal group ($P<0.01$). This increase was blunted by FDP-Sr and sildenafil. In contrast, testosterone had no effect on the hemodynamic or LV mass index abnormalities (Figure 3).

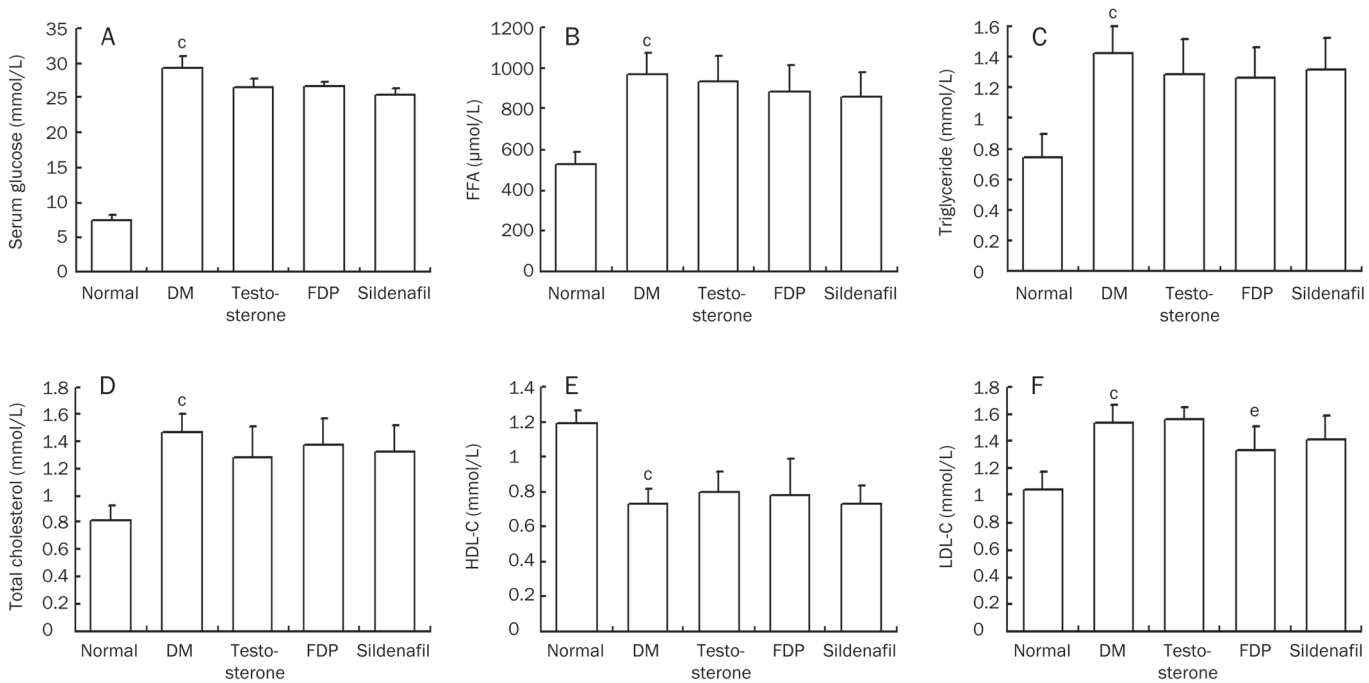

Figure 2. Changes in blood sugar and lipid were found in STZ-injected rats. The metabolic changes in DM rats were significant and testosterone propionate, sildenafil, and FDP-Sr had no effects on the altered sugar and lipid metabolism. (A) Serum glucose; (B) Free fatty acid (FFA); (C) Triglyceride; (D) Total cholesterol; (E) HDL-C; (F) LDL-C. Mean±SD. $n=10$. $^cP<0.01$ *vs* normal. $^eP<0.05$ *vs* DM.

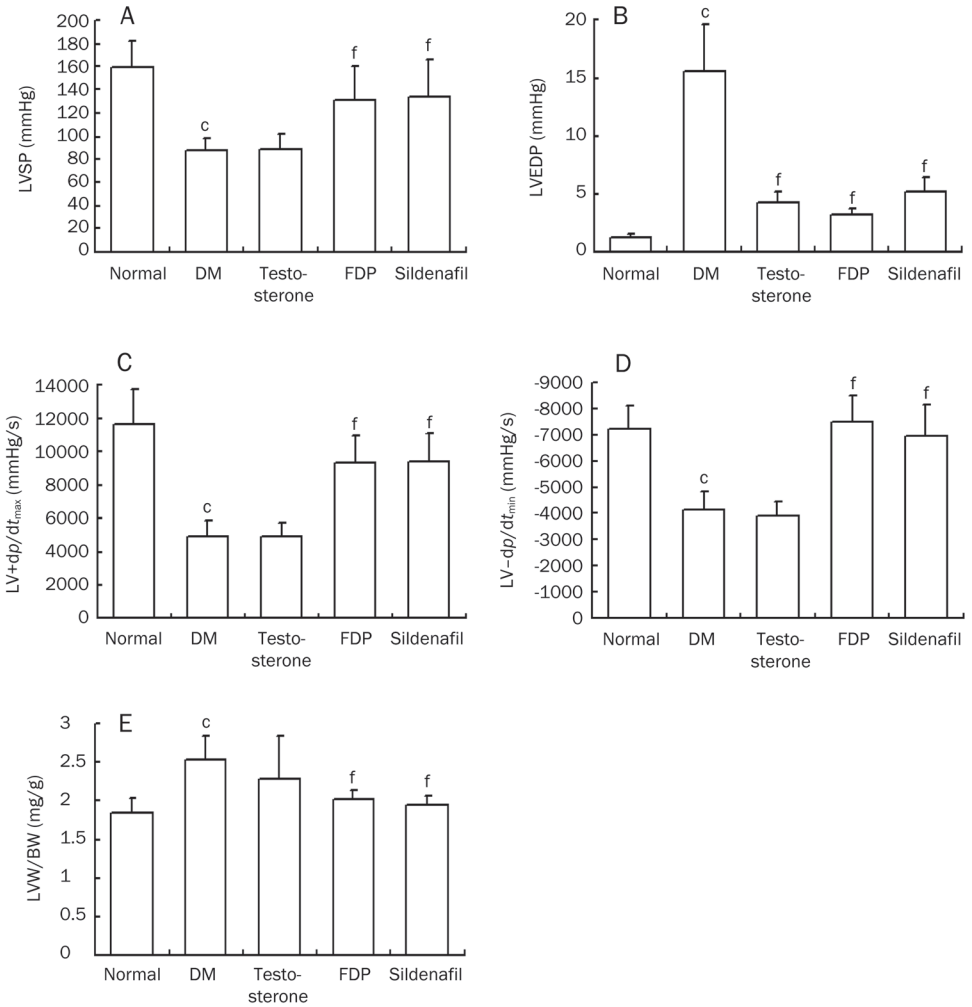

Figure 3. FDP-Sr and sildenafil improved hemodynamic parameters and heart weight index in STZ injected rats. (A) LVSP; (B) LVEDP; (C) LV+dp/dt_{max}; (D) LV-dp/dt_{min}; (E) the LV weight index. Mean±SD. n=10. ^{c}P<0.01 *vs* normal; ^{f}P<0.01 *vs* DM.

Oxidative stress

Plasma malondialdehyde (MDA), a measure of oxidants, was significantly elevated, and GSH-Px, an antioxidant marker, was significantly decreased in the diabetic untreated group compared to the non-diabetic group (P<0.01, respectively). Therefore, the diabetic rats had significant oxidative stress. Sildenafil and FDP-Sr suppressed MDA and raised GSH-PX levels compared to the diabetic untreated group (P<0.01, Figure 4). Thus, the antioxidant activity of sildenafil and FDP-Sr ameliorated the pathological changes in diabetic cardiomyopathy. Testosterone did not significantly block these pathological changes (Figure 4).

Cardiac iNOS, OBRb, and PKCε

In the diabetic rats the mRNA expression of iNOS and OBRb, a leptin receptor, was significantly increased (P<0.01). Additionally, PKCε mRNA expression was significantly increased (P<0.01). Sildenafil and FDP-Sr ameliorated the abnormal expression of iNOS, OBRb, and PKCε mRNA (P<0.01). In contrast, testosterone did not affect any of these biomarkers

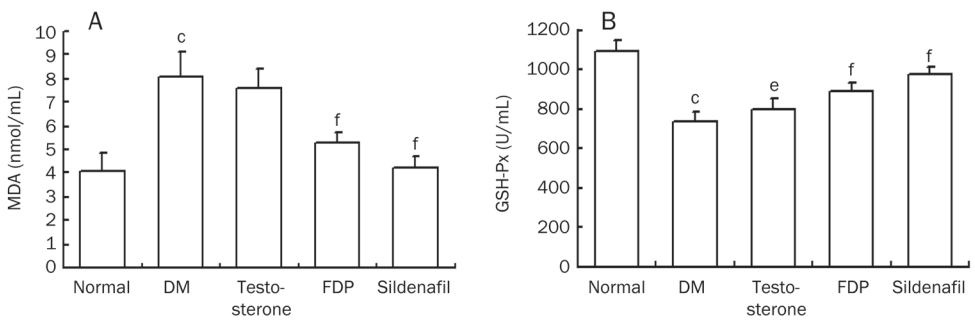

Figure 4. Changes of MDA and GSH-PX in serum were improved by FDP-Sr or sildenafil in diabetic rats. (A) MDA; (B) GSH-Px. Mean±SD. n=10. ^{c}P<0.01 *vs* normal; ^{e}P<0.05, ^{f}P<0.01 *vs* DM.

except iNOS mRNA (Figure 5).

Calcium homeostasis

Calcium homeostasis in the myocardium is maintained by the calcium-handling proteins, which control intracellular calcium release, uptake, and storage in the SR and are manipulated by bioactive molecules, including FKBP12.6, the main regulator of RyR2, as well as SERCA2a and CASQ2. In the diabetic rats, mRNA and protein expression of CASQ2, SERCA2a, and FKBP12.6 were reduced (P<0.01). This indicates that aspects of calcium homeostasis, such as calcium release, uptake during diastole, and calcium-storing capacity in the SR are impaired in diabetic cardiomyopathy. The biomarker abnormalities may lead to heart failure and severe arrhythmias, which are likely to appear in diabetic cardiomyopathy. Sildenafil and FDP-Sr attenuated the abnormal expression of these molecules (P<0.01). Testosterone ameliorated CASQ2 and SERCA2a mRNA expression but had no effects on their protein expression. Testosterone had no effects on both mRNA and protein expression of FKBP12.6 (Figure 6).

CASQ2 mRNA and protein expression were measured in cardiomyocytes grown in normal medium with normal glucose as well as sildenafil, FDP-Sr, and testosterone. No difference in CASQ2 expression was found in these cells compared to the cardiomyocytes in the absence of drug interventions (Figure 7). Therefore, we believe that sildenafil and FDP-Sr are effective in improving abnormal calcium homeostasis and cardiac dysfunction by suppressing the pathological processes due to hyperglycemia in the diabetic rats.

Discussion

In diabetic cardiomyopathy, low serum testosterone and changes in glucose and lipid metabolism are the main factors responsible for disease progression. The cardiac dysfunction and hypertrophy in diabetic rats responded significantly to sildenafil and FDP-Sr but not testosterone. However, sildenafil and FDP-Sr did not improve hyperglycemia or hypercholesterolemia. The metabolic changes were not linked directly to cardiac dysfunction. Intermediate events, such as ROS and inflammatory factors, are critical in the pathogenesis of diabetic cardiomyopathy.

In this study, cardiac dysfunction in rats likely correlates with low serum testosterone; thus, we treated the mice with exogenous testosterone, which is a common way to correct this deficiency[23]. FDP-Sr moderately raises serum testosterone, likely through improving pathological changes in the testes. In contrast, sildenafil plays no role in correcting low serum testosterone. As a result, sildenafil and FDP-Sr, rather than testosterone supplement, dramatically attenuate cardiac dysfunction and oxidative stress. Exogenous testosterone did not alleviate diabetic cardiomyopathy, likely because it lacks significant antioxidant activity and cannot overcome the pathological changes induced by hyperglycemia.

Increased oxidative stress *in vivo* has been shown to contribute to the pathogenesis of diabetic cardiomyopathy[24, 25]. MDA, a lipid oxidation end product, affects the mitochondrial respiratory chain complex and the activities of key enzymes in the mitochondria. Excess reactive oxygen species (ROS) come from mitochondria and result from the activities of NADPH

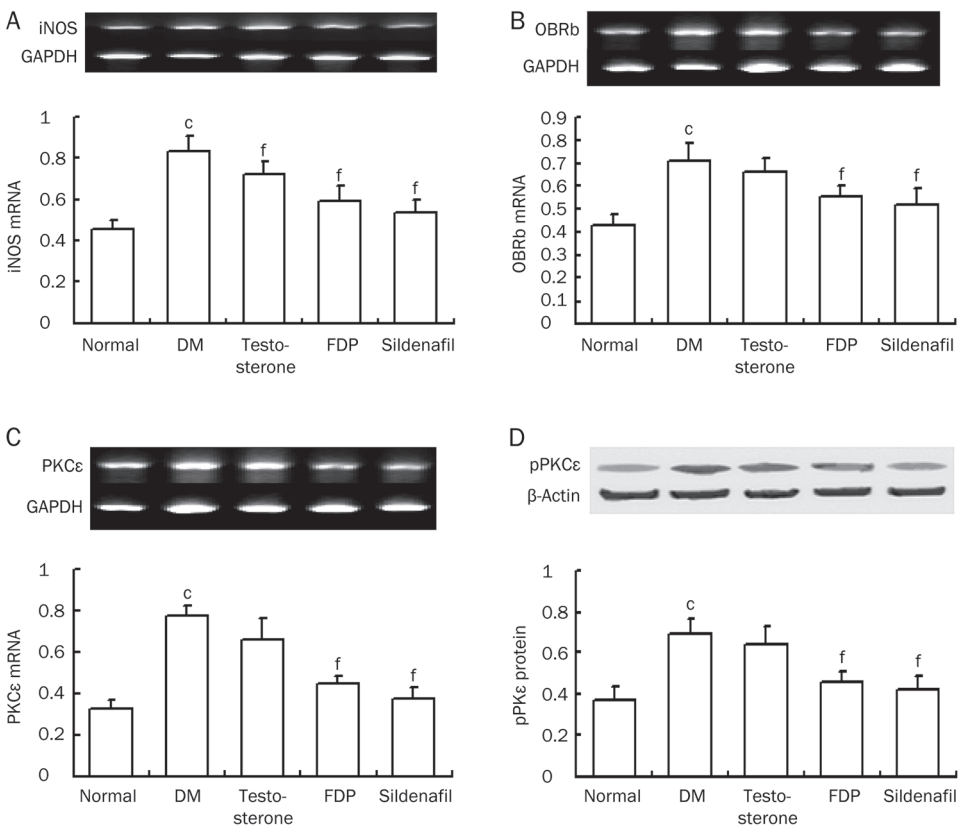

Figure 5. FDP-Sr and sildenafil inhibited abnormal mRNA expression of iNOS, OBRb, PKCε, and protein exprsssion of pPKCε. (A) iNOS mRNA; (B) OBRb mRNA; (C) PKCε mRNA; (D) pPKCε protein. Mean±SD. n=10. ^{c}P<0.01 *vs* normal; ^{f}P<0.01 *vs* DM.

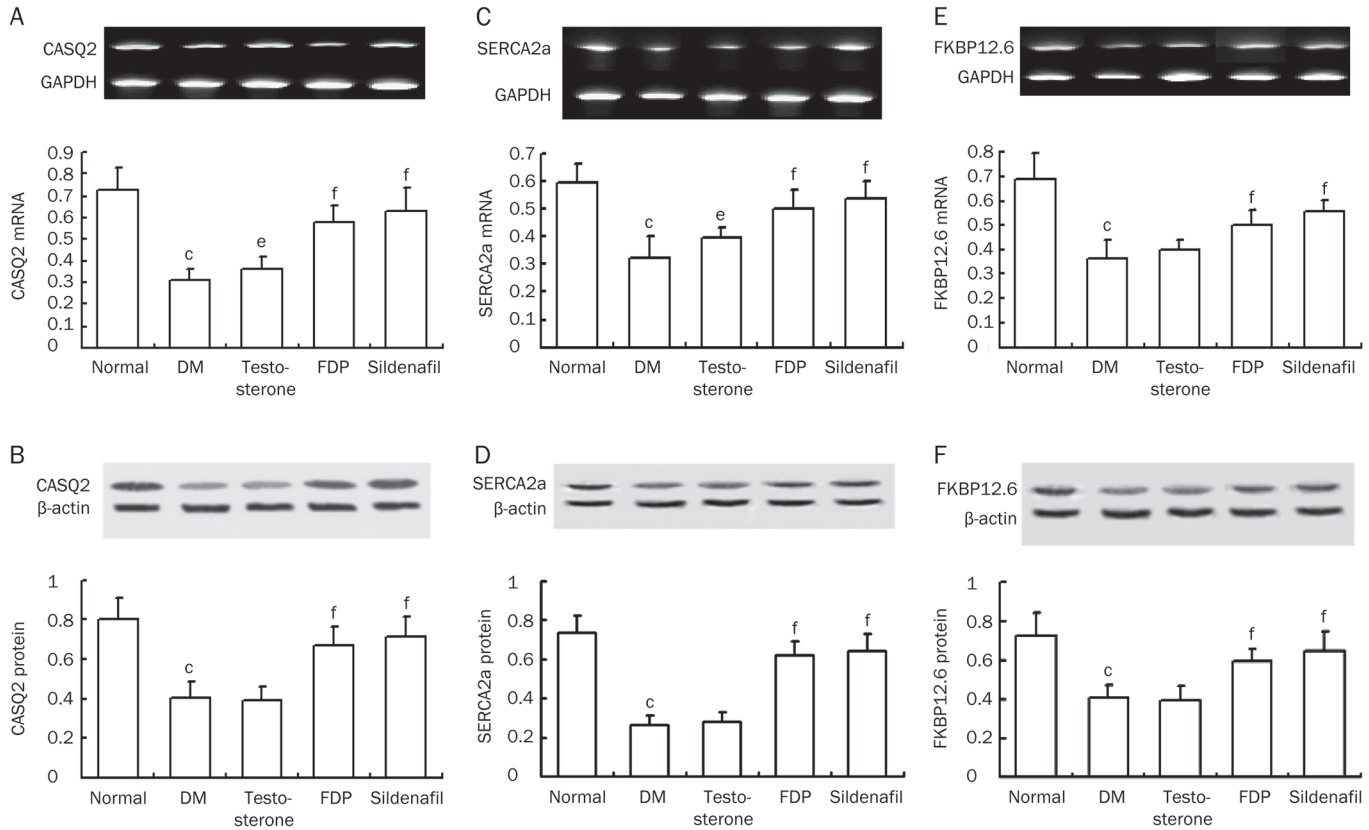

Figure 6. FDP-Sr and sildenafil improved abnormal mRNA and protein expressions of the calcium handing system. (A) CASQ2 mRNA. (B) CASQ2 protein. (C) SERCA2a mRNA. (D) SERCA2a protein. (E) FKBP12.6 mRNA. (F) FKBP12.6 protein. Mean±SD. n=10. ^{b}P<0.05, ^{c}P<0.01 *vs* normal; ^{e}P<0.05, ^{f}P<0.01 *vs* DM.

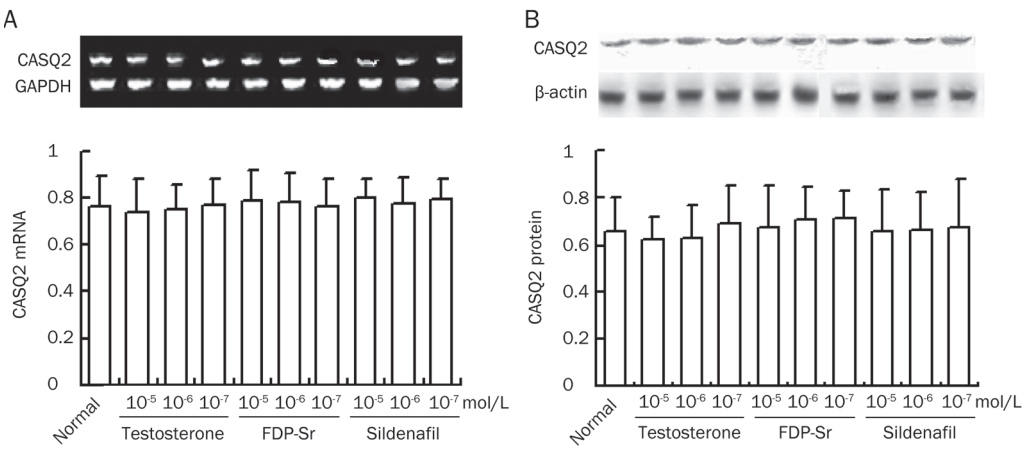

Figure 7. The mRNA and protein expression of CASQ2 in the absence of diabetes mellitus with the three compounds in cardiomyocytes. (A) CASQ2 mRNA. (B) CASQ2 protein. Mean±SD. n=10.

oxidase and induced NOS (iNOS) activity, which have been implicated in diabetic insults[26]. Increased ROS disturb many of the normal functions of the ER, induce cellular damage, and lead to apoptosis[27]. Activated iNOS can be combined with NO to form toxic peroxynitrite (ONOO·−), which impairs the subcellular apparatus of the myocardium. Upregulation of iNOS is associated with xanthine oxidase activation and upregulation of NADPH oxidase, p22phox, p40phox, and p47phox, leading to more cardiac dysfunction in diabetic cardiomyopathy[28]. These changes in calcium homeostasis and oxidative stress are consistent with our previous findings[8, 9]. In addition, oxidants and inflammatory cytokines, such as ROS, iNOS, endothelin-1, and leptin, damage DNA, leading to myocardial cell death.

Diabetes is often accompanied by obesity, abnormal lipid metabolism, and leptin upregulation[29, 30]. Leptin is a peptide

hormone secreted by fat cells that stimulates the satiety center in the hypothalamus. However, in pathological conditions, prolonged leptin upregulation eventually leads to leptin resistance and increased expression of the leptin receptor OBRb. OBRb serves as an inflammatory factor that mediates myocardial injury[22].

Disorder of calcium-modulating proteins, such as FKBP12.6 and SERCA2a, has been shown to play a role in diabetic or isoproterenol-induced cardiomyopathy, which causes oxidative stress and inflammation[8, 12, 21]. Downregulation of FKBP12.6 and SERCA2a leads to more intracellular Ca^{2+} at the end of diastole, known as calcium leak, which we found in *L*-thyroxine-induced cardiomyopathy[30]. Thus, downregulation of FKBP12.6 is a marker of calcium leak, which causes cardiac dysfunction and severe arrhythmias. Endothelin receptor antagonists and CPU86017, a berberine derivative, relieve these conditions[23, 30].

Mutation of CASQ2 may cause an autosomal recessive form of the life-threatening arrhythmia CPVT. Additionally, mutations of RyR2 can lead to an autosomal dominant form of CPVT[25]. Normally, CASQ2 and RyR2 form tetramers. When SR calcium is low, RyR2 places the tetramer in an inhibitory state. When SR calcium increases, the CASQ2-RyR2 complex is weakened. If CASQ2 is mutated, the tetramer is even more unstable, and RyR2 sensitivity to calcium increases. As a result, SR calcium leak was more likely[31, 32]. We found that downregulation of CASQ2 is an important event in diabetic cardiomyopathy. Also, downregulation of FKBP12.6 and SERCA2a are likely involved. For example, an increase in the cytosol:SR calcium ratio disrupts SERCA2a function. Therefore, concentrations of calcium in the cytoplasm increase, and excessive calcium flows through sodium calcium exchanger (NCX), leading to increased Na^+ influx into myocardial cells, delayed repolarization, and arrhythmias[33]. Interestingly, in addition to mutation, CASQ2 can be altered by posttranscriptional modifications due to either isoproterenol or hyperglycemia, which also lead to cardiac failure and tachyarrhythmias. CASQ2, FKBP12.6, and SERCA2a are sensitive markers of oxidative stress in the myocardium. Isoproterenol-induced downregulation of FKBP12.6, SERCA2a, and CASQ2 has been associated with increased ROS[34, 35]. ROS produced by hyperglycemia and AGEs are considered to be mediated by the same mechanism as the downregulation of FKBP12.6, SERCA2a, and CASQ2 in diabetic cardiomyopathy. Therefore, sildenafil and FDP-Sr were effective in blunting the abnormalities in calcium-handling proteins and proinflammatory cytokines, such as leptin, iNOS, and endothelin-1, through their antioxidant activities. As demonstrated in this study, changes in CASQ2, FKBP12.6, and SERCA2a are not affected by exogenous testosterone even though the low serum androgen levels were corrected. This is likely due to the mild antioxidant activity of testosterone.

Myocardial diacylglycerol (DAG) activates protein kinase C (PKC) signaling pathways. This process has been found in the vascular tissue of diabetic animals and leads to increased blood vessel susceptibility to hyperglycemia. The PKC/NFκB/c-fos pathway is activated in neonatal rat cardiomyocytes in high-glucose medium[36]. Activated PKCε has been found in isoproterenol-induced cardiomyopathy and in the vasculature of STZ-injected rats[37, 38]. PKCε overexpression may participate in downstream events, including K^+ channel and calcium-handling protein abnormalities, that are involved in diabetic or isoproterenol-induced cardiomyopathy[9, 12, 35]. In this study, PKCε mRNA expression was elevated, and pPKCε was increased in association with cardiac dysfunction. FDP-Sr and sildenafil decreased PKCε mRNA and pPKCε protein significantly, likely through their antioxidant activity .

Conclusion

In this study, CASQ2 was found to be abnormally expressed in diabetic cardiomyopathy. CASQ2 is actively involved in the pathogenesis of diabetic cardiomyopathy and is closely related to oxidative stress and inflammation. Furthermore, other calcium-handling proteins, such as SERCA2a and FKBP12.6, were abnormally expressed. Oxidants, iNOS, OBRb, and pPKCε serve as markers of the metabolic changes responsible for inducing diabetic cardiomyopathy. Sildenafil and FDP-Sr are beneficial for treating diabetic cardiomyopathy through their antioxidant and anti-inflammatory properties. However, FDP-Sr and sildenafil did not affect blood glucose or lipid metabolism, leaving the abnormal metabolic changes intact. Testosterone did not improve cardiac dysfunction or calcium homeostasis in the myocardium.

Acknowledgements

This project was supported by the National Natural Science Foundation of China (No 30873112).

Author contribution

Yu-si CHENG conducted the project, processed the data, and wrote the manuscript. Qi ZHANG provided the sildenafil. Hui JI assisted with the project and discussion of the manuscript. De-zai DAI and Yin DAI designed the hypothesis and project and revised the manuscript.

References

1 Lebeche D, Davidoff AJ, Hajjar RJ. Interplay between impaired calcium regulation and insulin signaling abnormalities in diabetic cardiomyopathy. Nat Clin Pract Cardiovasc Med 2008; 5: 715–24.
2 Aneja A, Tang WH, Bansilal S, Garcia MJ, Farkouh ME. Diabetic cardiomyopathy: insights into pathogenesis, diagnostic challenges, and therapeutic options. Am J Med 2008; 121: 748–57.
3 Asghar O, Al-Sunni A, Khavandi K, Khavandi A, Withers S, Greenstein A, *et al*. Diabetic cardiomyopathy. Clin Sci (Lond) 2009; 116: 741–60.
4 Montagnani M. Diabetic cardiomyopathy: how much does it depend on AGE? Br J Pharmacol 2008; 154: 725–26.
5 Tang M, Zhong M, Shang Y, Lin H, Deng J, Jiang H, *et al*. Differential regulation of collagen types I and III expression in cardiac fibroblasts by AGEs through TRB3/MAPK signaling pathway. Cell Mol Life Sci 2008; 65: 2924–32.
6 Hayat SA, Patel B, Khattar RS, Malik RA. Diabetic cardiomyopathy: mechanisms, diagnosis and treatment. Clin Sci (Lond) 2004; 107: 539–57.

7 Bidasee KR, Zhang Y, Shao CH, Wang M, Patel KP, Dincer UD, *et al*. Diabetes increases formation of advanced glycation end products on Sarco(endo)plasmic reticulum Ca^{2+}-ATPase. Diabetes 2004; 53: 463–73.
8 Qi MY, Xia HJ, Dai DZ, Dai Y. A novel endothelin receptor antagonist CPU0213 improves diabetic cardiac insufficiency attributed to up-regulation of the expression of FKBP12.6, SERCA2a, and PLB in rats. J Cardiovasc Pharmacol 2006; 47: 729–35.
9 Qi MY, Liu HR, Dai DZ, Li N, Dai Y. Total triterpene acids, active ingredients from Fructus Corni, attenuate diabetic cardiomyopathy by normalizing ET pathway and expression of FKBP12.6 and SERCA2a in streptozotocin-rats. J Pharm Pharmacol 2008; 60: 1687–94.
10 Boudina S, Abel ED. Diabetic cardiomyopathy revisited. Circulation 2007; 115: 3213–23.
11 Györke S. Molecular basis of catecholaminergic polymorphic ventricular tachycardia. Heart Rhythm 2009; 6: 123–9.
12 Li N, Jia N, Dai DZ, Hu C, Dai Y. Role of endothelin in the effects of isoprenaline on potassium currents and calsequestrin 2 expression in the heart. Clin Exp Pharmacol Physiol 2010; 37: 557–63.
13 Maggio M, Basaria S. Welcoming low testosterone as a cardiovascular risk factor. Int J Impot Res 2009; 21: 261–4.
14 Jones TH. Testosterone deficiency: a risk factor for cardiovascular disease? Trends Endocrinol Metab 2010; 21: 496–503.
15 Francomano D, Bruzziches R, Natali M, Aversa A, Spera G. Cardiovascular effect of testosterone replacement therapy in aging male. Acta Biomed 2010; 81: 101–6.
16 Mancini A, Leone E, Festa R, Grande G, Silvestrini A, de Marinis L, *et al*. Effects of testosterone on antioxidant systems in male secondary hypogonadism. J Androl 2008; 29: 622–9.
17 Montani D, Chaumais MC, Savale L, Natali D, Price LC, Jaïs X, *et al*. Phosphodiesterase type 5 inhibitors in pulmonary arterial hypertension. Adv Ther 2009; 26: 813–25.
18 Guazzi M. Sildenafil and phosphodiesterase-5 inhibitors for heart failure. Curr Heart Fail Rep 2008; 5: 110–4.
19 Zhang Q, Liu HR, Ying HJ, Dai DZ, Tang XY, Dai Y. Strontium fructose 1,6-diphosphate early diabetic testopathy by suppressing abnormal testicular matrix metalloproteinase system in streptozocin-treated rats. J Pharm Pharmacol 2009; 61: 229–36.
20 Xu M, Dai DZ, Zhang Q, Cheng YS, Dai Y. Upregulated NADPH oxidase contributes to diabetic testicular complication and is relieved by strontium fructose 1,6-diphosphate. Exp Clin Endocrinol Diabetes 2010; 118: 459–65.
21 Cheng YS, Dai DZ, Dai Y. Stress-induced cardiac insufficiency relating to abnormal leptin and FKBP12.6 is ameliorated by CPU0213, an endothelin receptor antagonist, which is not affected by the CYP3A suppressing effect of erythromycin. J Pharm Pharmacol 2009; 61: 569–76.
22 Na T, Dai DZ, Tang XY, Dai Y. Upregulation of leptin pathway correlates with abnormal expression of SERCA2a, phospholamban and the endothelin pathway in heart failure and reversal by CPU86017. Naunyn Schmiedebergs Arch Pharmacol 2007; 375: 39–49.
23 Casey RW, Barkin J. Testosterone replacement therapy for the primary care physician. Can J Urol 2008; 15: 71–7.
24 Bilginoglu A, Seymen A, Tuncay E, Zeydanli E, Aydemir-Koksoy A, Turan B. Antioxidants but not doxycycline treatments restore depressed beta-adrenergic responses of the heart in diabetic rats. Cardiovasc Toxicol 2009; 9: 21–9.
25 Adeghate E. Molecular and cellular basis of the aetiology and management of diabetic cardiomyopathy: a short review. Mol Cell Biochem 2004; 261: 187–91.
26 Violi F, Basili S, Nigro C, Pignatelli P. Role of NADPH oxidase in atherosclerosis. Future Cardiol 2009; 5: 83–92.
27 Münzel T. Endothelial dysfunction: pathophysiology, diagnosis and prognosis. Dtsch Med Wochenschr 2008; 133: 2465–70.
28 Rajesh M, Mukhopadhyay P, Bátkai S, Mukhopadhyay B, Patel V, Haskó G, *et al*. Xanthine oxidase inhibitor allopurinol attenuates the development of diabetic cardiomyopathy. J Cell Mol Med 2009; 13: 2330–41.
29 Iciek R, Wender-Ozegowska E, Seremak-Mrozikiewicz A, Drews K, Brazert J, Pietryga M. Leptin gene, leptin gene receptor polymorphisms and body weight in pregnant women with type 1 diabetes mellitus. Ginekol Pol 2008; 79: 592–601.
30 Zhang Y, Huang ZJ, Dai DZ, Feng Y, Na T, Tang XY, *et al*. Downregulated FKBP12.6 expression and upregulated endothelin signaling contribute to elevated diastolic calcium and arrhythmogenesis in rat cardiomyopathy produced by *L*-thyroxin. Int J Cardiol 2008; 130: 463–71.
31 Liu N, Rizzi N, Boveri L, Priori SG. Ryanodine receptor and calsequestrin in arrhythmogenesis: what we have learnt from genetic diseases and transgenic mice. J Mol Cell Cardiol 2009; 46: 149–59.
32 Györke S, Hagen BM, Terentyev D, Lederer WJ. Chain-reaction Ca^{2+} signaling in the heart. J Clin Invest 2007; 117: 1758–62.
33 Song L, Alcalai R, Arad M, Wolf CM, Toka O, Conner DA, *et al*. Calsequestrin 2 (CASQ2) mutations increase expression of calreticulin and ryanodine receptors, causing catecholaminergic polymorphic ventricular tachycardia. J Clin Invest 2007; 117: 1814–23.
34 Li N, Jia N, Dai DZ, Hu C, Dai Y. Role of endothelin in the effects of isoprenaline on potassium currents and calsequestrin 2 expression in the heart. Clin Exp Pharmacol Physiol 2010; 37: 557–63
35 Li N, Jia N, Dai DZ, Dai Y. Endothelin receptor antagonist CPU0213 and vitamin E reverse downregulation of FKBP12.6 and SERCA2a: a role of hyperphosphorylation of PKCepsilon. Eur J Pharmacol 2008; 591: 211–8.
36 Min W, Bin ZW, Quan ZB, Hui ZJ, Sheng FG. The signal transduction pathway of PKC/NF-kappaB/c-fos may be involved in the influence of high glucose on the cardiomyocytes of neonatal rats. Cardiovasc Diabetol 2009; 8: 8.
37 Cheng YS, Dai DZ, Dai Y. Isoproterenol disperses distribution of NADPH oxidase, MMP-9, and pPKCepsilon in the heart, which are mitigated by endothelin receptor antagonist CPU0213. Acta Pharmacol Sin 2009; 30: 1099–106.
38 Zheng YF, Dai DZ, Dai Y. NaHS ameliorates diabetic vascular injury by correcting depressed connexin 43 and 40 in the vasculature in streptozotocin-injected rats. J Pharm Pharmacol 2010; 62: 615–21.

Acta Pharmacologica Sinica (2011) 32: 449–455
 1671-4083/11 $32.00
www.nature.com/aps

Original Article

Telmisartan attenuates isoproterenol-induced cardiac remodeling in rats via regulation of cardiac adiponectin expression

Bing-yan GUO[1], Yong-jun LI[1, *], Rui HAN[2], Shao-ling YANG[4], Ying-hui SHI[3], De-rong HAN[3], Hong ZHOU[1], Mei WANG[1]

[1]Department of Cardiovascular Medicine, Second Affiliated Hospital, Hebei Medical University, Shijiazhuang 050017, China; [2]Department of Internal Neurology Medicine, First Affiliated Hospital, Hebei Medical University, Shijiazhuang 050017, China; [3]Department of Internal Medicine, Gucheng County Hospital, Gucheng 253800, China; [4]Department of Endocrinology Medicine, Norman Bethune International Peace Hospital, Shijiazhuang 050031, China

Aim: To investigate whether telmisartan (Telm) pretreatment attenuates isoproterenol (Iso)-induced postinfarction remodeling (PIR) in rats, and whether the effect of Telm is associated with cardiac expression of adiponectin.
Methods: PIR was induced in male Wistar rats with two consecutive injections of Iso (80 mg/kg, sc) at an interval of 24 h. Primary culture of ventricular myocytes from neonatal rats was prepared. Iso-induced cardiomyocyte injury was assessed based on cell growth and lactate dehydrogenase (LDH) activity. Cardiac adiponectin expression was measured using qRT-PCR and immunoblot analysis.
Results: In the rats with PIR, Telm (10 mg·kg^{-1}·d^{-1}, *po* for 65 d) suppressed Iso-induced increases in gravimetric parameters, cardiomyocyte diameter and collagen volume fraction, but had no effect on Iso-induced myocardial hypertrophy and interstitial fibrosis. The protective effect of Telm was associated with enhanced protein expression of cardiac adiponectin. In cultured cardiomyocytes, Telm (5–20 μmol/L) inhibited the cell death and LDH release induced by Iso (10 μmol/L), and reversed Iso-induced reduction in adiponectin protein expression. In cardiomyocytes exposed to Iso (20 μmol/L), GW9662 (30 μmol/L), a selective antagonist of PPAR-γ, blocked the effects of Telm pretreatment on adiponectin protein expression, as well as the protective effects of Telm on Iso-induced cell injury.
Conclusion: Telm attenuates Iso-induced cardiac remodeling and cell injury, which is associated with induction of cardiac adiponectin expression.

Keywords: telmisartan; angiotensin II receptor blocker; congestive heart failure; cardiac remodeling; cardiac fibrosis; adiponectin; isoproterenol

Acta Pharmacologica Sinica (2011) 32: 449–455; doi: 10.1038/aps.2010.231; published online 14 Mar 2011

Introduction

There are a variety of experimental models of chronic heart failure (CHF). Isoproterenol (Iso)-induced CHF is a widely used model due to its simple methodology, low cost, and the clinically representative pathophysiological changes it produces. In this model, subcutaneous administration of the beta adrenoceptor agonist Iso produces patchy myocardial necrosis in a dose-related manner while retaining intact coronary vasculature. The pathophysiological and morphological changes observed in Iso-treated rats have been found to be similar to those observed following human myocardial infarction (MI)[1]. MI results in asymmetrical left ventricular remodeling, characterized by fibrosis at both the site of infarct and in the noninfarcted myocardium, in addition to hypertrophy of viable myocytes[2]. These cardiac structural adaptations facilitate compensated hemodynamic performance, but ultimately result in a high incidence of CHF and sudden cardiac death[3].

Adiponectin acts as an anti-inflammatory and antiatherogenic cytokine and has been demonstrated to suppress cardiac hypertrophy in response to pressure overload[4, 5]. Adiponectin, a member of the adipokine superfamily, is expressed in adult ventricular cardiomyocytes and is upregulated by activation of peroxisome proliferator-activated receptor-gamma (PPAR-γ)[6]. Adiponectin was recently shown to be suppressed by tumor necrosis factor-alpha (TNF-α)[7], another cytokine that is expressed in and secreted from cardiomyocytes[8]. Locally generated TNF-α plays a role in cardiac remodeling via its ability to stimulate apoptosis and inflammatory and fibrogenic responses in a pressure-overloaded heart, which in turn contribute to cardiac dysfunction[9,10].

* To whom correspondence should be addressed.
E-mail lyjbs2009@yeah.net
Received 2010-06-23 Accepted 2010-12-23

Telmisartan (Telm) is a selective angiotensin II type 1 receptor antagonist that is widely used in the treatment of hypertension, CHF, and diabetic nephropathy[11–13]. It has been shown to have beneficial effects on postinfarct ventricular remodeling[14]. Recently, Telm was reported to have partial activity as a PPAR-γ agonist, enabling it to regulate metabolic and inflammatory pathways and improve left ventricular functions[15, 16]. Moreover, Telm treatment has been shown to reduce the expression of inflammatory cytokines, including TNF-α and its transcription factors[17–19]. Angiotensin receptor blocker (ARB) treatment increases circulating adiponectin concentrations in humans and adiponectin mRNA levels in adipose tissue in hypertensive rats[20–23]. ARB treatment also induces cardiac adiponectin expression in mice with viral myocarditis[24]. In addition, Telm was recently shown to be present in plasma at higher levels than other ARBs following oral administration[25], suggesting that it is absorbed well when administered orally. To date, however, the effects of Telm on cardiac adiponectin have not been studied.

The present study was designed to investigate the cardioprotective effects of Telm *in vitro* and *in vivo*, specifically its effects on cardiac adiponectin and TNF-α. We also examined the necessity of PPAR-γ activity in the stimulatory effects of Telm on adiponectin expression in cardiomyocytes. Cardiomyocyte viability and lactate dehydrogenase (LDH) activation, which is released when cell injury occurs, were employed as indexes of injury severity in our *in vitro* experiments.

Materials and methods

Animals

Forty male Wistar rats (200–250 g body weight; 6–8 weeks of age) were obtained from the Experimental Animal Center of Hebei Medical University. This research was carried out in accordance with the National Research Council protocol for the care and use of laboratory animals. The animals were housed in the Laboratory Animal Center under conditions of a controlled ambient temperature of 22–24 °C with a 12-h light/dark cycle. Animals were provided with free access to standard rodent chow and tap water and were allowed to acclimate for a period of 7 d.

Drugs and chemicals

Telm was obtained from Boehringer Ingelheim International GmbH (Germany). Iso hemisulfate was dissolved in 0.9% saline and used within 10 min of preparation. All chemicals used in this study were of analytical grade and purchased from Sigma Chemicals (St Louis, MO, USA).

Induction of cardiac remodeling

To induce PIR, rats were administered two subcutaneous injections of 80 mg/kg homologous Iso (Sigma-Aldrich) or vehicle at 24 h intervals on 2 consecutive days, as described by Palfi A *et al*[26].

Experimental groups

After 7 d of acclimatization, the experimental animals were divided into the following treatment groups: 1) Iso, n=10; 2) Iso+Telm, n=10; 3) Telm, n=10; and 4) control (vehicle), n=10. Rats in the Telm and Iso+Telm groups were administered Telm orally (10 $mg \cdot kg^{-1} \cdot d^{-1}$) by intragastric intubation for a period of 65 d. All rats were fed a standard diet throughout this experimental period. Changes in body weight and food and water intake were noted for all animals at regular intervals throughout the experimental period.

Tissue preparation

Two months after the last Iso injection, each rat was weighed and sacrificed by intravenous injection of 2–3 mL of 10% KCl through the femoral vein. Immediately after the KCl injection, the thorax was opened and the heart was excised, rinsed with saline, blotted dry, and weighed. The left ventricle (LV) was dissected out by incising the right ventricle along the septum and then weighed. Heart weight to body weight and LV weight to body weight ratios were calculated. One segment of the LV was then fixed in 4% paraformaldehyde and embedded in paraffin. The other segment was rapidly frozen in liquid nitrogen and stored at -80 °C for further analysis.

Histological examination and Masson staining

After being fixed for 24 h in 4% paraformaldehyde, the tissue blocks were dehydrated and embedded in paraffin; 5-μm-thick sections were then cut and stained with either hematoxylin-eosin or Masson's trichrome stain. Eight light microscope visual fields were randomly selected for each Masson's trichome stained section and viewed using a computer-assisted image analysis system (Motic Med 6.0 CMIAS, China). To assess cardiomyocyte diameter, the cross-sectional margins of cardiomyocytes in the LV were marked with the cursor using the Image Pro Plus 4.1 software and the mean diameter was calculated; only cardiomyocytes that had complete cell boundaries and clear round intra-cytoplasmic nuclei were measured. Approximately 60–70 cardiomyocytes were randomly selected from five to seven images captured randomly at different sites in each specimen and the average cross-sectional diameter was calculated. The collagen volume fraction (CVF) was measured in five fields for each LV section. CVF values were determined by quantitative morphometry using an automatic image analyzer (IBAS 2.5, Kontron, Germany), such that CVF=fibrosis area/total area of myocardium. The CVF excluded scars and perivascular collagen areas. The pathologist performing the histopathological evaluations was blinded to the treatment group designations.

Primary culture of neonatal rat ventricular myocytes (NRVMs)

NRVMs were prepared as described previously[27]. Briefly, ventricles from 1–3 d-old Wistar rats were minced and digested in phosphate-buffered saline (PBS) containing 0.1% trypsin and 0.04% type II collagenase for 8–10 cycles. The degraded tissue was then centrifuged and suspended in Dulbecco's modified Eagle's medium containing 15% fetal bovine serum. A single 2-h preplating step was performed to further increase the ratio of NRVMs to noncardiomyocytes. Noncar-

diomyocytes attached readily to the bottom of culture dishes, and the unattached myocytes were plated at 1×10^6 cells/cm^2 in the same medium as above and supplemented with 0.1 mmol/L BrdU. Cells were then held in serum-free medium for 24 h prior to being used in experiments. Morphological examination and staining with an anti-sarcomeric α-actin antibody were carried out to confirm the presence of NRVMs, with about 95% of the cells being identified as NRVMs.

Cell growth assay

The cytotoxic effect of Iso on cardiac myocytes was measured using the MTT assay as described elsewhere[28]. The cells were dispensed in 96-well flat bottomed microtiter plates (NUNC, Roskilde, Denmark) at a density of 5×10^5 cells/well. After 48 h of incubation, the cells were treated with Iso (10 μmol/L) and/or various concentrations of Telm for 48 h. Cell viability was calculated as follows:

$$\text{Viability (\%)}=(A_{490,\text{ sample}}-A_{490,\text{ blank}})/(A_{490,\text{ control}}-A_{490,\text{ blank}})\times100$$

LDH activity-based cytotoxicity assay

LDH content released into the culture medium was measured as an index of LDH activity. The cells were incubated with various concentrations of Telm for 1 h prior to a 48 h incubation in the presence of isoproterenol (10 μmol/L). The substrate reaction buffer for LDH [0.5 mmol/L, with or without lactic acid, 0.66 mmol/L INT, 0.28 mmol/L PMS, and 1.3 mmol/L NAD^+ in Tris-HCl, pH 8.2] was added to collected samples of culture media. The absorbance value (A) at 490 nm for the LDH reaction was assayed after 1 and 5 min.

Measurements of protein expression levels in myocardium and cultured cardiomyocytes

For immunoblot analysis, extracts of myocardial tissue and treated cells were matched for protein concentration (15 μg) with SDS-PAGE sample buffer, separated by SDS-PAGE, and transferred to a polyvinylidene difluoride membrane. The membranes were incubated with the indicated primary antibodies overnight at 4 °C; 50 μg of denatured protein was subjected to sodium dodecyl sulfate polyacrylamide gel electrophoresis (SDS-PAGE) on a 10% polyacrylamide gel (Bio-Rad, Hercules, CA, USA) and transferred to polyvinylidene difluoride (PVDF) membranes (Bio-Rad, Hercules, CA, USA) for detection of adiponectin levels. Nonspecific binding was prevented by incubation with 5% nonfat dry milk for 1 h. The PVDF membranes were incubated overnight at 4 °C with anti-Acrp30 and anti-GAPDH primary antibodies diluted in TBS-T (1:1000) (Santa-Cruz Biotechnology, Santa Cruz, CA, USA). After washing in Tween-20 buffer, the membranes were incubated with fluorescent secondary antibodies. Labeling was quantified using the Odyssey Infrared Imaging System (LI-COR Biosciences, Lincoln, USA). Acrp30 expression was corrected by comparison to the endogenous control GAPDH. Band densities were scanned and quantified using a LEIC-A550IW image analysis system.

Statistical analysis

All data are expressed as mean±SD. Group mean values were compared using one-way analysis of variance (ANOVA) followed by a Tukey's multiple comparison test where appropriate. For all comparisons, $P<0.05$ was used to establish statistically significant results.

Results

Influence of Telm on Iso-induced effects on gravimetric parameters

The gravimetric parameters in hearts of intact and PIR animals are presented in Figure 1. Rats treated with Iso alone showed significantly elevated heart mass normalized to body mass, while Iso-treated rats that had been pretreated with Telm did not show these unfavorable changes (Figure 1A). Telm pretreatment also reduced the gain in Iso-induced ventricular mass (Figure 1B). Heart mass and ventricle/body mass ratio did not differ between rats treated with Telm alone and control (no drug) rats (Figure 1).

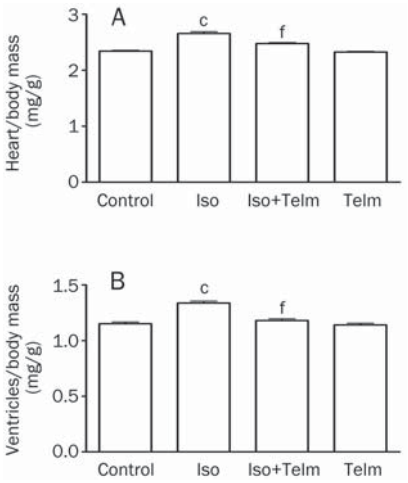

Figure 1. Effects of Telm and Iso on the gravimetric parameters in rats with PIR. Mean±SD. n=10. $^cP<0.01$ *vs* control group; $^fP<0.01$ *vs* Iso group.

Impact of Telm on Iso-induced myocardial hypertrophy and interstitial fibrosis

Compared to untreated PIR (isoprotrenol alone) animals, PIR animals given Telm showed significantly attenuated Iso-induced increases in mean myocyte diameter (Figure 2) and collagen volume fraction (Figure 3). Treatment with Telm alone had no effect on these values ($P>0.05$ *vs* control) (Figure 2, 3).

Protective effects of Telm against PIR are associated with enhanced protein expression of adiponectin

Relative to intact hearts, TNF-α expression in hearts with PIR was increased by about three-fold ($P<0.01$) while adiponectin expression in hearts with PIR was decreased by about half

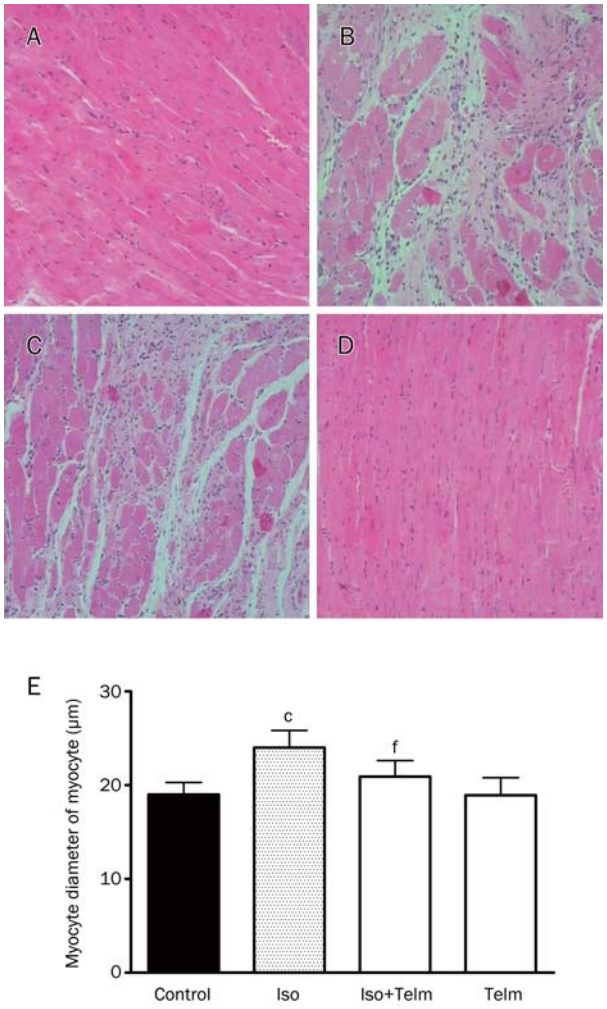

Figure 2. Effects of Telm and Iso on myocardial hypertrophy in rats with PIR. (A) control group; (B) Iso group; (C) Iso+Telm group; (D) Telm group; (E) Quantitative analysis of the myocyte diameter. Mean±SD. n=10. ^{c}P<0.01 *vs* control group; ^{f}P<0.01 *vs* Iso group.

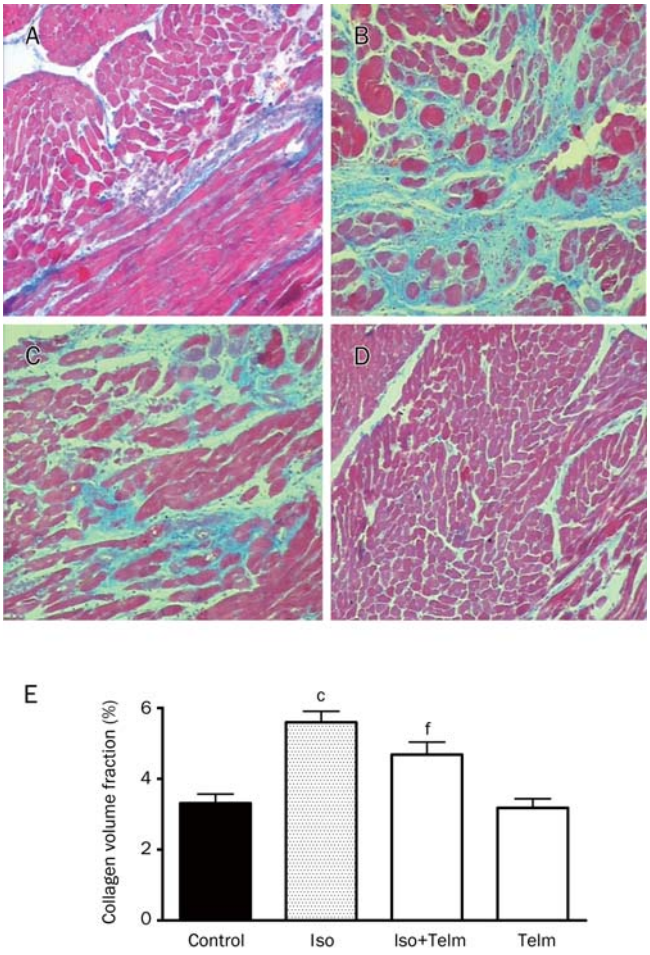

Figure 3. Effects of Telm and Iso on collagen volume fraction (CVF) in rats with PIR. (A) control group; (B) Iso group; (C) Iso+Telm group; (D) Telm group; (E) Quantative analysis of the CVF. Mean±SD. n=10. ^{c}P<0.01 *vs* control group. ^{f}P<0.01 *vs* Iso group.

(P<0.01) (Figure 4). Oral administration of Telm significantly attenuated these PIR-related changes in TNF-α and adiponectin expression (Figure 4).

Telm inhibits Iso-induced cell death in cardiomyocytes

Cardiomyocytes were exposed to Iso (10 μmol/L) alone, Iso (10 μmol/L) with Telm (5–20 μmol/L), or vehicle for 48 h. The cell death inhibition ratio of Telm-treated cells relative to Iso only-treated cells ranged from 40.2%±4.5% (5 μmol/L Telm) to 92.6%±7.1% (20 μmol/L Telm) (Figure 5A). Telm protected Iso-treated cardiomyocytes from cell death in a dose-dependent manner and had no cytotoxic effects on the cells.

It is worth noting that we observed a marked increase in the cardiomyocyte beating rate 6 h after Iso treatment. The cardiomyocyte beating rate was then weakened in a time-dependent manner such that by 48 h following Iso treatment, no cell beating was observed. On the contrary, cells that were exposed to Telm and Iso simultaneously continued to exhibit steady beating throughout the 48 h experimental period.

Telm inhibited Iso-induced LDH release in cardiomyocytes

Iso (10 μmol/L) nearly doubled LDH release in cardiomyocytes relative to cells not exposed to any drug (P<0.01). Pretreatment with Telm for 48 h reduced Iso-induced LDH release in a dose-dependent manner; at 20 μmol/L, Telm-pretreated, Iso-exposed cells had LDH release levels that were similar to those of untreated control cells (Figure 5B). Telm alone (5–20 μmol/L) did not affect LDH release (data not shown).

Telm treatment blocked Iso effects on adiponectin protein expression in cardiomyocytes via a mechanism involving PPAR-γ activation

After incubation with 10 μmol/L Iso, adiponectin protein expression in cardiomyocytes was decreased relative to cells not exposed to any drug. However, in cells that were pretreated with Telm (20 μmol/L), this decrease did not occur. Treating Iso-exposed cells with the selective PPAR-γ antagonist GW9662 (30 μmol/L) potently blocked the effects of Telm

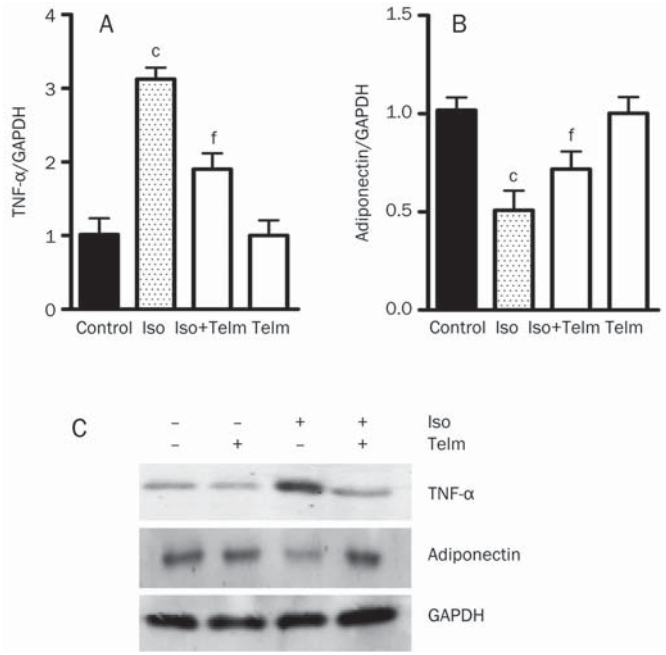

Figure 4. Effects of Telm and Iso on protein expression of cardiac adiponectin and TNF-α in rat hearts with PIR. GAPDH was used as a loading control. Mean±SD. n=10. ^{c}P<0.01 *vs* control group. ^{f}P<0.05 *vs* Iso group.

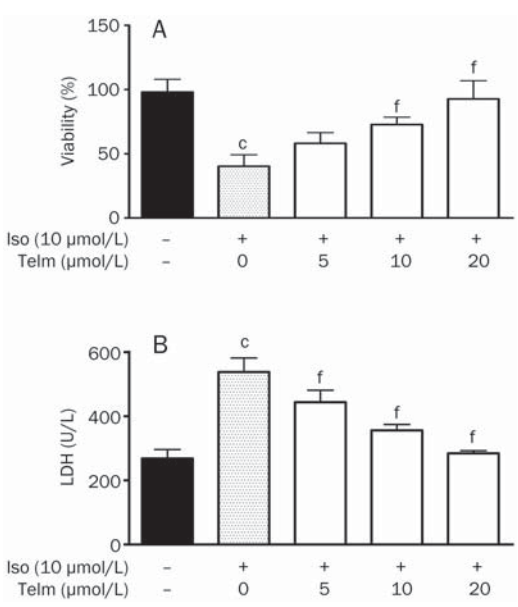

Figure 5. Telm protects against Iso-induced myocardial cell injury. Cells were incubated with Telm with or without Iso (10 μmol/L) for 48 h. (A) Cell viability was evaluated using the MTT method. (B) LDH activity was measured in the culture medium. Mean±SD. n=4. ^{c}P<0.05 *vs* control group. ^{f}P<0.01 *vs* Iso only group.

pretreatment on adiponectin expression (Figure 6). GW9662 in the absence of Telm did not change the Iso-induced decrease of adiponectin expression (data not shown).

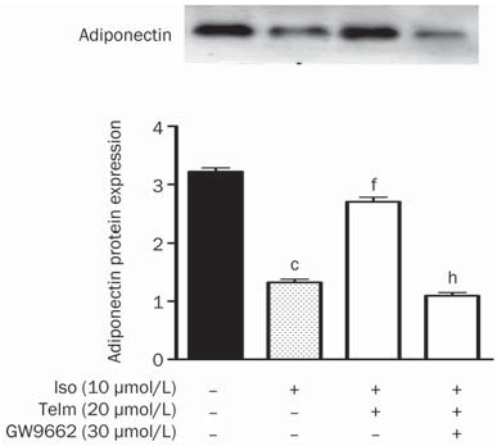

Figure 6. Telm upregulates adiponectin protein expression in Iso-treated cardiomyocytes via PPAR-γ activation. Cardiocytes were pre-incubated for 1 h in the presence or absence of the PPAR-γ antagonist GW9662 (30 μmol/L), and were then incubated in the presence or absence of Iso (10 μmol/L) and/or Telm (20 μmol/L) for the subsequent 24 h. Adiponectin protein levels were then measured immediately by immunoblot analysis. Protein levels are expressed relative to non-treated control cells (n=3). ^{c}P<0.05 *vs* control group. ^{f}P<0.01 *vs* Iso only group. ^{h}P<0.05 *vs* Iso+Telm group.

Inhibiting PPAR-γ activity with the selective antagonist GW9662 blocked the protective effects of Telm against Iso-induced cell injury

Inhibition of PPAR-γ activity with the selective antagonist GW9662 (30 μmol/L) potently blocked the protective effects of Telm against Iso-induced cell injury (Figure 7A and 7B). GW9662 alone (in the absence of Telm) had no observable effects on Iso-induced cell injury (data not shown).

Discussion

In the present study, oral Telm pretreatment prevented changes in gravimetric parameters and reduced myocardial hypertrophy and interstitial fibrosis in Iso-induced PIR hearts. Oral Telm pretreatment also reversed MI-induced decreases in adiponectin expression as well as MI-induced increases in TNF-α expression. Cardiac expression of adiponectin mRNA negatively correlated with expression of cardiac TNF-α mRNA. Importantly, heart size and interstitial fibrosis were not influenced by Telm in non-PIR hearts, and Telm led to an increased performance of the postinfarct heart. Cardiomyocytes treated *in vitro* with Iso alone showed elevated LDH activity accompanied by markedly inhibited cell growth; Telm inhibited Iso-induced cell death and LDH release in cardiomyocytes. Furthermore, we demonstrated that administration of the PPAR-γ antagonist GW9662 blocked the stimulatory effects of Telm on adiponectin expression in cardiomyocytes. The ability of Telm to promote preservation of myocardial adiponectin expression may represent an important mechanism for the beneficial effects of Telm in PIR.

Our demonstration that PPAR-γ activity was necessary for Telm-induced reversal of Iso-induced decreases in adiponectin

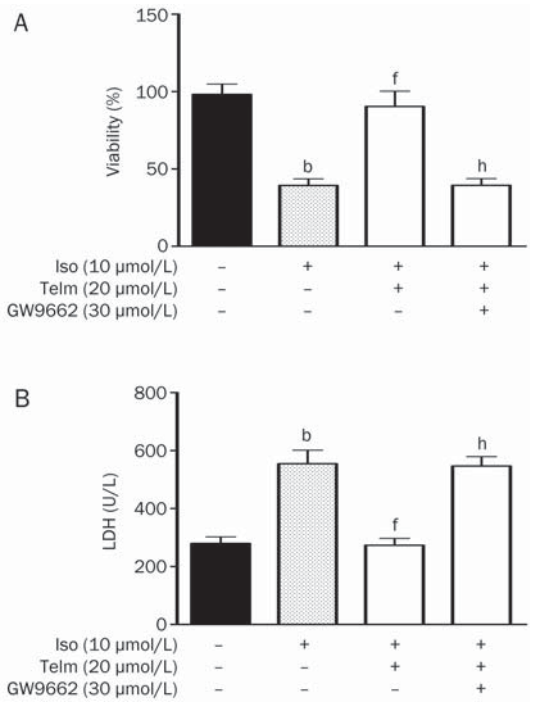

Figure 7. Effects of the selective PPAR-γ antagonist GW9662 on the inhibitory action of Telm on Iso-induced cardiomyocyte injury. Cardiomyocytes were pretreated with GW9662 (30 μmol/L), then incubated with Iso (10 μmol/L) and Telm (20 μmol/L). Treated cells were then subjected to measurements of cell viability (A) and LDH activity (B). Mean±SD. n=4. ^{b}P<0.05 *vs* control group. ^{f}P<0.01 *vs* Iso group. ^{h}P<0.05 *vs* Iso+Telm group.

protein expression complements the recent findings of Goyal *et al*[29], suggesting that Telm exerts its protective effects against Iso-induced cardiac injury *in vivo* in two ways, functioning as an ARB as well as a PPAR-γ activator. Moreover, activated PPAR-γ, which has anti-inflammatory and antioxidant effects[30], has been shown to stimulate adiponectin expression in adipocytes and to upregulate adiponectin plasma levels in animals and humans[31, 32].

Our findings showing increased expression of cardiac TNF-α protein accompanied by decreased expression of adiponectin in the presence of myocardial injury are consistent with prior studies suggesting that the two factors may work in opposition to each other. For example, adiponectin has been shown to provide protection against TNF-α-mediated myocardial injury and apoptosis in animal models of MI[33]. Furthermore, adiponectin knockout mice show elevated TNF-α expression, which can be attenuated by adiponectin[34]. Thus, TNF-α and adiponectin appear to have an antagonistic relationship, with one cytokine negatively regulating the expression of the other[35].

After MI, initial loss of the myocardium can induce progressive ventricular enlargement and deposition of interstitial collagen, changes which are intended to adapt the heart to its altered situation. However, increased muscle mass is achieved by the enlarging of cardiomyocytes rather than an increase in their number, which together with the increased interstitial fibrosis ultimately impairs heart performance and decreases its elasticity. Recently, inflammatory pathways and a pro-inflammatory cytokine mechanism have been invoked to explain Iso-induced PIR through the promotion of matrix metalloproteinase expression in cardiac fibroblasts[36]. These post-MI changes contribute to the progression toward CHF, characterized by a progressive deterioration in heart function. Autopsies have revealed the presence of adiponectin in the interstitium of early stage MI lesions, and the presence of adiponectin was further found to lie linearly along the border of vital myocardium and at the periphery of surviving cardiomyocytes around lesions in granulation stage MI lesions[37]. Expression of adiponectin has also been reported in the injured myocardium of patients with cardiomyopathy[38]. Our study reveals for the first time that the protective effects of Telm *in vivo* and *in vitro* are associated with enhanced expression of cardiac adiponectin. Thus we posit that Telm may induce cardiac adiponectin expression in the remodeling of hearts and in injured cardiomyocytes.

In summary, we have demonstrated that Telm treatment attenuates Iso-induced PIR in rats and exerts protective effects on Iso-treated rat cardiomyocytes. The cardioprotective actions of Telm may be mediated by the activation of ARB/PPAR-γ/adiponectin pathways and appear to involve cardiac expression of the anti-inflammatory cytokine, adiponectin, together with suppression of the inflammatory cytokine, TNF-α. The precise cardiac adiponectin-regulated signaling that occurs during Iso-induced PIR has yet to be delineated.

Author contribution

Yong-jun LI and Bing-yan GUO designed the study; Bing-yan GUO, Rui HAN, Shao-ling YANG, Hong ZHOU, and Mei WANG performed the research; Yong-jun LI, Ying-hui SHI, and De-rong HAN contributed new analytical tools and reagents; Bing-yan GUO analyzed the data; and Bing-yan GUO wrote the paper.

References

1 Devika PT, Stanely Mainzen Prince P. Protective effect of (–)-epigallocatechingallate (EGCG) on lipid peroxide metabolism in ISO induced myocardial infarction in male Wistar rats: a histopathological study. Biomed Pharmacother 2008; 62: 701–8.
2 Sun Y, Zhang JQ, Zhang J, Lamparter S. Cardiac remodeling by fibrous tissue after myocardial infarction. J Lab Clin Med 2000; 135: 316–23.
3 Palfi A, Toth A, Hanto K, Deres P, Szabados E, Szereday Z, *et al*. PARP Inhibition prevents postinfarction myocardial remodeling and heart failure via the protein kinase C/glycogen synthase kinase-3 beta pathway. J Mol Cell Cardiol 2006; 41: 149–59.
4 Matsuzawa Y. Therapy insight: adipocytokines in metabolic syndrome and related cardiovascular disease. Nat Clin Pract Cardiovasc Med 2006; 3: 35–42.
5 Shibata R, Ouchi N, Ito M, Kihara S, Shiojima I, Pimentel DR, *et al*. Adiponectin-mediated modulation of hypertrophic signals in the heart. Nat Med 2004; 10: 1384–9.
6 Ding G, Qin Q, He N, Francis-David SC, Hou J, Liu J, *et al*. Adiponectin

and its receptors are expressed in adult ventricular cardiomyocytes and upregulated by activation of peroxisome proliferator-activated receptor-gamma. J Mol Cell Cardiol 2007; 43: 73–84.
7 Wulster-Radcliffe MC, Ajuwon KM, Wang J, Christian JA, Spurlock ME. Adiponectin differentially regulates cytokines in porcine macrophages. Biochem Biophys Res Commun 2004; 316: 924–9.
8 Neumann FJ, Ott I, Gawaz M, Richardt G, Holzapfel H, Jochum M, *et al*. Cardiac release of cytokines and inflammatory responses in acute myocardial infarction. Circulation 1995; 92: 748–55.
9 Doughty RN, Whalley GA, Walsh HA, Gamble GD, Lopez-Sendon J, Sharpe N. Effects of carvedilol on left ventricular remodeling after acute myocardial infarction: the CAPRICORN Echo Substudy. Circulation 2004; 109: 201–6.
10 Sun M, Dawood F, Wen WH, Chen M, Dixon I, Kirshenbaum LA, *et al*. Excessive tumor necrosis factor activation after infarction contributes to susceptibility of myocardial rupture and left ventricular dysfunction. Circulation 2004; 110: 3221–8.
11 Yamana A, Arita M, Furuta M, Shimajiri Y, Sanke T. The angiotensin II receptor blocker telmisartan improves insulin resistance and has beneficial effects in hypertensive patients with type 2 diabetes and poor glycemic control. Diabetes Res Clin Pract 2008; 82: 127–31.
12 Grassi G, Quarti-Trevano F, Mancia G. Cardioprotective effects of telmisartan in uncomplicated and complicated hypertension. J Renin Angiotensin Aldosterone Syst 2008; 9: 66–74.
13 Bakris G, Burgess E, Weir M, Davidai G, Koval S. AMADEO Study Investigators. Telmisartan is more effective than losartan in reducing proteinuria in patients with diabetic nephropathy. Kidney Int 2008; 74: 364–9.
14 Geng DF, Wu W, Jin DM, Wang JF. Effect of peroxisome proliferator activated receptor gamma ligand rosiglitazone on left ventricular remodeling in rats with myocardial infarction. Int J Cardiol 2006; 113: 86–91.
15 Benson SC, Pershadsingh HA, Ho CI, Chittiboyina A, Desai P, Pravenec M, *et al*. Identification of telmisartan as a unique angiotensin II receptor antagonist with selective PPARgamma-modulating activity. Hypertension 2004; 43: 993–1002.
16 Schupp M, Janke J, Clasen R, Unger T, Kintscher U. Angiotensin type 1 receptor blockers induce peroxisome proliferator-activated receptor-gamma activity. Circulation 2004; 109: 2054–7.
17 Wu L, Iwai M, Nakagami H, Li Z, Chen R, Suzuki J, *et al*. Roles of angiotensin II type 2 receptor stimulation associated with selective angiotensin II type 1 receptor blockade with valsartan in the improvement of inflammation-induced vascular injury. Circulation 2001; 104: 2716–21.
18 Lorenzo O, Ruiz-Ortega M, Suzuki Y, Rupérez M, Esteban V, Sugaya T, *et al*. Angiotensin III activates nuclear transcription factor-kappaB in cultured mesangial cells mainly via AT(2) receptors: studies with AT(1) receptor-knockout mice. J Am Soc Nephrol 2002; 13: 1162–71.
19 Berthonneche C, Sulpice T, Tanguy S, O'Connor S, Herbert JM, Janiak P, *et al*. AT1 receptor blockade prevents cardiac dysfunction after myocardial infarction in rats. Cardiovasc Drugs Ther 2005; 19: 251–9.
20 Fujioka D, Kawabata K, Saito Y, Kobayashi T, Nakamura T, Kodama Y, *et al*. Role of adiponectin receptors in endothelin-induced cellular hypertrophy in cultured cardiomyocytes and their expression in infarcted heart. Am J Physiol Heart Circ Physiol 2006; 290: H2409–16.
21 Yilmaz MI, Sonmez A, Caglar K, Celik T, Yenicesu M, Eyileten T, *et al*. Effect of antihypertensive agents on plasma adiponectin levels in hypertensive patients with metabolic syndrome. Nephrology 2007; 12: 147–53.
22 Lely AT, Krikken JA, Bakker SJ, Boomsma F, Dullaart RP, Wolffenbuttel BH, *et al*. Low dietary sodium and exogenous angiotensin II infusion decrease plasma adiponectin concentrations in healthy men. J Clin Endocrinol Metab 2007; 92: 1821–6.
23 Zorad S, Dou JT, Benicky J, Hutanu D, Tybitanclova K, Zhou J, *et al*. Long-term angiotensin II AT(1) receptor inhibition produces adipose tissue hypotrophy accompanied by increased expression of adiponectin and PPARgamma. Eur J Pharmacol 2006; 552: 112–22.
24 Saegusa S, Fei Y, Takahashi T, Sumino H, Moriya J, Kawaura K, *et al*. Oral administration of candesartan improves the survival of mice with viral myocarditis through modification of cardiac adiponectin expression. Cardiovasc Drugs Ther 2007; 21: 155–60.
25 Lasek W, Wańkowicz A, Kuc K, Feleszko W, Giermasz A, Jakóbisiak M. Augmentation of antitumor efficacy by the combination of actinomycin D with tumor necrosis factor-alpha and interferon-gamma on a melanoma model in mice. Oncology 1996; 53: 31–7.
26 Palfi A, Bartha E, Copf L, Mark L, Gallyas F Jr, Veres B, *et al*. Alcohol-free red wine inhibits ISO-induced cardiac remodeling in rats by the regulation of Akt1 and protein kinase C alpha/beta II. J Nutr Biochem 2009; 20: 418–25.
27 Ouchi N, Shibata R, Walsh K. Cardioprotection by adiponectin. Trends Cardiovasc Med 2006; 16: 141–6.
28 Benson SC, Pershadsingh HA, Ho CI, Chittiboyina A, Desai P, Pravenec M, *et al*. Identification of telmisartan as a unique angiotensin II receptor antagonist with selective PPARgamma-modulating activity. Hypertension 2004; 43: 993–1002.
29 Goyal S, Arora S, Mittal R, Joshi S, Nag TC, Ray R, *et al*. Myocardial salvaging effect of telmisartan in experimental model of myocardial infarction. Eur J Pharmacol 2009; 619: 75–84.
30 Yi JH, Park SW, Brooks N, Lang BT, Vemuganti R. PPARgamma agonist rosiglitazone is neuroprotective after traumatic brain injury via anti-inflammatory and anti-oxidative mechanisms. Brain Res 2008; 1244: 164–72.
31 Combs TP, Wagne JA, Berger J, Doebber T, Wang WJ, Zhang BB, *et al*. Induction of adipocyte complement-related protein of 30 kilodaltons by PPARgamma agonists: a potential mechanism of insulin sensitization. Endocrinology 2002; 143: 998–1007.
32 Fasshauer M, Paschke R, Stumvoll M. Adiponectin, obesity, and cardiovascular disease. Biochimie 2004; 86: 779–84.
33 Kapadia SR, Oral H, Lee J, Nakano M, Taffet GE, Mann DL. Hemodynamic regulation of tumor necrosis factor-alpha gene and protein expression in adult feline myocardium. Circ Res 1997; 81: 187–95.
34 Maeda N, Shimomura I, Kishida K, Nishizawa H, Matsuda M, Nagaretani H, *et al*. Diet-induced insulin resistance in mice lacking adiponectin/ACRP30. Nat Med 2002; 8: 731–7.
35 Lihn AS, Richelsen B, Pedersen SB, Haugaard SB, Rathje GS, Madsbad S, *et al*. Increased expression of TNF-alpha, IL-6, and IL-8 in HALS: implications for reduced adiponectin expression and plasma levels. Am J Physiol Endocrinol Metab 2003; 285: E1072–80.
36 Li L, Wu L, Wang C, Liu L, Zhao Y. Adiponectin modulates carnitine palmitoyltransferase-1 through AMPK signaling cascade in rat cardiomyocytes. Regul Pept 2007; 139: 72–9.
37 Ishikawa Y, Akasaka Y, Ishii T, Yoda-Murakami M, Choi-Miura NH, Tomita M, *et al*. Changes in the distribution pattern of gelatin-binding protein of 28 kDa (adiponectin) in myocardial remodelling after ischaemic injury. Histopathology 2003; 42: 43–52.
38 Takahashi T, Saegusa S, Sumino H, Nakahashi T, Iwai K, Morimoto S, *et al*. Adiponectin, T-cadherin and tumor necrosis factor-alpha in damaged cardiomyocytes from autopsy specimens. J Int Med Res 2005; 33: 236–44.

Acta Pharmacologica Sinica (2011) 32: 456–464
 1671-4083/11 $32.00
www.nature.com/aps

Original Article

The vasorelaxing effect of hydrogen sulfide on isolated rat aortic rings versus pulmonary artery rings

Yan SUN[1], Chao-shu TANG[2, 3], Hong-fang JIN[1, *], Jun-bao DU[1, 3, *]

[1]*Department of Pediatrics, Peking University First Hospital, Beijing 100034, China;* [2]*Institute of Cardiovascular Research, First Hospital of Peking University, Beijing 100034, China;* [3]*Key Laboratory of Molecular Cardiology, Ministry of Education, Beijing 100083, China*

Aim: To compare the vasorelaxing effects of hydrogen sulfide (H_2S) on isolated aortic and pulmonary artery rings and to determine their action mechanisms.
Methods: H_2S-induced vasorelaxation of isolated rat aortic versus pulmonary artery rings under 95% O_2 and 5% CO_2 was analyzed. The expression of cystathinonine gamma-lyase (CSE), cystathionine beta synthase (CBS), 3-mercaptopyruvate sulfurtransferase (3MST), SUR2B and Kir6.1 was examined.
Results: NaHS caused vasorelaxation of rat aortic and pulmonary artery rings in a dose-dependent manner. NaHS dilated aortic rings to a greater extent (16.4%, 38.4%, 64.1%, 84.3%, and 95.9% at concentrations of 50, 100, 200, 500, and 1000 μmol/L, respectively) than pulmonary artery rings (10.1%, 22.2%, 50.6%, 73.6%, and 84.6% at concentrations of 50, 100, 200, 500 and 1000 μmol/L, respectively). The EC_{50} of the vasorelaxant effect for aortic rings was 152.17 μmol/L, whereas the EC_{50} for pulmonary artery rings was 233.65 μmol/L. The vasorelaxing effect of H_2S was markedly blocked b y cellular and mitochondrial membrane K_{ATP} channel blockers in aortic rings (P<0.01). In contrast, only the cellular membrane K_{ATP} channel blocker inhibited H_2S-induced vasorelaxation in pulmonary artery rings. SUR2B mRNA and protein expression was higher in aortic rings than in pulmonary artery rings. Cystathinonine gamma-lyase (CSE) but not cystathionine beta synthase (CBS) expression in aortic rings was higher than in pulmonary artery rings. 3-Mercapto pyruvate sulfurtransferase (3MST) mRNA was lower in aortic rings than in pulmonary artery rings.
Conclusion: The vasorelaxing effect of H_2S on isolated aortic rings was more pronounced than the effect on pulmonary artery rings at specific concentrations, which might be associated with increased expression of the K_{ATP} channel subunit SUR2B.

Keywords: hydrogen sulfide; aortic rings; pulmonary rings; vasorelaxation; cystathinonine gamma-lyase; cystathionine beta synthase; 3-mercapto pyruvate sulfurtransferase; glibenclamide, 5-hydroxydecanoate

Acta Pharmacologica Sinica (2011) 32: 456–464; doi: 10.1038/aps.2011.9

Introduction

The regulation of systemic and pulmonary circulation is a very important issue in cardiovascular research. Systemic circulation differs from pulmonary circulation in several important aspects. The same pathological stimuli may elicit different responses from either systemic or pulmonary circulation. For example, under hypoxia (20–60 mmHg p_{O2}), pulmonary arteries contract while systemic arteries relax[1]. Vasoactive substances such as endothelin (ET) and angiotensin II (Ang II) play very important roles in the cardiovascular system but induce different vascular responses in pulmonary and systemic circulation[2–4]. The above-mentioned studies have revealed many differences in the responses of systemic and pulmonary circulation to pathophysiological stimuli.

In their carefully performed study, Olson *et al* examined vertebrate vessels and found that H_2S produced temporally and quantitatively identical responses even though the responses varied from constriction (lamprey dorsal; IDA) to dilation (rat aorta; rA) to multiphasic (rat and bovine pulmonary arteries; rpA and bPA, respectively)[5]. They discovered that the concentration of vasoactive H_2S in the vessel was governed by a balance between endogenous H_2S production and its oxidation by available O_2[5]. In our study, we tried to analyze the difference between rat aorta and pulmonary artery at the vasorelaxant stage and further explored the role of K_{ATP} channels in the regulation of the vasorelaxant effect by hydrogen sulfide.

The endogenous gaseous signaling molecule hydrogen

* To whom correspondence should be addressed.
E-mail junbaodu1@126.com (Jun-bao DU);
jinghongfang51@126.com (Hong-fang JIN)
Received 2010-06-14 Accepted 2011-01-28

sulfide (H_2S) functions as a physiological regulator[6–12]. Recent studies have shown that cystathinonine gamma-lyase (CSE), cystathionine beta synthase (CBS), and 3-mercaptopyruvate sulfurtransferase (3MST) are three H_2S generating enzymes[13–14]. It is shown that H_2S relaxes blood vessels and lowers blood pressure by opening ATP-sensitive K^+ channels in vascular smooth muscle cells[15]. To examine and compare the pathways used for the endogenous production of H_2S in aortic and pulmonary arteries, we tested the expression of the above-mentioned enzymes. It has been demonstrated that H_2S acts as an endogenous K_{ATP} channel opener to regulate vascular tone and that Kir6.1 and SUR2B are the main K_{ATP} channel subunits expressed in the vascular smooth muscle cells. So we tested the protein and mRNA expression of SUR2B and Kir6.1 in aortic and pulmonary arteries to investigate the possible mechanisms responsible for the regulation of vasorelaxation by H_2S. H_2S deficiency has been observed in animal models of systemic and pulmonary hypertension[16–18]. It also plays important roles in the pathogenesis of cardiovascular diseases[16–24]. The main mechanism for the cardiovascular actions of H_2S was considered to be the activation of K_{ATP} channels, because H_2S increased whole-cell K_{ATP} channel currents in rat aortic vascular smooth muscle cells[15]. However, whether H_2S exerts different vasorelaxing effects on aortic and pulmonary artery rings is unknown. If it does, the potential mechanisms behind these effects are not understood. Therefore, this study was designed to observe the vasorelaxing effect of H_2S on isolated aortic and pulmonary artery rings of rats *in vitro* and to identify the possible mechanisms.

Materials and methods

Reagents

Glibenclamide (Gli), 5-hydroxydecanoate (5-HD), and nicardipine were purchased from American Sigma Aldrich Company. NaHS was dissolved in deionized water and freshly prepared solution was used.

Animal preparation

The animal experimental procedures conformed to the "Guide for the Care and Use of Laboratory Animals" published by the National Institutes of Health (NIH) in the United States and was approved by the Animal Research Committee of Peking University. Adult male Wistar-Kyoto (WKY) rats weighing 220–250 g were purchased from Vital River (Beijing, China). Rats were housed in cages and fed a standard laboratory diet and fresh water. The cages were kept in a room with controlled temperature (24 °C±1 °C), relative humidity (65%–70%), and a 12-h light/dark cycle.

Preparation for aortic and pulmonary artery rings

Male Wistar rats (n=10) were anesthetized with urethane (1 g/kg body weight) intraperitoneally. The thoracic cavity was opened quickly, and the thoracic aorta and pulmonary artery were rapidly dissected and cleaned from fat and connective tissues. The artery was separated as carefully as possible to maintain the vascular activity. Rings 2–3 mm in length were cut and placed in 0 °C Krebs solution and immersed in 20 mL of organ baths containing pre-warmed Krebs' bicarbonate buffer filled with 95% O_2–5% CO_2 at 37 °C. The composition of the Krebs solution was as follows (mmol/L): NaCl: 120, KCl: 5.5, $CaCl_2$: 2.5, $MgCl_2{\cdot}6H_2O$: 1.2, NaH_2PO_4: 1.2, $NaHCO_3$: 20, EDTA-Na_2: 0.03, glucose: 10, and pH: 7.2–7.4. Organ baths were filled with oxygenated (95% O_2–5% CO_2) Krebs solution.

Changes in tension were recorded using force transducers connected to a PowerLab (BL Newcentrary, TaiMeng, Chengdu, China). First, the aortic rings were stretched passively to a tension of 1 g, while the pulmonary rings were stretched at 0.6 g. The rings were equilibrated for 1 h before starting the experiment. The endothelia of the rings were kept functionally unbroken, as confirmed by their relaxation after acetylcholine treatment (1 μmol/L). The rings were contracted with norepinephrine (NE, 1 μmol/L). When the vasoconstriction curves of the rings reached the plateau phase of maximum tension, H_2S at 50–1000 μmol/L was given and the changes in tension were recorded. In another experiment, aortic and pulmonary artery rings were incubated with two kinds of K_{ATP} channel blockers for 30 min (at a concentration of 1×10^{-6} mol/L) before the physiological dose of 100 μmol/L NaHS was given to observe whether the vasorelaxing effect of H_2S could be blocked. The relaxation ratio was calculated by the relaxation degree and preshrinking degree and expressed as a percentage (%). The relaxation degree and shrinking degree, in grams, were recorded by electrophysiolograph.

Measurement of CSE, CBS, SUR2B and Kir6.1 expression in aortic and pulmonary artery rings by Western blotting

Aortic and pulmonary artery rings from Wistar rats (n=10) were homogenized and lysed. Equal amounts of proteins were boiled and separated by SDS-PAGE and electrophoretically transferred to nitrocellulose membranes according to the experimental protocol. The primary antibody dilutions were 1:1000 for CSE, 1:4000 for CBS, 1:500 for SUR2B, 1:200 for Kir6.1, and 1:4000 for GAPDH antibodies. Secondary antibody (Santa Cruz) was used at a 1:10000 dilution. The immunoreactions were visualized by electrochemiluminescence (ECL) and exposed to X-ray film (Kodak Scientific Imaging film).

Measurement of CSE, SUR2B and Kir6.1 expression in aortic and pulmonary rings by immunohistochemistry

After dewaxing by dimethylbenzene, sections of aortic and pulmonary artery rings were placed in distilled water and treated with 3% H_2O_2 for 12 min. The slides were washed with PBS three times for 5 min each. The antigens were then exposed for 15 min. The slides were rinsed again, and the samples were blocked for 30 min with goat serum working fluid. Polyclonal antibodies to CSE (1:150), SUR2B (1:50), and Kir6.1 (1:50) were added and incubated at 4 °C overnight. On the following day, slides were rinsed three times for 5 min in PBS and then incubated with biotinylated anti-mouse, goat, or rabbit IgG at 37 °C for 60 min. Slides were rinsed again in PBS three times, and horseradish peroxidase streptavidin was added for 30 min at 37 °C, followed by three 5 min-washes

with PBS. DAB was added for color development, and the sections were counter-stained with hematoxylin. The sections were dehydrated through a graded ethanol series, treated with dimethylbenzene, and then mounted on slides. The presence of brown granules in aortic and pulmonary smooth muscle cells and endothelial cells was defined as positive signal. For negative controls, sections were processed as described above except that the primary incubation was performed with non-immune goat serum instead of primary antibodies.

Measurement of SUR2B, Kir6.1, and 3MST mRNA expression in aortic and pulmonary artery rings using quantitative real-time polymerase chain reaction (PCR)

RNA from aortic and pulmonary artery rings of rats (n=7) was extracted using Trizol reagent (GibcoBRL) and reverse transcribed using an oligo d(T)18 primer and M-MLV reverse transcriptase. Primers and TaqMan probes used for the quantification of cDNAs in samples were designed using the Primer Express 3.0 software (Applied Biosystems, Foster City, CA, USA). Primers and probes were synthesized by the SBS Company, Limited (Beijing, China). Quantitative real-time PCR was carried out using an ABI PRISM 7300 instrument (Applied Biosystems). The sequences of the primers and probes are shown in Table 1. The PCR condition for SUR2B, Kir6.1 and 3MST were as follows: pre-denaturation at 94 °C for 5 min, then 94 °C for 30 s, 59.5 °C for 30 s, and 70 °C for 1 min for 40 cycles. The PCR condition for β-actin was 95 °C for 5 min, 95 °C for 15 s, and 60 °C for 1 min for 40 cycles. The amount of β-actin cDNA in the sample was used to calibrate the amount of sample needed for quantification.

Statistical analysis

The data were analyzed by Excel and SPSS 13.0 statistical software, and all values were expressed as mean±standard deviation. The relaxation reaction at different concentrations of NaHS on aortic and pulmonary artery rings was analyzed by an independent sample t-test. The relaxation reaction to treatment of aortic and pulmonary artery rings with physiological concentrations of NaHS (the WKY+NaHS, Gli+NaHS, and 5-HD+NaHS groups) was analyzed by one-way ANOVA. LSD analysis was used for comparing data between the two groups. The expression of SUR2B, Kir6.1, CSE, CBS, and 3MST in aortic and pulmonary arteries was compared using the paired-sample t analysis. A level of P<0.05 was set as statistically significant.

Results

The maximum diastolic effect of aortic and pulmonary artery rings to different concentrations of NaHS in rats

NaHS caused vasorelaxation in rat thoracic aortic and pulmonary artery rings pre-contracted with 1 μmol/L NE *in vitro* in a dose-dependent manner. H_2S at concentrations of 50–1000 μmol/L dilated aortic rings more noticeably than pulmonary artery rings (P<0.05, Figure 1). The EC_{50} of the vasorelaxant effect on aortic rings was 152.17 μmol/L, while the effect on pulmonary artery rings had an EC_{50} of 233.65 μmol/L.

The effects of a cytomembrane K_{ATP} channel blocker and mitochondrial membrane K_{ATP} channel blocker on the vasorelaxing effect of H_2S on aortic and pulmonary artery rings

The vasorelaxing effect of H_2S was markedly blocked by cytomembrane and mitochondrial membrane K_{ATP} channel blockers (Gli and 5-HD) in aortic rings (P<0.01, Figure 1). In contrast, the H_2S-induced vasorelaxing effect on pulmonary artery rings could only be blocked by the cytomembrane K_{ATP} channel blocker (P<0.01, Figure 1) but not by the mitochondrial membrane K_{ATP} channel blocker (P>0.05, Figure 1).

The different vasoactive response of aortic and pulmonary artery rings to different concentrations of NaHS in rats

Within 30 min, all concentrations of hydrogen sulfide (50–1000 μmol/L) gradually relaxed the rat aorta over time until it reached its maximum level of vasorelaxation. However, in rat pulmonary arteries, NaHS (concentrations of 50, 100 and 200 μmol/L) produced a constriction followed by a relaxation,

Table 1. The sequence of the primers and probes of SUR2B, Kir6.1, 3MST and β-actin.

SUR2B	Forward primer	SUR2B-F: 5′-ACCCGCGAGTACAACCTTCTT-3′
	Reverse primer	SUR2B-R: 5′- TCTCATCGCTCAAGAGAAACTCAT-3′
	Probe	SUR2B-P: 5′-AGCCATCATCAGCGTTCAGAAGCT-3′
Kir6.1	Forward primer	Kir6.1-F: 5′-ACCCGCGAGTACAACCTTCTT-3′
	Reverse primer	Kir6.1-R: 5′-TATCGTCATCCATGGCGAACT-3′
	Probe	Kir6.1-P: 5′-AGGTCATTCACTTCTGCGTTTCTCTTCTCCAT-3′
3MST	Forward primer	3MST-F: 5′-CGGCGCTTCCAGGTAGTG-3′
	Reverse primer	3MST-R: 5′-CTGGTCAGGAATTCAGTGAATGG-3′
	Probe	3MST-P: 5′-CGCAGCTGGCCGTTTCCA-3′
β-Actin	Forward primer	β-Actin-F: 5′-ACCCGCGAGTACAACCTTCTT-3′
	Reverse primer	β-Actin-R: 5′-TATCGTCATCCATGGCGAACT-3′
	Probe	β-Actin-P: 5′-CCTCCGTCGCCGGTCCACAC-3′

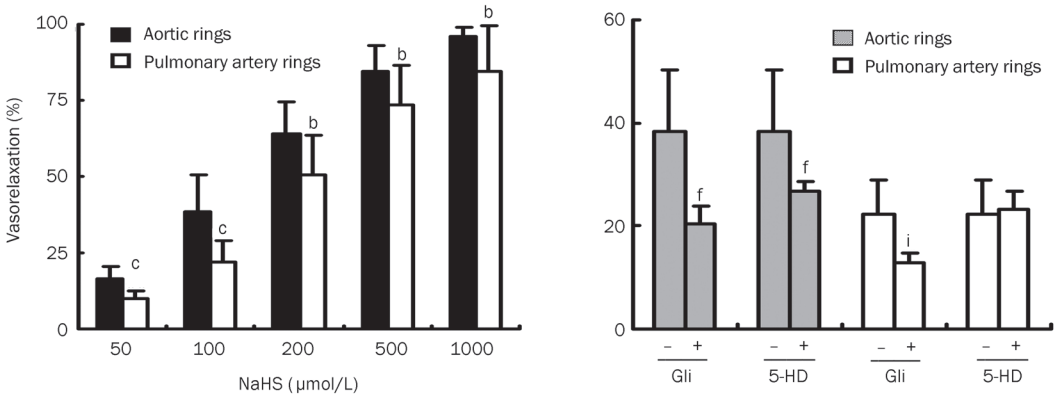

Figure 1. The maximum relaxation response of aortic and pulmonary artery rings to different concentrations of NaHS in rats, and the effect of a K_{ATP} channel blocker on the vasorelaxing effect of hydrogen sulfide on aortic and pulmonary artery rings (n=10). ^{b}P<0.05, ^{c}P<0.01 compared to aortic rings. ^{f}P<0.01 compared to aortic rings without giving K_{ATP} channel blocker. ^{i}P<0.01 compared to pulmonary artery rings without giving K_{ATP} channel blocker. Gli: glibenclamide, 5-HD: 5-hydroxydecanoate.

and then followed by a reduced relaxation. This effect was not obvious at higher concentrations (500 and 1000 μmol/L) in rat pulmonary arteries (Figure 2).

Immunohistochemical analysis of CSE expression in aortic and pulmonary artery rings

CSE protein in aortic and pulmonary artery rings of rats in the control group was strongly expressed in the inner membrane and tunica media vasorum. The presence of brown granules in aortic and pulmonary artery smooth muscle cells and endothelial cells was defined as a positive signal (Figure 3).

CSE and CBS expressions in aortic and pulmonary artery rings by Western blotting

Compared to that in pulmonary artery rings, the expression of CSE protein in aortic rings was notably enhanced (P<0.05, Figure 4). However, there was no difference in CBS protein expression between aortic and pulmonary artery rings (P>0.05, Figure 4).

Expression of SUR2B, Kir6.1 and 3MST by real-time PCR

As measured by semi-quantitative real-time PCR, SUR2B mRNA was higher in aortic rings than in pulmonary artery rings (P<0.05, Figure 5). However, Kir6.1 mRNA expression did not differ between aortic rings and pulmonary artery rings (P>0.05, Figure 5). 3MST mRNA was lower in aortic rings than in pulmonary artery rings (P<0.05, Figure 5).

Immunohistochemical analysis of SUR2B and Kir6.1 expression in aortic and pulmonary artery rings

The SUR2B and Kir6.1 proteins in aortic and pulmonary artery rings from WKY rats were mainly expressed in the medial layer of the vessel. The brown granules in both aortic and pulmonary artery smooth muscle cells and endothelial cells viewed were defined as positive signals (Figure 6).

SUR2B and Kir6.1 expression in aortic and pulmonary artery rings as shown by Western blotting

Compared to the pulmonary artery rings, the expression of SUR2B protein increased in the aortic rings of the Wistar rats (P<0.05, Figure 4), but there was no difference in Kir6.1 protein expression between aortic and pulmonary artery rings (P>0.05, Figure 4).

Discussion

In the present study we found that NaHS resulted in the vasorelaxation of rat thoracic aortic rings in a dose-dependent manner, which was more pronounced than the vasorelaxation that occurred in pulmonary artery rings. In aortic rings, both cellular and mitochondrial membrane K_{ATP} channel blockers markedly inhibited H_2S-induced vasorelaxation. In contrast, H_2S-induced vasorelaxation in pulmonary artery rings could only be blocked by a cellular, but not mitochondrial, membrane K_{ATP} channel blocker. The expression of SUR2B protein and mRNA in aortic rings increased compared to pulmonary artery rings.

H_2S, a novel gaseous signaling molecule, has been considered to play an important role in the regulation of cardiovascular functions[6–10]. Endogenous cardiovascular H_2S is mainly produced by CSE[8–10]. R ecent evidence from CSE knockout mice suggests that loss of CSE gene expression results in a decrease in H_2S production and a subsequent rise in blood pressure[16]. Furthermore, Shibuya *et al* and Olson *et al* showed that CSE, CBS, and 3MST were the three important H_2S generating enzymes[13, 14]. In our study, we found that the mRNA expression of 3MST in rat aorta was lower than that in the pulmonary artery, whereas the CSE protein was higher in the rat aorta than in the pulmonary artery. However, there was no difference in CBS protein expression in the rat aorta and pulmonary artery.

H_2S plays an important role in the regulation of systemic

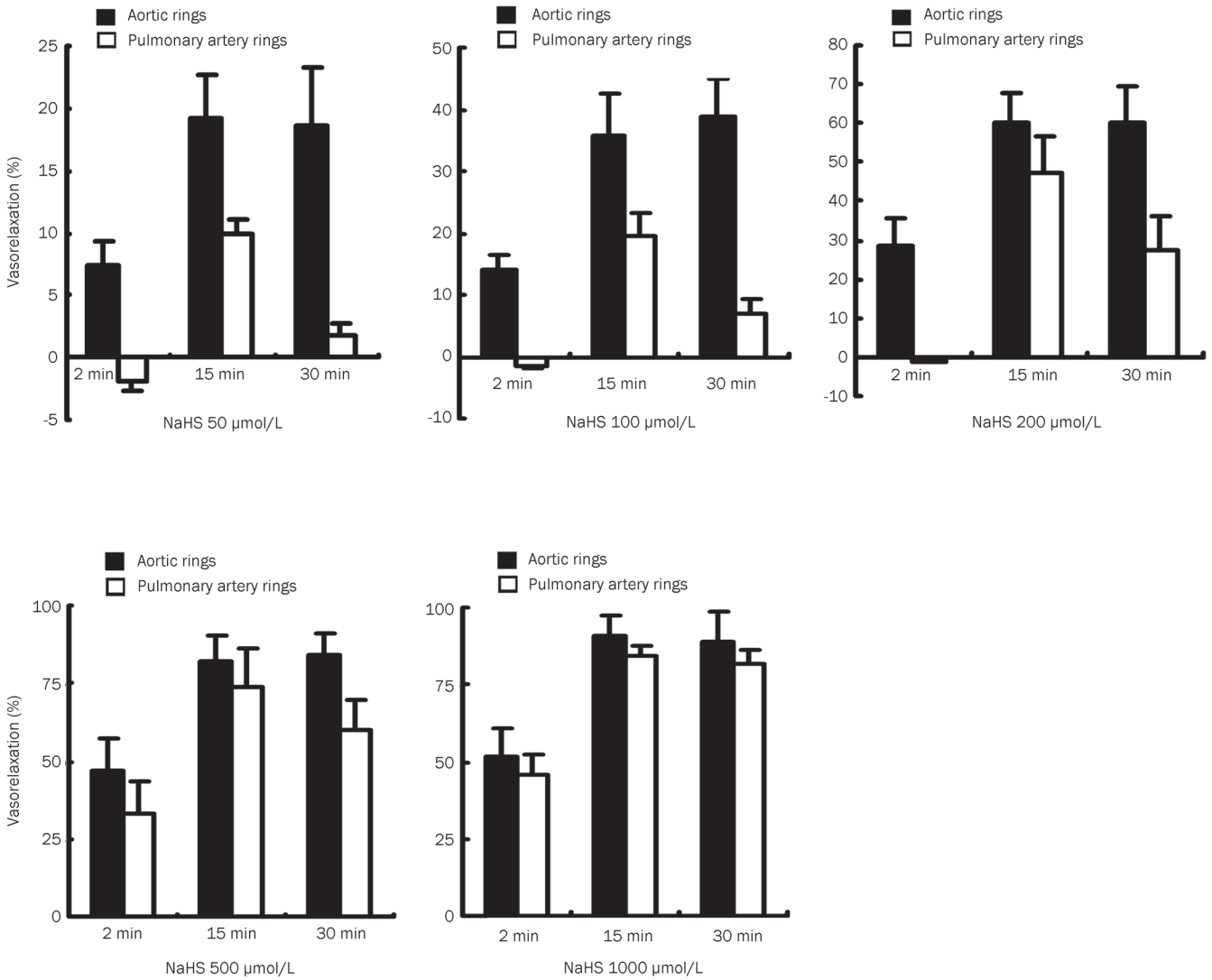

Figure 2. The different vasoactive response of aortic and pulmonary artery rings to different concentrations of NaHS in rats at the different time points.

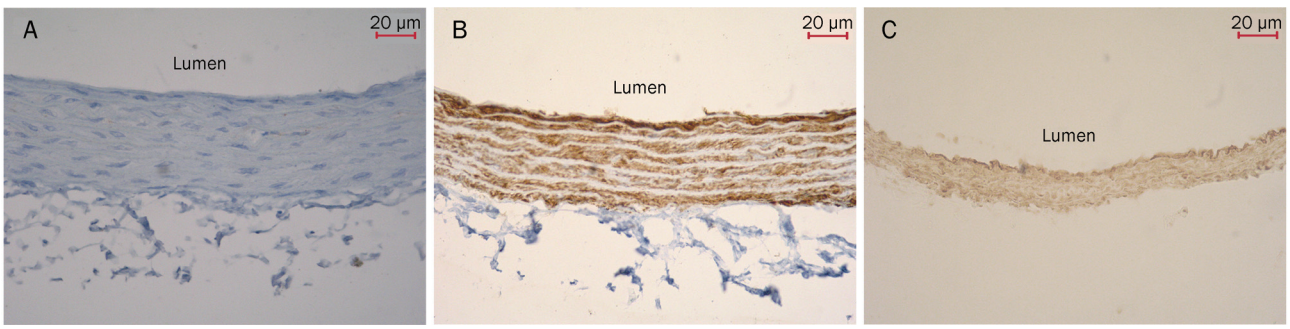

Figure 3. Immunohistochemical analysis of CSE expression in aortic and pulmonary artery rings (DAB×200). (A) The aortic ring negative control was processed without CSE primary antibody. The thickness of the inner elastic layer was uniform and the structure of smooth muscle cells was normal. (B) The aortic ring was processed with CSE antibody. CSE protein was strongly expressed in the inner membrane and tunica media vasorum. The brown granules in aortic smooth muscle cells and endothelial cells were defined as positive signals. (C) The pulmonary artery ring was processed with CSE antibody. The brown granules were observed in pulmonary artery smooth muscle cells and endothelial cells. CSE, cystathinonine gamma-lyase.

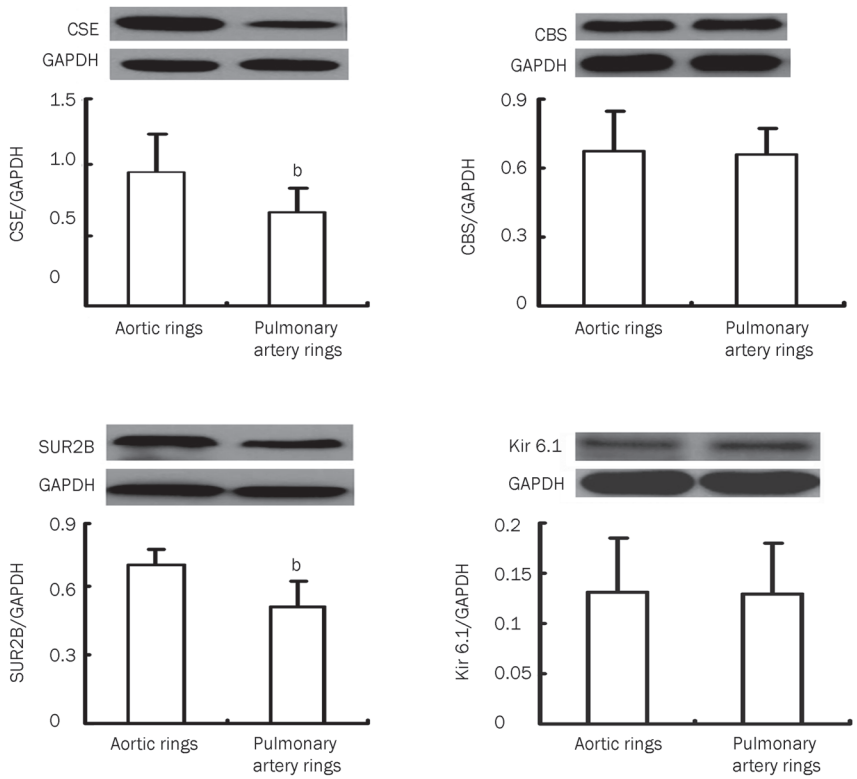

Figure 4. CSE, CBS, SUR2B and Kir6.1 expression in aortic and pulmonary artery rings as detected by Western blotting (n=10, mean±SD). $^bP<0.05$ compared to aortic rings. CSE, cystathinonine gamma-lyase; CBS, cystathionine beta synthase; SUR2B, a K_{ATP} channel subunit; Kir6.1, a K_{ATP} channel subunit.

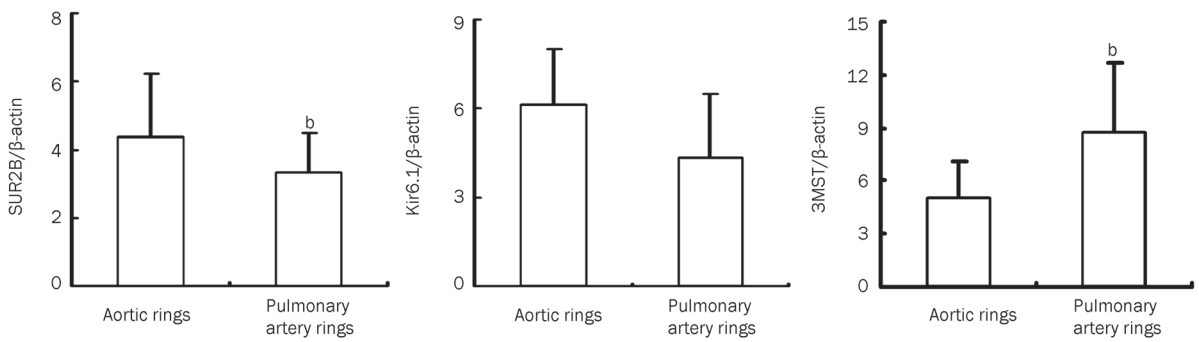

Figure 5. Expression of SUR2B, Kir6.1 and 3MST by real-time PCR (n=7, mean±SD). $^bP<0.05$ compared to aortic rings. SUR2B, a K_{ATP} channel subunit. Kir6.1, a K_{ATP} channel subunit. 3MPST, 3-mercaptopyruvate sulfurtransferase.

and pulmonary circulation[25–30]. Olson *et al* showed that in rat pulmonary arteries, NaHS produced a transit constriction followed by relaxation for 20 to 30 min, which was then followed by a second constriction[5]. In a later study, this same group carefully examined the effects of Na_2S on the conductance and resistance responses of the cow and sea lion pulmonary arteries and showed that the sea lion arteries had vasodilating characteristics[31]. We analyzed the vascular response to H_2S for 30 min. We found that in rat pulmonary arteries, NaHS at concentrations of 50, 100, and 200 μmol/L produced a transit constriction followed by a relaxation for about 20 min, which was then followed by a reduced relaxation. However, this did not occur in the rat aorta.

In this study, we found that NaHS caused vasorelaxation of rat thoracic aortic and pulmonary artery rings pre-contracted with 1 μmol/L NE *in vitro* in a dose-dependent manner. The mechanism for the vasoconstrictive response to norepinephine is the action of NE on the vascular alpha adrenaline receptors, resulting in the vasoconstrictive response. A previous study showed that in sheep *in vivo*, the vasoconstrictor response to alpha-adrenergic stimulation was less in the pulmonary circulation compared to the systemic circulation of the fetus[32]. This same study also indicated that alpha-adrenergic receptor density was less pronounced in fetal intrapulmonary vascular smooth muscle than that in fetal aortic VSM[32]. The vasorelaxing effect of H_2S on aortic and pulmonary rings is dependent

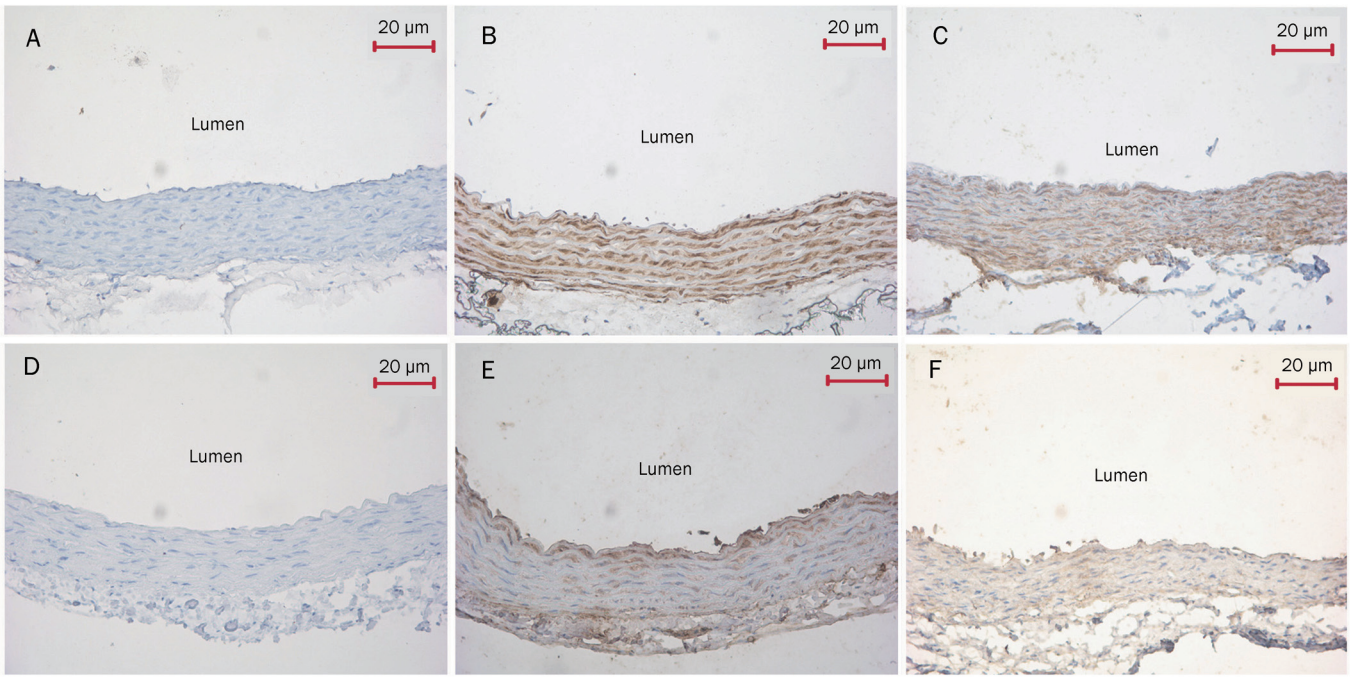

Figure 6. Immunohistochemical analysis of SUR2B and Kir6.1 expression in aortic and pulmonary artery rings (DAB×200). (A) The aortic ring negative control was processed without SUR2B primary antibody. This control had normal smooth muscle cell and endothelial cell structure without brown granules. (B) The aortic ring was treated with SUR2B antibody. SUR2B protein was strongly expressed in the inner membrane and tunica media vasorum. The presence of the brown granules in aortic smooth muscle cells and endothelial cells was defined as positive signals. (C) The pulmonary artery ring was processed with SUR2B antibody. Brown granules were observed in pulmonary artery smooth muscle cells and endothelial cells. (D) The aortic ring negative control was treated without Kir6.1 primary antibody. The structure of smooth muscle cells and endothelial cells was normal and had no brown granules. (E) The aortic ring was treated with Kir6.1 antibody. Brown granules were strongly expressed in the medial layer of aortic ring. (F) The pulmonary artery ring was processed with Kir6.1 antibody. The brown granules were observed in pulmonary artery smooth muscle cells and endothelial cells. SUR2B, a K_{ATP} channel subunit. Kir6.1, a K_{ATP} channel subunit.

on this initial pre-contraction. As far as we know, the differences in the vasorelaxing effects of H_2S between the aortic and pulmonary rings involve the following mechanisms: the mechanical properties of the blood vessels, the targeting ion channel K_{ATP} expressions and density where H_2S acts on. Thus, in our study, we attempted to examine if there were any K_{ATP} expression-mediated mechanisms in which H_2S acts on the different arteries. H_2S at concentrations of 50–1000 μmol/L dilated aortic rings more significantly than pulmonary artery rings. This result indicates that H_2S at the same dose induces a stronger vasorelaxing effect in aortic rings compared to pulmonary artery rings.

H_2S acts as a regulator of cardiovascular function[33, 34]. The opening of smooth K_{ATP} channels by H_2S has been suggested to be one of the mechanisms responsible for H_2S-induced vasorelaxation in vascular smooth muscle both *in vitro* and *in vivo*[24]. H_2S can open K_{ATP} channels in the cell membrane of aortic vascular smooth muscle, causing cytomembrane hyperpolarization. The K_{ATP} channel is very important in the cardiovascular system[35–41] and H_2S acts as an endogenous K_{ATP} channel opener. K_{ATP} channels are recognized for their cardioprotective role in ischemia[35]. Evidence suggests that Kir6.1 and SUR2B are the main K_{ATP} channel subunits expressed in the vascular smooth muscle[42–44].

Therefore, we investigated the possible mechanisms responsible for the differences in vasorelaxation between aortic and pulmonary artery rings induced by H_2S by targeting K_{ATP} channels using cell and mitochondrial membrane K_{ATP} channel blockers. The results showed that cellular (Gli) and mitochondrial (5-HD) membrane K_{ATP} channel blockers could block H_2S-induced vasorelaxation in aortic rings. In contrast, in pulmonary artery rings, only the cell membrane K_{ATP} channel blocker effectively blocked H_2S-induced vasorelaxation. In aortic rings, vasorelaxation by NaHS was 38.4% at a concentration of 100 μmol/L, which was reduced to 20.4% and 26.9% when aortic rings were pre-treated with cell and mitochondrial membrane K_{ATP} channel blockers, respectively. In pulmonary artery rings, the percent of vasorelaxation was 22.2% following 100 μmol/L NaHS, which was reduced to 12.8% when pre-treated with the cell membrane K_{ATP} channel blocker. However, pre-treatment with the mitochondrial membrane K_{ATP} channel blocker did not alter pulmonary artery ring vasorelaxation. We presume that H_2S likely induces more obvious vasorelaxation in aortic rings because H_2S opens the K_{ATP} channels more widely in aortic rings than in pulmonary artery rings.

Next, we further examined whether there was any differences in K_{ATP} channel expression between aortic and pulmo-

nary artery rings. The results showed that protein expression of the K_{ATP} channel subunit SUR2B was higher in aortic than pulmonary artery rings. Furthermore, the mRNA expression of SUR2B was higher in aortic rings than in pulmonary artery rings. These findings suggested that the relatively higher density of K_{ATP} channels in aortic rings was partly responsible for the pronounced vasorelaxation observed in isolated aortic rings compared to those observed in pulmonary artery rings at specific concentrations. The identification of more profound mechanisms involved in the H_2S-induced vasorelaxation of aortic and pulmonary artery rings requires further investigation.

Acknowledgments

This work was supported by the Foundation of the Ministry of Education, People's Republic of China (20070001702 and 20070001770); the National Natural Science Foundation of China 81070212, 30821001, and 30801251); the Major Basic Research Development Program of the People's Republic of China (2011CB503904); and the Beijing Natural Science Foundation (7082095).

We thank Shu-xu DU and Wei LU for their technical assistance.

Author contribution

Jun-bao DU and Hong-fang JIN designed the research; Yan SUN and Hong-fang JIN performed the research and contributed new analytical reagents and tools; Yan SUN, Hong-fang JIN, Chao-shu TANG, and Jun-bao DU analyzed data; and Yan SUN, Hong-fang JIN, and Jun-bao DU wrote the paper.

References

1 Aaronson PI, Robertson TP, Knock GA, Becker S, Lewis TH, Snetkov V, *et al*. Hypoxic pulmonary vasoconstriction: mechanisms and controversies. J Physiol 2006; 570: 53–8.
2 Gray GA, Webb DJ. The endothelin system and its potential as a therapeutic target in cardiovascular disease. Pharmacol Ther 1996; 72: 109–48.
3 Sata M, Fukuda D. Crucial role of renin-angiotensin system in the pathogenesis of atherosclerosis. J Med Invest 2010; 57: 12–25.
4 Lipworth BJ, Dagg KD. Vasoconstrictor effects of angiotensin II on the pulmonary vascular bed. Chest 1994; 105: 1360–4.
5 Olson KR, Dombkowski RA, Russell MJ, Doellman MM, Head SK, Whitfield NL, *et al*. Hydrogen sulfide as an oxygen sensor/transducer in vertebrate hypoxic vasoconstriction and hypoxic vasodilation. J Exp Biol 2006; 209: 4011–23.
6 Tang C, Li XH, Du JB. Hydrogen sulfide as a new endogenous gaseous transmitter in the cardiovascular system. Curr Vasc Pharmacol 2006; 4: 17–22.
7 Chen CQ, Xin H, Zhu YZ. Hydrogen sulfide: third gaseous transmitter, but with great pharmacological potential. Acta Pharmacol Sin 2007; 28: 1709–16.
8 Bhatia M. Hydrogen sulfide as a vasodilator. IUBMB Life 2005; 57: 603–6.
9 O'Sullivan SE. What is the significance of vascular hydrogen sulphide (H2S)? Br J Pharmacol 2006; 149: 609–10.
10 Bełtowski J. Hydrogen sulfide as a biologically active mediator in the cardiovascular system. Postepy Hig Med Dosw 2004; 58: 285–91.
11 Łowicka E, Bełtowski J. Hydrogen sulfide (H_2S)-the third gas of interest for pharmacologists. Pharmacol Rep 2007; 59: 4–24.
12 Szabó C. Hydrogen sulphide and its therapeutic potential. Nat Rev Drug Discov 2007; 6: 917–35.
13 Shibuya N, Mikami Y, Kimura Y, Nagahara N, Kimura H. Vascular endothelium expresses 3-mercaptopyruvate sulfurtransferase and produces hydrogen sulfide. J Biochem 2009; 146: 623–6.
14 Olson KR, Whitfield NL, Bearden SE, St Leger J, Nilson E, Gao Y, *et al*. Hypoxic pulmonary vasodilation: a paradigm shift with a hydrogen sulfide mechanism. Am J Physiol Regul Integr Comp Physiol 2010; 298: R51–60.
15 Zhao W, Zhang J, Lu Y, Wang R. The vasorelaxant effect of H_2S as a novel endogenous gaseous K_{ATP} channel opener. EMBO J 2001; 20: 6008–16.
16 Yang G, Wu L, Jiang B, Yang W, Qi J, Cao K, *et al*. H_2S as a Physiologic vasorelaxant: hypertension in mice with deletion of cystathionine gamma-lyase. Science 2008; 322: 587–90.
17 Yeager ME, Halley GR, Golpon HA, Voelkel NF, Tuder RM. Microsatellite instability of endothelial cell growth and apoptosis genes within plexiform lesions in primary pulmonary hypertension. Circ Res 2001; 88: 2–11.
18 Zhu P, Huang L, Ge X, Yan F, Wu R, Ao Q. Transdifferentiation of pulmonary arteriolar endothelial cells into smooth muscle-like cells regulated by myocardin involved in hypoxia-induced pulmonary vascular remodelling. Int J Exp Pathol 2006; 87: 463–74.
19 Chen YH, Wu R, Geng B, Qi YF, Wang PP, Yao WZ, et al. Endogenous hydrogen sulfide reduces airway inflammation and remodeling in a rat model of asthma. Cytokine 2009; 45: 117–23.
20 Patacchini R, Santicioli P, Giuliani S, Maggi CA. Pharmacological investigation of hydrogen sulfide (H_2S) contractile activity in rat detrusor muscle. Eur J Pharmacol 2005; 509: 171–7.
21 Geng B, Chang L, Pan C, Qi Y, Zhao J, Pang Y, *et al*. Endogenous hydrogen sulfide regulation of myocardial injury induced by isoproterenol. Biochem Biophys Res Commun 2004; 318: 756–63.
22 Geng B, Yang J, Qi Y, Zhao J, Pang Y, Du J, Tang C. H_2S generated by heart in rat and its effects on cardiac function. Biochem Biophys Res Commun 2004; 313: 362–8.
23 Su YW, Liang C, Jin HF, Tang XY, Han W, Chai LJ, *et al*. Hydrogen sulfide regulates cardiac function and structure in adriamycin-induced cardiomyopathy. Circ J 2009; 73: 741–9
24 Li L, Hsu A, Moore PK. Actions and interactions of nitric oxide, carbon monoxide and hydrogen sulphide in the cardiovascular system and in inflammation — a tale of three gases. Pharmacol Ther 2009; 123: 386–400
25 Wang YF, Shi L, Du JB. Impact of L-arginine on hydrogen sulfide/cystathionine-γ-lyase pathway in rats with high blood flow-induced pulmonary hypertension. Biochem Biophys Res Commun 2006; 345: 851–7
26 Yan H, Du JB, Tang CS. The possible role of hydrogen sulfide on the pathogenesis of spontaneous hypertension in rats. Biochem Biophys Res Commun 2004; 313: 22–7
27 Mancardi D, Penna C, Merlino A, Del Soldato P, Wink DA, Pagliaro P. Physiological and pharmacological features of the novel gasotransmitter: Hydrogen sulfide. Biochim Biophys Acta 2009; 1787: 864–72.
28 Sun YG, CaoYX, Wang WW, Ma SF, Yao T, Zhu YC. Hydrogen sulphide is an inhibitor of L-type calcium channels and mechanical contraction in rat cardiomyocytes. Cardiovasc Res 2008; 79: 632–41.
29 Wang YF, Mainali P, Tang CS, Shi L, Zhang CY, Yan H, *et al.* Effects of nitric oxide and hydrogen sulfide on the relaxation of pulmonary arteries in rats. Chin Med J 2008; 121: 420–3.

30 Wang Y, Zhao X, Jin H, Wei H, Li W, Bu D, *et al*. Role of hydrogen sulfide in the development of atherosclerotic lesions in apolipoprotein E knockout mice. Ateriosclerosis Thromb Vasc Biol 2009; 29: 173–9.

31 Olson KR, Whitfield NL, Bearden SE, St Leger J, Nilson E, Gao Y, *et al*. Hypoxic pulmonary vasodilation: a paradigm shift with a hydrogen sulfide mechanism. Am J Physiol Regul Integr Comp Physiol 2010; 298: R51–60.

32 Shaul PW, Magness RR, Muntz KH, DeBeltz D, Buja LM. Alpha 1-adrenergic receptors in pulmonary and systemic vascular smooth muscle. Alterations with development and pregnancy. Circ Res 1990; 67: 1193–200.

33 Rochette L, Vergely C. Hydrogen sulfide (H_2S), an endogenous gas with odor of rotten eggs might be a cardiovascular function regulator. Ann Cardiol Angeiol (Paris) 2008; 57: 136–8.

34 Du J, Hui Y, Cheung Y, Bin G, Jiang H, Chen X, *et al*. The possible role of hydrogen sulfide as a smooth muscle cell proliferation inhibitor in rat cultured cells. Heart Vessels 2004; 19: 75–80.

35 Seto SW, Ho YY, Hui HN, Au AL, Kwan YW. Contribution of glibenclamide-sensitive, ATP-dependent K^+ channel activation to acetophenone analogues-mediated *in vitro* pulmonary artery relaxation of rat. Life Sci 2006; 78: 631–9.

36 Fan LH, Tian HY, Wang J, Huo JH, Hu Z, Ma AQ, *et al*. Downregulation of Kir6.1/SUR2B channels in the obese rat aorta. Nutrition 2009, 25: 359–63.

37 Yang W, Yang GD, Jia XM, Wu LY, Wang R. Activation of K_{ATP} channels by H_2S in rat insulin-secreting cells and the underlying mechanisms. J Physiol 2005; 569: 519–31.

38 Lu T, Ye D, Wang X, Seubert JM, Graves JP, Bradbury JA, *et al*. Cardiac and vascular K_{ATP} channels in rats are activated by endogenous epoxyeicosatrienoic acids through different mechanisms. J Physiol 2006; 575: 627–44.

39 Wang T, Zhang ZX, Xu YJ. Effect of mitochondrial K_{ATP} channel on voltage- gated K^+ channel in 24 hour-hypoxic human pulmonary artery smooth muscle cells. Chin Med J 2005; 118: 12–9.

40 Cyrino FZ, Bottino DA, Coelho FC, Ravel D, Bouskela E. Effects of sulfonylureas on K_{ATP} channel-dependent vasodilation. J Diabetes Complications 2003; 17: 6–10.

41 Peter P, Ashcroft FM. Modeling K_{ATP} channel gating and its regulation. Prog Biophys Mol Biol 2009; 99: 7–19.

42 Fujita A, Kurachi Y. Molecular aspects of ATP-sensitive K^+ channels in the cardiovascular system and K^+ channel openers. Pharmacol Ther 2000; 85: 39–53.

43 Kane GC, Liu XK, Yamada S, Olson TM, Terzic A. Cardiac K_{ATP} channels in health and disease. J Mol Cell Cardiol 2005; 38: 937–43.

44 Cao K, Tang GH, Hu DH, Wang R. Molecular basis of ATP-sensitive K^+ channels in rat vascular smooth muscles. Biochem Biophys Res Commun 2002; 296: 463–9.

Acta Pharmacologica Sinica (2011) 32: 465–477

www.nature.com/aps

Original Article

Effects of diltiazem and propafenone on the inactivation and recovery kinetics of fKv1.4 channel currents expressed in *Xenopus* oocytes

Dong ZHANG[1, 2, *], Shi-min WANG[1], Hui CHEN[2], Xue-jun JIANG[1], Sheng-ping CHAO[2]

[1]*Department of Cardiology, Renmin Hospital, Wuhan University, Wuhan 430073, China;* [2]*Department of Cardiology, Zhongnan Hospital, Wuhan University , Wuhan 430071, China*

Aim: To investigate the effects of diltiazem, an L-type calcium channel blocker, and propafenone, a sodium channel blocker, on the inactivation and recovery kinetics of fKv1.4, a potassium channel that generates the cardiac transient outward potassium current.
Methods: The cRNA for fKv1.4ΔN, an N-terminal deleted mutant of the ferret Kv1.4 potassium channel, was injected into *Xenopus* oocytes to express the fKv1.4ΔN channel in these cells. Currents were recorded using a two electrode voltage clamp technique.
Results: Diltiazem (10 to 1000 μmol/L) inhibited the fKv1.4ΔN channel in a frequency-dependent, voltage-dependent, and concentration-dependent manner, suggesting an open channel block. The IC_{50} was 241.04±23.06 μmol/L for the fKv1.4ΔN channel (at +50 mV), and propafenone (10 to 500 μmol/L) showed a similar effect (IC_{50}=103.68±10.13 μmol/L). After application of diltiazem and propafenone, fKv1.4ΔN inactivation was bi-exponential, with a faster drug-induced inactivation and a slower C-type inactivation. Diltiazem increased the C-type inactivation rate and slowed recovery in fKv1.4ΔN channels. However, propafenone had no effect on either the slow inactivation time constant or the recovery.
Conclusion: Diltiazem and propafenone accelerate the inactivation of the Kv1.4ΔN channel by binding to the open state of the channel. Unlike propafenone, diltiazem slows the recovery of the Kv1.4ΔN channel.

Keywords: inactivation; recovery; Kv1.4; potassium channel; diltiazem; propafenone; two electrode voltage clamp technique

Acta Pharmacologica Sinica (2011) 32: 465–477; doi: 10.1038/aps.2010.234

Introduction

Transient outward potassium currents (I_{to}) contribute to the early repolarization phase of the cardiac action potential[1, 2]. Two types of I_{to} are known: I_{to} (fast), which shows fast recovery kinetics, and I_{to} (slow), which shows slow recovery kinetics that are related to accumulated inactivations[3]. As the major component of I_{to} (slow), the Kv1.4 channel plays an important role in the repolarization of cardiac myocytes. Kv1.4 channels were inactivated by two well-established processes: N- and C-type inactivation. N-type inactivation results from the occlusion of the intracellular side of the pore by a "ball and chain" mechanism formed by the NH_2 terminus of the channel molecule[4–9], while C-type inactivation involves conformational changes on the extracellular side of the pore[10]. These two mechanism are coupled[5]; C-type inactivation is more rapid in the presence of N-type inactivation[11] and can be affected by open channel blockers. Recovery from inactivation is controlled by the slower C-type mechanism[11], which makes it physiologically important.

The L-type calcium channel blocker diltiazem and the sodium channel blocker propafenone are widely used in clinics for the treatment of cardiovascular diseases of hypertension, cardiac angina (for diltiazem) and arrhythmias[12–14]. The therapeutic effects are generally believed to be related to the L-type calcium channel (for diltiazem) and the sodium channel (for propafenone). Recent studies demonstrated that diltiazem inhibited the hKv1.5 channel, which conducts ultra rapid delayed rectifier currents (I_{kur}), and I_{to}, encoded by Kv4.3 by binding to the open and the inactivated states of the channels[15–17]. There is evidence that diltiazem decreases Kv1.4 channel currents expressed in the oocytes of *Xenopus laevis*[16], and propafenone was shown to be an open channel antagonist of Kv1.4 channel currents[18], but their detailed characteristics have not been studied.

The present study, in which we used an N-terminal deletion construct of Kv1.4 (Kv1.4ΔN) that lacks rapid N-type inactivation but exhibits robust C-type inactivation[19] , was therefore designed for the following: (1) to study the properties of

* To whom correspondence should be addressed.
E-mail vividcurio@yahoo.com.cn
Received 2010-06-28 Accepted 2010-12-18

diltiazem blockade of the fKv1.4ΔN channel; (2) to study the effect of diltiazem on Kv1.4 channel C-type inactivation and recovery, and (3) to compare the electrophysiological effects of diltiazem on fKv1.4ΔN with those of propafenone.

Materials and methods

Molecular biology

The constructs and sequences of the cDNA fKv1.4ΔN used in this study have been previously described[19–21] and were a gift from professor Randall L RASMUSSON (University at Buffalo, SUNY). The construction of fKv1.4ΔN was performed by removal of 2–146 amino acid residues from the N-terminal domain of Kv1.4, which results in the loss of the fast component of inactivation but leaves the C-type inactivation pathway intact[19–21]. Transcribed fKv1.4ΔN cRNA was prepared *in vitro* using an mMessage mMachine kit (T3 kit, Ambion, USA).

Isolation of oocytes and incubation

Oocytes were collected from mature female *Xenopus laevis* frogs (Chinese Academy of Science, Beijing, China). Frogs were anesthetized (immersion in 1.5 g/L tricaine) for 30 min, followed by surgical removal of the ovarian lobes through a lateral incision in the lower abdomen. The incision was then sutured, and the frog was allowed to recover in a container with a small amount of water. When the frogs did not produce a high quality of oocytes, they were humanely killed *via* a high dose of tricaine. All procedures were approved by the Institutional Animal Care and Use Committee of the Wuhan University of China.

The follicular layer was removed enzymatically by placing the ovarian lobes in a collagenase-containing, Ca^{2+}-free OR_2 solution (mmol/L: 82.5 NaCl, 2 KCl, 1 $MgCl_2$ and 5 Hepes, pH 7.4, with 1–1.5 mg/mL collagenase (Type I, Sigma, USA). The oocytes were gently shaken for about 1 h and washed several times with Ca^{2+}-free OR_2 solution as previously described[13]. Finally, defolliculated (stage IV) oocytes were selected and placed in ND96 solution (mmol/L): 96 NaCl, 2 KCl, 1 $MgCl_2$, 1.8 $CaCl_2$ and 5 Hepes, pH 7.4. Each oocyte was injected with about 25–50 nL of fKv1.4ΔN cRNA using a microinjector (WPI, Sarasota) and incubated in an 18 °C environment in ND96 solution with 100 IU/mL penicillin for over 16 h.

Electrophysiology

The experiment was carried out using a two electrode voltage clamp technique. Oocytes were clamped using a preamplifier CA-1B (DAGAN, USA), and the current signals were filtered at 2.5 kHz. Microelectrodes were fabricated from 1.5 mm o.d. borosilicate glass tubing using a two-stage puller (NARISHIGE, Japan) to produce electrodes with resistances of 0.5–1.0 MΩ when filled with 3 mmol/L KCl. Currents were recorded at room temperature (20–24 °C). Recordings were made in 2 mol/L $[K^+]_o$. Diltiazem and propafenone were separately dissolved in distilled water with a stock solution of 100 mmol/L. During recording, oocytes were continuously perfused with a control (ND96) or drug-containing ND96 solution. Whenever drugs were used, 10 min of perfusion time was used to allow equilibration of the drug with the oocytes. After this wash-on period, a series of 500 ms depolarizing pulses (from -90 mV to +50 mV at a frequency of 1 Hz for 1 min) was employed to ensure a steady-state block before beginning the experimental protocols[20].

Data analysis

Data were recorded with a personal computer installed with pCLAMP 9.0 (Axon, USA) and analyzed using Clampfit 9.0 (Axon, USA) and Microsoft Excel software (Microsoft, USA). Unless otherwise stated, raw data traces were not leakage or capacitance subtracted. Data are shown as means±SEM. Significant differences were determined using Student's paired *t*-tests.

Results

Effects of diltiazem on fKv1.4ΔN currents

Voltage-, concentration-, and frequency-dependent blockade of diltiazem on fKv1.4ΔN currents

Figure 1A shows representative fKv1.4ΔN current traces recorded by applying 5 s pulses from -100 mV to +50 mV in 10 mV increments in the control, in the presence of 250 μmol/L diltiazem, and after the drug washout. The fKv1.4ΔN currents were substantially inhibited by the application of 250 μmol/L diltiazem and the effect recovered after washout of the drug for 10 min.

Peak-voltage relationships from the control, 250 μmol/L diltiazem-treated and drug washout oocyte groups were plotted against clamp potential in Figure 1B. In this figure, the I_{DIL}/I_{CON} ratio was plotted as a function of the membrane potential. Diltiazem decreased the peak currents at transmembrane potentials positive to the activation threshold (-30 mV). The blockade increased steeply in the voltage range coinciding with that of channel activation (between -40 mV and -20 mV) and remained constant at voltages above this range. The peak current was blocked by 52.21%±4.63% when the cell membrane was depolarized to +50 mV in 250 μmol/L diltiazem, and the effect was reversed by 95% after the drug washout. There was a voltage dependence to the action of diltiazem, a phenomenon typical of open channel block.

Figure 1C shows the concentration dependence of fKv1.4ΔN current inhibition by diltiazem. Inhibition of the currents in a concentration-dependent manner was measured at the end of a 300 ms pulse of +50 mV. A nonlinear least-squares fit of the Hill equation to the individual data points yielded an apparent dissociation constant, K_D, for an open channel blockade of 241.04±23.06 μmol/L (n=5).

To evaluate the longer-term effects of exposing the fKv1.4ΔN channel to diltiazem, we applied a series of 500 ms depolarizing pulses from -90 mV to +50 mV with a frequency of 1 Hz for a period of 1 min. Figure 2 shows the peak currents elicited by this protocol, before and after exposure to 250 μmol/L diltiazem, normalized to the first peak current under control conditions. With increasing pulse numbers, currents in both the control and the diltiazem-treated groups decreased. The first pulse of the pulse train in the presence of 250 μmol/L

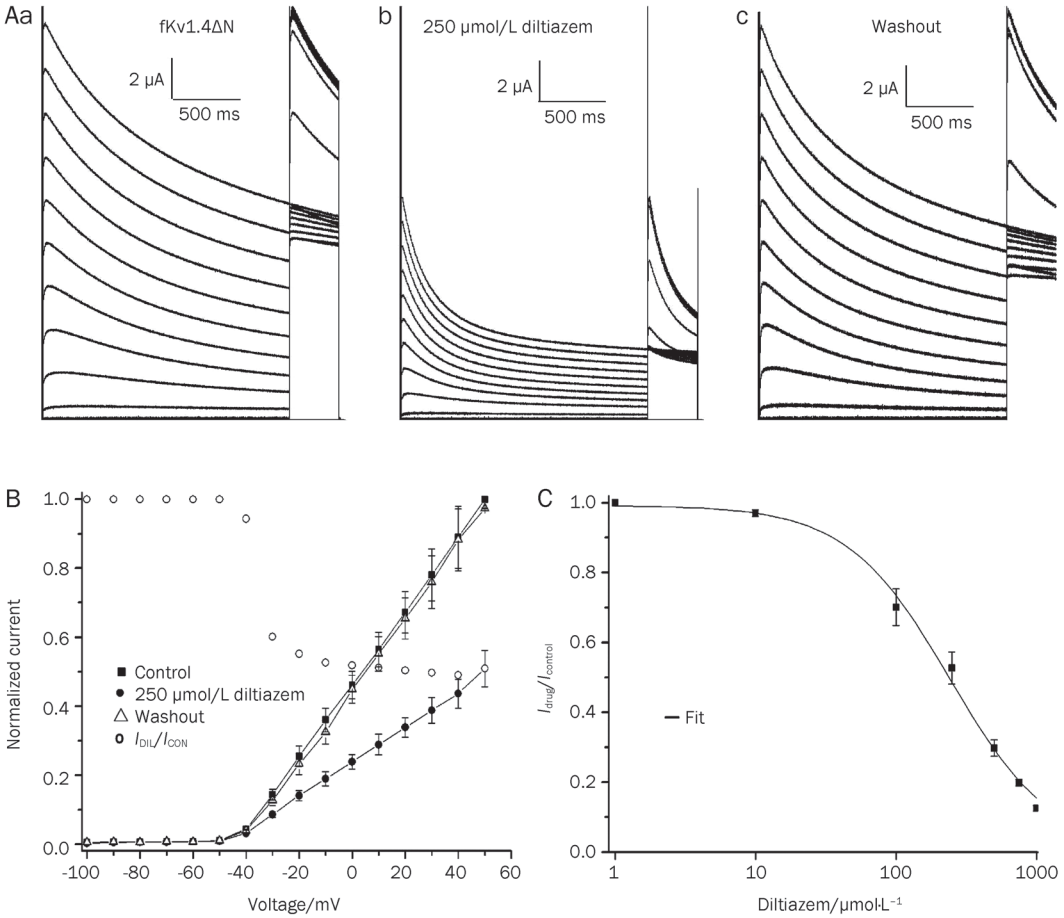

Figure 1. Voltage- and concentration-dependent blockade of fKv1.4ΔN currents by diltiazem. (A) Channels were expressed in *Xenopus* oocytes and recorded with the two electrode voltage clamp technique. Currents were obtained by applying 5 s pulses to potentials (P_1) ranging from -100 mV to +50 mV and were followed by the tail currents obtained upon repolarization to +50 mV (P_2) under control conditions (a), then in the presence of 250 μmol/L diltiazem (b), and finally after 10 min of washout (c). (B) Current-voltage relationships of fKv1.4ΔN channels under control conditions, in the presence of 250 μmol/L diltiazem, and after the drug washout for 10 min. Currents were normalized to the peak current at +50 mV under control conditions. The I_{DIL}/I_{CON} ratio was plotted as a function of the membrane potential. Data are shown as means±SEM. (n=5). (C) Dose-response relationships for diltiazem inhibition of fKv1.4ΔN channels at 2 mmol/L $[K^+]_o$. Data were obtained upon repolarization to -90 mV after 1 s pulses to +50 mV, holding potential -90 mV. All values shown were normalized to the peak current in the absence of drug in 2 mmol/L $[K^+]_o$. Continuous line was derived by fitting the data to the Hill equation: $f=K_D/(K_D+D)$, where f is fractional current, K_D is the apparent dissociation constant, and D is the diltiazem concentration. Symbols and error bar are means±SEM. fKv1.4ΔN current was reduced to 50% by 241.04±23.06 μmol/L.

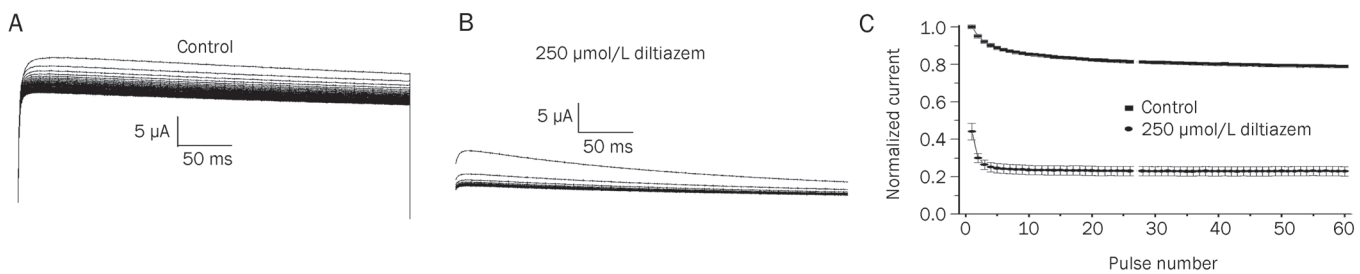

Figure 2. Frequency-dependent block of fKv1.4ΔN channels by diltiazem. Currents were elicited by applying a series of depolarising pulses from -90 mV to +50 mV with a frequency of 1 Hz in the absence (A) and in the presence of 250 μmol/L diltiazem (B). The peak currents shown in Panel A and B were normalized to the maximum control value without drug and plotted in Panel C. As pulse number increased, currents in both control and diltiazem-treated groups decreased. In control cells, there was a use-dependent reduction in the magnitude of the peak current. When cells were exposed to 250 μmol/L diltiazem for 10 min before stimulation, there was a reduction in the magnitude of the first peak current compared to the control value and then a use-dependent component. The use-dependent reduction in current with diltiazem was much greater than that seen in control.

diltiazem showed a decrease relative to the pre-drug control, and the magnitude of this reduction in current was similar to that seen under steady-state conditions when a sufficiently long recovery time was allowed between test pulses. In both the control and the 250 μmol/L diltiazem protocols, there was a use-dependent decrease in the peak current when stimulated at 1 Hz, but this use-dependent decrease was considerably greater in 250 μmol/L diltiazem than under the control conditions. In control oocytes, the peak current decayed mono-exponentially from 100% to 78.86%. In contrast, in 250 μmol/L diltiazem the current decayed from 44.14% to 23.07%.

Effect of diltiazem on the steady inactivation of peak Kv1.4ΔN currents

Figure 3A shows the time-dependent progression of the channel from the rapid open block conformation into a diltiazem-induced block during a single depolarizing step from -90 mV to +50 mV. For comparison, all current traces were normalized to the peak values under control conditions. In control conditions, the rate of inactivation of fKv1.4ΔN was mono-exponential with a time constant of 2.32±0.41 s (n=6). In the presence of 10 to 1000 μmol/L diltiazem, inactivation became bi-exponential, with a dominant fast exponential.

Figure 3B(a) shows steady-state inactivation as a function of holding potential for the fKv1.4ΔN channel both before and after exposure to diltiazem. The relationships were determined from the two pulse protocol by calculating the ratio of the magnitude of the peak current in P_2 to the maximum of the P_2 obtained when P_1 was -100 mV. In this panel, diltiazem can be seen to shift the voltage dependence of inactivation to the left. In order to correct the visual error caused by different minimum values, the steady-state inactivation relationships were renormalized [Figure 3B(b)], thus preferably displaying the drift of the steady inactivation curve before and after diltiazem treatment. Figure 3B(b) also shows this shift to the left. The half-inactivation ($V_{1/2}$) and slope factor (k) values from

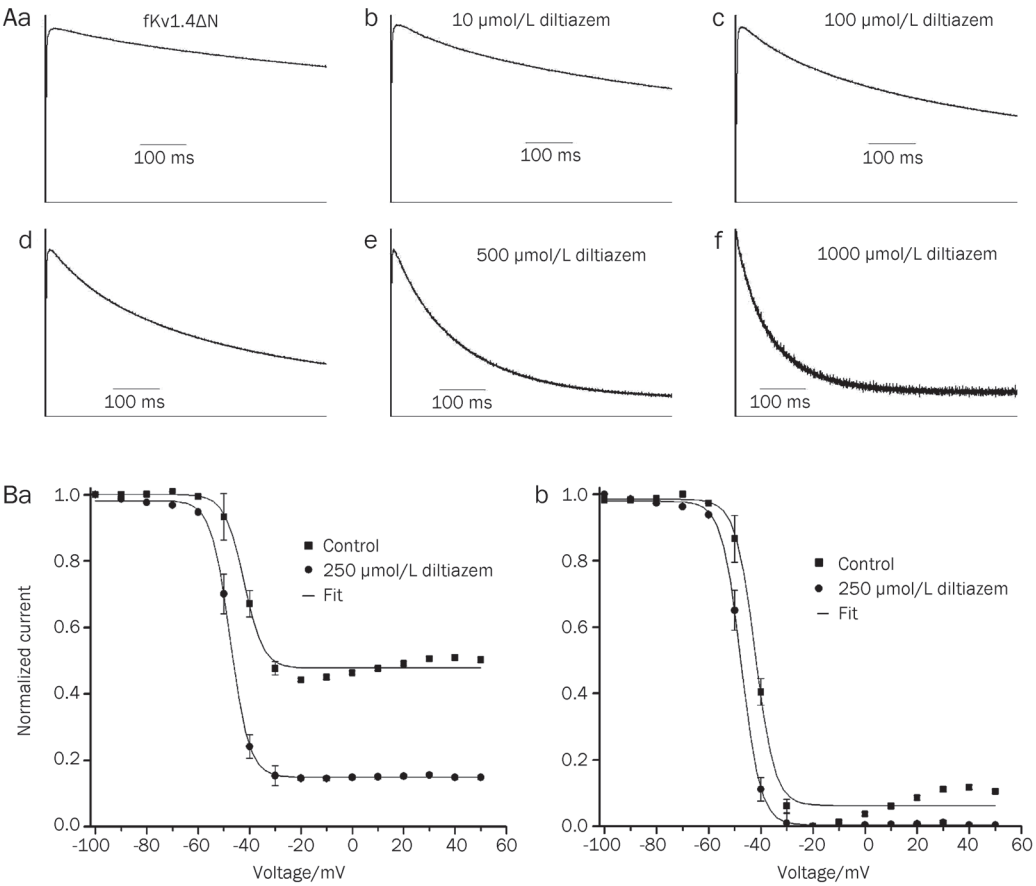

Figure 3. Effect of diltiazem on the steady inactivation of peak Kv1.4ΔN currents. (A) The time-dependent progression of channel currents. Currents were elicited by applying 1 s pulses from -90 mV to +50 mV in the absence and presence of increasing concentrations of diltiazem. For comparison, all current traces were normalized to the peak values under control conditions. The smooth continuous line superimposed on each trace is the best fit of an exponential function, used to determine the inactivation time constant (s). The control trace was best fitted by a mono-exponential function (Chebyshev method) (a), whereas in the presence of 10 μmol/L–1000 μmol/L diltiazem, inactivation was best fitted by a bi-exponential function (Levenberg-Marquardt) (b–f). (B) Steady-state inactivation relationships (a). The steady-state inactivation for each P_1 voltage was calculated as the magnitude of the peak current in P_2 compared with that from the maximum of the P_2 obtained when P_1 was -100 mV. Average data are shown as mean±SEM. Steady-state inactivation relationships are shown: fKv1.4ΔN (■) and fKv1.4ΔN+250 μmol/L diltiazem (●). Continuous lines represent the fit of the data to a Boltzmann equation: $f=1/\{1+\exp*[(V-V_{1/2})/k)]\}$. Steady-state inactivation relationships were re-normalized (b).

fKv1.4ΔN without diltiazem and fKv1.4ΔN with 250 μmol/L diltiazem presented in Figure 4A (a and b) are similar. No statistical difference was observed between the control and diltiazem conditions. The *K* was 4.58±0.75 (*n*=6) in the control and 5.06±0.78 (*n*=6) in the diltiazem treated group, and the $V_{1/2}$ was -38.38±0.81 mV in the control and -39.23±0.85 mV (*n*=6) in the diltiazem treated group.

Inactivation of fKv1.4ΔN is best fitted by a single exponential function (Figure 4B), with an inactivation time constant ($\tau_{inactivation}$) that averaged 2.32±0.41 s (*n*=6) at +50 mV. In the presence of diltiazem, the inactivation of fKv1.4ΔN is best fitted with a bi-exponential function, with τ_{fast}=0.41±0.04 s and τ_{slow}=1.78±0.29 s at +50 mV (*n*=6) [Figure 4A(c)], where τ_{fast} represents the time constant of inactivation induced by the drug and τ_{slow} represents the time constant of C-type inactivation. We found that C-type inactivation was obviously accelerated by 250 μmol/L diltiazem at +50 mV. Over the range 0 mV to +50 mV, there is no voltage sensitivity to $\tau_{inactivation}$ (*P*>0.05, *n*=6). In the presence of diltiazem, τ_{fast} is voltage independent, whereas τ_{slow} is voltage dependent. The time constant of C-type inactivation changes was independent of voltage, indicating that C-type inactivation of the fKv1.4ΔN channel is at least partly independent on activation. Thus, above 0 mV, C-type inactivation has nothing to do with the degree of depolarization of membrane voltage; however, C-type inactivation becomes correlated to activation in the presence of diltiazem.

Figure 4C shows the plot of the $1/\tau_{block}$ as a function of the diltiazem concentration for data obtained at concentrations between 10 μmol/L and 1000 μmol/L. The straight line is the least-squares fit to the equation ($1/\tau_{block}=k_{+1}[d]+k_{-1}$). Slope and intercept with the ordinate axis for the fitted relation yielded a k_{+1} and k_{-1} of $(0.01\pm0.002)\times10^6$ $(mol/L)^{-1}\cdot s^{-1}$ and

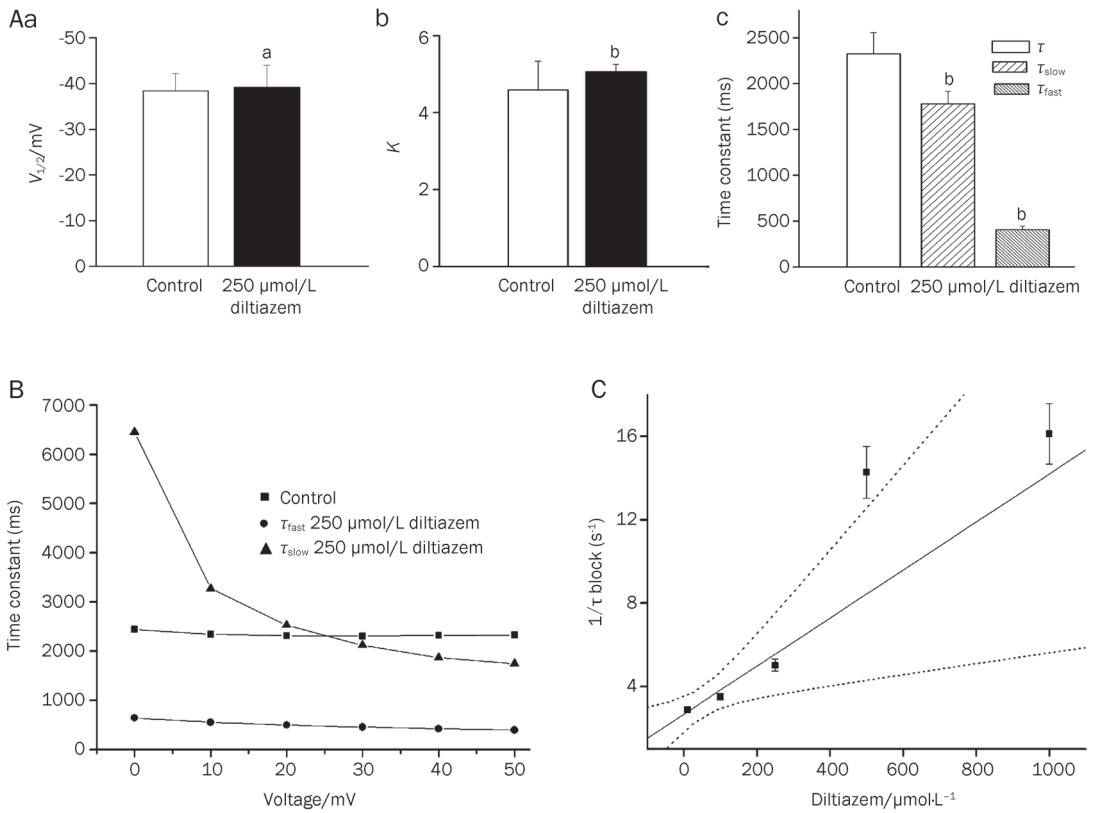

Figure 4. Comparison of the voltage for half-inactivation ($V_{1/2}$) and slope factor (*k*) from fKv1.4ΔN without diltiazem and fKv1.4ΔN with 250 μmol/L diltiazem (A(a) and A(b)). (A (a)) $V_{1/2,\ control}$=-38.38±0.81 mV (*n*=6), $V_{1/2,\ diltiazem}$=-39.23±0.85 mV (*n*=6), (A(b)) $K_{control}$=4.58±0.75 (*n*=6), $K_{diltiazem}$=5.06±0.78 (*n*=6). Average data are shown as means±SEM (^aP>0.05 *vs* control), (A(c)) The effect of diltiazem on the rate of inactivation of fKv1.4ΔN channels. The time constant of inactivation was acquired by fitting the current trace elicited at +50 mV (P_1) ranging from the beginning of the peak of P_1 to the end of 5 s. $\tau_{inactivation,\ control}$=2.32±0.41 s (*n*=6). In the presence of diltiazem, τ_{fast}=0.41±0.04 s and τ_{slow}=1.78±0.29 s (*n*=6). Average data are shown as means±SEM (^bP<0.05 *vs* control). (B) Diltiazem alters the rate of inactivation for fKv1.4ΔN channels. Inactivation of fKv1.4ΔN channels is well fitted by a single exponential function (Chebyshev method), and is voltage independent (■) over the range 0 mV to +50 mV. In the presence of diltiazem, the inactivation of fKv1.4ΔN is best fitted with a bi-exponential function (Levenberg-Marquardt). Over the range 0 mV to +50 mV, τ_{fast} is voltage independent (●), whereas τ_{slow} is voltage dependent (▲). (C) The reciprocal of the diltiazem-induced fast time constant ($1/\tau_{block}$) at +50 mV as a function of the diltiazem concentration for data obtained at concentrations in the range between 10 μmol/L and 1000 μmol/L. The straight line is the least-squares fit to equation: $1/\tau_{block}=k_{+1}[d]+k_{-1}$, where τ_{block} is the time constant of development of block, k_{+1} and k_{-1} are the apparent association rate constant and the apparent dissociation rate constant, respectively. The dotted lines is the 95% confidence interval of the fit, each point represents the means±SEM of 6 experiments.

2.67±0.25 s^{-1}, respectively.

Effects of diltiazem on the recovery kinetics of fKv1.4ΔN currents

The rate of recovery from inactivation of the Kv1.4 channel is governed by recovery from C-type inactivation. We measured the effect of diltiazem on the rate of recovery from inactivation in the fKv1.4ΔN channel using a standard gapped pulse protocol with a variable interstimulus interval. The ratio of the magnitude of the first and second pulse peak currents was used as an indication of the degree of the recovery from inactivation.

Figure 5A shows the fraction of fKv1.4 channels recovered plotted against the interstimulus interval. In the presence of 250 μmol/L diltiazem, there is a dramatic decrease in the rate of recovery of fKv1.4ΔN channels when compared to the control. The envelope of peak ratios was best fitted with a mono-exponential function. The presence of 250 μmol/L diltiazem increased the time constant for the rate of recovery from inactivation in fKv1.4ΔN. The mean time constants for recovery were 1.73±0.10 s (n=5) in the control and 2.66±0.14 s (n=5) in the diltiazem treated group (P<0.05; Figure 5B). The half time constant of recovery ($t_{1/2}$) for fKv1.4ΔN was 1.01±0.03 s in the control and 1.67±0.05 s in the presence of 250 μmol/L diltiazem (n=5, P<0.05; Figure 6). Diltiazem shifted the recovery from inactivation curve to the right and slowed the recovery time constant and $t_{1/2}$.

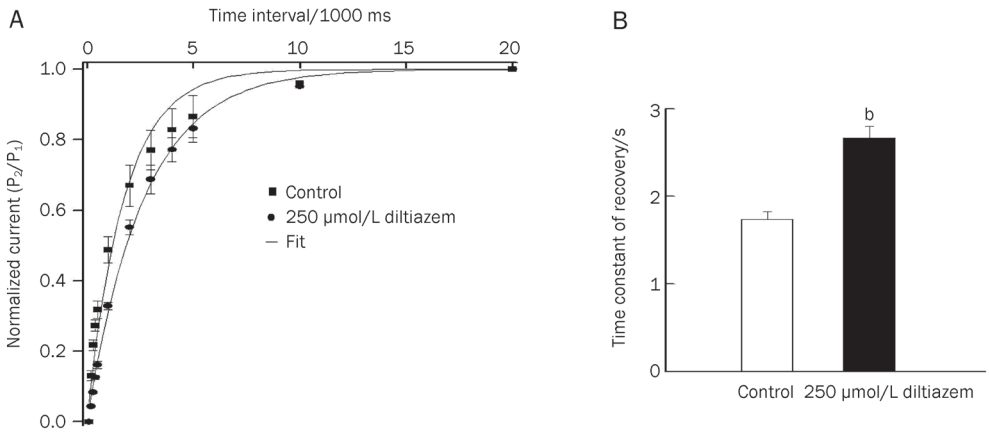

Figure 5. Effect of diltiazem on the rate of recovery from inactivation in fKv1.4ΔN. Recovery from inactivation was measured using a standard variable interval gapped pulse protocol. An initial 5 s pulse (P_1) from -90 mV to +50 mV was followed by a second pulse (P_2) to +50 mV after an interval of between 0.1 s and 20 s. (A) The ratio of the peak current elicited by the P_1 and P_2 pulses (P_2/P_1) is plotted against pulse interval to show the recovery from inactivation. The recovery of inactivation was best fitted using the function: f=1–A*exp(-τ/t), where t is duration (in s), τ is the time constant, A is the amplitude of the current. Recovery curves for fKv1.4ΔN and fKv1.4ΔN+diltiazem, holding potential=-90 mV. (B) Comparison of recovery rate data from fKv1.4ΔN without and with 250 μmol/L diltiazem. The mean time constants for recovery were 1.73±0.10 s (n=5) in control and 2.66±0.14 s (n=5) in the diltiazem treated group (^bP<0.05 *vs* control).

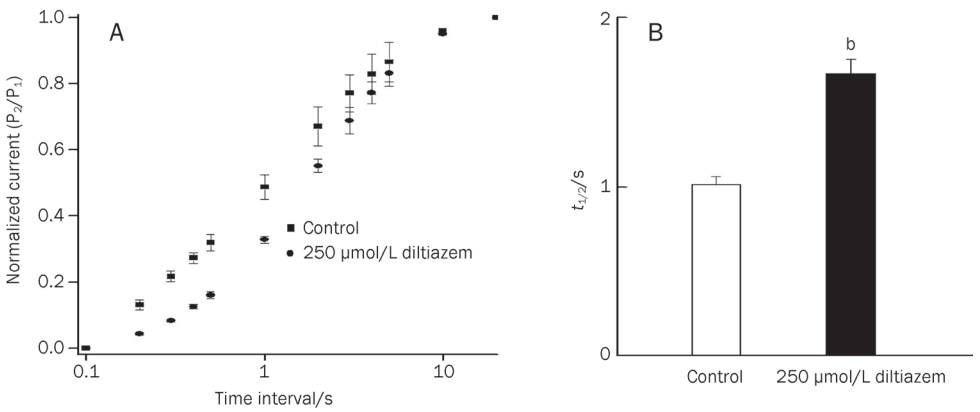

Figure 6. (A) Average recovery time course for fKv1.4ΔN without diltiazem and with 250 μmol/L diltiazem. Data were normalized between 0 and 1 presented with intervals on a log scale. (B) $t_{1/2}$ for fKv1.4ΔN was 1.01±0.03 s (n=5) and $t_{1/2}$ was 1.67±0.05 s (n=5) in the presence of 250 μmol/L diltiazem (^bP<0.05 *vs* control).

Effects of propafenone on fKv1.4ΔN currents

Voltage-, concentration-, and frequency-dependent blockade of propafenone on fKv1.4ΔN currents

Figure 7A shows typical fKv1.4ΔN current traces recorded by applying 5 s pulses from -100 mV to +50 mV followed by the tail currents obtained upon repolarization to +50 mV under control conditions, in the presence of 100 μmol/L propafenone, and after the drug washout. As shown, 100 μmol/L propafenone decreased fKv1.4ΔN currents, with the effect recovered upon a 10 min washout.

Peak-voltage relationships under control conditions, 100 μmol/L propafenone, and after washout are shown in Figure 7B. In this figure, the I_{PRO}/I_{CON} ratio is plotted as a function of the membrane potential. Propafenone substantially decreased the current amplitude at potentials positive to -30 mV. The I_{PRO}/I_{CON} ratio was plotted as a function of the membrane potential; the blockade increased steeply in the voltage range coinciding with that of channel activation (between -40 mV and -20 mV), and it remained constant thereafter. The peak current was blocked by 51.82%±2.35% when depolarized to +50 mV in 100 μmol/L propafenone, and the effect was reversed by 96% after the drug washout. There was a voltage dependence related to the action of propafenone, a phenomenon typical of open channel block.

The concentration dependence of open channel propafenone block of peak fKv1.4ΔN currents at 2 mmol/L $[K^+]_o$ is shown in Figure 7C. Data were obtained upon repolarization to -90 mV after 1 s pulses to +50 mV (holding potential: -90 mV). The concentration dependence of the blockade of fKv1.4ΔN currents was best fitted to the Hill equation. The K_D value for open channel block of fkv1.4ΔN was 103.68±11.25 μmol/L (n=5).

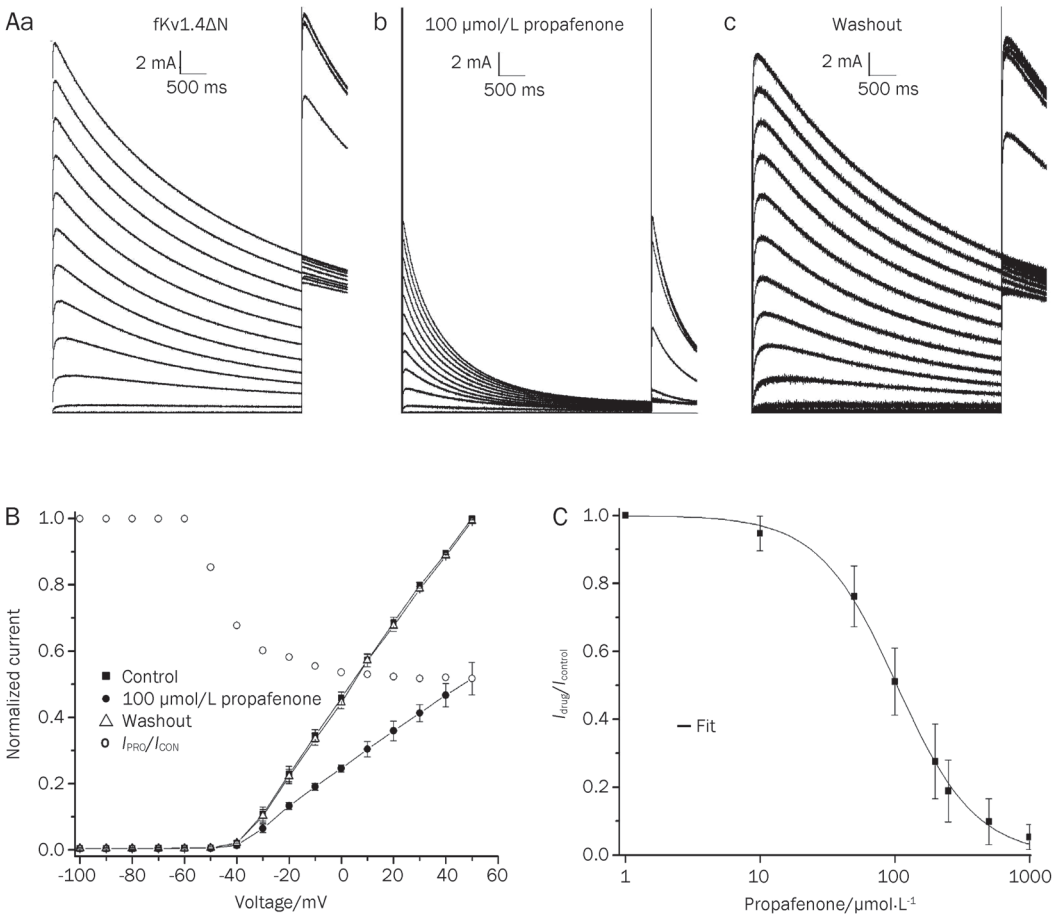

Figure 7. Voltage- and concentration-dependent blockade by propafenone on fKv1.4ΔN currents. (A) Current recordings from two-electrode voltage clamp of oocytes expressing fKv1.4ΔN. Currents were obtained by applying 5 s pulses to potentials (P_1) ranging from -100 mV to +50 mV followed by the tail currents obtained upon repolarization to +50 mV (P_2) under control conditions (a), then in the presence of 100 μmol/L propafenone (b), and finally after 10 min of washout (c). (B) Current-voltage relationships of fKv1.4ΔN channels under control conditions, in the presence of 100 μmol/L propafenone, and after the drug washout for 10 min. Currents were normalized to the peak current at +50 mV under control conditions. The I_{PRO}/I_{CON} ratio was plotted as a function of the membrane potential. Data are shown as means±SEM (n=5). (C) Dose-response relationships for propafenone inhibition of fKv1.4ΔN channels at 2 mmol/L $[K^+]_o$. Data were obtained upon repolarization to -90 mV after 1 s pulses to +50 mV, holding potential -90 mV. All values shown were normalized to the peak current in the absence of drug in 2 mmol/L $[K^+]_o$. Continuous line was derived by fitting the data to the Hill equation: $f=K_D/(K_D+D)$, where f is fractional current, K_D is the apparent dissociation constant, and D is the propafenone concentration. Symbols and error bar are means±SEM. fKv1.4ΔN current was reduced to 50% by 103.68±11.25 μmol/L.

To determine the longer-term effects of exposing the fKv1.4ΔN channel to propafenone, we applied a series of 500 ms depolarizing pulses from -90 mV to +50 mV with a frequency of 1 Hz for a period of 1 min. Figure 8 shows the peak currents recorded by this protocol, before and after exposure to 100 μmol/L propafenone, normalized to the first peak current under control conditions. With increasing pulse numbers, the currents in both the control and the propafenone-treated groups decreased. The first pulse of the pulse train in the presence of 100 μmol/L propafenone showed a decrease relative to the pre-drug control, and the magnitude of this reduction was similar to that seen under steady-state conditions when an adequately long recovery time was allowed between test pulses. In both the control and the 100 μmol/L propafenone protocols, there was a use-dependent decrease in the peak current when stimulated at 1 Hz, but this use-dependent decrease was much greater in 100 μmol/L propafenone than in the control. In control oocytes, the peak current decayed mono-exponentially from 100% to 74.52%. By contrast, in 100 μmol/L propafenone, the current decreased from 49.72% (due to initial rapid open channel block) to 35.20% in the steady state.

Effect of propafenone on the steady inactivation of peak Kv1.4ΔN currents

The time-dependent progression of the channel from the rapid open block conformation into a propafenone-induced block was studied during a single depolarizing step from -90 mV to +50 mV (Figure 9A). For comparison, all current traces were normalized to the peak values under control conditions. In control conditions, the rate of inactivation of fKv1.4ΔN was mono-exponential with a time constant of 2.32±0.41 s (n=6). In the presence of 10 to 500 μmol/L propafenone, inactivation became bi-exponential, with a dominant fast exponential.

Figure 9B(a) shows the inactivation curves in the absence and presence of 100 μmol/L propafenone. The steady-state inactivation relationships were determined from the two pulse protocol by calculating the ratio of the magnitude of the peak current in P_2 to the maximum of the P_2 obtained when P_1 was -100 mV. In this panel, propafenone can be seen to shift the voltage dependence of inactivation to the left. However, after steady-state inactivation relationships were renormalized [Figure 9B(b)], we found that propafenone did not shift the voltage dependence of inactivation. Under control conditions, the $V_{1/2}$ and K values averaged -41.29±5.21 mV and 1.13±0.09 (n=6), and 100 μmol/L propafenone did not modify either the $V_{1/2}$ (-50.62±6.77 mV) or the K (1.62±0.27) (n=6) [Figure 10A(a and b)].

Inactivation of fKv1.4ΔN is best fitted by a single exponential function (Figure 10B), with $\tau_{inactivation}$=2.32±0.41 s (n=6) at +50 mV. In the presence of propafenone, the inactivation of fKv1.4ΔN is best fitted with a bi-exponential function, with τ_{fast}=0.44±0.03 s and τ_{slow}=2.23±0.23 s (n=6) at +50 mV [Figure 10A(c)]. We found that C-type inactivation was not shifted by 100 μmol/L propafenone at +50 mV. Over the range of 0 mV to +50 mV, there was no voltage sensitivity to $\tau_{inactivation}$ (P>0.05, n=6). In the presence of propafenone, both τ_{fast} and τ_{slow} were voltage independent.

Figure 10C shows the plot of the $1/\tau_{block}$ as a function of the propafenone concentration for data obtained at concentrations between 10 μmol/L and 500 μmol/L. The straight line is the least-squares fit to the equation ($1/\tau_{block}=k_{+1}[d]+k_{-1}$), and the apparent association and dissociation rate constants were $(0.02\pm0.002)\times10^6$ $(mol/L)^{-1}\cdot s^{-1}$ and 1.87±0.15 s^{-1}, respectively.

Effects of propafenone on the recovery kinetics of fKv1.4ΔN currents

The effects of propafenone on the recovery kinetics of the fKv1.4ΔN channel expressed in *Xenopus* oocytes are presented in Figure 11A. The fraction of fKv1.4 channels recovered was plotted against the interstimulus interval. The mean time constants of recovery from the steady-state inactivation were 1.78±0.09 s (n=5) in the control and 1.86±0.14 s (n=5) in the propafenone treated group (P>0.05; Figure 11B). In the presence of 100 μmol/L propafenone, there is no significant change in the rate of recovery of fKv1.4ΔN compared to the control. The half time constant of recovery for fKv1.4ΔN was 1.14±0.04 s in the control and 1.49±0.05 s in the presence of 100 μmol/L propafenone (n=5, P>0.05; Figure 12). These results

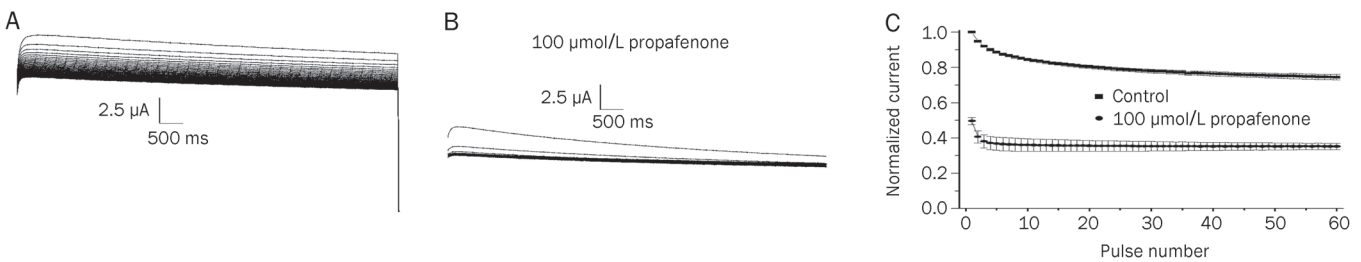

Figure 8. Frequency-dependent block of fKv1.4ΔN channel by propafenone. Currents were elicited by using a series of depolarising pulses from -90 mV to +50 mV with a frequency of 1 Hz in the absence (A) and in the presence of 100 μmol/L propafenone (B). The peak currents shown in Panel A and B were normalized to the maximum control value without drug and plotted in Panel C. As pulse number increased, currents in both control and propafenone-treated groups decreased. In control cells, there was a use-dependent reduction in the magnitude of the peak current. When cells were exposed to 100 μmol/L propafenone for 10 min before stimulation, there was a reduction in the magnitude of the first peak current compared to the control value and then a use-dependent component. The use-dependent reduction in current with propafenone was obviously greater than that seen in control.

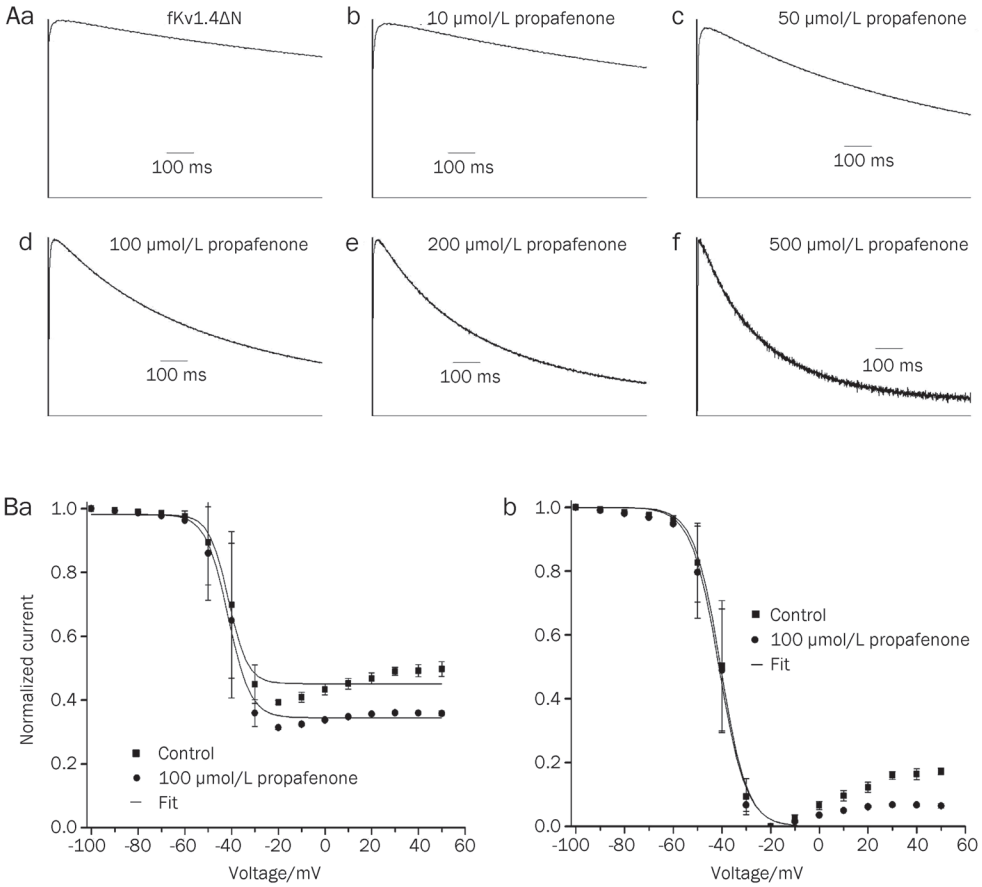

Figure 9. Effect of propafenone on the steady inactivation of peak Kv1.4ΔN currents. (A) The time-dependent progression of channel currents. Currents were recorded by using 1 s pulses from -90 mV to +50 mV in the absence and presence of increasing concentrations of propafenone. For comparison, all current traces were normalized to the peak values under control conditions. The smooth continuous line superimposed on each trace is the best fit of an exponential function, used to determine the inactivation time constant (s). The control trace was best fitted by a mono-exponential function (Chebyshev method) (a), whereas in the presence of 10–500 μmol/L propafenone, inactivation was best fitted by a bi-exponential function (Levenberg-Marquardt) (b–f). (B) Steady-state inactivation relationships (a). The steady-state inactivation for each P_1 voltage was calculated as the magnitude of the peak current in P_2 compared with that from the maximum of the P_2 obtained when P_1 was -100 mV. Average data are shown as mean±SEM. Steady-state inactivation relationships are shown: fKv1.4ΔN (■) and fKv1.4ΔN+100 μmol/L propafenone (●). Continuous lines represent the fit of the data to a Boltzmann equation: $f=1/\{1+\exp*[(V-V_{1/2})/k)]\}$. Steady-state inactivation relationships were re-normalized (b).

indicate that propafenone does not affect the recovery of fKv1.4ΔN channels from inactivation.

Discussion

The L-type calcium channel blocker diltiazem and the sodium channel blocker propafenone have been reported to block several cloned potassium channels, including Kv1.1, Kv1.2, Kv1.4, Kv1.5, Kv2.1, Kv4.2, and hERG channel currents[16, 21-24]. For instance, diltiazem, at concentrations of 0.01 nmol/L to 500 μmol/L, suppressed the hKv1.5 potassium channel expressed in mouse fibroblasts with an estimated IC_{50} of 42.3 μmol/L[17]. But in human atrial myocytes, I_{Kur} was blocked by diltiazem at relatively low concentrations (IC_{50}=11.2 μmol/L)[25]. In Chinese hamster ovary cells, diltiazem (109.9 μmol/L) was reported to suppress the Kv4.3 channel by 50%[17]. Diltiazem blocked I_{to} (fast) in human atrial myocytes with an IC_{50} of 29.2 μmol/L[26]. Propafenone was shown to depress hERG channel currents in human embryonic kidney cells with an IC_{50} of 440 μmol/L[22], and it was shown to block hKv1.5 channels in a concentration-, voltage-, time- and use-dependent manner with an IC_{50} value of 4.4 mmol/L[23]. Propafenone was also shown to inhibit I_{to} in rabbit atrial myocytes and rat ventricular myocytes[26], as well as to inhibit the hyperpolarization-activated inward current in isolated human atrial myocytes[27] and I_{Kr} in sinoatrial node cells, rabbit atrial myocytes and guinea pig ventricular myocytes[26, 28–29].

Limited data are available for the Kv1.4 potassium channel. In *Xenopus* oocytes, diltiazem and propafenone have been reported to reduce fKv1.4 potassium channel currents, and 100 μmol/L diltiazem and 100 μmol/L propafenone were reported to suppress Kv1.4 potassium channel tail currents by 10% and 11%, respectively[16]. Propafenone was shown to be an open channel antagonist of Kv1.4 channel currents[18], but the mechanism of the drug block was not examined. Our find-

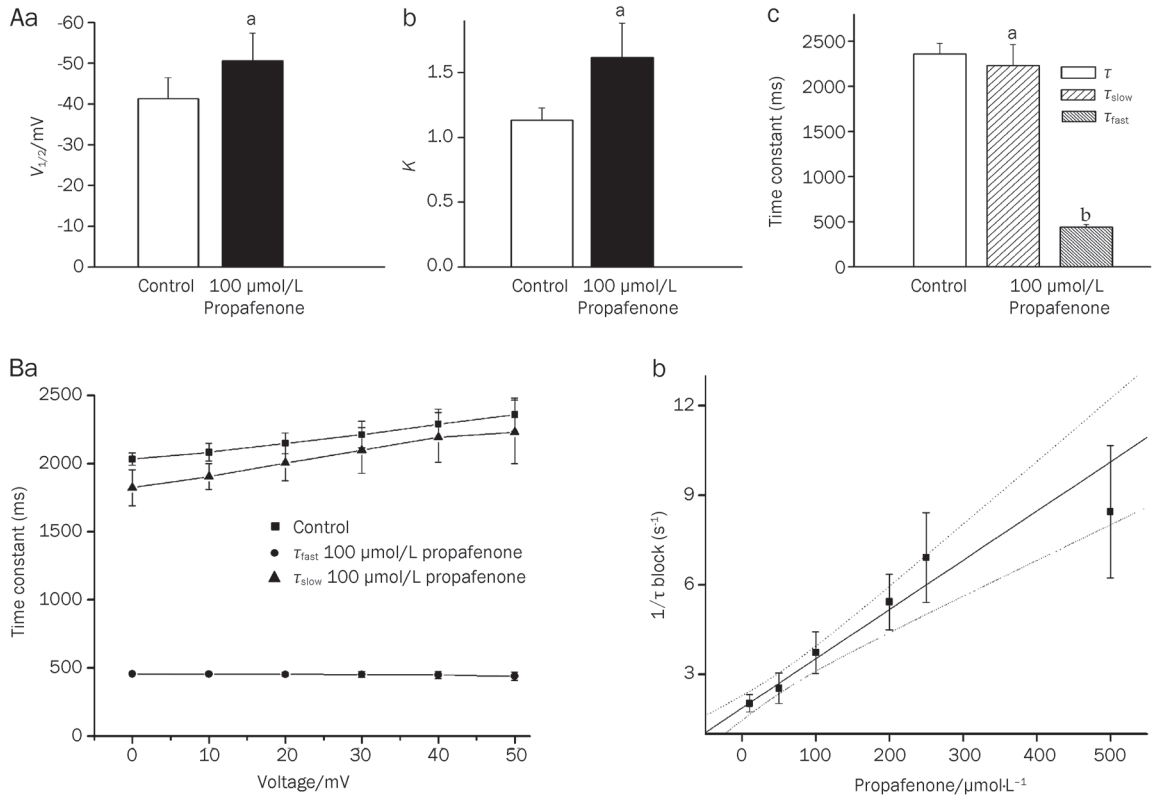

Figure 10. Comparison of the voltage for $V_{1/2}$ and K from fKv1.4ΔN without propafenone and fKv1.4ΔN with 100 μmol/L propafenone [A(a) and A(b)]. [A(a)] $V_{1/2,\ control}$=-41.29±5.21 mV (n=6), $V_{1/2,\ propafenone}$=-50.62±6.77 mV (n=6); [A(b)] $K_{control}$=1.13±0.09 (n=6), $K_{propafenone}$=1.62±0.27 (n=6); [A(c)] The effect of propafenone on the rate of inactivation of fKv1.4ΔN channels. The time constant of inactivation was acquired by fitting the current trace elicited at +50 mV (P_1) ranging from the beginning of the peak of P_1 to the end of 5 s. $\tau_{inactivation,\ control}$=2.32±0.41 s ($n$=6). In the presence of propafenone, τ_{fast}=0.44±0.03 s and τ_{slow}=2.32±0.23 s (n=6). Average data are shown as means±SEM (^aP>0.05, ^bP<0.05 *vs* control). (B) Effect of propafenone on the rate of inactivation for fKv1.4ΔN channels. Inactivation of fKv1.4ΔN channels is well fitted by a single exponential function (Chebyshev method), and is voltage independent (■) over the range of 0 mV to +50 mV. In the presence of propafenone, the inactivation of fKv1.4ΔN is best fitted with a bi-exponential function (Levenberg-Marquardt). Over the range of 0 mV to +50 mV, both τ_{fast} (●) and τ_{slow} (▲) are voltage independent. (C) The reciprocal of the propafenone-induced fast time constant ($1/\tau_{block}$) at +50 mV as a function of the propafenone concentration for data obtained at concentrations in the range between 10 and 500 μmol/L. The straight line is the least-squares fit to equation: $1/\tau_{block}=k_{+1}[d]+k_{-1}$, where τ_{block} is the time constant of development of block, k_{+1} and k_{-1} are the apparent association rate constant and the apparent dissociation rate constant, respectively. The dotted lines is the 95% confidence interval of the fit, each point represents the means±SEM of 6 experiments.

ings agree with these reports; however, we found that blockade required relatively high drug concentrations.

In the current study, it has been shown that both diltiazem and propafenone are blockers of the fKv1.4 channel. Starting with concentrations of 10 μmol/L, up to 50% of the fKv1.4 channel currents were blocked with 241 μmol/L diltiazem and 103 μmol/L propafenone. Although the concentrations required were higher, in interpreting the results, it has to be further considered that in the oocyte expression system, a fivefold to ten fold higher concentration of antiarrhythmic drugs is needed to obtain an effect comparable to that seen in mammalian cells lines[16]. Thus, it can be assumed that in cardiomyocytes, both diltiazem and propafenone have an even stronger effect on the Kv1.4 channel than that reported in this study in *Xenopus* oocytes.

Diltiazem and propafenone are different types of antiarrhythmic drugs. The electrophysiological effects of the two drugs on fKv1.4ΔN channel inactivation have been determined. Both drugs decrease fKv1.4ΔN channel currents in voltage-, concentration-, and frequency-dependent manners. However, the difference between the two drugs is three fold. First, our results have demonstrated that diltiazem exhibits a similarly high affinity for fKv1.4 channels and that the concentration of blockade is slightly higher than that needed to block L-type calcium channels[16], while propafenone exhibits a higher binding affinity for fKv1.4 channels compared with diltiazem. Second, in the presence of diltiazem, the magnitude of the peak current is obviously reduced, and the rate of inactivation is increased compared with the control. The $\tau_{inactivation}$ values we found were 2.32±0.21 s and 1.78±0.19 s in the absence and presence of 250 μmol/L diltiazem, respectively; however, 100 μmol/L propafenone did not increase the C-type inactivation time constant. Third, diltiazem slows recovery from inactivation, but propafenone has no effect on this process.

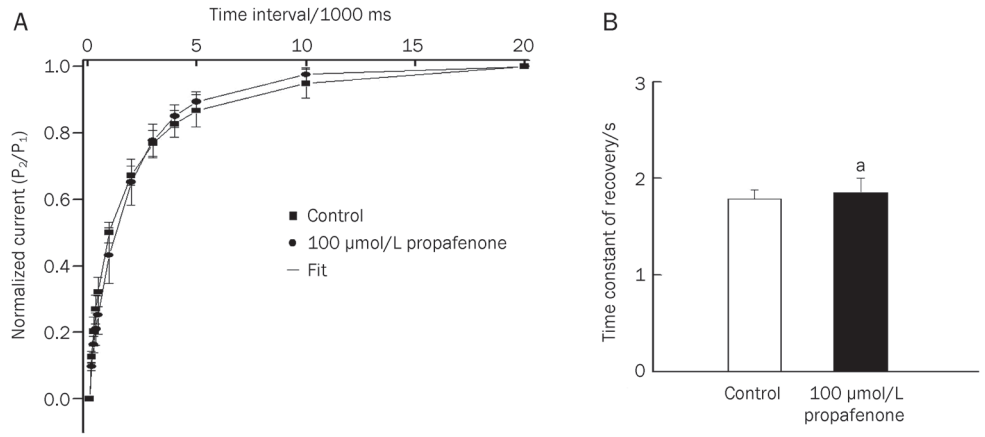

Figure 11. Effect of propafenone on the rate of recovery from inactivation in fKv1.4ΔN. Recovery from inactivation was measured using a standard variable interval gapped pulse protocol. An initial 5 s pulse (P_1) from -90 mV to +50 mV was followed by a second pulse (P_2) to +50 mV after an interval between 0.1 and 20 s. (A) The ratio of the peak current elicited by the P_1 and P_2 pulses (P_2/P_1) is plotted against pulse interval to show the recovery from inactivation. The recovery of inactivation was best fitted using the function: $f=1-A*\exp(-\tau/t)$, where t is duration (in s), τ is the time constant, A is the amplitude of the current. Recovery curves for fKv1.4ΔN and fKv1.4ΔN+propafenone, holding potential=-90 mV. (B) Comparison of recovery rate data from fKv1.4ΔN without and with 100 μmol/L propafenone. The mean time constants for recovery were 1.78±0.09 s (n=5) in control and 1.86±0.14 s (n=5) in the propafenone treated group (^aP>0.05 *vs* control).

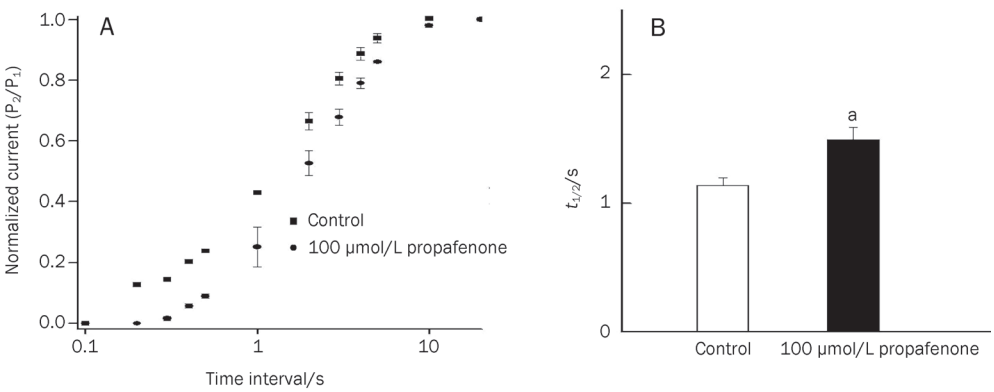

Figure 12. (A) Average recovery time course for fKv1.4ΔN without propafenone and with 100 μmol/L propafenone. Data were normalized between 0 and 1 presented with intervals on a log scale. (B) $t_{1/2}$ for fKv1.4ΔN was 1.14±0.04 s (n=5) and $t_{1/2}$ was 1.49±0.05 s (n=5) in the presence of 100 μmol/L propafenone (^aP>0.05 *vs* control).

Diltiazem induced a voltage-dependent block of fKv1.4 channels that increased over the voltage range of channel activation. When channel activation reached saturation, the block induced by diltiazem remained increased, an effect that resembles the action of propafenone on fKv1.4[18], and there was a voltage dependence to the action of both drugs.

The rate of fKv1.4 current decay in the control could be fitted to a single exponential function, and in the presence of diltiazem and propafenone, the inactivation became biexponential, characterized by the extremely fast drug-induced inactivation and the relatively slower C-type inactivation. The diltiazem-induced C-type inactivation was much faster than that seen under control conditions, which may be explained by the mechanism in which binding of drug to the intracellular site of the channel triggers a conformational change at the external mouth of the pore that facilitates C-type inactivation. This phenomenon was also observed in the same channel induced by quinidine and verapamil[18, 20]. However, propafenone did not increase the C-type inactivation time constant, demonstrating that binding of propafenone to the channel did not induce a conformational change at the external mouth of the pore.

The two drug-induced extra component of inactivation [rapid inactivation(τ_{fast})] had a time constant that was much faster than that of slow inactivation; therefore, this fast time constant can be considered to represent the interaction of the drug with the open state. Using the time constants of development for fKv1.4 blockade obtained in the range of 10–1000 μmol/L (for diltiazem) and 10–500 μmol/L (for propafenone), the k_{+1} and k_{-1} constants for diltiazem and propafenone were obtained. Assuming a first order reaction drug/channel inter-

action, the ratio k_{-1}/k_{+1} would give the apparent IC_{50} of 267 μmol/L (for diltiazem) and 113 μmol/L (for propafenone)[30, 31]. This estimate was independent of but similar to the IC_{50} calculated from the respective concentration-response curve. The similarity of the IC_{50} values obtained by the two independent methods supports the open-channel block model used to calculate the rate constants for the Kv1.4 channel. Diltiazem and propafenone-induced blockade of Kv1.4 channels developed during depolarization, and no blockade happened when the channel closed, which strongly suggests that both drugs are open state blockers of the Kv1.4 channel.

From this study, we found that diltiazem blockade of the fKv1.4ΔN channel was a complex process that may involve more than one conformational state. First, diltiazem blocks the open channel with rapid kinetics as fast as activation kinetics because diltiazem does not change the steady state activation. Second, diltiazem binds to the channel and blocks it in a voltage- and time-dependent manner. Finally, the binding of diltiazem to the channel enhances C-type inactivation. Based on previous results showing that retardation of C-type inactivation dramatically reduced E-4031 binding affinity in hERG channels[32], we concluded that an interaction between drug binding and C-type inactivation exists.

Clinically, diltiazem is widely used as an anti-arrhythmic and anti-anginal drug. It has been reported that the cardiac action potentials in mice were lengthened by 10 nmol/L diltiazem, a finding that may be explained by diltiazem-induced blockade of the I_{to} (slow) currents generated by the Kv1.4 channel[33]. The Kv1.4 channel, as the major component of I_{to} (slow), which in turn is a major contributor to phase 1 and the early part of phase 2 of the action potential, plays an important role in the repolarization of the endocardial region of the left ventricle[34]. Therefore, the reduction of Kv1.4 induced by diltiazem prolongs action potential durations. Propafenone has a similar effect.

In this study, we found that in response to the faster frequency stimulations, fKv1.4ΔN channel currents were significantly reduced. Opening the channel with a faster frequency may facilitate entry of the drug into the channel. These conformation-specific drug-binding properties lead to some clinically important issues, such as use dependence. The effects of micromolar diltiazem on fKv1.4 are moderate but are likely to be enhanced during tachyarrhythmias due to the frequency dependence of the drug's action, and propafenone shares these characteristics. Decreasing recovery rates could attenuate the shortening of the action potential duration caused by diltiazem-induced inhibition of L-type calcium channels. Because diltiazem and propafenone have different antiarrhythmic effects, their blockade actions on the Kv1.4ΔN channel must be considered when diltiazem is applied in combination with propafenone or other potassium channel blockers such as amiodarone.

Acknowledgements

We thank Dr RASMUSSON (University at Buffalo, SUNY) for the fKv1.4ΔN cDNA.

Author contribution

Dong ZHANG, Hui CHEN, and Shi-min WANG designed the research; Dong ZHANG, Hui CHEN, Sheng-ping CHAO, and Xue-jun JIANG performed the research; Dong ZHANG and Shi-min WANG analyzed the data; Dong ZHANG and Hui CHEN wrote the paper.

References

1 Campbell DL, Rasmusson RL, Qu Y, Strauss HC. The calcium-independent transient outward potassium current in isolated ferret right ventricular myocytes. I. Basic characterization and kinetic analysis. J Gen Physiol 1993; 101: 60–6.

2 Greenstein JL, Wu R, Po S, Tomaselli GF, Winslow RL. Role of the calcium-independent transient outward current Ito1 in shaping action potential morphology and duration. Circ Res 2000; 87: 1026–33.

3 Wettwer E, Amos GJ, Posival H, Ravens U. Transient outward current in human ventricular myocytes of subepicardial and subendocardial origin. Circ Res 1994; 75: 473–82.

4 Holmgren M, Jurman ME, Yellen G. N-type inactivation and the S4-S5 region of the Shaker K^+ channel. J Gen Physiol 1996; 108: 195–206.

5 Hoshi T, Zagotta WN, Aldrich RW. Biophysical and molecular mechanisms of Shaker potassium channel inactivation. Science 1990; 250: 533–8.

6 Isacoff EY, Jan YN, Jan LY. Putative receptor for the cytoplasmic inactivation gate in the Shaker K^+ channel. Nature 1991; 353: 86–90.

7 Jerng HH, Covarrubias M. K^+ channel inactivation mediated by the concerted action of the cytoplasmic N- and C-terminal domains. Biophys J 1997; 72: 163–74.

8 Lopez GA, Jan YN, Jan LY. Evidence that the S6 segment of the Shaker voltage-gated K^+ channel comprises part of the pore. Nature 1994; 367: 179–82.

9 Zagotta WN, Hoshi T, and Aldrich RW. Restoration of inactivation in mutants of Shaker potassium channels by a peptide derived from ShB. Science 1990; 250: 568–71.

10 Liu Y, Jurman ME, Yellen G. Dynamic rearrangement of the outer mouth of a K^+ channel during gating. Neuron 1996; 16: 859–67.

11 Rasmusson RL, Morales MJ, Castellino RC, Zhang Y, Campbell DL, Strauss HC. C-type inactivation controls recovery in a fast inactivating cardiac K^+ channel (Kv1.4) expressed in Xenopus oocytes. J Physiol 1995; 489: 709–21.

12 Kumar S, Hall RJ. Drug treatment of stable angina pectoris in the elderly: defining the place of calcium channel antagonists. Drugs Aging 2003; 20: 805–15.

13 Hohnloser SH, Kuck KH, Lilienthal J. Rhythm or rate control in atrial fibrillation -pharmacological intervention in atrial fibrillation (PIAF): a randomised trial. Lancet 2000; 356: 1789–94.

14 Gorenek B, Cavusoglu Y, Goktekin O, Birdane A, Kudaiberdieva G, Ata N, *et al*. Amiodarone versus sotalol and propafenone for prevention of immediate recurrence of atrial fibrillation after internal cardioversion: importance of P wave analysis. Int J Cardiol 2006; 106: 268–9.

15 Grissmer S, Nguyen AN, Aiyar J, Hanson DC, Mather RJ, Gutman GA, *et al*. Pharmacological characterization of five cloned voltage gated K^+ channels, types Kv1.1, 1.2, 1.3, 1.5, and 3.1, stably expressed in mammalian cell lines. Mol Pharmacol 1994; 45: 1227–34.

16 Rolf S, Haverkamp W, Borggrefe M, Musshoff U, Eckardt L, Mergenthaler J, *et al*. Effects of antiarrhythmic drugs on cloned cardiac voltage-gated potassium channels expressed in *Xenopus* oocytes. Naunyn Schmiedebergs Arch Pharmacol 2000; 362: 22-31.

17 Caballero R, Gómez R, Núñez L, Moreno I, Tamargo J, Delpón E. Diltiazem inhibits hKv1.5 and Kv4.3 currents at therapeutic concentrations. Cardiovasc Res 2004; 64: 457–66.
18 Xu L, Huang C, Chen J, Jiang X, Li X, Bett GC, *et al*. Effect of amiodarone on Kv1.4 channel C-type inactivation: comparison of its effects with those induced by propafenone and verapamil. Pharmazie 2008; 63: 475–9.
19 Comer MB, Campbell DL, Rasmusson RL, Lamson DR, Morales MJ, Zhang Y, *et al*. Cloning and characterization of an Ito-like potassium channel from ferret ventricle. Am J Physiol 1994 ; 267: H1383–95.
20 Wang S, Morales MJ, Qu YJ, Bett GC, Strauss HC, Rasmusson RL. Kv1.4 channel block by quinidine: evidence for a drug induced allosteric effect. J Physiol 2003; 546: 387–401.
21 Madeja M, Leicher T, Friederich P, Punke MA, Haverkamp W, Musshoff U, *et al*. Molecular site of action of the antiarrhythmic drug propafenone at the voltage-operated potassium channel Kv2.1. Mol Pharmacol 2003; 63: 547–56.
22 Arias C, González T, Moreno I, Caballero R, Delpón E, Tamargo J, *et al*. Effects of propafenone and its main metabolite, 5-hydroxypropafenone, on hERG channels. Cardiovasc Res 2003; 57: 660–9.
23 Franqueza L, Valenzuela C, Delpón E, Longobardo M, Caballero R, Tamargo J. Effects of propafenone and 5-hydroxy-propafenone on hKv1.5 channels. Br J Pharmacol 1998; 125: 969–78.
24 Paul AA, Witchel HJ, Hancox JC. Inhibition of the current of heterologously expressed hERG potassium channels by flecainide and comparison with quinidine, propafenone and lignocaine. Br J Pharmacol 2002; 136: 717–29.
25 Gao Z, Sun H, Chiu SW, Lau CP, Li GR. Effects of diltiazem and nifedipine on transient outward and ultra rapid delayed rectifier potassium currents in human atrial myocytes. Br J Pharmacol 2005; 144: 595–604.
26 Duan D, Fermini B, Nattel S. Potassium channel blocking properties of propafenone in rabbit atrial myocytes. J Pharmacol Exp Ther 1993; 264: 1113–23.
27 Hoppe UC, Beuckelmann DJ. Modulation of the hyperpolarization activated inward current (If) by antiarrhythmic agents in isolated human atrial myocytes. Nauny Schmiedebergs Arch Pharmacol 1998; 358: 635–40.
28 Satoh H, Hashimoto K. Effect of propafenone on the membrane currents of rabbit sino-atrial node cells. Eur J Pharmacol 1984; 99: 185–91.
29 Delpon E, Valenzuela C, Perez O, Casis O, Tamargo J. Propafenone preferentially blocks the rapidly activating component of delayed rectifier K^+ current in guinea pig ventricular myocytes. Voltage-independent and time-dependent block of the slowly activating component. Circ Res 1995; 76: 223–35.
30 Snyders J, Knoth KM, Roberds SL, Tamkun MM. Time-, voltage-, and state-dependent block by quinidine of a cloned human cardiac potassium channel. Mol Pharmacol 1992; 41: 322–30.
31 Slawsky MT, Castle NA. K^+ channel blocking actions of flecainide compared with those of propafenone and quinidine in adult rat ventricular myocytes. J Pharmacol Exp Ther 1994; 269: 66–74.
32 Wang S, Morales MJ, Liu S, Strauss HC, Rasmusson RL. Modulation of hERG affinity for E-4031 by $[K^+]_o$ and C-type inactivation. FEBS Lett 1997; 417: 43–47.
33 Nerbonne JM, Nichols CG, Schwarz TL, Escande D. Genetic manipulation of cardiac K^+ channel function in mice: what have we learned, and where do we go from here? Circ Res 2001; 89: 944–56.
34 Strauss HC, Morales MJ, Wang S, Brahmajothi MV, Campbell DL. Voltage-dependent K^+ channels. In: Sperelakis N, Kurachi Y, Terzic A , Cohen MV editors; Heart physiology and pathophysiology. San Diego (California): Academic Press; 2001. p 259–80.

Acta Pharmacologica Sinica (2011) 32: 478–486
 1671-4083/11 $32.00
www.nature.com/aps

Original Article

Chitosan oligosaccharides suppress LPS-induced IL-8 expression in human umbilical vein endothelial cells through blockade of p38 and Akt protein kinases

Hong-tao LIU[1], Pei HUANG[2], Pan MA[1], Qi-shun LIU[2], Chao YU[2, *], Yu-guang DU[1, *]

[1]*Dalian Institute of Chemical Physics, Chinese Academy of Sciences, Dalian 116023, China;* [2]*Institute of Life Sciences, Chongqing Medical University, Chongqing 400016, China*

Aim: To investigate whether and how COS inhibited IL-8 production in LPS-induced human umbilical vein endothelial cells (HUVECs).
Methods: RT-PCR, enzyme-linked immunosorbent assays (ELISA) and Western blotting were used to study IL-8 expression and related signaling pathway. Wound healing migration assays and monocytic cell adhesion analysis were used to explore the chemotactic and adhesive activities of HUVECs.
Results: COS 50–200 μg/mL exerted a significant inhibitory effect on LPS 100 ng/mL-induced IL-8 expression in HUVECs at both the transcriptional and translational levels. In addition, COS 50–200 μg/mL inhibited LPS-induced HUVEC migration and U937 monocyte adhesion to HUVECs in a concentration-dependent manner. Signal transduction studies suggest that COS blocked LPS-induced activation of nuclear factor-κB (NF-κB) and activator protein-1 (AP-1) as well as phosphorylation of p38 mitogen-activated protein kinase (MAPK) and phosphokinase Akt. Further, the over-expression of LPS-induced IL-8 mRNA in HUVECs was suppressed by a p38 MAPK inhibitor (SB203580, 25 μmol/L) or a phosphatidylinositol 3-kinase (PI3K) inhibitor (LY294002, 50 μmol/L).
Conclusion: COS inhibited LPS-induced IL-8 expression in HUVECs through the blockade of the p38 MAPK and PI3K/Akt signaling pathways.

Keywords: anti-inflammatory agents; arteriosclerosis; lipopolysaccharides; endothelial cells; chemokine; MAPK; phosphatidylinositol 3-kinase; interleukin-8; NF-kappa B; chitosan oligosaccharides

Acta Pharmacologica Sinica (2011) 32: 478–486; doi: 10.1038/aps.2011.10

Introduction

Endothelial cells (ECs) located in the inner lining of the vascular space play a key role in maintaining essential physiological processes of the vasculature[1]. Serving as a barrier between the bloodstream and vascular wall, ECs are sensitive to pathological stimuli in the body. Once activated by extracellular mediators, ECs initiate a variety of inflammatory responses, which ultimately lead to the formation of cardiovascular diseases. Lipopolysaccharide (LPS), the major portion of the outer membrane of gram-negative bacteria, is a strong risk factor for vascular inflammation[2]. In the pathogenesis of infectious diseases, high levels of LPS directly lead to the occurrence of inflammatory responses elicited by ECs, including enhancement of endothelial permeability, secretion of chemokines and recruitment of circulating leukocytes[3]. Among these activities, LPS-induced interleukin-8 (IL-8) expression should receive more attention for its substantial contribution to endothelial damage. As an early chemotactic signal in an inflammation reaction, IL-8 not only promotes the recruitment and adhesion of leucocytes but also mediates the complex activation of ECs[4, 5]. Therefore, the inhibition of IL-8 expression in activated ECs has been considered as a potential therapeutic strategy against vascular inflammation.

Chitosan, the deacetylated derivative of chitin, is a linear polymer of β-(1,4)-linked *D*-glucosamine[6]. Chitosan oligosaccharides (COS) are depolymerized products of chitosan by either chemical or enzymatic hydrolysis. As a cellulose-like biopolymer, COS are mainly produced from the exoskeleton of crustaceans and the cell walls of fungi and insects. Traditionally, COS were recommended as a healthy food in Asian countries for their diverse pharmacological effects such as antioxidant, antimicrobial, antitumor and antidiabetic activities[7–10]. In addition, recent studies suggest that COS have potential anti-inflammatory properties *in vivo* and *in vitro*. For example, Song *et al* reported that COS may be a potential immunoadjuvant for the treatment of metastatic tumors[11]. In the studies

* To whom correspondence should be addressed.
E-mail yuchaom@163.com
Received 2010-11-14 Accepted 2011-02-14

by Villiers *et al*, chitosan was found to regulate the balance of dendritic cell-induced IL-10 and IL-12 production[12]. In addition, COS were shown to inhibit the production of nitric oxide, IL-6 and tumor necrosis-α (TNF-α) in activated murine macrophages (RAW264.7)[13, 14]. To the best of our knowledge, however, no studies have been performed to examine the effect of COS on LPS-induced IL-8 production in ECs, which may be helpful for determining the effect of COS in the treatment of vascular diseases.

Human umbilical vein endothelial cells (HUVECs) were demonstrated to be a useful *in vitro* model for studying the expression and regulation of inflammatory cytokines in response to exogenous stimuli[15]. The aim of this study was to explore whether and how COS inhibited IL-8 production in LPS-induced HUVECs. We evaluated the inhibition of IL-8 gene expression by COS in HUVECs at the transcriptional and translational levels. In addition, we assayed the suppressive effects of COS on LPS-induced HUVEC migration and U937 monocyte adhesion to HUVECs. To identify the underling mechanism(s) by which COS inhibits IL-8 over-production in HUVECs, we explored the roles of nuclear factor κB (NF-κB), p38 mitogen-activated protein kinase (MAPK) and phosphokinase Akt after LPS exposure.

Materials and methods

Chemicals and reagents

COS were prepared by our laboratory (the degree of deacetylation was over 95%) and were free of endotoxin according to a limulus amebocyte lysate test[16]. The weight percentages of COS with degrees of polymerization (DP) of 2–6 in an oligo-mixture were 3.7%, 16.1%, 28.8%, 37.2%, and 14.2%, respectively. LPS from *Escherichia coli* and 3-(4,5-dimethylthiazol-2-yl)-2,5-diphenyltetrazolium bromide (MTT) were obtained from Sigma (St Louis, MO, USA). The p38 MAPK inhibitor (SB203580) was purchased from Invitrogen Corporation (Carlsbad, CA, USA). The phosphatidylinositol 3-kinase (PI3K) inhibitor (LY294002), rabbit anti-NF-κB p65 polyclonal antibody and 2′,7′-*bis*-(2-carboxyethyl)-5-(and-6)-carboxyfluorescein, acetoxymethyl ester (BCECF AM) were obtained from Beyotime Institute of Biotechnology (Jiangsu, China). Rabbit anti-p38 MAPK, anti-phospho-p38 (p-p38) MAPK, anti-Akt, anti-phospho-Akt (p-Akt), anti-c-Jun, anti-phospho-c-Jun (p-c-Jun) and anti-GAPDH polyclonal antibodies and horseradish peroxidase (HRP)-conjugated goat anti-rabbit IgG were purchased from Santa Cruz Biotechnology (Santa Cruz, CA, USA). Dulbecco's-modified Eagle's medium F12 (DMEM-F12), RPMI-1640 medium and fetal bovine serum (FBS) were obtained from Gibco (Grand Island, NY, USA).

Cell culture and drug treatment

HUVECs were isolated from normal human umbilical cords, digested with 0.05% trypsin and 0.02% EDTA, and eluted with DMEM-F12. Cells were grown in DMEM-F12 containing 5 units/mL heparin, 30 μg/mL endothelial cell growth supplements, 100 units/mL penicillin, 100 units/mL streptomycin and 10% FBS. At confluence, the cells were subcultured at a 1:3 ratio and then cultured in an atmosphere of 95% air and 5% CO_2 at 37 °C. Passage 2–6 was chosen for experiments. The U937 monocytic cell line from Wuhan Institute of Cell Biology (Wuhan, China) was maintained in RMPI-1640 medium supplemented with 10% FBS and antibiotics.

After reaching sub-confluence, the HUVECs were pretreated with vehicle or COS (50–200 μg/mL) in DMEM-F12 with 1% FBS for 24 h. The cells were then washed with phosphate-buffered saline (PBS, pH 7.4) and exposed to 100 ng/mL of LPS for different time intervals.

Cell viability assay

HUVECs were plated at a density of 5×10^3 cells/well into 96-well plates containing 150 μL of DMEM-F12 with 10% FBS and incubated overnight. Cells were treated with 150 μL of COS (50–200 μg/mL) or LPS (100 ng/mL) in DMEM-F12 with 1% FBS for 24 h. After the treatment, the cells were washed with PBS and incubated with MTT (5 mg/mL) in culture medium with 1% FBS. Following 3 h of incubation at 37 °C, the medium was discarded, and the formazan blue, which formed inside the cells, was dissolved in 100 μL of DMSO. The optical density at 490 nm was determined with a Sunrise Remote Microplate Reader (Grodig, Austria). The cell viability of each well was presented as percentage of the control level.

Reverse transcriptase-polymerase chain reaction (RT-PCR)

Total RNA was extracted from HUVECs using TRIZOL (Takara, Dalian, China). Reverse transcription was performed in 10-μL reaction mixtures containing 1 μg total RNA, 2.5 units AMV reverse transcriptase, 25 pmol oligo-dT primer, 10 nmol dNTP mixture and 20 units RNase inhibitor (Bioer, Hangzhou, China) at 42 °C for 1 h and 95 °C for 5 min. To quantify the IL-8 mRNA expression in HUVECs, RT-PCR was carried out in 20-μL PCR reaction mixtures containing 1 μL cDNA reaction mixture, 10 nmol dNTP mixture, 10 pmol sense and antisense primers, and 2 units BioReady rTaq polymerase (Bioer, Hangzhou, China). The following primers were used for mRNA amplification: IL-8 (292 bp, sense 5′-ATG ACT TCC AAG CTG GCC GTG GCT-3′; antisense 5′-TCT CAG CCC TCT TCA AAA ACT TCT C-3′) and GAPDH (230 bp, sense 5′-CTC TCT GCT CCT CCT GTT CGA CAG-3′; antisense 5′-GTG GAA TCA TAT TGG AAC ATG T-3′). The thermal cycling program was as follows: 4 min at 94 °C for initial denaturation and 30 cycles of 30 s at 94 °C, 30 s at 60 °C for IL-8 and 54 °C for GAPDH, and 30 s at 72 °C. For PCR product analysis, 6 μL of each reaction mixture was electrophoresed on a 1.5% agarose gel containing 1% GoldView™. Band intensities were analyzed with ImageJ software (NIH, USA) and are presented as a percentage of GAPDH expression.

Enzyme-linked immunosorbent assay (ELISA) for IL-8

The concentration of IL-8 in the culture medium was detected with an ELISA kit according to the manufacturer's instructions (R&D Systems, Minneapolis, USA). Briefly, 100 μL of experimental supernatants or IL-8 standard dilution was added into a microplate pre-coated with anti-IL-8 human monoclonal

antibody and incubated for 1.5 h at 37 °C. The microplate was then washed, reacted with detection antibody for 1 h and washed again. Next, horse radish peroxidase (HRP) was added for a 30-min incubation before another wash and subsequent incubation with the substrate solution for 15 min. Finally, the reaction was stopped with 2 mol/L H_2SO_4 and the absorbance of each well was measured at 450 nm using a Sunrise Remote Microplate Reader (Grodig, Austria). The concentration of IL-8 (pg/mL) was acquired by comparing the absorbance values to those obtained from a standard curve.

Wound healing migration assay

HUVECs were seeded at a density of 10^5 cells/well in 24-well plates in DMEM-F12 with 10% FBS. After reaching subconfluency, the cells were pretreated with COS as described above. Subsequently, the cell monolayer was scratched with a pipette tip to obtain a "wounded" zone. The medium and dislodged cells were aspirated, and then the remaining cells were exposed to LPS (100 ng/mL) for 12 h. After incubation, the cells were washed with PBS, fixed with 4% paraformaldehyde, and stained with hematoxylin and eosin. Cell migration was observed, and photos were taken using a phase contrast microscope (Wetzlar, Germany). The number of migrated cells in the wounded area under different experimental conditions was counted using a pre-defined frame.

Monocytic cell adhesion assay

HUVECs were grown in DMEM-F12 with 10% FBS at a density of 10^5 cells/well in 24-well plates. After growth to subconfluence, the cells were pretreated with COS as described above. Following the pretreatment, the cells were washed with PBS and exposed to LPS (100 ng/mL) for 4 h. U937 monocytes were incubated in RPMI-1640 medium containing 10% FBS and 10 μmol/L of fluorescent dye BCECF-AM at 37 °C for 1 h. Fluorescence-labeled U937 cells were washed with PBS twice and seeded at a density of 5×10^4 cells/well onto HUVECs treated with COS and/or LPS. After incubation at 37 °C for 1 h, non-adherent U937 cells were removed by gentle washing with PBS, and the images of random fields were captured using a Leica DMRX microscope (Wetzlar, Germany). The fluorescent intensity of each image was measured with Image-Pro Plus 6.0 software (Media Cybernetics, USA).

Preparation of cell lysates

Nuclear and cytoplasmic fractions were separated using a nuclear and cytoplasmic protein extraction kit (Beyotime, Jiangsu, China). Briefly, cells were washed with ice-cold PBS (pH 7.4), harvested and resuspended in 200 μL lysis buffer A (10 mmol/L Hepes with pH 7.9, 10 mmol/L KCl, 0.1 mmol/L EDTA, 1 mmol/L dithiothreitol, 0.4% Igepal CA-630, 5 μmol/L leupeptin, 2 μmol/L pepstatin A, 1 μmol/L aprotinin and 1 mmol/L phenylmethylsulfonyl fluoride). Following a violent vortex, the obtained lysates were incubated for 10 min on ice and centrifuged at 12 000×*g* for 5 min at 4 °C. The supernatant, consisting of the cytoplasmic fraction, was aliquoted for analysis. The pellets were resuspended in 50 μL nuclear extraction buffer B (20 mmol/L Hepes with pH 7.9, 0.4 mol/L NaCl, 1 mmol/L EDTA, 1 mmol/L dithiothreitol and 1 mmol/L phenylmethylsulfonyl fluoride) and then agitated for 30 min at 4 °C. After centrifugation at 12 000×*g* for 10 min, the supernatant containing nuclear extracts was collected. For isolation of total cell extracts, the cells were lysed in RIPA lysis buffer (50 mmol/L Tris with pH 7.4, 150 mmol/L NaCl, 1% Triton X-100, 1% sodium deoxycholate, 0.1% sodium dodecyl sulfate and 0.05 mmol/L EDTA) for 15 min on ice. The lysates were centrifuged at 12 000×*g* for 10 min at 4 °C, and the supernatants were collected. Protein content of extracted samples was measured using a bicinchoninic acid protein assay kit (BioMed, Beijing, China). All samples were stored at -80 °C until further analysis.

Western blot analysis

To evaluate the expression of target proteins, cell lysates were boiled in 5×loading buffer (125 mmol/L Tris·HCl, pH 6.8, 10% SDS, 8% dithiothreitol, 50% glycerol and 0.5% bromochlorophenol blue) for 10 min. Equal amounts of protein (50 μg) were separated on 8%–12% SDS-polyacrylamide gels and transferred to 0.45 μm polyvinylidene fluoride membranes. The membranes were blocked with 5% skim milk in PBS with 0.1% Tween 20 (PBST) for 1 h and incubated with primary antibodies overnight at 4 °C, including NF-κB p65 (1:250), phosphorylated (p)-p38 (1:500), p38 (1:500), p-Akt (1:1000), Akt (1:1000), c-Jun(1:1000), p-c-Jun (1:1000) and GAPDH (1:1000). Then the membranes were washed with PBST and incubated with HRP-conjugated secondary antibodies for 1 h at room temperature. After the final wash, specific protein bands were visualized using enhanced chemiluminescence reagents (ECL), and densitometric analysis was performed with the use of a PDI Imageware System (Bio-Rad, Hercules, CA, USA).

Statistics

Statistical analyses were performed using SPSS 10.0 package (SPSS Inc, Chicago, IL, USA). Data are represented as means±SD. One-way ANOVA and Student's *t*-tests were performed to determine statistical significance. Values with $P<0.05$ were considered significant.

Results

COS fail to decrease the cell viability of HUVECs

Because COS have been reported to stimulate the growth of normal cells and to induce tumor cell apoptosis[17, 18], their effect on the cell viability of HUVECs was assessed. After treatment with COS (50, 100, and 200 μg/mL) or LPS (100 ng/mL) alone for 24 h, no difference was observed compared to the vehicle-treated group (data not shown), indicating that both COS and LPS at the above concentrations failed to cause cytotoxic effects on HUVECs.

COS inhibit LPS-induced IL-8 expression in HUVECs at the transcriptional and translational levels

To investigate whether COS are capable of inhibiting LPS-induced IL-8 expression in HUVECs at the transcriptional

level, the cells were pretreated with COS as described previously and then exposed to LPS (100 ng/mL) for 4 h. As indicated in Figure 1A, stimulation with LPS caused a 333.7%±36.7% increase in the mRNA level of IL-8 compared to the vehicle-treated group (P<0.01). COS (100 and 200 μg/mL) pretreatment for 24 h significantly inhibited LPS-induced over-expression of IL-8 mRNA (48.9%±2.9% and 47.7%±4.3% of that of the LPS-treated group, respectively, P<0.01).

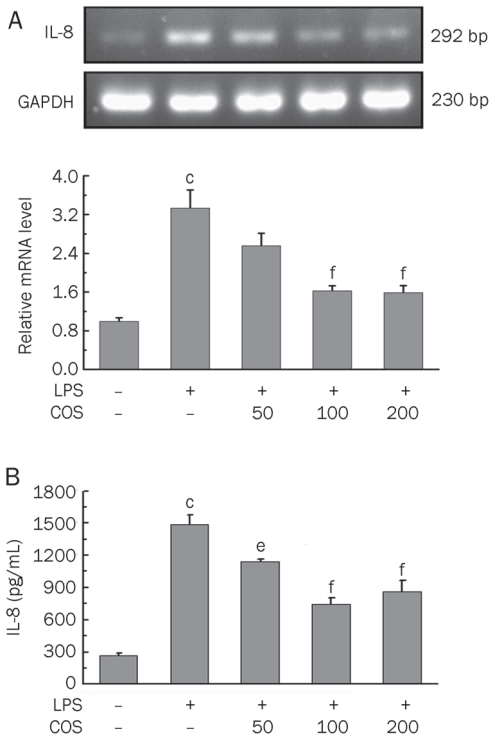

Figure 1. Inhibition of LPS-induced IL-8 expression in HUVECs by COS at transcription and translation levels. (A) Cells were pretreated with COS (50, 100, and 200 μg/mL) for 24 h and then exposed to LPS (100 ng/mL) for 4 h. After treatment, the IL-8 mRNA level was determined by RT-PCR analysis as described in Materials and methods. (B) Cells were pretreated with COS (50, 100, and 200 μg/mL) for 24 h and then exposed to LPS (100 ng/mL) for 8 h. After treatment, the concentration of IL-8 in culture medium was determined by ELISA analysis as described in Materials and methods. Data are expressed as means±SD (n=3). ^{c}P<0.01 compared to the vehicle-treated group; ^{e}P<0.05, ^{f}P<0.01 compared to the LPS-treated group.

The effect of COS on LPS-induced IL-8 secretion in HUVECs was also determined using ELISAs. As expected, we found that the secretion of IL-8 in the supernatant fraction of HUVECs was significantly increased by an LPS (100 ng/mL) challenge for 8 h (550.5%±33.5% of the vehicle-treated group, P<0.01) (Figure 1B), whereas pretreatment with COS (50, 100, and 200 μg/mL) markedly reduced the IL-8 concentration to 77.0%±1.4% (P<0.05), 50.0%±3.8% (P<0.01) and 58.3%±6.4% (P<0.01) of that of the LPS-treated group, respectively.

COS suppress LPS-induced HUVEC migration

To evaluate the suppressive effect of COS on LPS-induced HUVEC migration, a wound-healing method was used with some modifications[19]. As shown in Figure 2, after exposure to LPS (100 ng/mL) for 12 h, the number of cells migrating into the "wounded" zone was increased to 261.0%±20.9% of the vehicle-treated group (P<0.01), whereas COS (50, 100 and 200 μg/mL) pretreatment for 24 h led to a concentration–dependent decrease in HUVEC migration (50 μg/mL, 89.5%±12.5%, P=0.42; 100 μg/mL, 69.8%±4.2%, P<0.05; 200 μg/mL, 62.5%±1.9%, P<0.05, *vs* the LPS-treated group).

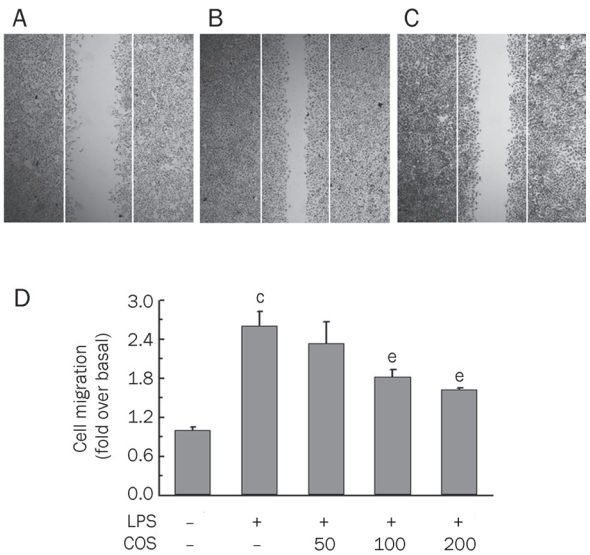

Figure 2. Suppressive effect of COS on LPS-induced HUVEC migration. (A) After wounding of the HUVEC monolayer, cells were stimulated with vehicle for 12 h. (B) After wounding of the HUVEC monolayer, cells were stimulated with LPS (100 ng/mL) for 12 h. (C) After pretreatment with COS (200 μg/mL) for 24 h, the HUVEC monolayer was wounded and then exposed to LPS (100 ng/mL) for 12 h. (D) HUVEC migration was presented as a percentage of the vehicle-treated group. Cells migrated into the denuded area were counted as described in Materials and methods. Data are expressed as means±SD. (n=3). ^{c}P<0.01 compared to the vehicle-treated group; ^{e}P<0.05 compared to the LPS-treated group.

COS inhibit U937 cell adhesion to LPS-induced HUVECs

To determine whether the inhibition of IL-8 expression by COS in LPS-induced HUVECs was associated with a decrease in monocyte adhesion, we assessed U937 cell adhesion to HUVECs challenged by LPS. There was a 348.2%±43.5% increase in the rate of U937 cell adhesion to HUVECs after LPS exposure (100 ng/mL) for 4 h compared to the vehicle-treated group (P<0.01) (Figure 3). When HUVECs were pretreated with COS for 24 h before exposure to LPS, the number of adherent U937 cells was strikingly reduced (50 μg/mL, 60.8%±3.6%, P<0.05; 100 μg/mL, 41.3%±4.1%, P<0.01; 200 μg/mL, 37.2%±1.9%, P<0.01 *vs* the LPS-treated group).

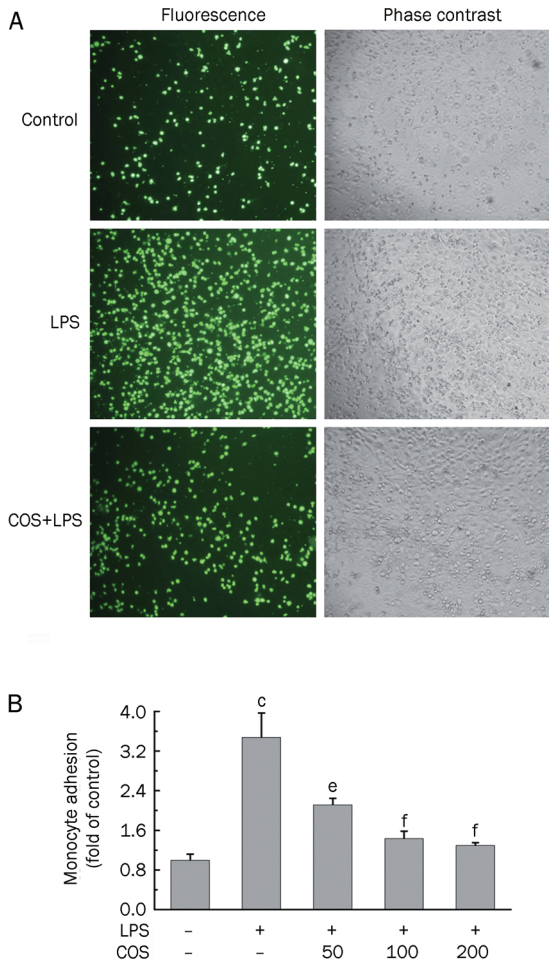

Figure 3. Inhibitory effect of COS on U937 cell adhesion to LPS-induced HUVECs. Cells were pretreated with COS (50, 100, and 200 μg/mL) or vehicle for 24 h, exposed to LPS (100 ng/mL) for 4 h and then incubated with fluorescent-labeled U937 cells for 1 h. (A) Representative fluorescence and phase contrast images of HUVECs were shown. (B) Monocyte adhesion was presented as a percentage of total fluorescent intensity of the vehicle-treated group. Data are expressed as means±SD. (n=3). ^{c}P<0.01 compared to the vehicle-treated group; ^{e}P<0.05, ^{f}P<0.01 compared to the LPS-treated group.

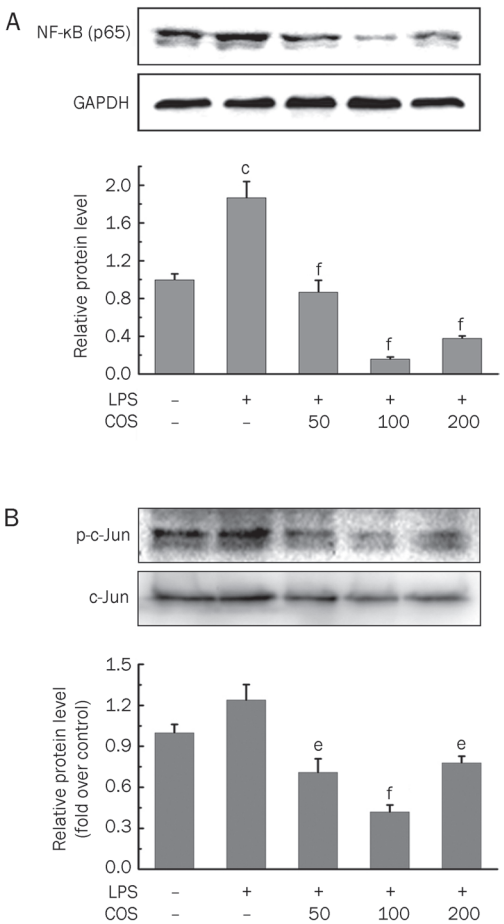

Figure 4. Blocking effect of COS on LPS-induced NF-κB and AP-1 translocation into nucleus of HUVECs. (A) Relative protein levels of NF-κB in nucleus of HUVECs. (B) Relative protein levels of AP-1 in nucleus of HUVECs. Cells were pretreated with COS (50, 100, and 200 μg/mL) for 24 h and then exposed to LPS (100 ng/mL) for 4 h. After treatment, nuclear and cytoplasmic fractions were analyzed for detection of NF-κB by Western blot analysis as described in Materials and methods. Data are representative of three experiments (mans±SD). ^{c}P<0.01 compared to the vehicle-treated group; ^{e}P<0.05, ^{f}P<0.01 compared to the LPS-treated group.

COS display a blocking effect on LPS-induced NF-κB and AP-1 translocation into the nuclei of HUVECs

Because increased expression of IL-8 is known to be associated with the activation of NF-κB and AP-1[20, 21], we tested the inhibitory effects of COS on LPS-induced nuclear translocation of both transcription factors in HUVECs. As shown in Figure 4A, in comparison to the vehicle-treated group, LPS (100 ng/mL) exposure for 4 h stimulated NF-κB translocation into the nucleus of HUVECs, as indicated by an increased protein level of NF-κB p65 in the nucleus (187.5%±16.9%, P<0.01). However, this translocation was remarkably down-regulated by COS pretreatment for 24 h (50 μg/mL, 46.6%±6.5%, P<0.01; 100 μg/mL, 8.8%±1.1%, P<0.01; 200 μg/mL, 20.1%±1.2%, P<0.01, *vs* the LPS-treated group). In parallel, COS pretreatment also suppressed LPS-induced AP-1 activation in the nucleus of HUVECs, which was presented as the relative expression of c-Jun, a major component of AP-1 (50 μg/mL, 56.9%±8.0%, P<0.05; 100 μg/mL, 34.0%±4.1%, P<0.01; 200 μg/mL, 63.1%±3.9%, P<0.05, *vs* the LPS-treated group) (Figure 4B). These results suggest that COS effectively inhibited LPS-induced NF-κB and Ap-1 activation in HUVECs.

COS inhibit LPS-induced over-expression of phosphorylated p38 MAPK and Akt in HUVECs

Next, we determined the effect of COS on the p38 MAPK signaling pathway, which is involved in the regulation of upstream gene expression in HUVECs[22]. The results in Figure 5A show that LPS (100 ng/mL) exposure for 10 min induced a rapid increase in p-p38 protein levels in HUVECs (120.6%±14.5% of the vehicle-treated group, P<0.01). After

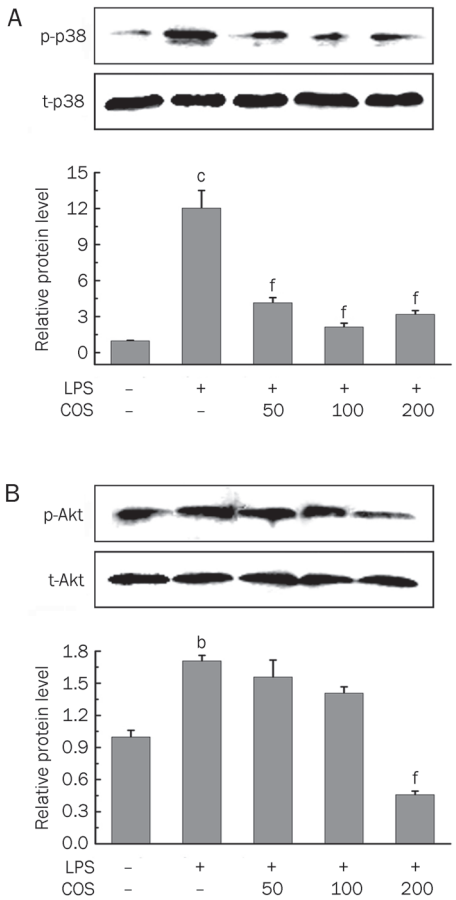

Figure 5. Inhibitory effect of COS on LPS-induced over-expression of phosphorylated p38 MAPK (A) and Akt (B) in HUVECs. Cells were pretreated with COS (50, 100, and 200 μg/mL) for 24 h and then exposed to LPS (100 ng/mL) for 10 min for p38 detection and for 1 h for Akt detection. After treatment, cell lysates were extracted and the protein levels of phosphorylated p38 (p-p38) MAPK, total p38 (t-p38) MAPK, phosphorylated Akt (p-Akt) and total Akt (t-Akt) were determined by Western blot analysis as described in Materials and methods. Data are representative of three experiments (mans±SD). $^{b}P<0.05$, $^{c}P<0.01$ compared to the vehicle-treated group; $^{f}P<0.01$ compared to the LPS-treated group.

pretreatment with COS at concentrations of 50, 100, and 200 μg/mL for 24 h, the level of p-p38 was reduced to 34.6%±3.5% ($P<0.01$), 17.8%±2.5% ($P<0.01$) and 26.6%±2.4% ($P<0.01$) of that of the LPS-treated group, respectively.

Several studies have reported the activation of the phosphatidylinositol 3-kinase (PI3K)/Akt pathway and its contribution to the up-regulated production of inflammatory cytokines in activated endothelial cells[23]. Thus, we analyzed the effect of COS on LPS-induced PI3K/Akt activation in HUVECs. As shown in Figure 5B, the level of p-Akt in HUVECs was increased to 171.5%±10.8% of that of the vehicle-treated group ($P<0.05$) after LPS (100 ng/mL) exposure for 1 h. COS pretreatment for 24 h failed to inhibit LPS-induced Akt phosphorylation from 50 to 100 μg/mL. However, COS at 200 μg/mL exhibited a significant inhibition of p-Akt (26.6%±1.9% of that of the LPS-treated group, $P<0.01$).

p38 MAPK and PI3K inhibitors suppress LPS-induced IL-8 mRNA levels in HUVECs

A p38 inhibitor, SB203580, and a PI3K inhibitor, LY294002, were used in this study to determine whether COS inhibited LPS-induced IL-8 expression in HUVECs through the blockade of the p38 MAPK and PI3K/Akt signaling pathways. When cells were pretreated with SB203580 (25 μmol/L) or LY294002 (50 μmol/L) for 1 h and then challenged with LPS (100 ng/mL) for 4 h, LPS-induced expression of IL-8 mRNA was reduced to 52.4%±2.6% ($P<0.01$) and 56.4%±3.4% ($P<0.05$), respectively, in comparison to the LPS-treated group (Figure 6A and 6B). Additionally, treatment with the inhibitors alone had no effect on IL-8 mRNA expression in HUVECs that were not treated with LPS. These results indicate that the p38 MAPK and PI3K/Akt pathways are required for LPS-induced

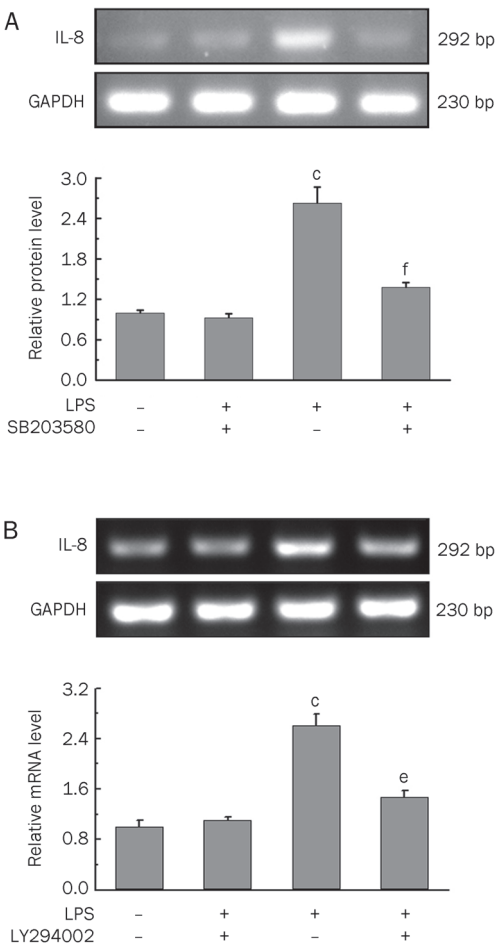

Figure 6. Suppressive effects of p38 MAPK inhibitor, SB203580 (A) and PI3K inhibitor, LY294002 (B) on LPS-induced IL-8 mRNA level in HUVECs. Cells were pretreated with SB203580 (25 μmol/L) or LY294002 (50 μmol/L) for 1 h and then exposed to LPS (100 ng/mL) for 4 h. After treatment, the mRNA expression of IL-8 was analyzed by RT-PCR as described in Materials and methods. Data are representative of three experiments (mans±SD). $^{c}P<0.01$ compared to the vehicle-treated group; $^{e}P<0.05$, $^{f}P<0.01$ compared to the LPS-treated group.

IL-8 expression at the mRNA level.

Discussion

Endothelial dysfunction, the early stage of vasculopathy, is closely related to the vascular inflammatory process, and excessive secretion of pro-inflammatory cytokines released by damaged ECs may indicate a dysregulation of the host defense against invasive stimuli *in vivo*[22]. This view is supported by Papadopoulou *et al* and by Seino *et al*[24, 25], who found that over-expression of IL-8, IL-6, monocyte chemoattractant protein-1 (MCP-1) and other chemokines occurred in ECs and the intima of atherosclerotic lesions. Therefore, the inhibition of IL-8 and other mediators in activated ECs through drugs or specific nutrients might be of great benefit in the maintenance of endothelial homeostasis and the prevention of vascular diseases. Several intervention studies have shown that COS can regulate immune responses by decreasing the production of pro-inflammatory cytokines[12–14]. Our results provide the first evidence that COS inhibit the production of IL-8 in LPS-induced HUVECs through the blockade of the p38 MAPK and PI3K/Akt signaling pathways.

As a key mediator in acute inflammatory responses, IL-8 can be produced in ECs stimulated by IL-1β, TNF-α, LPS, and other infectious agents[23, 26, 27]. In this context, drugs with anti-inflammatory activities have been investigated to ameliorate endothelial damage by limiting the synthesis and release of IL-8. For example, ghrelin, a newly discovered hormone, was verified to inhibit TNF-α-induced IL-8 production in ECs[28]. Moreover, ciprofloxacin, one of the quinolone antibiotics, displayed a suppressive effect on IL-8 mRNA expression in ECs[29]. In this study, we determined the mRNA expression and protein secretion of IL-8 in LPS-induced HUVECs. We found that pre-incubation with COS ameliorated the elevated production of IL-8 by LPS stimulation. Because incubation of COS (50–200 μg/mL) alone for 24 h showed no inhibitory effect on the cell viability of HUVECs, it was apparent that the inhibition of IL-8 production by COS pretreatment was not due to a decrease in cell numbers but to a down-regulation in the cellular production of IL-8. The data support our hypothesis that COS may exert a blunting effect on LPS-induced IL-8 production in ECs.

In the process of vascular inflammation, chemotactic stimuli direct the migration of leukocytes toward damaged vessel walls and the subsequent adhesion to ECs[30]. In addition, activated ECs by themselves can migrate to surrounding tissues to spur the formation of new blood vessels, which is essential for the aggravation of vascular diseases[31]. In experimental studies, LPS has been shown to promote human endothelial cell migration by inducing the activation of related inflammatory cytokines such NF-κB and IL-8, which is the main tissue-derived chemoattractant for leukocytes and partly contributes to the interaction of leukocytes with ECs[32, 33]. Based on these reports, we examined the effects of COS on LPS-induced HUVEC migration and monocyte (U937 cell line) adhesion to HUVECs. As expected, LPS stimulation not only promoted HUVEC migration but also intensified U937 cell adhesion to HUVECs, and these effects were reversed by COS pretreatment. Considering the excessive production of IL-8 in HUVECs challenged by LPS, it can be speculated that COS might lessen LPS-induced HUVEC migration and U937 cell adhesion through inhibition of IL-8 production. Conversely, the study by Park *et al* provided a different observation that chitosan treatment elicited neutrophil migration, which was enhanced with an increasing degree of *N*-acetylation of chitosan[34]. As the *N*-acetylation degree of COS (<1 kDa) used in the present study is below 5%, perhaps it is the different *N*-acetylation degree and different molecular weight between chitosan and COS that led to the opposite pharmaceutical effects in the two observations.

Among the known cell signaling pathways, NF-κB, and AP-1 are two well-studied transcription factors and have been demonstrated to induce the production of inflammatory cytokines such as IL-8, IL-6, and adhesion molecules[27, 35]. In resting cells, NF-κB exists in its canonical form as a p50/p65 heterodimer bound to the inhibitor factor-κB (IκB) in the cytoplasm[36]. In response to extracellular stimulation such as by LPS and TNF-α, the degradation of IκB through proteolysis is initiated, which allows for the translocation of NF-κB from the cytoplasm into the nucleus, where it activates the transcription of target genes[4]. AP-1, a heterodimer formed by the products of the c-Fos and c-Jun, is another nuclear transcription factor that is involved in inflammation by binding to the upstream promoters of inflammatory cytokines[37]. In this study, COS pretreatment suppressed LPS-induced NF-κB and AP-1 activation by reducing the levels of both transcription factors in the nuclei of HUVECs, from which we therefore speculate that the inhibitory effect of COS on IL-8 over-production in LPS-induced HUVECs may result from the suppression of NF-κB and AP-1 activation.

Among the cell signaling pathways in ECs, p38 MAPK and PI3K/Akt are reported to act upstream of NF-κB and AP-1. In the case of TNF-α-induced IκB degradation and subsequent NF-κB activation in HUVECs, a pivotal role for p38 MAPK has been identified[21]. Additionally, p38 activity is necessary for the recruitment of AP-1, which subsequently promotes IL-8 expression[38]. Studies by Isoda *et al* and Kim *et al* showed that the release of pro-inflammatory cytokines was positively related to the activation of NF-κB and AP-1 through the up-regulation of phosphorylated PI3K and Akt levels[27, 39]. Hence, we assessed the effect of COS on LPS-induced phosphorylation of p38 MAPK and Akt. Our findings suggest that COS pretreatment suppressed the phosphorylation of these two pro-inflammatory kinases in HUVECs challenged by LPS. More importantly, the LPS-induced IL-8 mRNA expression was partially, but significantly, inhibited by pretreatment with specific inhibitors of p38 MAPK (SB203580) and PI3K (LY294002), implying a critical role for both signaling pathways in the regulation of IL-8 expression[40, 41]. On the other hand, the partial effects of SB203580 and LY294002 also revealed potential roles for other signaling pathways. Taken together, these results might indicate that COS blocked LPS-induced signal transduction of IL-8 in HUVECs at least partly

by suppressing the phosphorylation of p38 MAPK and Akt and the translocation of NF-κB and AP-1.

Binding of COS to a specific receptor is thought to be a prerequisite for enhancing cell activation[42]. In studies by Feng *et al*, oligochitosan was found to interact with the mannose receptor in macrophages and was subsequently internalized into cells[43]. Regretfully, it remains to be determined whether COS can also be internalized into HUVECs and, if so, which membrane molecules are involved in COS-mediated inhibition of pro-inflammatory cytokine production. These puzzling presumptions indicate that the action of COS on endothelial cells may be complex, and further efforts are required to explore the underlying mechanisms by which COS exert their anti-inflammatory effects.

In conclusion, our investigation demonstrated that COS exerted an inhibitory effect on LPS-induced IL-8 expression in HUVECs at the transcriptional and translational levels. Furthermore, COS inhibited LPS-induced HUVEC migration and U937 monocyte adhesion to HUVECs. Signal transduction studies suggest that COS act by interfering with the phosphorylation of p38 MAPK and Akt and the translocation of NF-κB and AP-1. Our findings underscore a role of COS in ameliorating endothelial dysfunction by exogenous insults to the vasculature.

Acknowledgements

This work was supported by the National Programs for High Technology Research and Development (863 Programs, 2006AA100313 and 2007AA10Z343), the Major National Sci-Tech Projects (2009ZX09501-011) and by the Science Fund of Chongqing Medical University, China (XBZD200806).

Author contribution

Yu-guang DU and Chao YU designed the experiments; Hong-tao LIU, Pei HUANG, and Pan MA performed the research; Qi-shun LIU analyzed the data; and Hong-tao LIU wrote the paper.

References

1 Schumann RR, Pfeil D, Lamping N, Kirschning C, Scherzinger G, Schlag P, *et al*. Lipopolysaccharide induces the rapid tyrosine phosphorylation of the mitogen-activated protein kinases erk-1 and p38 in cultured human vascular endothelial cells requiring the presence of soluble CD14 Blood; 1996; 87: 2805–14.

2 Zhu YM, Azahri NS, Yu DC, Woll PJ. Effects of COX-2 inhibition on expression of vascular endothelial growth factor and interleukin-8 in lung cancer cells. BMC Cancer 2008; 8: 218.

3 Anand AR, Cucchiarini M, Terwilliger EF, Ganju RK. The tyrosine kinase Pyk2 mediates lipopolysaccharide-induced IL-8 expression in human endothelial cells. J Immunol 2008; 180: 5636–44.

4 Oh GS, Pae HO, Choi BM, Lee HS, Kim IK, Yun YG, *et al*. Penta-O-galloyl-beta-*D*-glucose inhibits phorbol myristate acetate-induced interleukin-8 [correction of intereukin-8] gene expression in human monocytic U937 cells through its inactivation of nuclear factor-kappaB. Int Immunopharmacol 2004; 4: 377–86.

5 Hashimoto S, Gon Y, Matsumoto K, Maruoka S, Takeshita I, Hayashi S, *et al*. Selective inhibitor of p38 mitogen-activated protein kinase inhibits lipopolysaccharide-induced interleukin-8 expression in human pulmonary vascular endothelial cells. J Pharmacol Exp Ther 2000; 293: 370–5.

6 Harish Prashanth KV, Tharanathan RN. Depolymerized products of chitosan as potent inhibitors of tumor-induced angiogenesis. Biochim Biophys Acta 2005; 1722: 22–9.

7 Mendis E, Kim MM, Rajapakse N, Kim SK. An *in vitro* cellular analysis of the radical scavenging efficacy of chitooligosaccharides. Life Sci 2007; 80: 2118–27.

8 Xu JG, Zhao XM, Han XW, Du YG. Antifungal activity of oligochitosan against *Phytophthora capsici* and other plant pathogenic fungi *in vitro*. Pestic Biochem Phys 2007: 220–8.

9 Nam KS, Shon YH. Suppression of metastasis of human breast cancer cells by chitosan oligosaccharides. J Microbiol Biotechnol 2009; 19: 629–33.

10 Yuan WP, Liu B, Liu CH, Wang XJ, Zhang MS, Meng XM, *et al*. Anti-oxidant activity of chito-oligosaccharides on pancreatic islet cells in streptozotocin-induced diabetes in rats. World J Gastroenterol 2009; 15: 1339–45.

11 Song S, Zhou F, Nordquist RE, Carubelli R, Liu H, Chen WR. Glycated chitosan as a new non-toxic immunological stimulant. Immunopharmacol Immunotoxicol 2009; 31: 202–8.

12 Villiers C, Chevallet M, Diemer H, Couderc R, Freitas H, Van Dorsselaer A, *et al*. From secretome analysis to immunology: chitosan induces major alterations in the activation of dendritic cells via a TLR4-dependent mechanism. Mol Cell Proteomics 2009; 8: 1252–64.

13 Wu GJ, Tsai GJ. Chitooligosaccharides in combination with interferon-gamma increase nitric oxide production via nuclear factor-kappaB activation in murine RAW264.7 macrophages. Food Chem Toxicol 2007; 45: 250–8.

14 Yoon HJ, Moon ME, Park HS, Im SY, Kim YH. Chitosan oligosaccharide (COS) inhibits LPS-induced inflammatory effects in RAW 264.7 macrophage cells. Biochem Biophys Res Commun 2007; 358: 954–9.

15 Lidington EA, Moyes DL, McCormack AM, Rose ML. A comparison of primary endothelial cells and endothelial cell lines for studies of immune interactions. Transpl Immunol 1999; 7: 239–46.

16 Zhang H, Du Y, Yu X, Mitsutomi M, Aiba S. Preparation of chitooligosaccharides from chitosan by a complex enzyme. Carbohydr Res 1999; 320: 257–60.

17 Dou JL, Tan CY, Du YG, Bai XF, Wang KY, Ma XJ. Effects of chitooligosaccharides on rabbit neutrophils *in vitro*. Carbohyd Polym 2007; 69: 209–13.

18 Xu QS, Dou JL, Wei P, Tan CY, Yun XJ, Wu YH, *et al*. Chitooligosaccharides induce apoptosis of human hepatocellular carcinoma cells via up-regulation of Bax. Carbohyd Polym 2008; 71: 509–14.

19 Shen J, DiCorleto PE. ADP stimulates human endothelial cell migration via P2Y1 nucleotide receptor-mediated mitogen-activated protein kinase pathways. Circ Res 2008; 102: 448–56.

20 Madi A, Lakhdari O, Blottière HM, Guyard-Nicodème M, Le Roux K, Groboillot A, *et al*. The clinical *Pseudomonas* fluorescens MFN1032 strain exerts a cytotoxic effect on epithelial intestinal cells and induces Interleukin-8 via the AP-1 signaling pathway. BMC Microbiol 2010; 10: 215.

21 Bowie AG, O'Neill LA. Vitamin C inhibits NF-kappa B activation by TNF via the activation of p38 mitogen-activated protein kinase. J Immunol 2000; 165: 7180–8.

22 Dauphinee SM, Karsan A. Lipopolysaccharide signaling in endothelial cells. Lab Invest 2006; 86: 9–22.

23 Huang NL, Chiang SH, Hsueh CH, Liang YJ, Chen YJ, Lai LP. Metformin inhibits TNF-alpha-induced IkappaB kinase phosphorylation, IkappaB-alpha degradation and IL-6 production in endothelial cells through

PI3K-dependent AMPK phosphorylation. Int J Cardiol 2009; 134: 169–75.
24 Papadopoulou C, Corrigall V, Taylor PR, Poston RN. The role of the chemokines MCP-1, GRO-alpha, IL-8 and their receptors in the adhesion of monocytic cells to human atherosclerotic plaques. Cytokine 2008; 43: 181–6.
25 Seino Y, Ikeda U, Ikeda M, Yamamoto K, Misawa Y, Hasegawa T, *et al*. Interleukin 6 gene transcripts are expressed in human atherosclerotic lesions. Cytokine1994; 6: 87–91.
26 Bierhaus A, Chen J, Liliensiek B, Nawroth PP. LPS and cytokine-activated endothelium. Semin Thromb Hemost 2000; 26: 571–87.
27 Isoda K, Young JL, Zirlik A, MacFarlane LA, Tsuboi N, Gerdes N, *et al*. Metformin inhibits proinflammatory responses and nuclear factor-kappaB in human vascular wall cells. Arterioscler Thromb Vasc Biol 2006; 26: 611–7.
28 Li WG, Gavrila D, Liu X, Wang L, Gunnlaugsson S, Stoll LL, *et al*. Ghrelin inhibits proinflammatory responses and nuclear factor-kappaB activation in human endothelial cells. Circulation 2004; 109: 2221–6.
29 Galley HF, Dhillon JK, Paterson RL, Webster NR. Effect of ciprofloxacin on the activation of the transcription factors nuclear factor kappaB, activator protein-1 and nuclear factor-interleukin-6, and interleukin-6 and interleukin-8 mRNA expression in a human endothelial cell line. Clin Sci (Lond) 2000; 99: 405–10.
30 Baggiolini M, Clark-Lewis I. Interleukin-8, a chemotactic and inflammatory cytokine. FEBS Lett 1992; 307: 97–101.
31 Folkman J. Tumor angiogenesis: therapeutic implications. N Engl J Med 1971; 285: 1182–6.
32 Kim TH, Bae JS. *Ecklonia cava* extracts inhibit lipopolysaccharide induced inflammatory responses in human endothelial cells. Food Chem Toxicol 2010; 48: 1682–7.
33 Jang SI, Kim YJ, Kim HJ, Lee JC, Kim HY, Kim YC, *et al*. Scoparone inhibits PMA-induced IL-8 and MCP-1 production through suppression of NF-kappaB activation in U937 cells. Life Sci 2006; 78: 2937–43.
34 Park CJ, Gabrielson NP, Pack DW, Jamison RD, Wagoner Johnson AJ. The effect of chitosan on the migration of neutrophil-like HL60 cells, mediated by IL-8. Biomaterials 2009; 30: 436–44.
35 Abdel-Malak NA, Srikant CB, Kristof AS, Magder SA, Di Battista JA, Hussain SN. Angiopoietin-1 promotes endothelial cell proliferation and migration through AP-1-dependent autocrine production of interleukin-8. Blood 2008; 111: 4145–54.
36 Luppi P, Cifarelli V, Tse H, Piganelli J, Trucco M. Human C-peptide antagonises high glucose-induced endothelial dysfunction through the nuclear factor-kappaB pathway. Diabetologia 2008; 51: 1534–43.
37 Allison CC, Kufer TA, Kremmer E, Kaparakis M, Ferrero RL. *Helicobacter pylori* induces MAPK phosphorylation and AP-1 activation via a NOD1-dependent mechanism. J Immunol 2009; 183: 8099–109.
38 Ferreiro I, Barragan M, Gubern A, Ballestar E, Joaquin M, Posas F. The p38 SAPK is recruited to chromatin via its interaction with transcription factors. J Biol Chem 2010; 285: 31819–28.
39 Kim JE, Son JE, Jung SK, Kang NJ, Lee CY, Lee KW, *et al*. Cocoa polyphenols suppress TNF-α-induced vascular endothelial growth factor expression by inhibiting phosphoinositide 3-kinase (PI3K) and mitogen-activated protein kinase kinase-1 (MEK1) activities in mouse epidermal cells. Br J Nutr 2010; 104: 957–64.
40 Guan SM, Zhang M, He JJ, Wu JZ. Mitogen-activated protein kinases and phosphatidylinositol 3-kinase are involved in *Prevotella intermedia*-induced proinflammatory cytokines expression in human periodontal ligament cells. Biochem Biophys Res Commun 2009; 386: 471–6.
41 Kuntz S, Kunz C, Rudloff S. Carbonyl compounds methylglyoxal and glyoxal affect interleukin-8 secretion in intestinal cells by superoxide anion generation and activation of MAPK p38. Mol Nutr Food Res 2010; 54: 1458–67.
42 Porporatto C, Bianco ID, Riera CM, Correa SG. Chitosan induces different *L*-arginine metabolic pathways in resting and inflammatory macrophages. Biochem Biophys Res Commun 2003; 304: 266–72.
43 Feng J, Zhao L, Yu Q. Receptor-mediated stimulatory effect of oligochitosan in macrophages. Biochem Biophys Res Commun 2004; 317: 414–20.

Acta Pharmacologica Sinica (2011) 32: 487–494
 1671-4083/11 $32.00
www.nature.com/aps

Original Article

Contractile effect of tachykinins on rabbit small intestine

Marta Sofía VALERO, Diego Santos FAGUNDES, Laura GRASA, María Pilar ARRUEBO, Miguel Ángel PLAZA, María Divina MURILLO*

Departamento de Farmacología y Fisiología (Fisiología), Facultad de Veterinaria, Universidad de Zaragoza, Miguel Servet 177, 50013 Zaragoza (Spain)

Aim: To study the role of the tachykinin receptors in spontaneous contractions of longitudinal and circular smooth muscle from rabbit small intestine and to determine the mechanism of action of Substance P (SP).
Methods: Rabbit duodenum, jejunum and ileum segments were prepared. The spontaneous contractions of longitudinal and circular smooth muscle were recorded using a computer via an isometric force transducer. The specific agonists and antagonists of tachykinin receptors were added into the organ bath.
Results: The agonists of tachykinin NK1 receptor (SP and [Sar9] SP), NK2 receptor (NKA and (β-Ala8)-NKA), and NK3 receptor (NKB and Senktide) all induced contractions in the small intestine. The contractions were diminished by NK1 receptor antagonist L-733,060, NK2 receptor antagonist GR-94800, and NK3 receptor antagonist SB 218795. Contractions caused by SP were also reduced by atropine, verapamil, PKC inhibitor staurosporine, and PLC inhibitor U73122.
Conclusion: Ttachykinin NK1, NK2, and NK3 receptors mediate the contractions of the smooth muscle in rabbit intestine. Furthermore, SP acts directly on smooth muscle cells through the tachykinin NK1 receptor.

Keywords: tachykinin receptors; substance P; small intestine; rabbits; staurosporine; U73122; L-733,060; GR-94800; SB 218795

Acta Pharmacologica Sinica (2011) 32: 487–494; doi: 10.1038/aps.2010.227; published online 28 Mar 2011

Introduction

Tachykinins (TKs) are a family of neuropeptides distributed throughout the mammalian central and peripheral nervous systems. TKs act as neurotransmitters on neurons and cells (such as smooth muscle, secretory epithelium, and glands) in the gastrointestinal tract of mammals[1–3]. They are important excitatory neurotransmitters in the enteric nervous system, are involved in the coordination of gastrointestinal motility, and are powerful spasmogens in almost every region of the mammalian intestine[1–6]. Substance P (SP), neurokinin A (NKA) and neurokinin B (NKB) are tachykinins derived from two preprotachykinin (PPT) genes[1, 7–10]. Substance P and neurokinin A (NKA) are present in neurons of the enteric nervous system, where they appear to coexist with acetylcholine (ACh)[11]. SP, NKA, and NKB contract nearly all parts of the gastrointestinal tract, acting on different types of receptors[4, 12].

Receptors of TKs have been implicated in normal, defensive, and pathological gastrointestinal (GI) functions[13–16]. The three types of tachykinin receptors, which have been identified based on their genomic and molecular structure, are currently termed NK1, NK2, and NK3 tachykinin receptors[1]. They are heterogeneously distributed within each species. The tachykinin NK1 receptor is widely expressed in the nervous system at both the central and the peripheral level, and it is present in neurons, muscle, and different types of immune cells[2, 3]. The tachykinin NK2 receptor is detected primarily in the periphery nerves, and its expression in the central nervous system (CNS) appears to be restricted to specific brain nuclei[3, 17]. Tachykinin NK1, NK2, and/or their receptors are expressed by neurons, interstitial cells of Cajal, intestinal muscle, epithelium, vasculature and the immune system in a cell-specific, region-specific, and species-specific manner[1, 15, 18, 19]. In contrast, the tachykinin NK3 receptor is primarily expressed in the CNS and has been detected only in certain peripheral tissues, such as human and rat uterus, rat mesenteric vein, and certain enteric neurons from the gut of various species[15, 20, 21].

TKs influence gastrointestinal motor activity not only through their direct effect on the muscle but also through their action on other motility-regulating systems[8]. The aims of this work were to study *in vitro* the role of tachykinin receptors on

* To whom correspondence should be addressed.
E-mail dmurillo@unizar.es
Received 2010-06-19 Accepted 2010-12-17

spontaneous contractions of longitudinal and circular smooth muscle from rabbit small intestine using specific agonists and antagonists of each tachykinin receptor as well as to determine the mechanism of action of SP.

Materials and methods

Male New Zealand rabbits weighing 2–2.5 kg were maintained at a constant temperature (22 °C) with standard rabbit fodder and free access to water. The equipment used and the handling and sacrifice of animals complied with European Council legislation 86/609/EEC concerning experimental animal protection. The experimental protocols were approved by the Ethical Committee of the University of Zaragoza (Spain).

Solutions and substances

The Krebs solution contained the following (in mmol/L): NaCl 120, KCl 4.7, $CaCl_2$ 2.4, $MgSO_4$ 1.2, $NaHCO_3$ 24.5, KH_2PO_4 1, and glucose 5.6 at 37 °C to achieve pH 7.4. Some experiments were conducted with a Ca^{2+}-free Krebs solution from which $CaCl_2$ was omitted and to which EGTA 0.5 mmol/L was added.

Acetylcholine (ACh), atropine, guanethidine, verapamil, hexamethonium, N^{ω}-nitro-*L*-arginine (*L*-NNA), ethylene glycol-*bis* (β-aminoethylether)-*N*,*N*′-tetraacetic acid (EGTA), ryanodine, and Substance P (SP) were purchased from Sigma (Madrid, Spain). Neurokinin A (NKA), neurokinin B (NKB), [Sar9] SP, (β-Ala8)-neurokinin A [(β-Ala8)-NKA], [succinyl-Asp6, Me-Phe8]-SP (senktide), and GR-94800 were obtained from American Peptide (Sunnyvale, CA, USA). Tetrodotoxin (TTX), staurosporine, U 73122, L-733060, and SB 218795 were acquired from Tocris (Bristol, UK). Thapsigargin was kindly donated by Alomone Labs (Jerusalem, Israel). All chemicals were of analytical grade. TTX and staurosporine were dissolved in acidic buffer (pH 4.8) and ethanol, respectively. Thapsigargin, ryanodine, and U 73122 were prepared in dimethyl sulphoxide (DMSO). The remaining drugs were dissolved in Milli-Q water. All solutions were stored at -20 °C, and fresh dilutions were made daily.

Preparation of smooth muscle segments

After 24 h of fasting, animals were humanely euthanized by means of a blow to the head. Pieces of rabbit duodenum, jejunum, and ileum were removed, washed, freed from mesenteric attachment, and cut into smaller segments. Whole thickness segments (10 mm long) were suspended in the direction of longitudinal and circular smooth muscle fibers in a thermostatically controlled (37 °C) organ bath (10 mL capacity) containing Krebs solution and were continuously gassed with 95% O_2 and 5% CO_2.

Each segment was connected to an isometric force transducer (Pioden UF1, Graham Bell House, Canterbury, UK) and passively stretched to an initial tension of 20 mN. The signal output of the mechanical activity was amplified, recorded on a computer for later analysis using Mac Lab System/8e computer program (AD Instruments Inc, Milford, MA, USA), and digitized at two samples per second per channel. Prior to testing, segments were allowed to equilibrate in Krebs solution for 60 min.

Experimental protocols

Each experimental protocol was systematically performed on two or three segments of duodenum, jejunum, and ileum taken from the same rabbit and repeated in three or four different animals. Segments that showed no spontaneous activity were discarded; thus, each preparation served as its own control.

Noncumulative concentration-response curves of SP (agonist of NK1, NK2, and NK3 receptors) were established by adding SP (1 nmol/L to 10 μmol/L) to the bath for 3 min.

To identify the tachykinin receptor subtypes, we tested several specific agonists of tachykinin receptors in the bath for 3 min: [Sar9] SP (100 nmol/L, agonist of NK1 receptor), NKA and (β-Ala8)-NKA (100 nmol/L, agonists of NK2 receptor), and NKB and Senktide (100 nmol/L, agonists of NK3 receptor). Furthermore, we assayed L-733060 (1 μmol/L), GR-94800 (100 nmol/L), and SB 218795 (1 μmol/L), antagonists of NK1, NK2, and NK3 receptors, respectively, on SP-invoked contractions. In addition, L-733060, GR-94800, and SB 218795 were assayed on [Sar9] SP-, (β-Ala8)-NKA-, and Senktide-invoked contractions, respectively, in longitudinal and circular muscle of small intestine. The antagonists or inhibitors used in this work were added to the bath 15 min before the respective agonist was added.

To examine neuronal transmission, the segments were incubated with tetrodotoxin (1 μmol/L) or hexamethonium (100 μmol/L) for 15 min before adding [Sar9] SP, (β-Ala8)-NKA, or Senktide.

To investigate cholinergic transmission, segments were incubated with atropine (1 μmol/L); the adrenergic transmission was assessed by incubating segments with atropine (1 μmol/L)+guanethidine (1 μmol/L); neuronal transmission was studied by adding atropine (1 μmol/L)+tetrodotoxin (1 μmol/L), and NO release was studied by incubating the samples with atropine (1 μmol/L)+*L*-NNA (100 μmol/L).

To study the effect of Ca^{2+} on the SP-invoked contractions of longitudinal and circular smooth muscle in the small intestine, segments were exposed to Ca^{2+}-free Krebs solutions containing 0.5 mmol/L EGTA; verapamil (100 nmol/L), a voltage-dependent Ca^{2+}-channel inhibitor; thapsigargin (100 nmol/L), an inhibitor of sarco-endoplasmic reticulum Ca^{2+}-ATPases; or ryanodine (100 nmol/L), an inhibitor of Ca^{2+} release from the sarcoplasmic reticulum. Furthermore, effects of staurosporine (100 nmol/L), a protein kinase C (PKC) inhibitor, and U 73122 (100 nmol/L), a phospholipase C (PLC) inhibitor, on SP-invoked contractions were tested.

Data analysis

All intestinal segments included in the analyses showed spontaneous contractions. The tachykinin receptor agonists' motor responses (MR) were measured in terms of integrated mechanical activity (IMA) per second, expressed as mN/s, and normalized per square millimeter of cross-sectional area

(CSA), as we have previously described[22]. Results were expressed as a percentage of the control values of the various agonists (100%).

Median effective concentration (EC_{50}, the concentration of SP required to produce 50% of the effect) and 95% confidence limits were calculated using a linear least-squares regression.

Values are expressed as means±SEM. Comparisons between means were made using one-way analysis of variance (ANOVA), and *P*-values were verified using the Scheffé *F* test. Differences in *P*-values of <0.05 were considered statistically significant.

Results

Effects of tachykinin receptor agonists on spontaneous motility

Muscle of rabbit duodenum, jejunum and ileum exhibited cyclic, phasic and rhythmic spontaneous contractions *in vitro*[23]. To study the role of the tachykinin receptors in the spontaneous motility of rabbit small intestine, we tested specific agonists of these receptors. SP (1 nmol/L to 10 μmol/L), an NK1, NK2, and NK3 receptor agonist, induced tonic contractions in longitudinal and circular smooth muscle of rabbit duodenum, jejunum, and ileum. These SP-induced contractions were concentration-dependent (Table 1 and Figure 1). The EC_{50} calculated from the noncumulative concentration-response curves in longitudinal and circular smooth muscle, were 40 nmol/L and 160 nmol/L in the duodenum, 120 nmol/L and 200 nmol/L in the jejunum, and 80 nmol/L and 200 nmol/L in the ileum, respectively.

[Sar9] SP (100 nmol/L, NK1 receptor agonist), NKA and (β-Ala-8)-NKA (100 nmol/L, NK2 receptor agonists), and NKB and Senktide (100 nmol/L, NK3 receptor agonists) induced contractions in three segments of the longitudinal and circular muscle of the intestine (Figure 2). We compared the contractile responses of the different agonists with the response to SP (Table 2). [Sar9] SP-evoked contractions were similar to those evoked by SP in both types of smooth muscle of the three segments of small intestine. (β-Ala8)-NKA, NKB, and Senktide invoked weaker contractions than SP in both types of smooth muscle. The order of potency of agonists tested was [Sar9] SP>SP>NKA>NKB>(β-Ala8)-NKA=Senktide (Table 2).

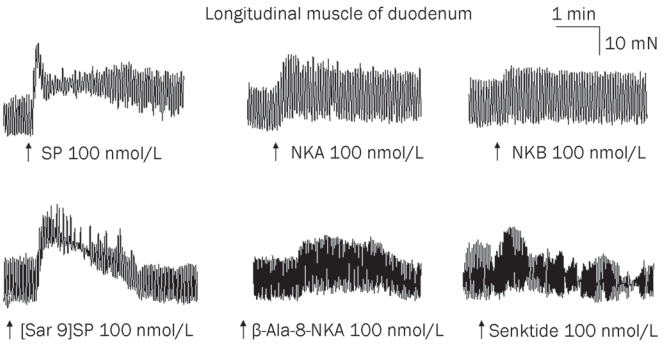

Figure 2. Effect of SP (100 nmol/L), NKA (100 nmol/L), NKB (100 nmol/L), [Sar9] SP (100 nmol/L), (β-Ala-8)-NKA (100 nmol/L), and Senktide (100 nmol/L) on spontaneous contractions in longitudinal smooth muscle of rabbit duodenum. Arrowheads indicate the addition of agents.

Effects of tachykinin receptor antagonists

We also tested the effect of specific antagonists of TK receptors

Table 1. Effects of different doses of substance P (SP). Average values of the motor response ($mN \cdot s^{-1} \cdot mm^{-2}$) to SP of the longitudinal and circular muscle of the duodenum, jejunum and ileum of rabbits. In brackets it expresses in number of segments.

	Duodenum		Jejunum		Ileum	
	L	C	L	C	L	C
SP 1 nmol/L	0.0±0.0 (8)	0.0±0.0 (13)	0.0±0.0 (10)	0.0±0.0 (11)	0.1±0.0 (9)	0.1±0.0 (11)
SP 10 nmol/L	0.0±0.0 (9)	0.0±0.0 (13)	0.0±0.0 (10)	0.0±0.0 (11)	0.0±0.0 (9)	0.0±0.0 (11)
SP 100 nmol/L	0.2±0.0 (9)	0.0±0.0 (13)	0.3±0.1 (10)	0.1±0.0 (11)	0.4±0.1 (9)	0.1±0.0 (11)
SP 1 μmol/L	0.1±0.0 (9)	0.0±0.0 (13)	0.2±0.1 (10)	0.1±0.0 (11)	0.4±0.1 (9)	0.1±0.0 (11)
SP 10 μmol/L	0.1±0.0 (8)	0.1±0.0 (12)	0.5±0.0 (8)	0.2±0.0 (10)	0.5±0.1 (8)	0.1±0.0 (10)

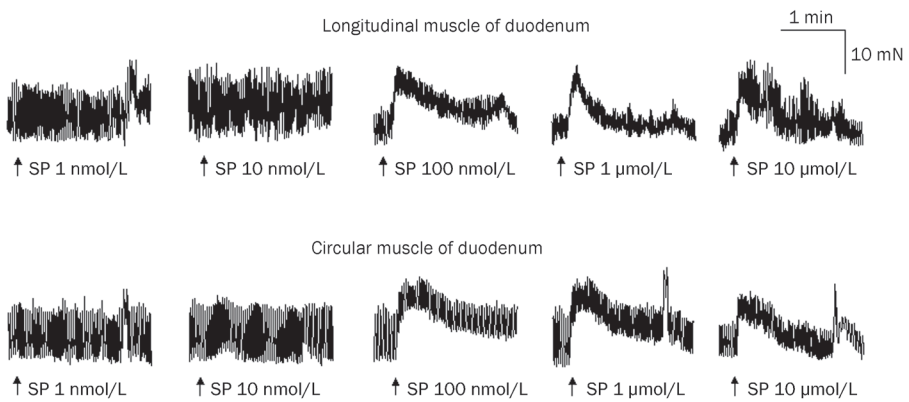

Figure 1. Concentration-dependent effects of SP (1 nmol/L–10 μmol/L) on spontaneous contractions in longitudinal and circular smooth muscle of rabbit duodenum. Arrowheads indicate the addition of agents.

Table 2. Comparison of the effects of [Sar9] SP (100 nmol/L), NKA (100 nmol/L), (β-Ala-8) NKA (100 nmol/L), NKB (100 nmol/L), and Senktide (100 nmol/L) with respect to SP (100 nmol/L, 100%), on contractions of longitudinal (L) and circular (C) smooth muscle of rabbit duodenum, jejunum, and ileum. Values of integrated mechanical activity (% of SP) are the mean±SEM. Numbers in brackets indicate number of segments. $^{c}P<0.01$

	Duodenum		Jejunum		Ileum	
	L	C	L	C	L	C
SP	100 (11)	100 (8)	100 (8)	100 (12)	100 (11)	100 (10)
[Sar9] SP	103.1±15.2 (8)	128.3±28.4 (8)	134.5±29.6 (8)	131.1±21.3(8)	116.2±19.2 (12)	144.1±20.7 (8)
NKA	87.9±4.1 (10)	89.5±8.5 (6)	90.9±2.1 (9)	96.0±2.3 (5)	98.2±5.0 (9)	97.2±3.9 (8)
(β-Ala-8)NKA	15.8±2.3 (8)^{c}	22.4±6.4 (8)^{c}	39.5±7.4 (8)^{c}	17.2±6.4 (8)^{c}	32.8±5.2 (10)^{c}	24.7±8.4 (9)^{c}
NKB	69.1±4.5 (10)^{c}	79.4±12.5 (6)	72.5±4.1 (9)^{c}	91.2±5.1 (5)	73.7±4.8 (14)^{c}	80.2±6.4 (5)
Senktide	26.1±3.4 (10)^{c}	36.3±17.8 (5)	8.9±2.2 (8)^{c}	8.3±2.6 (5)^{c}	6.5±1.0 (9)^{c}	6.9±0.4 (5)^{c}

on the SP-, [Sar9] SP-, (β-Ala8)-NKA-, and Senktide-induced contractions. L-733060 (1 μmol/L), GR-94800 (100 nmol/L), and SB 218795 (1 μmol/L), antagonists of NK1, NK2, and NK3, respectively, reduced contractions caused by SP (100 nmol/L) (Table 3). L-733060 (1 μmol/L) reduced contractions caused by [Sar9] SP (100 nmol/L) in all intestinal segments except for the longitudinal muscle of the ileum (Figure 3A, 3D). GR-94800 (100 nmol/L) reduced contractions caused by (β-Ala8)-NKA (100 nmol/L) in all intestinal segments except for the circular muscle of the duodenum (Figure 3B, 3E). SB 218795 (1 μmol/L) slightly reduced the Senktide-induced contractions (100 nmol/L), although this reduction was only statistically significant for the circular muscle of the ileum (Figure 3C, 3F).

Effects of tetrodotoxin (TTX) and hexamethonium on contractions induced by TK receptor agonists

We examined whether TK receptor agonists act directly on the muscle or indirectly at the nerve level with the use of TTX (1 μmol/L), a blocker of Na^{+} channels in neurons, and hexamethonium (100 μmol/L), a blocker of nicotinic receptors. TTX and hexamethonium reduced the contractions induced by [Sar9] SP (100 nmol/L) in all segments except for the longitudinal muscle of the jejunum (Figure 3A, 3D). TTX and hexamethonium decreased the contractions induced by (β-Ala8)-NKA (100 nmol/L) in the circular muscle of all three intestinal segments (Figure 3E). Hexamethonium, but not TTX, decreased these contractions in the longitudinal muscle (Figure 3B). TTX reduced the contractions induced by Senktide (100 nmol/L) in all intestinal segments except for the jejunum and the longitudinal muscle of the ileum (Figure 3C, 3F). Hexamethonium reduced these contractions in all intestinal segments except for the circular muscle of the jejunum (Figure 3C, 3F).

Effect of atropine, guanethidine, TTX, and *L*-NNA on the effects of SP

To examine the mechanism involved in SP responses, we investigated whether SP acted directly on the muscle or indirectly at the nerve level. Pretreatment of the intestinal segments for 15 min with atropine (1 μmol/L) decreased the SP-induced contractions in longitudinal and circular muscle of the small intestine (Figure 4A, 4B). No additive effects were observed with respect to contractions to SP reduced by atropine (1 μmol/L) when the three intestinal segments were incubated with atropine (1 μmol/L) plus guanethidine (1 μmol/L), atropine (1 μmol/L) plus TTX (1 μmol/L), or atropine (1 μmol/L) plus *L*-NNA (100 μmol/L) (Figures 4A, 4B).

Intracellular mechanisms for the action of SP

SP-induced contractions (100 nmol/L, 3 min) were reduced in Ca^{2+}-free Krebs solution containing 0.5 mmol/L EGTA or in the presence of verapamil (100 nmol/L, 15 min), a voltage-dependent Ca^{2+}-channel inhibitor, in longitudinal and circular muscle of the duodenum, jejunum, and ileum (Figures 5A, 5B). However, incubation of intestinal segments for 15 min

Table 3. Comparison of the effects of different tachykinin receptor antagonists with respect to Substance P. Effect of L-733060 (1 μmol/L), GR-94800 (100 nmol/L), and SB 218795 (1 μmol/L) on SP (100 nmol/L) contractions on longitudinal (L) and circular (C) smooth muscle of rabbit duodenum, jejunum, and ileum. Values of integrated mechanical activity (% of SP) are the mean±SEM. Numbers in brackets indicate number of segments. $^{b}P<0.05$; $^{c}P<0.01$.

	Duodenum		Jejunum		Ileum	
	L	C	L	C	L	C
SP	100 (11)	100 (8)	100 (8)	100 (12)	100 (11)	100 (10)
L-733060+SP	73.7±3.2 (9)^{c}	77.7±2.3 (10)^{c}	70.1±3.4 (8)^{c}	77.6±6.3 (9)^{c}	74.5±7.7 (7)^{c}	96.5±1.1 (7)
GR-94800+SP	74.6±5.5 (6)^{c}	75.9±5.2 (7)^{c}	92.5±3.6 (5)^{b}	86.7±6.2 (7)	85.2±1.4 (5)^{c}	70.9±6.3 (6)^{c}
SB 218795+SP	70.9±6.1 (8)^{c}	79.7±9.1 (8)^{c}	61.5±11.4 (9)^{c}	81.9±1.5 (9)^{c}	71.7±12.5 (8)^{b}	70.7±14.8 (8)

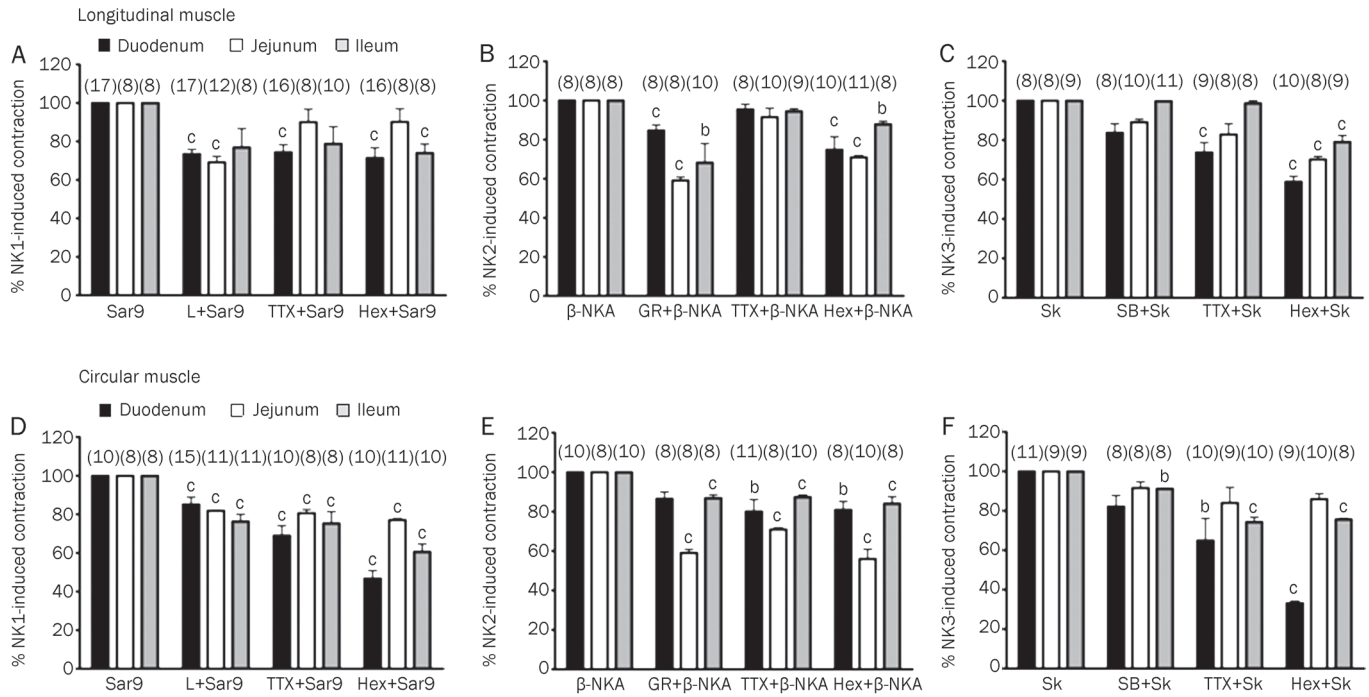

Figure 3. (A and D) Effects of L-733060 (L, 10^{-6} mol/L), tetrodotoxin (TTX, 10^{-6} mol/L), and hexamethonium (Hex, 10^{-4} mol/L) on contractions caused by the agonist of tachykinin NK1, [Sar9] SP (Sar9, 100 nmol/L), in longitudinal and circular smooth muscle from rabbit duodenum, jejunum, and ileum. (B and E) Effects of GR-94800 (GR, 100 nmol/L), TTX, and Hex on contractions caused by the agonist of tachykinin NK2, (β-Ala 8)-NKA (β-NKA, 100 nmol/L), in longitudinal and circular smooth muscle from rabbit duodenum, jejunum, and ileum. (C and F) Effects of SB 218795 (SB, 100 nmol/L), TTX, and Hex on contractions caused by the agonist of tachykinin NK3, Senktide (Sk, 100 nmol/L), in longitudinal and circular smooth muscle from rabbit duodenum, jejunum, and ileum. Columns indicate the mean values of integrated mechanical activity (% of TK agonist), and vertical bars indicate SEM. $^{b}P<0.05$, $^{c}P<0.01$. Numbers in brackets indicate the number of segments.

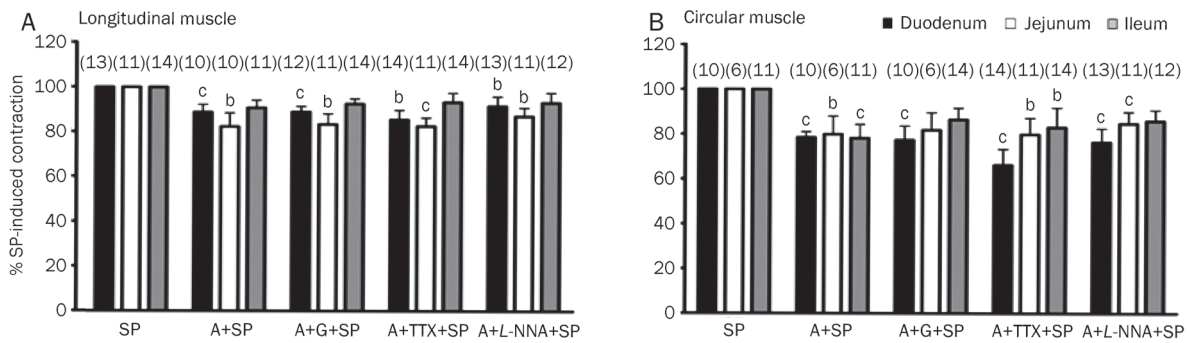

Figure 4. Effect of atropine (A, 1 μmol/L), atropine plus guanethidine (A+G, 1 μmol/L), atropine plus TTX (A+TTX, 1 μmol/L), and atropine (1 μmol/L) plus *L*-NNA (100 μmol/L) (A+*L*-NNA) on contractions caused by SP (100 nmol/L) in longitudinal (A) and circular (B) smooth muscle of rabbit duodenum, jejunum, and ileum. Columns indicate the mean values of integrated mechanical activity (% of SP), and vertical bars indicate SEM. $^{e}P<0.05$, $^{c}P<0.01$. Numbers in brackets indicate the number of segments.

with thapsigargin (100 nmol/L), an inhibitor of sarco-endoplasmic reticulum Ca^{2+}-ATPases, or ryanodine (100 nmol/L), an inhibitor of Ca^{2+} release from sarcoplasmic reticulum, did not change the contractile response to SP (Figures 5A, 5B); however, SP-induced contractions were reduced in the presence of staurosporine (1 μmol/L, 15 min), a PKC inhibitor, and U 73122 (100 nmol/L, 15 min), a PLC inhibitor, in longitudinal and circular muscle of the small intestine (Figures 5A, 5B).

Discussion

In the present study, SP and [Sar9] SP, agonists of the NK1 receptor, invoked contractions in the longitudinal and circular smooth muscle of rabbit small intestine; the contractions were higher in the presence of [Sar9] SP. L-733060, a potent NK1 antagonist, significantly reduced the SP- and [Sar9] SP-induced contractions. This suggests the existence of NK1 receptors that modulate these contractions in the rabbit small

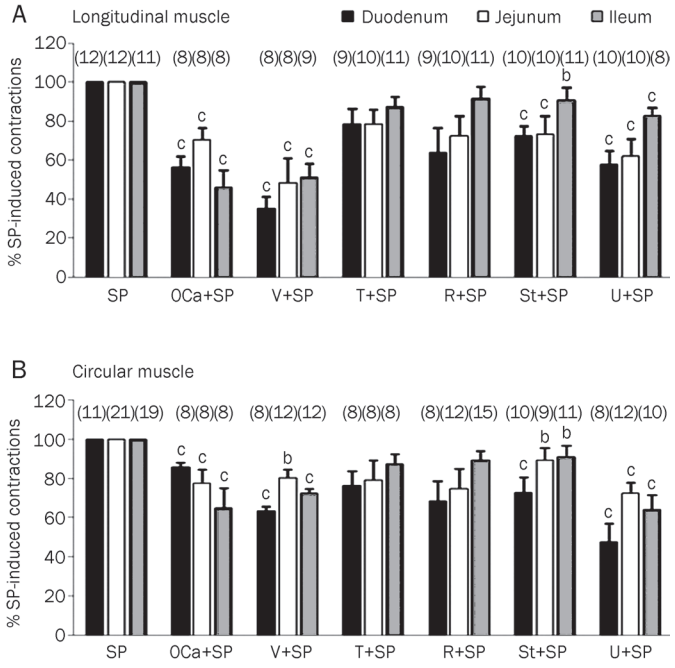

Figure 5. Effect of Ca^{2+}-free solutions containing 0.5 mmol/L EGTA (0Ca), verapamil (V, 100 nmol/L), thapsigargin (T, 100 nmol/L), ryanodine (R, 100 nmol/L), staurosporine (St, 100 nmol/L), and U 73122 (U, 100 nmol/L) on contractions caused by SP (100 nmol/L) in longitudinal (A) and circular (B) smooth muscle of rabbit duodenum, jejunum, and ileum. Columns indicate the mean values of integrated mechanical activity (% of SP), and vertical bars indicate SEM. $^{b}P<0.05$, $^{c}P<0.01$. Numbers in brackets indicate the number of segments.

intestine. Our results agree with other authors' findings that tachykinin NK1 receptors are implicated in intestinal peristalsis[24] and in excitatory nonadrenergic and noncholinergic (NANC) transmission in the mouse ileum[25].

As demonstrated in our experimental model, NKA and (β-Ala8)-NKA, as well as NKB and Senktide, agonists of tachykinin NK2 and NK3 receptors, respectively, invoked contractions in the longitudinal and circular smooth muscle of rabbit small intestine, but these contractions were weaker than those that were SP-invoked. At the same concentrations, NKA and NKB caused stronger contractions than (β-Ala8)-NKA and Senktide. Moreover, GR-94800 and SB 218795, potent and selective NK2 and NK3 antagonists, respectively, diminished SP-invoked contractions, and GR-94800 reduced (β-Ala8)-NKA-invoked contractions. SB 218795 partly reduced contractions caused by Senktide in all of the intestinal segments, although not significantly. In rabbit, peristalsis regulation in the isolated distal colon is most likely mediated by the activation of postjunctional excitatory tachykinin NK1 receptors[24]. NK1 receptors are also implicated in the descending relaxant reflex responses and in ascending contraction[26]. NK1 and NK2 receptors are activated in the contractile responses induced by SP and NKA in canine ileum circular muscle[27] and mediate nonadrenergic, noncholinergic excitatory neurotransmission in hamster ileum[28]. In muscle cells of rat intestine, the coexistence of NK1, NK2, and NK3 tachykinin receptors has been described[29].

In our study, the potency of the agonists tested was ranked as follows: [Sar9] SP>SP>NKA>NKB>(β-Ala8)-NKA=Senktide. This finding is in accordance with other studies for the three subtypes of TK receptors in which the rank order of potency for NK1 receptors was SP=hHK-1≥NKA>NKB, while it is NKA>NKB>SP>hHK-1 (Human hemokinin 1) for the NK2 receptor and NKB>NKA>hHK-1 (Human hemokinin 1)>SP for the NK3 receptor[5, 30–32].

We examined whether the TK receptor agonists act directly on the muscle or indirectly at the nerve level using TTX, a blocker of Na^+ channels in neurons, and hexamethonium, a blocker of nicotinic receptors. TTX and hexamethonium reduced the contractions induced by [Sar9] SP, (β-Ala8)-NKA, and Senktide in longitudinal and circular smooth muscle, suggesting that preganglionar neural pathways are involved. However, the fact that only a small part of the TK agonist response was blocked by TTX or hexamethonium suggests that the main contractility response is due to TK receptors located on smooth muscle cells. Indeed, TTX and hexamethonium do not alter the contractions caused by various TK receptor agonists in the Suncus murinus ileum[6, 33]. Tachykinin NK1, NK2, and/or their receptors have been reported to be expressed by neurons, interstitial cells of Cajal, intestinal muscle, epithelium, vasculature, and the immune system in a cell-specific, region-specific and species-specific manner[1, 3, 18, 19]. In contrast, the tachykinin NK3 receptor is primarily expressed in the central nervous system and has been detected only in certain peripheral tissues, such as the human and rat uterus, the rat mesenteric vein, and certain enteric neurons from the gut of various species[3, 20].

In this study, we investigated the mechanism of action of SP on smooth muscle in rabbit small intestine. SP induced concentration-dependent contractions in longitudinal and circular smooth muscle of the duodenum, jejunum, and ileum. The EC_{50}s in circular muscle were slightly higher than those in longitudinal muscle of the small intestine. These results are in accordance with the contractions caused by SP described in isotonic recordings in longitudinal muscle of rabbit ileum[34].

Our results showed that the contractions induced by SP were reduced in Ca^{2+}-free solutions and in the presence of verapamil, whereas they were not modified in the presence of thapsigargin or ryanodine. These results show that extracellular Ca^{2+} is more important in SP-induced contractions than intracellular Ca^{2+} and that extracellular Ca^{2+} enters the cell through voltage-dependent Ca^{2+} channels. Staurosporine, a PKC inhibitor, and U 73122, a PLC inhibitor, diminished SP-invoked contractions in small intestine longitudinal and circular muscle, suggesting a role for these intracellular messengers. Verapamil reduces the effect of SP on rabbit ileum[34]. Ca^{2+} antagonists such as verapamil, nifedipine, and diltiazem diminish spontaneous activity in sheep duodenum[35]. In murine colonic myocites, SP at low concentrations hyperpolarizes the muscle cells and, at higher concentrations, increases basal cytoplasmic Ca^{2+} concentration by increasing Ca^{2+} influx

through L-type Ca^{2+} channels. Furthermore, nifedipine and GF 109203, a PKC inhibitor, blocked SP-induced effects[36]. NK1 antagonists competitively inhibit the activation of phospholipase C by [Pro9] SP in cultured cortical astrocytes[37]. In previous studies, the amplitude of spontaneous contractions of intestine was diminished by Ca^{2+}-free solutions, verapamil and nifedipine and was increased by thapsigargin and cyclopiazonic acid; however, extracellular and intracellular Ca^{2+} mediate ACh- and KCl-induced contractions[23], and K^+ channels mediate spontaneous contractions in rabbit intestine[38].

In this study, atropine (1 μmol/L) decreased SP-induced contractions in longitudinal and circular muscle of the duodenum, jejunum, and ileum, whereas atropine plus guanethidine, atropine plus TTX (1 μmol/L), or atropine plus *L*-NNA did not invoke additional effects when compared with atropine alone. These results suggest that in SP-invoked contractions, a cholinergic neural pathway is involved through the activation of muscarinic receptors. In contrast, our results do not favor a role of adrenergic and nitrergic pathways because guanethidine and *L*-NNA do not alter SP responses; however, atropine (0.35 μmol/L) or TTX (0.31 μmol/L) added to the bath 2 min before the addition of SP has no impact on SP-induced effects in rabbit ileum[34]. This author tested the short-time effects of atropine on the amplitude of contractions at a lower concentration. Atropine (1 μmol/L) inhibits the velocity of propulsion of rabbit colon, which is mediated by NK2 and reduces the effect of TK receptor agonists in Sancus murinus ileum[33, 39]. Our results are partially consistent with those of other reports where the contractions induced by NK1 agonists were reduced by atropine and augmented by *L*-NNA[25, 40]. These authors propose that excitatory nonadrenergic and non-cholinergic transmission in the circular muscle layer is mediated by tachykinins that principally act on NK1 receptors on cholinergic nerves and smooth muscle cells.

In conclusion, our study demonstrates that tachykinin NK1, NK2, and NK3 receptors invoke contractions in the smooth muscle of rabbit intestine. Furthermore, extracellular Ca^{2+}, PKC, phospholipase C, and cholinergic neurons mediate the contractions caused by SP. We suggest that the SP acts directly on smooth muscle cells through the tachykinin NK1 receptor.

Acknowledgements

This work was supported by the Ministerio de Educación y Ciencia of Spain (AGL2006-04317 and ERDF) and the Grupo de Investigación Consolidado del Gobierno de Aragón (B61/2009, Spain).

Author contribution

María Divina MURILLO designed the study and wrote the paper. Marta Sofía VALERO and Diego Santos FAGUNDES performed research and analyzed data. Laura GRASA wrote the paper. Miguel Angel PLAZA and María Pilar ARRUEBO contributed to the Discussion section of the paper.

References

1 Holzer P, Holzer-Petsche U. Tachykinin receptors in the gut: physiological and pathological implications. Curr Opin Pharmacol 2001; 1: 583–90.
2 Pennefather JN, Lecci A, Candenas ML, Patak E, Pinto FM, Maggi CA. Tachykinins and tachykinin receptors: a growing family. Life Sci 2004; 74: 1445–63.
3 Lecci A, Capriati A, Altamura M, Maggi CA. Tachykinins and tachykinin receptors in the gut, with special reference to NK2 receptors in human. Auton Neurosci 2006; 126–127: 232–49.
4 Bartho L, Holzer P. Search for a physiological role of substance P in gastrointestinal motility. Neuroscience 1985; 16: 1–32.
5 Maggi CA. Principles of tachykininergic co-transmission in the peripheral and enteric nervous system. Regul Pept 2000; 93: 53–64.
6 Maggi CA, Catalioto RM, Criscuoli M, Cucchi P, Giuliani S, Lecci A, *et al*. Tachykinin receptors and intestinal motility. Can J Physiol Pharmacol 1997; 75: 696–703.
7 Nawa H, Hirose T, Takashima H, Inayama S, Nakanishi S. Nucleotide sequences of cloned cDNAs for two types of bovine brain substance P precursor. Nature 1983; 306: 32–6,
8 Holzer P, Holzer-Petsche U. Tachykinins in the gut. Part I. Expression, release and motor function. Pharmacol Ther 1997; 73: 173–217.
9 Hökfelt T, Pernow B, Wahren J. Substance P: a pioneer amongst neuropeptides. J Intern Med 2001; 249: 27–40.
10 Yunker AM, Krause JE, Roth KA. Neurokinin B- and substance P-like immunoreactivity are co-localized in enteric nerves of rat ileum. Regul Pept 1999; 80: 67–74.
11 Costa M, Furness J. Histochemistry of the enteric nervous system. In: Llewellyn-Smith IJ, editor. Physiol Gastrointest Tract 1987; 1: 1–40.
12 Osakada F, Kubo K, Goto K, Kanazawa I, Munekata E. The contractile activities of neurokinin A, B and related peptides on smooth muscles. Eur J Pharmacol 1986; 120: 201–8.
13 Goldhill JM, Shea-Donohue T, Ali N, Piñeiro-Carrero VM. Tachykinergic neurotransmission is enhanced in small intestinal circular muscle in a rabbit model of inflammation. J Pharmacol Exp Ther 1997; 282: 1373–8.
14 Al-Saffar A, Hellstrom PM. Contractile responses to natural tachykinins and selective tachykinin analogs in normal and inflamed ileal and colonic muscle. Scand J Gastroenterol 2001; 36: 485–93.
15 Lecci A, Valenti C, Maggi CA. Tachykinin receptor antagonists in irritable bowel syndrome. Curr Opin Investig Drugs 2002; 3: 589–601.
16 Sanger GJ. Neurokinin NK1 and NK3 receptors as targets for drugs to treat gastrointestinal motility disorders and pain. Br J Pharmacol 2004; 141: 1303–12.
17 Saffroy M, Torrens Y, Glowinski J, Beaujouan JC. Autoradiographic distribution of tachykinin NK2 binding sites in the rat brain: comparison with NK1 and NK3 binding sites. Neuroscience 2003; 116: 761–73.
18 Vannucchi MG, Faussone-Pellegrini MS. NK1, NK2, and NK3 tachykinin receptor localization and tachykinin distribution in the ileum of the mouse. Anat Embryol (Berl) 2000; 202: 247–55.
19 Southwell BR, Furness JB. Immunohistochemical demonstration of the NK(1) tachykinin receptor on muscle and epithelia in guinea pig intestine. Gastroenterology 2001; 120: 1140–51.
20 Fioramonti J, Gaultier E, Toulouse M, Sanger GJ, Bueno L. Intestinal anti-nociceptive behaviour of NK3 receptor antagonism in conscious rats: evidence to support a peripheral mechanism of action. Neurogastroenterol Motil 2003; 15: 363–9.
21 Lecci A, Maggi CA. Peripheral tachykinin receptors as potential therapeutic targets in visceral diseases. Expert Opin Ther Targets 2003; 7: 343–62.

22 Grasa L, Arruebo MP, Plaza MA, Murillo MD. The role of tyrosine kinase in prostaglandin E2 and vanadate-evoked contractions in rabbit duodenum *in vitro*. J Physiol Pharmacol 2006; 57: 279–89.
23 Grasa L, Rebollar E, Arruebo MP, Plaza MA, Murillo MD. The role of Ca^{2+} in the contractility of rabbit small intestine *in vitro*. J Physiol Pharmacol 2004; 55: 639–50.
24 Onori L, Aggio A, Taddei G, Loreto MF, Ciccocioppo R, Vicini R, *et al*. Peristalsis regulation by tachykinin NK1 receptors in the rabbit isolated distal colon. Am J Physiol Gastrointest Liver Physiol 2003; 285: G325–31.
25 De Schepper HU, De Winter BY, Seerden TC, Herman AG, Pelckmans PA, De Man JG. The role of tachykinins in circular muscle contractility of the murine ileum: a functional investigation. Auton Neurosci 2006; 126–127: 273–6.
26 Hahn A, Storr M, Allescher HD. Effect of tachykinins on ascending and descending reflex pathway in rat small intestine. Acta Pharmacol Sin 2002; 23: 289–95.
27 Daniel EE, Parrish MB, Watson EG, Fox-Threlkeld JE, Regoli D, Rainsford KD. The tachykinin receptors inducing contractile responses of canine ileum circular muscle. Am J Physiol 1995; 268: G161–70.
28 El-Mahmoudy A, Matsuyama H, Khalifa M, Shimizu Y, Takewaki T. Tachykinins mediate non-adrenergic, non-cholinergic excitatory neurotransmission to the hamster ileum via NK1 and NK2 receptors. Life Sci 2003; 73: 1939–51.
29 Hellstrom PM, Murthy KS, Grider JR, Makhlouf GM. Coexistence of three tachykinin receptors coupled to Ca^{++} signaling pathways in intestinal muscle cells. J Pharmacol Exp Ther 1994; 270: 236–43.
30 Lordal M, Hellstrom PM. The tachykinins neurokinin A and substance P, but not neurokinin B, stimulate contraction of isolated muscle cells from rat small intestine. Acta Physiol Scand 1999; 166: 75–6.
31 Regoli D, Boudon A, Fauchére JL. Receptors and antagonists for substance P and related peptides. Pharmacol Rev 1994; 46: 551–99.
32 Kurtz MM, Wang R, Clements MK, Cascieri MA, Austin CP, Cunningham BR, *et al*. Identification, localization and receptor characterization of novel mammalian substance P-like peptides. Gene 2002; 296: 205–12.
33 Cheng FH, Chan SW, Rudd JA. Contractile effect of tachykinins on *Suncus murinus* (house musk shrew) isolated ileum. Neuropeptides 2008; 42: 671–9.
34 Holzer P. An enquiry into the mechanism by which substance P facilitates the phasic longitudinal contractions of the rabbit ileum. J Physiol 1982; 325: 377–92.
35 Murillo MD, Plaza MA, de Pedro MJ, Arruebo MP. The effect of Ca^{2+} antagonists on spontaneous motility from sheep duodenum. J Pharm Pharmacol 1994; 46: 138–40.
36 Bayguinov O, Hagen B, Sanders KM. Substance P modulates localized calcium transients and membrane current responses in murine colonic myocytes. Br J Pharmacol 2003; 138: 1233–43.
37 Beaujouan JC, Heuillet E, Petitet F, Saffroy M, Torrens Y, Glowinski J. Higher potency of RP 67580, in the mouse and the rat compared with other nonpeptide and peptide tachykinin NK1 antagonists. Br J Pharmacol 1993; 108: 793–800.
38 Lamarca V, Grasa L, Fagundes DS, Arruebo MP, Plaza MA, Murillo MD, *et al*. K^+ channels involved in contractility of rabbit small intestine. J Physiol Biochem 2006; 62: 227–36.
39 Onori L, Aggio A, Taddei G, Tonini M. Contribution of NK(2) tachykinin receptors to propulsion in the rabbit distal colon. Am J Physiol Gastrointest Liver Physiol 2000; 278: G137–47.
40 De Schepper HU, De Winter BY, Seerden TC, Herman AG, Pelckmans PA, De Man JG. Functional characterisation of tachykinin receptors in the circular muscle layer of the mouse ileum. Regul Pept 2005; 130: 105–15.

Acta Pharmacologica Sinica (2011) 32: 495–502
 1671-4083/11 $32.00
www.nature.com/aps

Original Article

A protective effect of melatonin on intestinal permeability is induced by diclofenac *via* regulation of mitochondrial function in mice

Qiao MEI*, Lei DIAO, Jian-ming XU, Xiao-chang LIU, Juan JIN

Department of Gastroenterology, First Affiliated Hospital of Anhui Medical University, Key Laboratory for Digestive Diseases of Anhui Province, Hefei 230022, China

Aim: This study investigated the effect of intragastrically administered melatonin on intestinal mucosal permeability induced by diclofenac in mice.
Methods: Intestinal mucosal permeability was induced in mice by intragastric administration of diclofenac (2.5 mg/kg). Melatonin was given intragastrically (10 mg/kg) once per day for 3 d after diclofenac administration. The small intestine was examined macroscopically and microscopically for pathologic injury to the intestinal mucosa. Intestinal mucosal permeability was evaluated by Evans blue and FITC-dextran methods. Mitochondrial functional parameters, including mitochondrial membrane potential, mitochondrial ATPase and succinate dehydrogenase (SDH) activity, were assessed. The malondialdehyde (MDA) and myeloperoxidase (MPO) levels were determined from small intestinal mucosal homogenates.
Results: As compared with control mice, the permeability, pathologic score, MDA and MPO levels and ulceration of the intestinal mucosa were increased significantly by diclofenac treatment, and a broadened junctional complex and enlarged intercellular space were observed by transmission electron microscopy (TEM). Melatonin treatment significantly reduced the intestinal mucosal permeability, pathologic score, MDA, and MPO levels and ulceration of the intestinal mucosa. By TEM, the small intestine villus morphology and intercellular spaces were nearly normal in melatonin-treated mice. At the level of the mitochondria, melatonin treatment significantly restored the activities of ATPase and SDH.
Conclusion: The intestinal damage and increased intestinal permeability induced by diclofenac in mice was limited by melatonin; moreover, melatonin preserved several aspects of mitochondrial function.

Keywords: melatonin; intestinal mucosal permeability; mitochondria; diclofenac

Acta Pharmacologica Sinica (2011) 32: 495–502; doi: 10.1038/aps.2010.225; published online 28 Mar 2011

Introduction

Non-steroidal anti-inflammatory drugs (NSAIDs) cause damage to the small intestine. Many clinical and experimental investigations have documented a propensity of diclofenac and other NSAIDs to injure the small intestine, resulting in small intestinal perforation, ulcers, and strictures requiring surgery[1–3]. A recent report on 312 patients who received NSAIDs for rheumatologic conditions, including 166 who received diclofenac, showed a 44% prevalence of enteropathy. Capsule endoscopy presented evidence of macroscopic injury to the small intestine resulting from 2 weeks of slow-release diclofenac ingestion in up to 68% of volunteers[4, 5]. NSAIDs have been linked to the development of serious gastrointestinal side effects, and numerous strategies have been employed to reduce the likelihood of mucosal damage. Various approaches, including proton pump inhibitors and prostaglandin analogues, have been used for this purpose. However, none of these approaches has solved the problem of NSAID-induced gastrointestinal damage.

The pathogenesis of NSAID-induced enteropathy is a multi-stage process involving specific biochemical and subcellular organelle damage followed by an inflammatory tissue reaction. Increased intestinal permeability has been implicated in the pathogenesis of NSAID-induced enteropathy. This altered permeability allows for dietary macromolecules, bile acids, pancreatic juices, bacteria, and other intra-luminal toxins to access the usually intact intestinal epithelium. The increased intestinal permeability is presumably related to cellular damage resulting from energy depletion. Glutamine, a major energy source for the intestinal epithelium, has been

* To whom correspondence should be addressed.
E-mail meiqiaomq@yahoo.com.cn
Received 2010-10-05 Accepted 2010-12-14

shown to play an important role in the protection of the intestinal mucosa against exogenous substance-mediated injury[6]. Thus, it has been hypothesized that glutamine might prevent NSAID-induced changes in intestinal permeability.

Melatonin plays a fundamental role in the neuroimmunoendocrine system[7]. The levels of melatonin and melatonin receptors are highly concentrated in the intestine[8]; melatonin concentrations in the gut are 10–100 times greater than those found in the plasma[9]. Moreover, it has been suggested that the intestine is the major site for extra-pineal melatonin production[10]. Melatonin was found to have a beneficial effect in experimental models of gastric injury, such as ischemia-reperfusion (I/R), ethanol and indomethacin[11–14]. This protection was attributed to melatonin's function as an antioxidant[15–17]; therefore, melatonin may play an important role in the regulation of the intestinal mucosa. Additionally, melatonin has significant anti-apoptotic effects, which could protect the gastric mucosa from NSAID-induced apoptosis and gastropathy and make it useful as a potential therapy against the gastric damage that occurs with NSAID treatment[18]. There is also evidence that melatonin exerts some effect against the pathogenesis associated with NSAID-induced enteropathy[14]. Most previous studies have focused on the protection provided by melatonin against NSAID-related gastric mucosal injury, but there is a shortage of data as to whether melatonin can improve NSAID-related small intestinal mucosa injury. Thus, in the current study, we investigated the protective ability of melatonin in a mouse model of diclofenac-induced enteropathy.

Materials and methods

Mice

Male Kunming mice weighing 20±2 g were supplied by the Experimental Animal Center of Anhui Medical University. The mice were maintained in a controlled environment at (20±1) °C for 1 week with a 12-h light/dark cycle and 50%±5% relative humidity throughout the experimental period. All mice were allowed free access to water and chow diet. The experiments were conducted in accordance with local institutional guidelines for the care and use of laboratory animals.

Reagents

Melatonin, diclofenac, FITC-D, rhodamine 123, and succinate were all purchased from Sigma (Saint Louis, Missouri, USA). Glutamine and acetylcysteine were obtained from Beijing Solarbio Science & Technology Co, Ltd (Beijing, China). Succinate dehydrogenase (SDH), ATPase and kits for assaying malondialdehyde (MDA) and myeloperoxidase (MPO) were obtained from the Nanjing Jiancheng Institute of Biotechnology (Nanjing, China). The other reagents were all of analytical grade.

Induction of small intestinal mucosal injury with diclofenac

Mice were administered diclofenac (2.5 mg/kg) dissolved in 0.2% methylcellulose daily by oral gavage for 3 d. Controls received only the methylcellulose vehicle by gavage.

Treatment schedule

The animals were randomly divided into four groups: the control group, diclofenac-treated group, the glutamine-treated group (1000 mg/kg) and the melatonin-treated group (10 mg/kg). Melatonin and glutamine were given intragastrically (ig) once per day for 3 d beginning 4 h after diclofenac administration. In the control and diclofenac-treated groups, saline was given instead of melatonin. At the end of the experiment, mice were decapitated, and their plasma and intestines were collected for biochemical analyses.

Morphological analyses

The small intestine was removed and fixed in 2% neutral buffered formalin for 24 h and then transferred to 70% ethanol. The mucosa of the small intestine was exposed by cutting along the anti-mesenteric side and pinning it out on a piece of cork for assessment of macroscopic damage. The number and size of ulcers (longest diameter >5 mm) and the areas (mm^2) of visible lesions were measured[19]. A piece of ileum initially fixed in 10% neutral buffered formalin was embedded in paraffin for histological analysis. Full-thickness (5-μm) sections were stained with hematoxylin and eosin and examined microscopically by a pathologist blinded to the treatment groups. The severity of intestinal injury was graded on a scale of 0–4 and expressed as the pathological index according to a standard scoring system[20]. A portion of ileum approximately 0.5 cm from the ileocecal junction that was approximately 1 cm in length was excised with a scalpel. Specimens processed for TEM were fixed in 2.5% glutaraldehyde for 4 h at 4 °C followed by fixation in osmic acid and embedding in Epon. Ultrathin sections were examined with a Hitachi transmission electron microscope.

Determination of intestinal permeability using fluorescein isothiocyanate dextran (FD-4)

Intestinal mucosal permeability to the fluorescent tracer fluorescein isothiocyanate dextran (4000 Da) was determined using the method previously described by Chen *et al*. A 5-cm segment of the ileal sac was ligated beginning at 3 cm proximal to the ileocecal valve, 0.2 mL of PBS (pH 7.4) containing 25 mg/mL FD-4 was injected into the ileal sac with a syringe, and the abdomen was sutured closed. After 30 min, a blood sample (100 μL) was collected from the portal vein and immediately diluted with 1.9 mL of 50 mmol/L Tris (pH 10.3) containing 150 mmol/L chloride natrium. The diluted plasma was centrifuged at 3000×*g* for 10 min, and plasma FD-4 concentrations were determined by fluorescence spectrophotometry at an excitation wavelength of 480 nm and an emission wavelength of 520 nm[21].

Determination of intestinal permeability by Evans blue

Small intestine sacs were prepared as previously described[22]. Briefly, small intestine was incised, and the fecal contents were washed out gently with 2–3 mL of PBS. The proximal and distal intestines were ligated, and 0.2 mL of 1.5% (*w/v*) Evans blue (EB) in PBS was infused into the lumen. The intestinal

sacs were incubated in 20 mL of Krebs buffer at 95% O_2 and 37 °C. They were removed 30 min later, washed three times in 6 mmol/L acetylcysteine, dried on filter paper at 37 °C for 24 h and then incubated with 1 mL of formamide at 50 °C for 24 h. The amount of dye eluted was estimated using a wavelength of 655 nm. The amount of EB permeating into the intestinal wall was calculated based on a standard curve of EB in formamide.

Detection of intestinal homogenates

Dissected intestine were excised, all fat and mesenterium was removed and intestinal mucosal specimens were scraped and cut into pieces using sharp scissors and forceps. The tissue was gently washed and weighed (all samples were approximately 100 mg), homogenated in physiologic saline and temporarily stored at -20 °C prior to detection of MDA content and MPO activity with their respective kits according to the manufacturer's instructions (Nanjing Jiancheng Institute of Biotechnology, Nanjing, China). Protein content was determined by the Lowry method[23].

Preparation of liver mitochondria

Mouse liver mitochondria were isolated and used for these studies because it is exceedingly difficult to obtain a high yield of mitochondria from intestinal tissue[24]. A liver mitochondrial fraction was prepared according to the method described by Schneider and Hogeboom[25]. Briefly, the liver was rapidly removed and placed in ice-cold 0.9% saline, cut into approximately 1-cm^3 pieces and homogenized in 50 mL of ice-cold homogenizing solution [250 mmol/L sucrose, 10 mmol/L Tris-HCl buffer (pH 7.4), 0.5 mmol/L EDTA] by six strokes with a tight-fitting Teflon pestle. The homogenate was then centrifuged at 600×*g* for 10 min, and the resulting supernatant was further centrifuged at 15 000×*g* for 10 min. Finally, the pellet was removed and resuspended in 10 mL of homogenizing solution and centrifuged for 10 min at 15 000×*g* to give the resulting mitochondrial-enriched pellet used for the experiments. All procedures were performed at 4 °C. Mitochondrial protein concentration was determined using Lowry's method. The pellets were resuspended in mitochondria separating medium (pH 7.4) to make a final suspension containing 5 mg/mL mitochondrial proteins, which was stored at -20 °C.

Determination of mitochondrial membrane potential (MMP)

MMP was evaluated from the uptake of rhodamine 123[26], which electrophoretically accumulates into energized mitochondria in response to their internal negative membrane potential. First, 1800 μL of phosphate buffer (250 mmol/L sucrose, 5 mmol/L KH_2PO_4, pH 7.2 at 25 °C), 3 mmol/L succinate and 0.3 μmol/L rhodamine 123 were added to the cuvette, and the scanning fluorescence of the rhodamine 123 was monitored using a fluorescence spectrometer at excitation and emission wavelengths of 503 and 527 nm, respectively. After 30 s, mitochondria (0.5 mg/mL) were added. Finally, the fluorescence intensity of the mitochondria suspension was recorded continuously at 25 °C for 5 min. Each measurement was expressed as a relative value as compared with the baseline intensity.

Measurement of mitochondrial swelling

Mitochondrial swelling was assessed by measuring the change in absorbance of the suspension at 520 nm ($\Delta A_{520\ nm}$) over time according to the procedure described by Hernández-Muñoz *et al*[27]. The standard incubation conditions used for the swelling assay were 250 mmol/L sucrose, 10 mmol/L Tris (pH 7.4), 5 mmol/L succinate, and 0.3 mmol/L $CaCl_2$. Mitochondria (0.5 mg) were suspended in 3.6 mL of phosphate buffer. A quantity of 1.8 mL of this suspension was added to both sample and reference cuvettes; then 6 mmol/L succinate was added to the sample cuvette only, and the $A_{520\ nm}$ scanning was started and recorded continuously at 25 °C for 10 min. The extent of the swelling of the mitochondria was evaluated according to the decrease in values obtained at 520-nm absorption.

Determination of mitochondrial succinate dehydrogenase (SDH) and ATPase activity

The activities of mitochondrial SDH and ATPase were detected according to the instructions provided with their respective kits[28, 29]. The quantity of Pi produced was representative of the activities of the ATPase, with the active unit mmoL (Pi)/(h·mg) protein. SDH activity was expressed as units/mg protein.

Statistical analysis

All results are expressed as mean±SEM. Statistical comparisons were made using a one-way analysis of variance (ANOVA) test. The level of significance was set at P=0.05. All tests were two-sided.

Results

Effect of melatonin on intestinal mucosal injury induced by diclofenac in mice

As compared with the control group, intestinal mucosal injuries, such as edema and small ulcers, were observed macroscopically (P<0.05), and microscopic assessment of the intestinal mucosa showed disarranged villi, epithelial exfoliation, inflammatory cell infiltration and ulceration in the diclofenac group. In contrast, melatonin reduced the observed intestinal mucosal injury both macroscopically and microscopically. Histological scoring based on the Chiu scale showed that melatonin decreased the intestinal damage score significantly in comparison with the diclofenac group (4.8±0.4 *vs* 1.8±0.4). Therefore, melatonin administration protected mice from diclofenac-induced intestinal inflammation and injury (Figure 1).

Effect of melatonin on intestinal mucosal barrier function induced by diclofenac in mice

As compared with the control group (Figure 2A), the intestinal mucosa in the diclofenac group showed a focal reduction in the thinning of the microvillous carpet and the disarrangement of the epithelial surface as viewed by TEM. In addition,

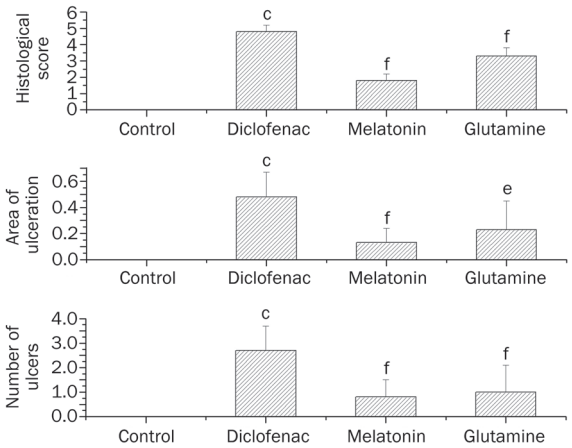

Figure 1. Effects of melatonin on the intestinal mocusal injury induced by diclofenac in mice. Melatonin (10 mg/kg) was given intragastrically (ig) once a day for 3 d at 4 h after diclofenac (2.5 mg/kg) administration. n=8. Mean±SEM. ^{c}P<0.01 *vs* control group. ^{e}P<0.05, ^{f}P<0.01 *vs* diclofenac group.

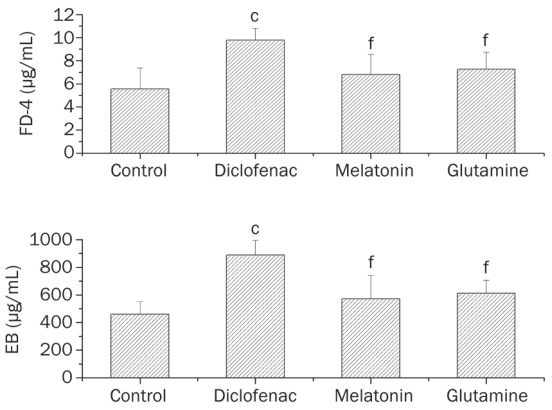

Figure 3. Effects of melatonin on the intestinal mocusal permeability induced by diclofenac in mice. Melatonin (10 mg/kg) was treated intragastrically (ig) once a day for 3 d at 4 h after diclofenac (2.5 mg/kg) administration. n=8. Mean±SEM. ^{c}P<0.01 *vs* control group. ^{f}P<0.01 *vs* diclofenac group. EB: Evans blue; FD-4: fluorescent tracer fluorescein isothiocyanate dextran.

we observed irregular widening of the intercellular space, decurtated and broadened junctional complexes and partially damaged surface epithelium in the diclofenac group (Figure 2B). Melatonin-treated intestine exhibited an attenuation of the surface epithelial damage that was observed in the diclofenac-treated intestine along with a regular microvillous carpet and an improved tight junction structure (Figure 2C). Accordingly, the amount of EB permeating into the intestinal wall and the plasma FD-4 concentrations in diclofenac group were much greater than those recorded in the control group (P<0.01); in contrast, the increases in dye movements were suppressed effectively by melatonin, indicating that melatonin significantly decreased the permeability of the intestinal mucosa (Figure 3).

Effect of melatonin on the MDA and MPO levels in intestinal mucosal homogenates

As shown in Figure 4, the MDA levels of intestinal mucosal homogenates increased in the diclofenac group (1.65±0.32 nmol/mg protein), whereas melatonin significantly decreased MDA production (1.12±0.22 nmol/mg protein). Correspondingly, MPO activity was also increased in the intestinal mucosal homogenates obtained from the diclofenac group (0.236±0.027 U/g homogenate). Melatonin treatment effec-

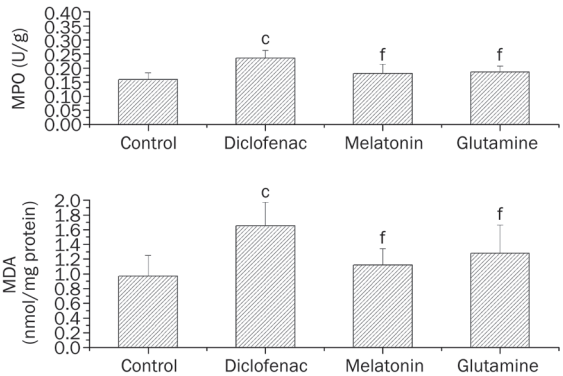

Figure 4. Effects of melatonin on the MDA and MPO levels of intestinal mocusal injury induced by diclofenac in mice. Melatonin (10mg/kg) was treated intragastrically (ig) once a day for 3 d at 4 h after diclofenac (2.5 mg/kg) administration. n=8. Mean±SEM. ^{c}P<0.01 *vs* control group. ^{f}P<0.01 *vs* diclofenac group. MDA: malondialdehyde; MPO: myeloperoxidase.

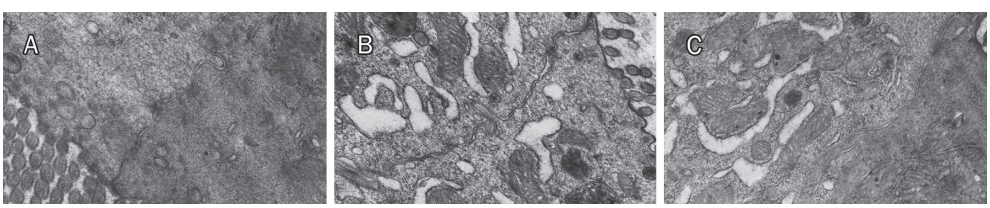

Figure 2. Effects of melatonin on the epithelial ultrastructure morphology of small intestine in the mice under TEM (original magnification ×20 000). (A) Control group; (B) Diclofenac group; (C) Melatonin group (10 mg/kg). Melatonin (10 mg/kg) was given intragastrically (ig) once a day for 3 d at 4 h after diclofenac (2.5 mg/kg) administration. In diclofenac group, reduced and shorter microvillous carpet, irregular widening of the intercellular space, decurtated and broaden junctional complex were observed (B). Melatonin group showed a much more regular and intensive microvillous carpet, and ameliorated tight junction (C).

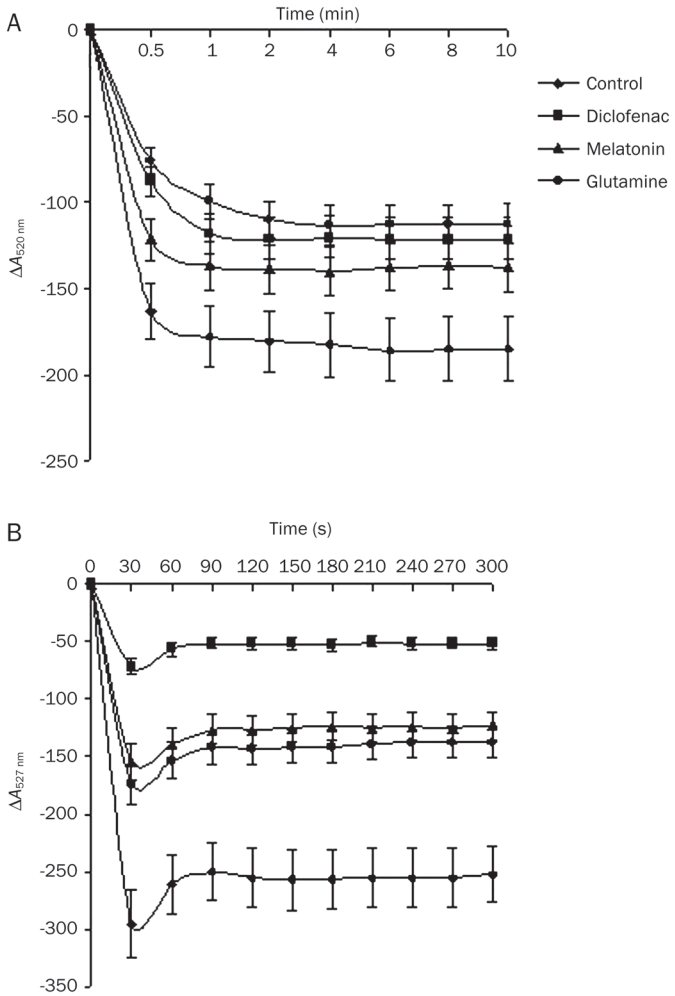

Figure 5. (A) Effect of melatonin on liver mitochondrial swelling after intestinal mucosal injury induced by diclofenac in mice. (B) Effect of melatonin on liver mitochondrial membrane potential after intestinal mucosal injury induced by diclofenac in mice. Melatonin (10 mg/kg) was given intragastrically (ig) once a day for 3 d at 4 h after diclofenac (2.5 mg/kg) administration.

tively inhibited the increase of MPO activity in the intestine (0.181±0.330 U/g homogenate).

Effect of melatonin on liver mitochondrial swelling and MMP in the diclofenac mouse model of intestinal mucosal injury

Mitochondrial permeability transition (MPT) occurrence was assessed by measurement of the resulting large-amplitude swelling. After energizing with succinate, the swelling rate of mitochondria isolated from the diclofenac group was less than that of the control group. The administration of melatonin partly prevented the diclofenac effect on mitochondrial volume. Mitochondria isolated from the control group had a significant reduction in fluorescence intensity by 30 s after adding the reaction solution. The fluorescence intensity of mitochondria isolated from the diclofenac group decreased less than did that of the control group, and melatonin effectively restored

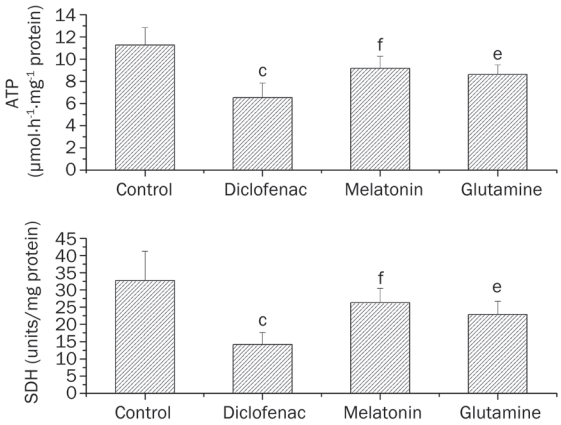

Figure 6. Effects of melatonin on the activities of SDH and ATPase of liver mitochondria after intestinal mocusal injury induced by diclofenac in mice. Melatonin (10 mg/kg) was given intragastrically (ig) once a day for 3 d at 4 h after diclofenac (2.5 mg/kg) administration. n=8. Mean±SEM. ^{c}P<0.01 *vs* control group. ^{e}P<0.05, ^{f}P<0.01 *vs* diclofenac group. ATP: adenosine triphosphate; SDH: succinate dehydrogenase.

the decrease in fluorescence intensity induced by diclofenac. This observation shows that melatonin improved the impaired mitochondrial function that occurred as a result of diclofenac treatment and maintained a normal MMP (Figure 5).

Effect of melatonin on liver mitochondrial SDH and ATPase activities in diclofenac-treated mice

As shown in Figure 6, as compared with the values of the control group, marked decreases in the activities of ATPase and SDH in mitochondria were found in the diclofenac group (P<0.01). Melatonin clearly restored the activities of ATPase and SDH in mitochondria and, thus, contributed to maintenance of a normal energy metabolism.

Discussion

NSAID enteropathy is a frequent complication that occurs upon treatment with diclofenac and other NSAIDs. Newer imaging modalities, such as capsule endoscopy studies, suggest that small bowel erosions may be common in nonselective NSAID users. In two retrospective studies of 268 and 188 patients, hospitalization due to intestinal perforations or hemorrhage were twice as likely to develop in patients on NSAIDs than in controls[30]. Bjarnason *et al*[31] reported that up to 70% of patients receiving long-term NSAID therapy, including diclofenac therapy, developed small intestinal NSAID enteropathy. Numerous studies have demonstrated that an increase in intestinal permeability is the central mechanism that translates biochemical damage to tissue damage in the pathogenesis of NSAID enteropathy. NSAIDs increase intestinal permeability in the human within 24 h of ingestion, and this increase is equally evident when NSAIDs are taken long term[32]. As an alternative to intestinal ulceration, intestinal permeability has been investigated as a method for measuring the level of NSAID-induced gut damage in the rat and

then developed as a method for routine measurement. Consequently, it has become a potential therapeutic target for the prevention of NSAID enteropathy.

Several recent publications have presented evidence that melatonin has a significant protective action against gastrointestinal damage. Furthermore, other studies have shown that melatonin has a beneficial effect in experimental models of gastric injury[33, 34]. This protective effect of melatonin, which is believed to be related to its antioxidant activity, has also been demonstrated in the rat small intestine experimental model of I/R. However, it was not clear whether melatonin could improve NSAID-related small intestinal mucosa injury. In the current study, we found that melatonin treatment protected mice from the intestinal mucosal injury induced by diclofenac. Mice treated with melatonin exhibited significantly reduced numbers of and areas of intestinal ulceration, and histological staining showed that melatonin administration strongly attenuated intestinal inflammation. The beneficial effect of melatonin appeared to be related to its reinforcement of intestinal barrier function, as demonstrated by the attenuation of the diclofenac-induced intestinal permeability and the improvement in the ultrastructure observations of the intestinal mucosa in the melatonin-treated group as compared with the diclofenac-treated group.

Lipid peroxidation is considered a major mechanism of oxygen free radical attack and an indicator for oxidative stress and reactive oxygen species production. Experimental evidence has been presented that connects melatonin to the prevention or treatment of gastrointestinal disorders with the scavenging properties of active oxygen[35]. In separate experiments, cotreatment of rats with melatonin and ranitidine or omeprazole was found to protect against stress ulceration in doses at which none of these alone could protect the stomach. These findings raise the possibility that melatonin, although an effective gastroprotective agent individually, may function even better when used in conjunction with ranitidine or omeprazole. Melatonin likely exerts its gastroprotective effects through direct and indirect antioxidant activities[36–38]. Accordingly, our results demonstrate that melatonin treatment decreased intestinal mucosal oxidative injury induced by diclofenac.

NSAID-induced enteropathy has now been shown to be multifactorial, involving a combination of biochemical events that direct mucosal toxicity, mitochondrial damage, and the breakdown of intercellular integrity. This allows mucosal exposure to luminal damaging agents (bacteria and their degradation products, bile acids, *etc*) with predictable inflammatory reactions. This inflammation varies in intensity from mild to that producing erosions and ulcers. NSAIDs were recently reported to cause mitochondrial injury, resulting in dissipation of the mitochondrial transmembrane potential and induction of a mitochondrial permeability transition pore, which liberates cytochrome *c*[39]. Cytochrome *c* generates reactive oxygen species and thereby triggers the caspase cascade and cellular lipid peroxidation, resulting in cellular apoptosis. The pathogenesis of mitochondrial damage induced by NSAIDs alters intestinal permeability with consequent intestinal damage. Accordingly, our results indicate that melatonin strongly protects against intestinal mucosal injury induced by diclofenac in mice. This protective effect of melatonin appears to be mediated by its action on mitochondria. Melatonin protects against alterations in various mitochondrial bioenergetic parameters associated with NSAIDs. Specifically, we found that melatonin significantly restored the activities of ATPase and SDH in mitochondria, thus helping to maintain a normal energy metabolism. This observation suggests that melatonin improved the impaired mitochondrial function induced by diclofenac and maintained a normal MMP.

A role for melatonin in the improvement of mitochondrial function and an increase in ATP production in different experimental conditions has been widely reported. The results of Kim *et al*[40] suggest that melatonin ameliorates I/R-induced hepatocyte damage by inhibiting the level of oxidative stress and the induction of the apoptotic pathway. The degree of mitochondrial swelling, which reflects the extent of the MPT was greater after 5 h of reperfusion, but this increase was attenuated by melatonin treatment. In this experiment, melatonin limited the release of cytochrome *c* into the cytosol and the activation of caspase-3 observed in I/R rats. Thus, melatonin protected against mitochondrial injury by reducing mitochondrial oxidative stress and improving I/R-induced hepatic energy metabolism[41] and by directly inhibiting formation of the mitochondrial permeability transition pore and reducing the membrane potential[42, 43]. Martín *et al*[44] showed that melatonin counteracted mitochondrial oxidative stress and increased the activity of the mitochondrial oxidative phosphorylation enzymes both *in vivo* and *in vitr*o. Melatonin also increased the production of ATP in control mitochondria. Acuña-Castroviejo *et al* documented that melatonin counteracted mitochondrial oxidative damage induced by *t*-butyl hydroperoxide, recovering glutathione levels and ATP production[45, 46]. These data, along with other findings, suggest that melatonin regulates mitochondrial homeostasis[47].

In conclusion, our results demonstrate that pharmacological concentrations of melatonin strongly protect against the intestinal mucosal injury and ameliorate the increased intestinal permeability induced by diclofenac. The mechanism of protection is likely to be due, at least in part, to the preservation of mitochondrial function mediated by melatonin.

Author contribution

Qiao MEI and Jian-ming XU designed research; Lei DIAO, Xiao-chang LIU, and Juan JIN performed research; Qiao MEI, Lei DIAO and Xiao-chang LIU analyzed data; Lei DIAO wrote the paper.

References

1 Fortun PJ, Hawkey CJ. Nonsteroidal antiinflammatory drugs and the small intestine. Curr Opin Gastroenterol 2005; 21: 169–75.
2 Arrieta MC, Bistritz L, Meddings JB. Alterations in intestinal permeability. Gut 2006; 55: 1512–20.
3 Sigthorsson G, Tibble J, Hayllar J, Menzies I, Macpherson A, Moots R,

et al. Intestinal permeability and inflammation in patients on NSAIDs. Gut 1998; 43: 506–11.
4 Tibble JA, Sigthorsson G, Foster R, Scott D, Fagerhol MK, Roseth A, *et al*. High prevalence of NSAID enteropathy as shown by a simple faecal test. Gut 1999; 45: 362–6.
5 Maiden L. Capsule endoscopic diagnosis of nonsteroidal anti-inflammatory drug-induced enteropathy. J Gastroenterol 2009; 44: 64–71.
6 van der Hulst RR, van Kreel BK, von Meyenfeldt MF, Brummer RJ, Arends JW, Deutz NE, *et al*. Glutamine and the preservation of gut integrity. Lancet 1993; 341: 1363–5.
7 Carrillo-Vico A, Guerrero JM, Lardone PJ, Reiter RJ. A review of the multiple action of melatonin on the immune system. Endocrine 2005; 27: 189–200.
8 Dobocovich M, Mankowsha M. Functimal MP1 and MP2 melatonin receptors in mammals. Endocrine 2005; 27: 101–10.
9 Bubenik GA. Localization, physiological significance and possible clinical implication of gastrointestinal melatonin. Biol Signals Recept 2001; 10: 350–66.
10 Huether G. Melatonin synthesis in the gastrointestinal tract and the impact of nutritional factors on circulating melatonin. Ann NY Acad Sci 1994; 719: 146–58.
11 Cabeza J, Motilva V, Martín MJ, de la Lastra CA. Mechanisms involved in gastric protection of melatonin against oxidant stress by ischemia-reperfusion in rats. Life Sci 2001; 68: 1405–15.
12 Bilici D, Süleyman H, Banoğlu ZN, Kiziltunç A, Avci B, Ciftçioğlu A, *et al*. Melatonin prevents ethanol-induced gastric mucosal damage possibly due to its antioxidant effect. Dig Dis Sci 2002; 47: 856–61.
13 Alarcón de la Lastra C, Motilva V, Martín MJ, Nieto A, Barranco MD, Cabeza J, *et al*. Protective effect of melatonin on indomethacin-induced gastric injury in rats. J Pineal Res 1999; 26: 101–7.
14 Konturek PC, Konturek SJ, Ketal C. Role of melatonin in mucosal gastroprotection against aspirin-induced gastric lesions in human. J Pineal Res 2004; 48: 318–23.
15 Poeggeler B, Reiter RJ, Tan DX, Chen LD, Manchester LC. Melatonin, hydroxyl radical-mediated oxidative damage, and aging: a hypothesis. J Pineal Res 1993; 14: 151–68.
16 Reiter RJ. Melatonin: lowering the high price of free radicals. News Physiol Sci 2000; 15: 246–50.
17 Reiter RJ, Paredes SD, Manchester LC, Tan DX. Reducing oxidative/nitrosative stress: a newly-discovered genre for melatonin. Crit Rev Biochem Mol Biol 2009; 44: 175–200.
18 Maity P, Bindu S, Dey S, Goyal M, Alam A, Pal C, *et al*. Melatonin reduces indomethacin-induced gastric mucosal cell apoptosis by preventing mitochondrial oxidative stress and the activation of mitochondrial pathway of apoptosis. J Pineal Res 2009; 46: 314–23.
19 Atchison CR, West AB, Balakumaran A, Hargus SJ, Pohl LR, Daiker DH, *et al*. Drug enterocyte adducts: possible causal factor for diclofenac enteropathy in rats. Gastroenterology 2000; 119: 1537–47.
20 Chiu CJ, McArdle AH, Brown R, Scott HJ, Gurd FN. Intestinal mucosal lesion in low-flow states. I. A morphological, hemodynamic, and metabolic reappraisal. Arch Surg 1970; 101: 478–83.
21 Lambert GP, Gisolfi CV, Berg DJ, Moseley PL, Oberley LW, Kregel KC. Selected contribution: Hyperthermia-induced intestinal permeability and the role of oxidative and nitrosative stress. J Appl Physiol 2002; 92: 1750–61.
22 Lange S, Delbro DS, Jennische E. Evans blue permeation of intestinal mucosa in the rat. Scand J Gastroenterol 1994; 29: 38–46.
23 Lowry OH, Rosebrough NJ, Farr A L, Randall RJ. Protein measurement with the Folin phenol reagent. J Biol Chem 1951; 193: 265–75.
24 Somasundaram S, Rafi S, Hayllar J, Sigthorsson G, Jacob M, Price AB, *et al*. Mitochondrial damage: a possible mechanism of the "topical" phase of NSAID induced injury to the rat intestine. Gut 1997; 41: 344–53.
25 Schneider WC, Hogeboom KEO. Intracellular distribution of enzymes. V. Further studies on the distribution of cytochrome *c* in rat liver homogenates. J Biol Chem 1950; 183: 123–8.
26 Emaus RK, Grunwald R, Lemaster JJ. Rhodamine 123 as a probe of transmembrane potential in isolated rat-liver mitochondria. Biochim Biophys Acta 1986; 850: 436–48.
27 Hernández-Muñoz R, Díaz-Muñoz M, Chagoya de Sánchez V. Effects of adenosine administration on the function and membrane composition of liver mitochondria in carbon tetrachloride-induced cirrhosis. Arch Biochem Biophys 1992; 294: 160–7.
28 Veeger C, Vartanian DV, Zeylemaker WP. Succinate dehydrogenase. In: Methods in enzymology. Lowenstein JM, editors. New York: Academic Press; 1969. p 81–90.
29 Parmar DV, Ahmed G, Khandkar MA, Katyare SS. Mitochondrial ATPase: a target for paracetamol-induced hepatotoxicity. Eur J Pharmacol 1995; 293: 225–9.
30 Davies NM, Saleh JY, Skjodt NM. Detection and prevention of NSAID-induced enteropathy. J Pharm Pharm Sci 2000; 3: 137–55.
31 Bjarnason I, Zanelli G, Smith T, Prouse P, Williams P, Smethurst P, *et al*. Nonsteroidal antiinflammatory drug-induced intestinal inflammation in humans. Gastroenterology 1987; 93: 480–9.
32 Bjarnason I, Takeuchi K. Intestinal permeability in the pathogenesis of NSAID-induced enteropathy. J Gastroenterol 2009; 44: 23–9.
33 Ozturk H, Oztürk H, Yagmur Y, Uzunlar AK. Effects of melatonin administration on intestinal adaptive response after massive bowel resection in rats. Dig Dis Sci 2006; 51: 333–7.
34 Cabeza J, Alarcón-de-la-Lastra C, Jiménez D, Martín MJ, Motilva V. Melatonin modulates the effects of gastric injury in rats: role of prostaglandins and nitric oxide. Neurosignals 2003; 12: 71–7.
35 Bandyopadhyay D, Bandyopadhyay A, Das PK, Reiter RJ. Melatonin protects against gastric ulceration and increases the efficacy of ranitidine and omeprazole in reducing gastric damage. J Pineal Res 2002; 33: 1–7.
36 Hardeland R, Tan DX, Reiter RJ. Kynuramines, metabolites of melatonin and other indoles:the resurrection of an almost forgotton class of biogenic amines. J Pineal Res 2009; 47: 109–24.
37 Gitto E, Pellegrino S, Gitto P, Barberi I, Reiter RJ. Oxidative stress of the newborn in the pre-and postnatal period and the clinical utility of melatonin. J Pineal Res 2009; 44: 128–39.
38 Pablos MI, Reiter RJ, Ortiz GG, Guerrero JM, Agapito MT, Chuang JI, *et al*. Rhythms of glutathione peroxidase and glutathione reductase in brain of chick and their inhibition by light. Neurochem Int 1998; 32: 69–75.
39 Jou MJ, Peng TI, Hsu LF, Jou SB, Reiter RJ, Yang CM, *et al*. Visualization of melatonin's multiple mitochondrial levels of protection against mitochondrial Ca^{2+}-mediated permeability transition and beyond in rat brain astrocytes. J Pineal Res 2010; 48: 20–38.
40 Kim SH, Lee SM. Cytoprotective effects of melatonin against necrosis and apoptosis induced by ischemia/reperfusion injury in rat liver. J Pineal Res 2008; 44: 165–71.
41 Okatani Y, Wakatsuki A, Reiter RJ, Enzan H, Miyahara Y. Protective effect of melatonin against mitochondrial injury induced by ischemia and reperfusion of rat liver. Eur J Pharmacol 2003; 469: 145–52.
42 Andrabi SA, Sayeed I, Siemen D, Wolf G, Horn TF. Direct inhibition of the mitochondrial permeability transition pore: a possible mechanism responsible for anti-apoptotic effects of melatonin. FASEB J 2004; 18: 869–71.
43 López A, García JA, Escames G, Venegas C, Ortiz F, López LC, *et al*.

Melatonin protects the mitochondria from oxidative damage reducing oxygen consumption, membrane potential, and superoxide anion production. J Pineal Res 2009; 46: 188–98.

44 Martín M, Macías M, León J, Escames G, Khaldy H, Acuña-Castroviejo D. Melatonin increases the activity of the oxidative phosphorylation enzymes and the production of ATP in rat brain and liver mitochondria. Int J Biochem Cell Biol 2002; 34: 348–57.

45 Acuña-Castroviejo D, Escames G, León J, Carazo A, Khaldy H. Mitochondrial regulation by melatonin and its metabolites. Adv Exp Med Biol 2003; 527: 549–57.

46 Acuña-Castroviejo D, Martín M, Macías M, Escames G, León J, Khaldy H, *et al*. Melatonin, mitochondria, and cellular bioenergetics. J Pineal Res 2001; 30: 65–74.

47 Paradies G, Petrosillo G, Paradies V, Reiter RJ, Ruggiero FM. Melatonin, cardiolirin and mitochondrial bioenergetics in health and disease. J Pineal Res 2010; 48: 297–310.

Acta Pharmacologica Sinica (2011) 32: 503–511
 1671-4083/11 $32.00
www.nature.com/aps

Original Article

Triptolide inhibits the proliferation of cells from lymphocytic leukemic cell lines in association with downregulation of NF-κB activity and miR-16-1*

Hai-tao MENG[1], Li ZHU[1], Wan-mao NI[1], Liang-shun YOU[1], Jie JIN[1], Wen-bin QIAN[1, 2, *]

[1]*Institute of Hematology, the First Affiliated Hospital, College of Medicine, Zhejiang University, Hangzhou 310003, China;* [2]*Xinyuan Institute of Medicine and Biotechnology, College of Life Sciences, Zhejiang Sci-Tech University, Hangzhou 310018, China*

Aim: To examine the effects of triptolide (TPL) on T-cell leukemia cells and identify their underlying mechanisms.
Methods: The cytotoxicity of TPL was assessed by MTT assay. Cell apoptosis was determined using annexin V and DAPI staining and analyzed by flow cytometry or fluorescence microscopy. The activation of caspase pathways and the expression of nuclear factor κB (NF-κB) p65 were examined by Western blotting. Differences in microRNA (miRNA) expression in Molt-4 and Jurkat cells before and after TPL treatment were identified using microarrays and real-time RT-PCR, respectively.
Results: TPL 20−160 nmol/L treatment potently inhibited cell growth and induced apoptosis in T-cell lymphocytic leukemia cell lines. Molt-4 and Jurkat cells, however, were more sensitive to TPL than L428 and Raji cells. After 24 h of treatment, bortezomib abrogated the growth of Molt-4 and Jurkat cells with an IC_{50} of 15.25 and 24.68 nmol/L, respectively. Using Molt-4 cells, we demonstrated that TPL 20−80 nmol/L inhibited the translocation of NF-κB p65 from the cytoplasm to the nucleus and that phosphorylated NF-κB p65 in nuclear extracts was down-regulated in a dose-dependent manner. Similar results were also seen in Jurkat cells but not in L428 cells, as these cells are resistant to TPL and bortezomib (a NF-κB inhibitor). Twenty-three miRNAs were differentially expressed after TPL treatment. Functional analysis revealed that TPL treatment could inhibit expression of miR-16-1* and that transfection of miR-16-1* led to significantly decreased apoptosis induced by TPL.
Conclusion: Our *in vitro* studies suggest that TPL might be an effective therapeutic agent for treatment of T-cell lymphocytic leukemia and that its cytotoxic effects could be associated with inhibition of NF-κB and down-regulation of miR-16-1*.

Keywords: triptolide; T-cell lymphocytic leukemia; NF-κB; miR-16-1*; bortezomib

Acta Pharmacologica Sinica (2011) 32: 503–511; doi: 10.1038/aps.2010.237; published online 28 Mar 2011

Introduction

Triptolide (PG490, TPL) is a diterpene triepoxide purified from the Chinese herb *Tripterygium wilfordii* hook F. This compound has been used to treat a variety of autoimmune diseases' it has also been used as an immunosuppressant in patients who have undergone organ and tissue transplantations[1, 2]. Recent studies analyzing the mechanisms of action of TPL have revealed many properties of this compound that are relevant not only to anti-inflammatory activity but also to anticancer activity. Shamon *et al*[3], for example, found that TPL could inhibit the growth of several human cancer-derived cell lines (including breast, prostate, and lung) under cell culture conditions. In hematologic tumors produced by acute myeloid leukemia (AML) cells, TPL treatment caused caspase-dependent cell death that was mediated via the mitochondrial pathway[4]. This treatment also down-regulated Bcr-Abl expression in K562 cells and induced apoptosis in STI571-resistant chronic myeloid leukemia (CML) cells[5, 6], suggesting that it lacks cross-resistance with currently available treatments. Our previous study showed that TPL also induced apoptosis in the multiple myeloma (MM) cell line 8226 and in U266 cells. We observed no cytotoxicity in the peripheral blood mononuclear cells examined from normal volunteers[7]. Importantly, clinical trials performed in China examining TPL treatment have shown that this drug can induce remission rates of 71% and 87% in mononucleocytic and granulocytic leukemia, respectively[8]. A succinate salt derivative of TPL (PG490-88) that is water soluble has recently been approved for Phase I clinical trials in France[9]. Results show that 3 out of 19 patients diagnosed with refractory or relapsing AML achieved complete remission[10]. These data imply a possible clinical application of TPL for leukemia treatment. Data on the ability of TPL to

* To whom correspondence should be addressed.
E-mail qianwenb@yahoo.com.cn
Received 2010-10-07 Accepted 2010-12-31

induce lymphoblastic leukemia cell death, however, are limited, and underlying mechanisms regulating the action of this compound are not well characterized.

Nuclear factor κB (NF-κB) plays a critical role in many biological processes, including cell cycle progression, apoptosis, oncogenesis, inflammation, and various autoimmune diseases[11, 12]. Abnormal constitutive NF-κB activation is widely seen in a number of solid tumors and in diverse types of hematopoietic malignancies, such as CML[13], AML[14], lymphoma[15, 16], and acute lymphoblastic leukemia (ALL)[17–19]. In particular, constitutively activated NF-κB is found selectively in leukemia stem cells and not in normal hematopoietic stem cells[20]. As such, NF-κB may be a potential therapeutic target for the selective eradication of leukemia stem cells. The NF-κB family is composed of five members: p65 (RelA), RelB, c-Rel, p50 (NF-κB1), and p52 (NF-κB2). Activation of p50 homodimers and p50/p65 heterodimers are detected in childhood ALL[17]. A recent study revealed a novel stromal cell function of RelB that promotes T-cell leukemogenesis[21]. Furthermore, inhibition of NF-κB activity was found to sensitize ALL cells to interferon β treatment[22]. Targeting NF-κB thus provides an attractive strategy for the treatment of lymphoblastic leukemia.

MicroRNAs (miRNAs or miRs) are a small (about 22 nucleotides), highly conserved noncoding class of regulatory RNA molecules expressed in a tissue- and development-specific manner[23]. They can play an important role in several types of cancers and in various other aspects of cancer biology[24–26]. Currently, extensive studies suggest that several miRNAs may act as oncogenes, tumor-suppressor genes[27], or even modulators of cancer stem cell growth and metastasis[28, 29]. The theory that miRNAs are involved in cancer is derived from the finding that miR-15a and miR-16-1* are downregulated or deleted in most patients diagnosed with CLL[30]. More interestingly, recent findings indicate that miRNAs can substantially modulate sensitivity and resistance to anticancer drugs[31]. A study by Kovalchuk *et al*[32] shows that miR-451 regulates the expression of multidrug resistance 1 gene and that transfection of miR-451 results in the increased sensitivity of breast cancer cells to doxorubicin. In contrast, miR-214 has been shown to induce cell survival and cisplatin resistance in ovarian cancer cells through inhibiting PTEN translation and activation of the Akt pathway[33]. Based on these observations, we hypothesized that miRNAs could affect the response of leukemia cells to TPL. In this study, we examined the effects of TPL on human T-cell leukemia cell lines and investigated the mechanisms underlying TPL-induced cell death. We found that TPL treatment at low nanomolar concentrations potently induced cell death in T-cell lymphocytic leukemia cells in association with inhibition of NF-κB and down-regulation of miR-16-1*.

Materials and methods

Cell culture and transfection

The human T-cell lymphocytic leukemia cell lines Molt-4 and Jurkat, the Burkitt lymphoma cell line Raji, and the Hodgkin's disease cell line L428 were purchased from American Type Culture Collection (ATCC, Rockville, USA). They were maintained in RPMI-1640 (Hyclone Laboratories, Logan, USA) supplemented with 10% fetal bovine serum (Hyclone Laboratories), 1% *L*-glutamine and 0.1% gentamicin at 37 °C in a humidified incubator containing 5% CO_2 in air. For functional analysis, leukemia cells were washed and resuspended in Opti-MEM I medium (Invitrogen, Carlsabad, USA), and miR-16-1* mimics and non-targeting miRNA mimics (GenePharma, Shanghai, China) were used. The miR mimics and control RNA were transfected into the appropriate cells using Lipofectamine 2000 (Invitrogen) according to the manufacturer's instructions. In brief, cells were plated in 6-well plates. For each well, miR-16-1* mimic (100 nmol/L), control RNA (100 nmol/L) and 5 μL of Lipofectamine 2000 Transfection Reagent were separately added into 250 μL of antibiotic-free Opti-MEM I medium and then mixed together to form the transfection complex. The transfection complex was added to cells and incubated for 6 h before replacing the medium.

Cell viability measurements

Leukemia cells were plated on 96-well plates at 1.0×10^5/well and then treated with or without TPL at the indicated dosages for 24 h and 48 h, respectively. The cell viability was evaluated by 3-(4,5-dimethylthiazol-2-yl)-2,5-diphenyltetrazolium bromide (MTT) assay (Sigma, St Louis, USA) as previously described[34].

Assessment of apoptosis

Apoptosis was determined using an annexin V-FITC and propidium iodide (PI) apoptosis detection kit (Biouniquer, Suzhou, China), according to the manufacturer's instructions. Prepared cells were analyzed with FACScan flow cytometer and CELLQuest software (Becton Dickinson, Franklin Lakes, USA). To detect chromatin condensation and nuclear fragmentation, cells were fixed with 4% paraformaldehyde and then stained with 5 μg/mL Hoechst 33258 (Sigma) for 20 min at room temperature. Apoptotic cells were determined by fluorescence microscopy (Olympus, Tokyo, Japan).

Immunofluorescence studies

Molt-4 cells were treated with PBS or TPL at 40 nmol/L and subjected to immunofluorescence analysis after 24 h. Briefly, cells were plated on glass slides for fixation by 4% paraformaldehyde for 30 min at room temperature followed by three washes with PBS. Cells were then incubated with a blocking buffer. The blocking buffer was then removed, and cells were incubated with an anti-human NF-κB p65 subunit antibody (Cell Signaling, Danvers, USA) at 4 °C overnight. After being washed three times with PBS, slides were incubated with Texas Red-conjugated goat anti-rabbit antibody for 30 min in the dark at room temperature, and secondary antibody was then removed. Next, slides were stained with 1 μmol/L DAPI (SouthernBiotech, Birmingham, USA) for 5 min in the dark and washed three times with PBS. They were then mounted on a coverslip and observed under a fluorescence microscope (Olympus, Tokyo, Japan).

Western blotting

Cells were harvested and extracted with lysis buffer (Cell Signaling), and nuclear extracts were collected by using a nuclear extraction kit (Millipore, Billerica, USA) according to the manufacturer's instructions. Western blot analysis was performed as described previously[35], with equal protein loading on 12% SDS-PAGE. The primary antibodies used were caspase-3, poly (ADP-ribose) polymerase (PARP), NF-κB p65, and Phosphor-NF-κB p65 (Ser536), all purchased from Cell Signaling Technology. Actin and Lamin B antibodies were used as housekeeping protein control. They were obtained from Santa Cruz Biotechnology (Santa Cruz, USA). After incubation with secondary antibodies (MultiSciences Biotech, Hangzhou, China), blots were revealed by enhanced chemiluminescene (ECL) procedures according to the manufacturer's recommendation.

miRNA microarray expression analysis

Total RNA was extracted from Molt-4 and TPL-treated-Molt-4 cells using TRIzol (Invitrogen) and the RNeasy mini kit (Qiagen, Valencia, USA) according to the manufacturer's instructions. The miRNA microarray analysis was done by KangChen (Shanghai, China). After passing RNA measurement on the Nanodrop instrument, the samples were labeled using the miRCURY™ Hy3™/Hy5™ Power labeling kit and hybridized on the miRCURY™ LNA Array (v 14.0). Experiments were carried out in triplicate. Scanning was performed with the Axon GenePix 4000B (Axon, Sunnyvale, USA) microarray scanner. GenePix pro V6.0 was used to read the raw intensity of the image. A *t* test analysis was conducted comparing Molt-4 and TPL-treated-Molt-4 samples, and miRNA with *P* values < 0.05 were selected for cluster analysis. The clustering analysis was performed using a hierarchical method as well as average linkage and Euclidean distance metrics[36].

Real-time quantitative RT-PCR of micro-RNA

The quantitative real-time PCR (qRTPCR) was done by using Hairpin-it miRNAs qPCR Quantitation Kit (GenePharma) according to manufacturer's specified guidelines. Total RNA was isolated by using TRIzol (Invitrogen) and further subjected to DNase (Invitrogen) digestion, following the manufacturer's protocol. The RNA levels were quantified by spectrophotometry. One microgram of total RNA was incubated with DNase I and reverse-transcribed using MMLV reverse transcriptase (Invitrogen). The reverse transcription product was amplified using primer pairs specific for miR-16-1* and miR-138-2*. U6 were used as controls for quantification. qRT-PCR was performed using an iQ5 Multicolor Real-Time PCR Detection System (Bio-Rad, Berkeley, USA). The level of each miRNA expression was measured using the $2^{-DeltaDeltaCt}$ method.

Statistical analysis

Means were compared using the 2-tailed Student's *t* test. $P<0.05$ was considered statistically significant in all calculations. All data analyses were performed using GraphPad Prism software version 4.0 (GraphPad, San Diego, USA).

Results

Effect of TPL on the proliferation of lymphocytic leukemia cells *in vitro*

To investigate the effects of TPL on growth and survival of lymphocytic leukemia cells, we treated various leukemia cell lines, including Molt-4, Jurkat, Raji and L428 cells, with increasing concentrations of TPL. As shown in Figure 1, after 1 or 2 d of treatment, the proliferation of the leukemia cells was significantly inhibited by TPL in a dose-dependent manner, as indicated by MTT assay. Molt-4 and Jurkat cells, however, were more sensitive to TPL than L428 and Raji cells. Next, we compared the efficacy of TPL with that of bortezomib, a proteasome inhibitor that potently inhibits NF-κB activity. After 24 h of treatment, bortezomib abrogated the growth of Motl-4 and Jurkat cells with an IC_{50} of 15.25 and 24.68 nmol/L, respectively. In contrast, a much higher concentration of bortezomib (326.23 nmol/L) was required to achieve a 50% inhibition in L428 cells.

TPL inhibits NF-κB and induces apoptosis in leukemia cells

To understand the mechanisms of TPL-induced cell death in leukemic cells, we examined the ability of TPL to induce apoptosis using Annexin V/PI and DAPI staining followed by flow cytometry and fluorescence microscopy analyses, respectively. As shown in Figure 2A, TPL treatment in nanomolar concentration (80 nmol/L) for 12 h resulted in apoptosis in a large percentage of cells. L428 and Raji cells, however, were resistant to apoptosis induced by TPL. Analysis of Molt-4 nuclei after Hoechst staining confirmed that TPL-treated cells exhibited morphologic changes characteristic of apoptosis, such as chromatin condensation and formation of micronuclei (Figure 2B). Next, we tested for molecules that control apoptosis. Western blot analysis was used to confirm our flow cytometric findings by demonstrating that TPL treatment activated two key molecules in the apoptosis pathway, namely, caspase-3 and PARP in Molt-4 and Jurkat cells, but not in L428 cells (Figure 2C).

Several tumor-cell types, including myeloma and leukemia, are known to constitutively express NF-κB through a mechanism yet to be fully defined[37]. To determine the role of NF-κB in the process of TPL-induced cell death in lymphoblastic leukemia cells, we treated Molt-4, Jurkat cells, which are sensitive to TPL, and L428 cells, which are resistant to TPL, with the indicated concentrations of TPL. We then used Western blot analysis to determine the possible influence of TPL on the subcellular localization of p65. As shown in Figure 3A, TPL treatment inhibited the nuclear accumulation of p65 in Molt-4. Phosphor-NF-κB p65 (Ser536) in nuclear extracts of Molt-4 cells was reduced in a dose-dependent manner. Similar results were seen in Jurkat cells (data not shown). However, this result was not observed in L428 cells. Immunofluorescence staining using a specific antibody against p65 also indicated a decrease in the nuclear translocation of NF-κB in TPL-treated Molt-4 cells and confirmed the results of the immunoblotting analysis (Figure 3B). Collectively, these data demonstrate that TPL inhibits the nuclear accumulation of NF-κB.

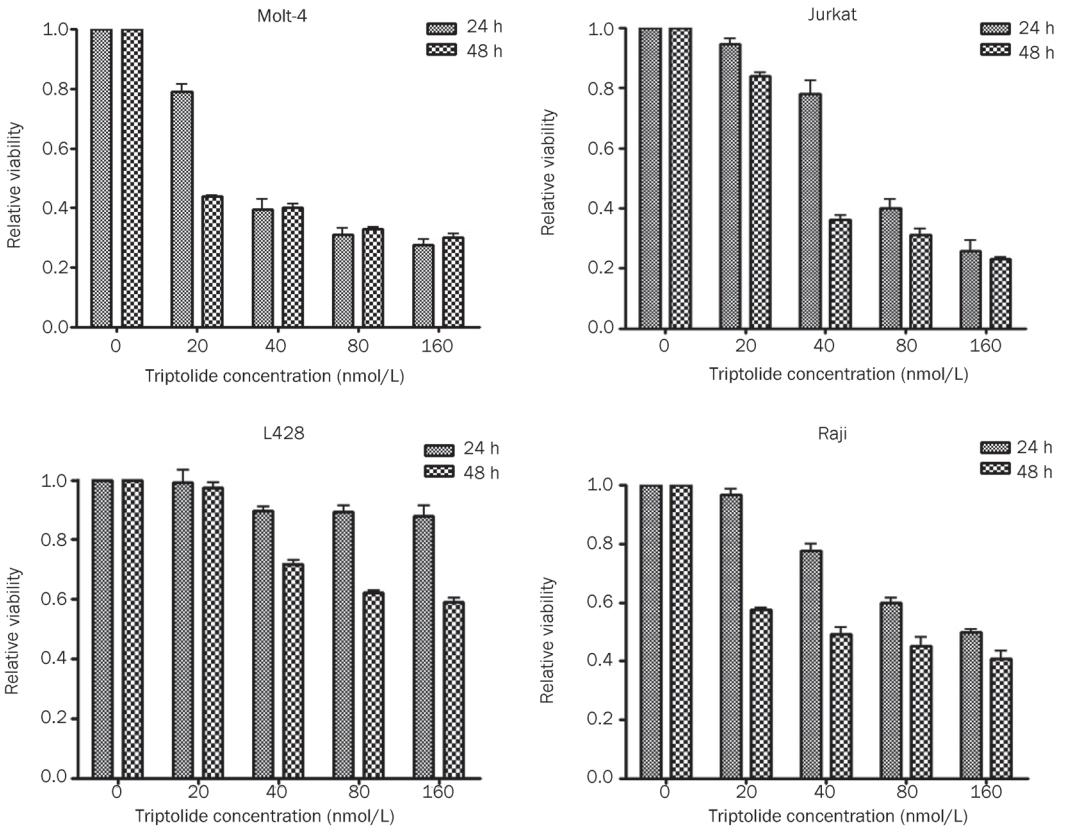

Figure 1. Effect of triptolide on cell growth in lymphocytic leukemia cell lines. Exponentially growing cells were seeded into 96-well plates, and then treated with the indicated concentrations of triptolide for 24 and 48 h, respectively. The proliferation of cells was determined by a MTT assay. Mean±SD. *n*=3 independent experiments. bars, SD.

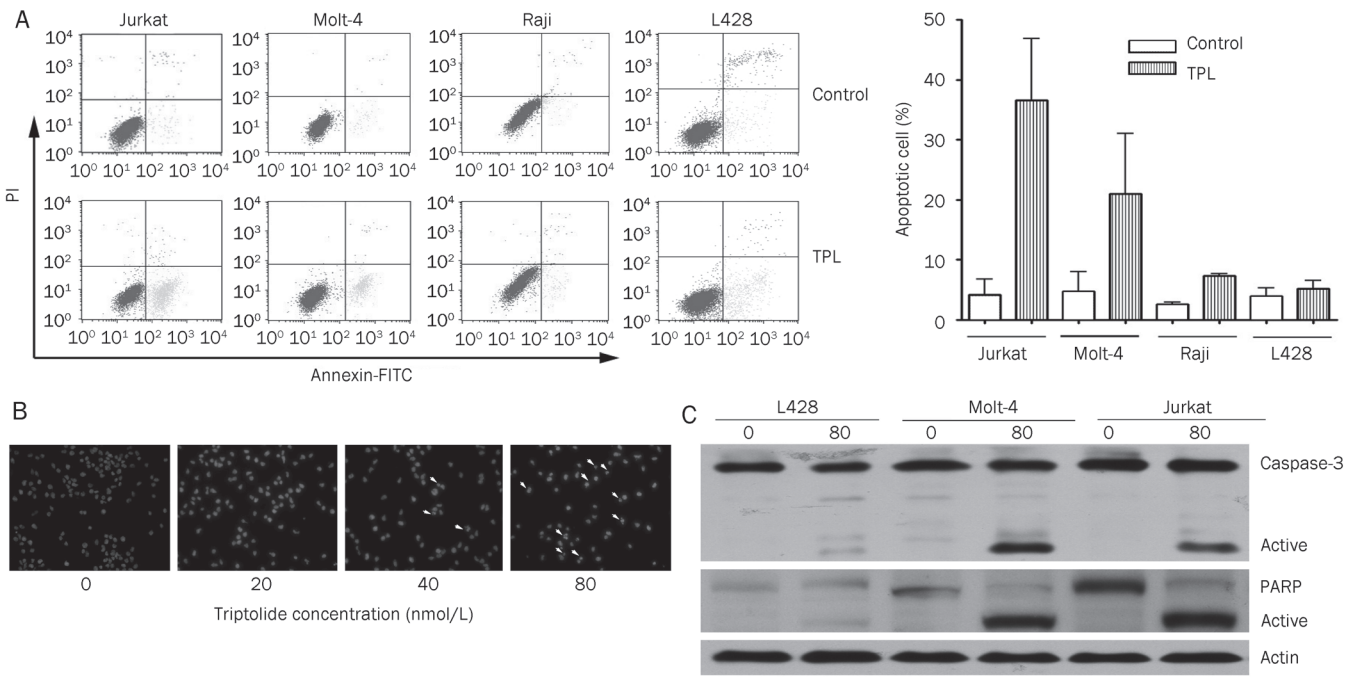

Figure 2. Apoptosis induced by triptolide. (A) After treatment with triptolide at 80 nmol/L for 12 h, cells were collected and detected by the annexin-V/propidium iodide (PI)-staining method. The results were expressed as mean±SD (*n*=3). (B) After treatment with triptolide at indicated concentrations for 12 h, Molt-4 cells were stained with Hoechst 33258 and then observed under a fluorescence microscope. Arrows, apoptotic nuclei. (C) Leukemia cell lines were incubated with 80 nmol/L of triptolide for 12 h, and then cell extractions were subjected to Western blotting analysis using anti-caspase-3 and PARP antibodies. The results are the representatives of three separate experiments.

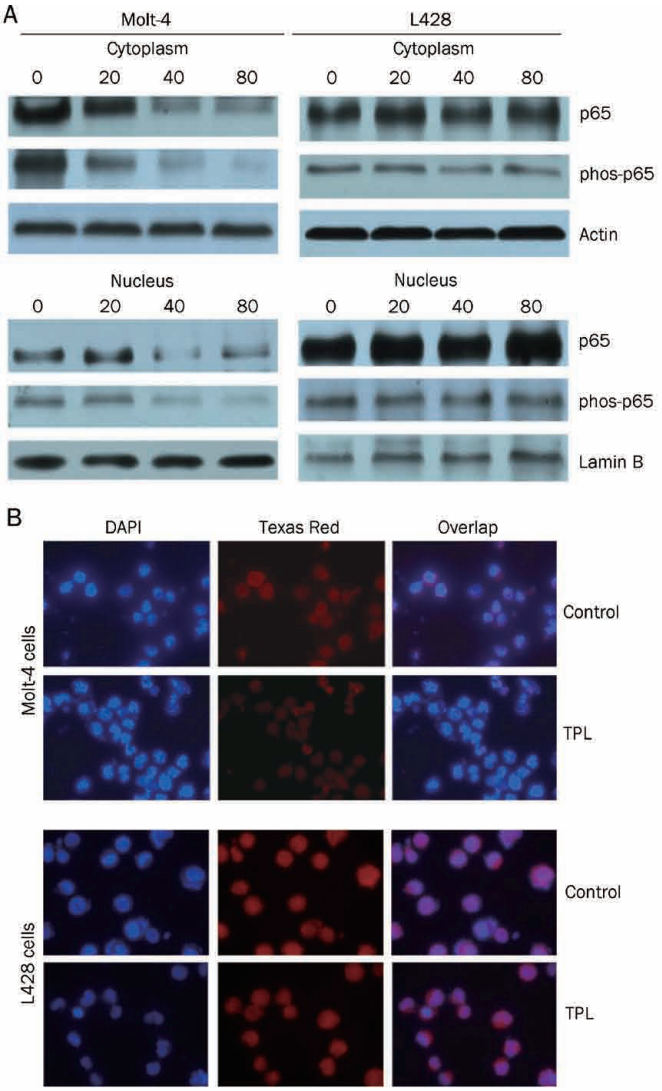

Figure 3. Triptolide inhibits the expression of NF-κB and the accumulation of p65 in nucleus. (A) Cells were treated with triptolide at the indicated concentrations for 24 h. The nuclear and cytoplasm fractions of cells were harvested, and then were analyzed by Western blotting using anti-nuclear factor κB (NF-κB) p65 and phos-p65 antibodies. The blots were blotted with actin or lamin B antibody to control for sample loading. Results shown are representative of three separate experiments. (B) Cells treated with 40 nmol/L of triptolide were fixed, permeabilized, and then subjected to immunofluorescent double staining with antibody against p65 subunit of NF-κB by Texas Red. Nuclei were counterstained with DAPI.

Comparative analysis of miRNA expression profile in Molt-4 cells before and after TPL treatment

We analyzed the miRNA expression profiles in the human leukemia Molt-4 cell line and TPL-treated Molt-4 cells. The clusters analysis revealed that the Molt-4 cells treated with TPL demonstrated significant changes in miRNA expression. We identified 23 miRNA genes (17 up-regulated and 6 down-regulated) that were differentially expressed (P<0.05) in the TPL-treated Molt-4 cells, compared to the parental Molt-4 cells (Figure 4A). Among these identified miRNAs, miR-16[38] and miR-138 family members[39–40] have been previously implicated in tumorigenesis and cancer cell death. As such, qRT-PCR was used to determine the expression differences of miR-16-1* and miR-138-2* in the paired lymphocytic leukemia cell lines. Upregulation of miR-138-2* and downregulation of miR-16-1* by TPL in a time- and dose-dependent manner was observed in Molt-4 cells (Figure 4B and C). Similar results were obtained in Jurkat cells (Figure 4D). These results confirmed the microarray findings for miR-138-2* and miR-16-1*.

Downregulation of miR-16-1* may contribute to TPL-induced cell death

To investigate the involvement of miR-16-1* down-regulation in TPL-induced cell death, functional analyses were performed to test the effects of miR-16-1* on cell apoptosis. As shown in Figure 5, ectopic transfection of miR-16-1* mimics led to significantly decreased apoptosis of TPL-treated Molt-4 cells (23% *vs* 17%, P<0.05), suggesting that miR-16-1* may provide partial protection against the cytotoxicity of TPL. It should be noted that transfection of negative control oligonucleotides into Molt-4 cells did not affect their sensitivity to TPL. Collectively, out data indicate that downregulation of miR-16-1* may be associated with the cytotoxicity of TPL in T-cell lymphocytic leukemia cells.

Discussion

Acute lymphocytic leukemia in adults is the most aggressive neoplastic disorder of lymphocytes. Over the last several decades, survival rates of the patients have remarkably improved due to progress in therapeutic protocols; however, a higher proportion of the patients cannot expect long-term remission because of frequent relapse with poor clinical outcome. As such, novel biological therapeutics need to be developed, either alone or in combination with conventional chemotherapy[18]. NF-κB is a major factor underlying malignant T-cell transformation, drug resistance, and apoptosis. It was found that adult T-cell leukemia cells possess constitutively activated NF-κB and that inhibition of NF-κB by the proteasome inhibitor bortezomib or by Bay 11-7082 induces cell death in adult T-cell leukemia cells[41–43]. We became interested in TPL because it was reported that TPL is a potent inhibitor of NF-κB activation. In this regard, Qiu *et al*[44] showed that TPL at 200 ng/mL and 1000 ng/mL caused nearly complete inhibition of IκBα protein expression in activated T-cells. In the present study, we demonstrate that TPL at low nanomolar concentration (20–80 nmol/L) potently inhibits cell growth of T-cell lymphocytic leukemia cell lines and induces apoptosis, as demonstrated by annexin V staining and Hoechst staining. The cleavage of caspase-3 and PARP was observed in the T-cell lymphocytic leukemia cells, suggesting that the activation of caspase pathway is involved in TPL-induced apoptosis. These results concur with those obtained in AML cells treated with TPL[4]. We also show that the responses appear to be dependent upon inhibition of NF-κB activity, as treatment with TPL induced a dose-dependent decrease of phospho-p65 level in T-cell leukemia cell lines accompanied by a reduced

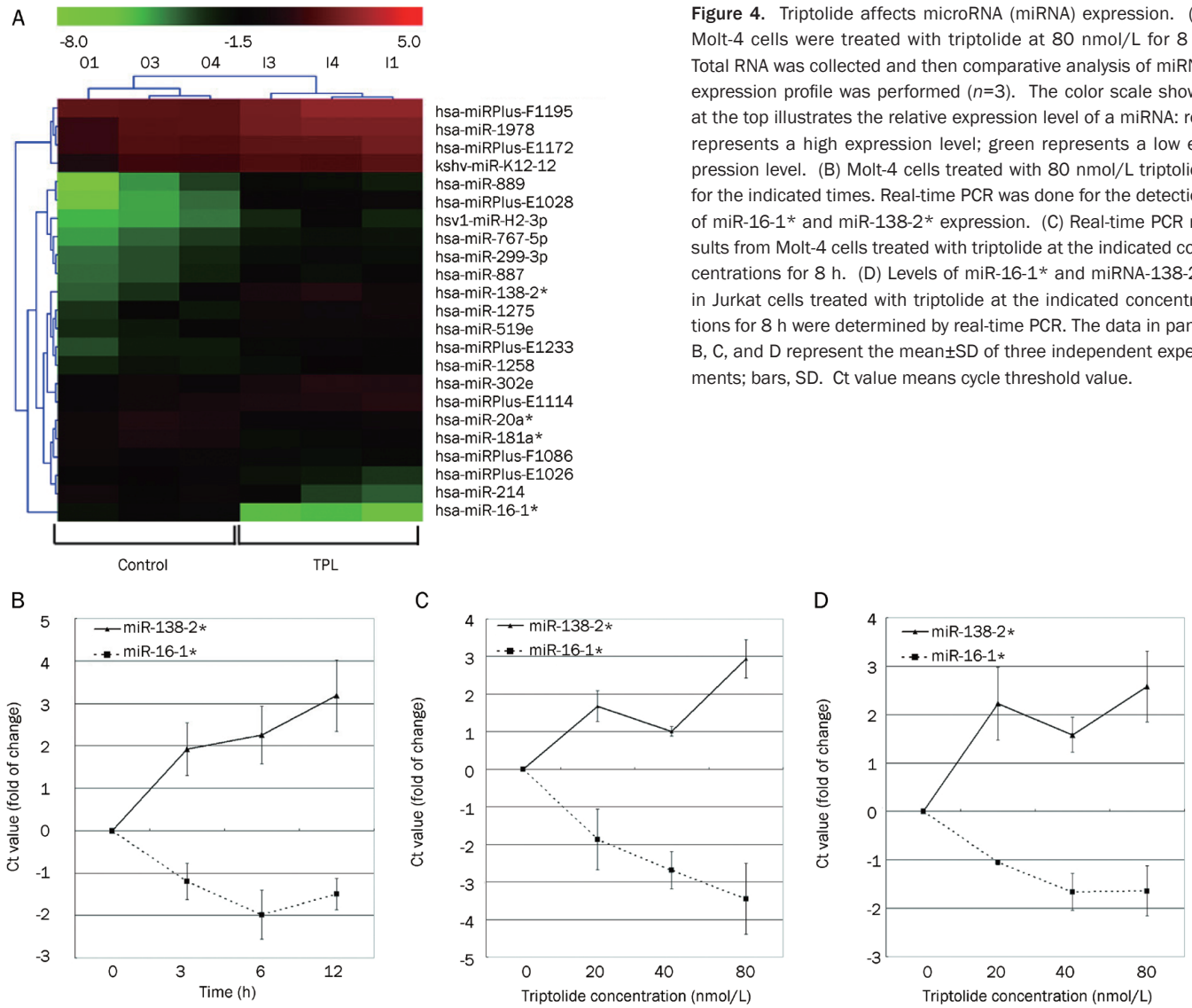

Figure 4. Triptolide affects microRNA (miRNA) expression. (A) Molt-4 cells were treated with triptolide at 80 nmol/L for 8 h. Total RNA was collected and then comparative analysis of miRNA expression profile was performed (n=3). The color scale shown at the top illustrates the relative expression level of a miRNA: red represents a high expression level; green represents a low expression level. (B) Molt-4 cells treated with 80 nmol/L triptolide for the indicated times. Real-time PCR was done for the detection of miR-16-1* and miR-138-2* expression. (C) Real-time PCR results from Molt-4 cells treated with triptolide at the indicated concentrations for 8 h. (D) Levels of miR-16-1* and miRNA-138-2* in Jurkat cells treated with triptolide at the indicated concentrations for 8 h were determined by real-time PCR. The data in panel B, C, and D represent the mean±SD of three independent experiments; bars, SD. Ct value means cycle threshold value.

nuclear accumulation of NF-κB p65. In contrast, similar results were not found in L428 cells, which are resistant to TPL and bortezomib. Together, these data suggest that the ability of TPL to inhibit NF-κB could explain the underlying mechanism.

Previous studies suggest that cellular effects and mechanisms of action of TPL in cancer cells are highly complex and undoubtedly involve multiple biological pathways. In addition to NF-κB inhibition, down-regulation of XIAP[45,46], activation of functional p53 pathway[9], inhibition of Bcr-abl transcription[5,6], and decreased HSP70 mRNA and protein levels[47, 48] are also responsible for TPL-induced cell death. In this study, we performed miRNA expression profiling using Molt-4 cells with or without TPL treatment, and we showed that 23 miRNA genes were differentially expressed at a level of P<0.05. The function of majority of the identified miRNA genes, however, is still unknown. We thus focused on miR-16-1* and miR-138-2*, as miR-16 and miR-138 are reported to be functionally associated with the apoptosis of cancer cells[39, 49]. The results of qRTPCR, which are consistent with our microarray data, showed that TPL treatment decreased miR-16-1* expression and increased miR-138-2*. Furthermore, functional analysis revealed that miR-16-1* could partly abrogate the effects of TPL in Molt-4 cells, suggesting that inhibition of miR-16-1* expression may contribute to TPL-induced cell death. The miR-16 family contains miRNAs that have been shown to regulate Bcl-2[49] and cell cycle genes[50, 51], including cyclin D1, cyclin D3, cyclin E1, and CDK6, which together can result in cell cycle arrest and the apoptosis of cancer cells. Recently, miR-16-1 has been considered as a possible tumor suppressor gene[38] because its levels have been found to be reduced or completely ablated in >65% of CLL cases examined[52, 53]. Also, forced expression of this gene can induce apoptosis through the targeting of Bcl-2[49]. Although it remains unclear why miR-16-1*, a miR-16 family member, acts in a functionally different manner than miR-16-1, these seem-

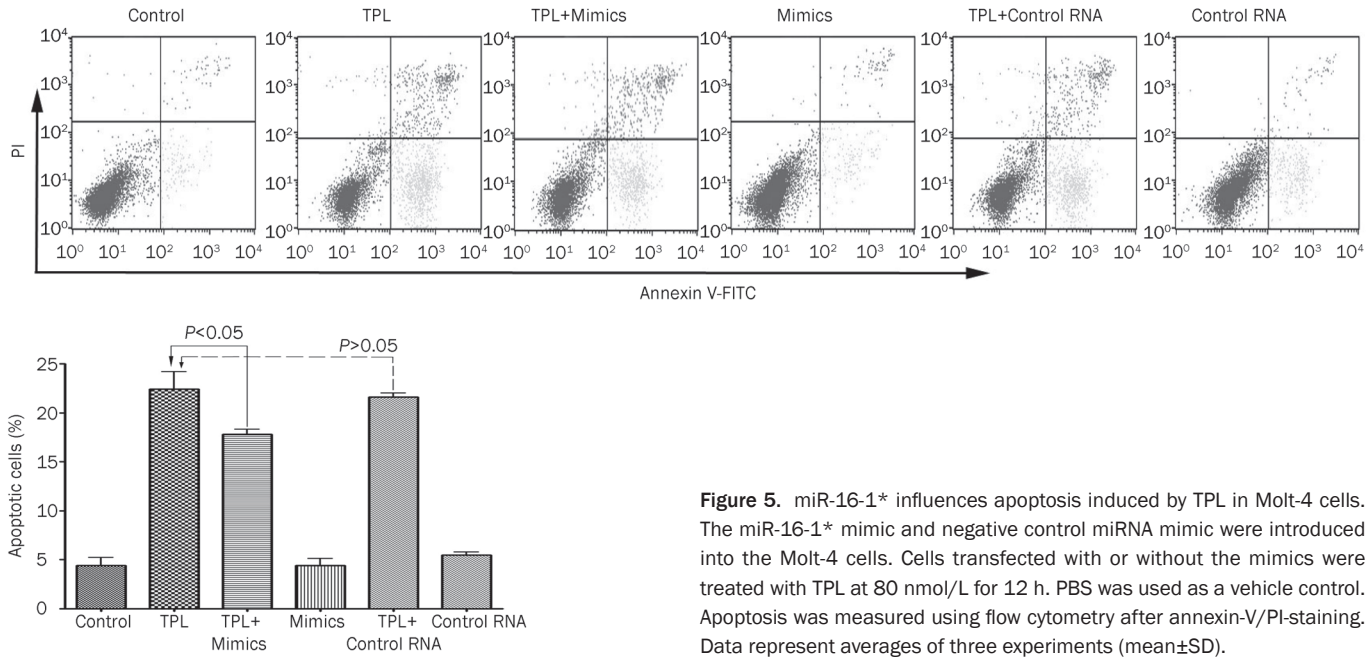

Figure 5. miR-16-1* influences apoptosis induced by TPL in Molt-4 cells. The miR-16-1* mimic and negative control miRNA mimic were introduced into the Molt-4 cells. Cells transfected with or without the mimics were treated with TPL at 80 nmol/L for 12 h. PBS was used as a vehicle control. Apoptosis was measured using flow cytometry after annexin-V/PI-staining. Data represent averages of three experiments (mean±SD).

ingly contradictory findings are not surprising. In fact, CLL patients presenting with deletions of 13q14, where miR-15a and miR-16-1 reside, have been shown to exhibit a more favorable prognosis[54]. In contrast, Calin *et al* [52] reported that high expression levels of miR-16-1/miR-16-2 were observed in CLL patients with a poor prognosis. Taken together, these data indicate that the roles of alterations in the miR-16 family genes in the leukemia are complicated. Here, we also show that TPL up-regulates the expression of miR-138-2*. It was previously reported that miR-138, which can repress hTERT mRNA, was down-regulated in thyroid cancer cells[40]. A recent study shows that miR-138 suppresses invasion and promotes apoptosis in head and neck squamous cell carcinoma cell lines and suggests that miR-138-1 and miR-138-2 may function as tumor suppressor genes[39]. Thus, further investigation is required for evaluating the roles of miR-138-2* in TPL-induced cell death.

In summary, our data suggest that TPL at low nanomolar concentrations can potently inhibit cell growth and induce apoptosis in T-cell lymphocytic leukemia cells and that the inhibition of NF-κB may, in part, contribute to the toxicity of TPL. Additionally, TPL treatment resulted in the marked alteration of 23 miRNA genes. Among these genes, miR-138-2* expression was up-regulated and miR-16-1* was down-regulated. As this may contribute to the cytotoxic effects of TPL, our data suggest that miRNAs could be a potential target for T-cell leukemia treatment. Future work is required to gain a deeper understanding of the proteins targeted by these miRNAs.

Acknowledgements

This work was supported by the National key Technology R&D Program for the 11th Five-Year plan (No 2008BAI61B01); Zhejiang Provincial Natural Science Foundation of China (No R2090392).

Author contribution

Wen-bin QIAN designed the research; Hai-tao MENG, Li ZHU, Wan-mao NI, Liang-shun YOU, and Jie JIN performed the research; and Wen-bin QIAN and Li ZHU analyzed the data and wrote the paper.

References

1 Chen BJ. Triptolide, a novel immunosuppressive and anti-inflammatory agent purified from a Chinese herb *Tripterygium wilfordii* Hook F. Leuk Lymphoma 2001; 42: 253–65.

2 Tao XL, Sun Y, Dong Y, Xiao YL, Hu DW, Shi YP, *et al.* A prospective, controlled, double-blind, cross-over study of *Tripterygium wilfodii* hook F in treatment of rheumatoid arthritis. Chin Med J (Engl) 1989; 102: 327–32.

3 Shamon LA, Pezzuto JM, Graves JM, Mehta RR, Wangcharoentrakul S, Sangsuwan R, *et al*. Evaluation of the mutagenic, cytotoxic, and antitumor potential of triptolide, a highly oxygenated diterpene isolated from *Tripterygium wilfordii*. Cancer Lett 1997; 112: 113–7.

4 Carter BZ, Mak DH, Schober WD, McQueen T, Harris D, Estrov Z, *et al*. Triptolide induces caspase-dependent cell death mediated via the mitochondrial pathway in leukemic cells. Blood 2006; 108: 630–7.

5 Lou YJ, Jin J. Triptolide down-regulates bcr-abl expression and induces apoptosis in chronic myelogenous leukemia cells. Leuk Lymphoma 2004; 45: 373–6.

6 Shi X, Jin Y, Cheng C, Zhang H, Zou W, Zheng Q, *et al*. Triptolide inhibits Bcr-Abl transcription and induces apoptosis in STI571-resistant chronic myelogenous leukemia cells harboring T315I mutation. Clin Cancer Res 2009; 15: 1686–97.

7 Yinjun L, Jie J, Yungui W. Triptolide inhibits transcription factor NF-kappaB and induces apoptosis of multiple myeloma cells. Leuk Res 2005; 29: 99–105.

8 Lu LH, Lian YY, He GY, Lin SP, Huan SH, Chen ZZ, *et al*. Clinical study of triptolide in treatment of acute leukemia. Clin Exp Investig Hematol

1992; 3: 1–3.
9 Kiviharju TM, Lecane PS, Sellers RG, Peehl DM. Antiproliferative and proapoptotic activities of triptolide (PG490), a natural product entering clinical trials, on primary cultures of human prostatic epithelial cells. Clin Cancer Res 2002; 8: 2666–74.
10 Harousseau JL, Dombret H, Pigneux A, Michallet M, Brandely M. Phase I study of F60008, a triptolide derivative, in patients with refractory or relapsing acute leukemias. Haematologica 2008; 93(s1): 14 abs. 0038.
11 Karin M, Lin A. NF-kappaB at the crossroads of life and death. Nat Immunol 2002; 3: 221–7.
12 Baud V, Karin M. Is NF-kappaB a good target for cancer therapy? Hopes and pitfalls. Nat Rev Drug Discov 2009; 8: 33–40.
13 Lounnas N, Frelin C, Gonthier N, Colosetti P, Sirvent A, Cassuto JP, *et al*. NF-kappaB inhibition triggers death of imatinib-sensitive and imatinib-resistant chronic myeloid leukemia cells including T315I Bcr-Abl mutants. Int J Cancer 2009; 125: 308–17.
14 Guzman ML, Rossi RM, Neelakantan S, Li X, Corbett CA, Hassane DC, *et al*. An orally bioavailable parthenolide analog selectively eradicates acute myelogenous leukemia stem and progenitor cells. Blood 2007; 110: 4427–35.
15 Staudt LM. The molecular and cellular origins of Hodgkin's disease. J Exp Med 2000; 191: 207–12.
16 Rosenwald A, Wright G, Chan WC, Connors JM, Campo E, Fisher RI, *et al*. Lymphoma/Leukemia Molecular Profiling Project. The use of molecular profiling to predict survival after chemotherapy for diffuse large-B-cell lymphoma. N Engl J Med 2002; 346: 1937–47.
17 Kordes U, Krappmann D, Heissmeyer V, Ludwig WD, Scheidereit C. Transcription factor NF-kappaB is constitutively activated in acute lymphoblastic leukemia cells. Leukemia 2000; 14: 399–402.
18 Zhao WL. Targeted therapy in T-cell malignancies: dysregulation of the cellular signaling pathways. Leukemia 2010; 24: 13–21.
19 Cardoso BA, Gírio A, Henriques C, Martins LR, Santos C, Silva A, *et al*. Aberrant signaling in T-cell acute lymphoblastic leukemia: biological and therapeutic implications. Braz J Med Biol Res 2008; 41: 344–50.
20 Guzman ML, Neering SJ, Upchurch D, Grimes B, Howard DS, Rizzieri DA, *et al*. Nuclear factor-kappaB is constitutively activated in primitive human acute myelogenous leukemia cells. Blood 2001; 98: 2301–7.
21 dos Santos NR, Williame M, Gachet S, Cormier F, Janin A, Weih D, *et al*. RelB-dependent stromal cells promote T-cell leukemogenesis. PLoS ONE 2008; 3: e2555.
22 Tracey L, Streck CJ, Du Z, Williams RF, Pfeffer LM, Nathwani AC, *et al*. NF-kappaB activation mediates resistance to IFN beta in MLL-rearranged acute lymphoblastic leukemia. Leukemia 2010; 24: 806–12.
23 Ambros V. The evolution of our thinking about microRNAs. Nat Med 2008; 14: 1036–40.
24 Nicoloso MS, Spizzo R, Shimizu M, Rossi S, Calin GA. MicroRNAs-the micro steering wheel of tumour metastases. Nat Rev Cancer 2009; 9: 293–302.
25 Leung AK, Sharp PA. MicroRNAs: a safeguard against turmoil? Cell 2007; 130: 581–5.
26 Mi S, Lu J, Sun M, Li Z, Zhang H, Neilly MB, *et al*. MicroRNA expression signatures accurately discriminate acute lymphoblastic leukemia from acute myeloid leukemia. Proc Natl Acad Sci U S A 2007; 104: 19971–6.
27 Gaur A, Jewell DA, Liang Y, Ridzon D, Moore JH, Chen C, *et al*. Characterization of microRNA expression levels and their biological correlates in human cancer cell lines. Cancer Res 2007; 67: 2456–68.
28 Cho WC. MicroRNAs: potential biomarkers for cancer diagnosis, prognosis and targets for therapy. Int J Biochem Cell Biol 2010; 42: 1273–81.
29 Cho WC. MicroRNAs in cancer-form research to therapy. Biochim Biophys Acta 2010; 1805: 209–17.
30 Calin GA, Dumitru CD, Shimizu M, Bichi R, Zupo S, Noch E, *et al*. Frequent deletions and down-regulation of micro- RNA genes miR15 and miR16 at 13q14 in chronic lymphocytic leukemia. Proc Natl Acad Sci U S A 2002; 99: 15524–9.
31 Climent J, Dimitrow P, Fridlyand J, Palacios J, Siebert R, Albertson DG, *et al*. Deletion of chromosome 11q predicts response to anthracycline-based chemotherapy in early breast cancer. Cancer Res 2007; 67: 818–26.
32 Kovalchuk O, Filkowski J, Meservy J, Ilnytskyy Y, Tryndyak VP, Chekhun VF, *et al*. Involvement of microRNA-451 in resistance of the MCF-7 breast cancer cells to chemotherapeutic drug doxorubicin. Mol Cancer Ther 2008; 7: 2152–9.
33 Yang H, Kong W, He L, Zhao JJ, O'Donnell JD, Wang J, *et al*. MicroRNA expression profiling in human ovarian cancer: miR-214 induces cell survival and cisplatin resistance by targeting PTEN. Cancer Res 2008; 68: 425–33.
34 Qian W, Liu J, Tong Y, Yan S, Yang C, Yang M, *et al*. Enhanced antitumor activity by a selective conditionally replicating adenovirus combining with MDA-7/interleukin-24 for B-lymphoblastic leukemia via induction of apoptosis. Leukemia 2008; 22: 361–9.
35 Yang C, Tong Y, Ni W, Liu J, Xu W, Li L, *et al*. Inhibition of autophagy induced by overexpression of MDA/Interleukin-24 using a PI3K inhibitor results in significant enhanced antileukmia activity *in vivo*. Cancer Gene Ther 2010; 17: 109–19.
36 Eisen MB, Spellman PT, Brown PO, Botstein D. Cluster analysis and display of genome-wide expression patterns. Proc Natl Acad Sci U S A 1998; 95: 14863–8.
37 Harikumar KB, Kunnumakkara AB, Ahn KS, Anand P, Krishnan S, Guha S, *et al*. Modification of the cysteine residues in IkappaBalpha kinase and NF-kappaB (p65) by xanthohumol leads to suppression of NF-kappaB-regulated gene products and potentiation of apoptosis in leukemia cells. Blood 2009; 113: 2003–13.
38 Calin GA, Cimmino A, Fabbri M, Ferracin M, Wojcik SE, Shimizu M, *et al*. MiR-15a and miR-16-1 cluster functions in human leukemia. Proc Natl Acad Sci U S A 2008; 105: 5166–71.
39 Liu X, Jiang L, Wang A, Yu J, Shi F, Zhou X. MicroRNA-138 suppresses invasion and promotes apoptosis in head and neck squamous cell carcinoma cell lines. Cancer Lett 2009; 286: 217–22.
40 Santarpia L, Nicoloso M, Calin GA. MicroRNAs: a complex regulatory network drives the acquisition of malignant cell phenotype. Endocr Relat Cancer 2010; 17: F51–75.
41 Mori N, Fujii M, Ikeda S, Yamada Y, Tomonaga M, Ballard DW, *et al*. Constitutive activation of NF-κB in primary adult T-cell leukemia cells. Blood 1999; 93: 2360–8.
42 Satou Y, Nosaka K, Koya Y, Yasunaga JI, Toyokuni S, Matsuoka M. Proteasome inhibitor, bortezomib, potently inhibits the growth of adult T-cell leukemia cells both *in vivo* and *in vitro*. Leukemia 2004; 18: 1357–63.
43 Mori N, Yamada Y, Ikeda S, Yamasaki Y, Tsukasaki K, Tanaka Y, *et al*. Bay 11-7082 inhibits transcription factor NF-κB and induces apoptosis of HTLV-I-infected T-cell lines and primary adult T-cell leukemia cells. Blood 2002; 100: 1828–34.
44 Qiu D, Zhao G, Aoki Y, Shi L, Uyei A, Nazarian S, *et al*. Immunosuppressant PG490 (triptolide) inhibits T-cell interleukin-2 expression at the level of purine-box/nuclear factor of activated T-cells and NF-κB transcriptional activation. J Biol Chem 1999; 274: 13443–50.
45 Carter BZ, Mak DH, Schober WD, Dietrich MF, Pinilla C, Vassilev LT, *et al*. Triptolide sensitizes AML cells to TRAIL-induced apoptosis via decrease of XIAP and p53-mediated increase of DR5. Blood 2008; 111:

3742–50.

46 Choi YJ, Kim TG, Kim YH, Lee SH, Kwon YK, Suh SI, *et al*. Immunosuppressant PG490 (triptolide) induces apoptosis through the activation of caspase-3 and down-regulation of XIAP in U937 cells. Biochem Pharmacol 2003; 66: 273–80.

47 Westerheide SD, Kawahara TL, Orton K, Morimoto RI. Triptolide, an inhibitor of the human heat shock response that enhances stress-induced cell death. J Biol Chem 2006; 281: 9616–22.

48 Phillips PA, Dudeja V, McCarroll JA, Borja-Cacho D, Dawra RK, Grizzle WE, *et al*. Triptolide induces pancreatic cancer cell death via inhibition of heat shock protein 70. Cancer Res 2007; 67: 9407–16.

49 Cimmino A, Calin GA, Fabbri M, Iorio MV, Ferracin M, Shimizu M, *et al*. MiR-15 and miR-16 induce apoptosis by targeting BCL2. Proc Natl Acad Sci U S A 2005; 102: 13944–9.

50 Wang F, Fu XD, Zhou Y, Zhang Y. Down-regulation of the cyclin E1 oncogene expression by microRNA-16-1 induces cell cycle arrest in human cancer cells. BMB Rep 2009; 42: 725–30.

51 Liu Q, Fu H, Sun F, Zhang H, Tie Y, Zhu J, *et al*. MiR-16 family induces cell cycle arrest by regulating multiple cell cycle genes. Nucleic Acids Res 2008; 36: 5391–404.

52 Calin GA, Ferracin M, Cimmino A, Di Leva G, Shimizu M, Wojcik SE, *et al*. A microRNA signature associated with prognosis and progression in chronic lymphocytic leukemia. N Engl J Med 2005; 353: 1793–801.

53 Calin GA, Liu CG, Sevignani C, Ferracin M, Felli N, Dumitru CD, *et al*. MicroRNA profiling reveals distinct signatures in B cell chronic lymphocytic leukemias. Proc Natl Acad Sci U S A 2004; 101: 11755–60.

54 Caligaris-Cappio F, Hamblin TJ. B-cell chronic lymphocytic leukemia: a bird of a different feather. J Clin Oncol 1999; 17: 399–408.

Acta Pharmacologica Sinica (2011) 32: 512–518
 1671-4083/11 $32.00
www.nature.com/aps

Original Article

CaIPF14030 negatively modulates intracellular ATP levels during the development of azole resistance in *Candida albicans*

Xin-ming JIA[1, 2, *], Ying WANG[2], Jun-dong ZHANG[2], Hong-yue TAN[2], Yuan-ying JIANG[3], Jun GU[2, *]

[1]*Department of Immunology, Tongji University School of Medicine, Shanghai 200092, China;* [2]*Department of Dermatology, Changhai Hospital, Second Military Medical University, Shanghai 200433, China;* [3]*Department of Pharmacology, School of Pharmacy, Second Military Medical University, Shanghai 200433, China*

Aim: Widespread and repeated use of azoles, particularly fluconazole, has led to the rapid development of azole resistance in *Candida albicans*. We investigated the role of *CaIPF14030* during the development of azole resistance in *C albicans*.
Methods: The expression of *CaIPF14030* was measured by quantitative RT-PCR, and *CaIPF14030* was disrupted by the hisG-URA3-hisG (URA-blaster) method. The sensitivity of *C albicans* to azoles was examined using a spot assay, and the intracellular ATP concentrations were measured by a luminometer.
Results: *CaIPF14030* expression in *C albicans* was up-regulated by Ca^{2+} in a calcineurin-dependent manner, and the protein was overexpressed during the stepwise acquisition of azole resistance. However, disruption or ectopic overexpression of *CaIPF14030* did not affect the sensitivity of *C albicans* to azoles. Finally, we demonstrated that disruption of *CaIPF14030* significantly increased intracellular ATP levels, and overexpression significantly decreased intracellular ATP levels in *C albicans*.
Conclusion: *CaIPF14030* may negatively modulate intracellular ATP levels during the development of azole resistance in *C albicans*.

Keywords: *Candida albicans*; CaIPF14030; calcineurin pathway; azole resistance; intracellular ATP

Acta Pharmacologica Sinica (2011) 32: 512–518; doi: 10.1038/aps.2010.232

Introduction

Candida albicans (*C albicans*), a major human fungal pathogen, causes disorders ranging from mild infections to life-threatening diseases[1, 2]. *C albicans* is often treated with fluconazole, which is a fungistatic drug. However, there is a rapid acquisition of resistance to azoles in *C albicans*. This is due to a limited number of multidrug resistance related genes, which include *ERG11*, *CDR1*, *CDR2*, and *CaMDR1*[3–6]. Recently, DNA microarray and proteomic analyses have revealed many differentially regulated genes in either laboratory[7, 8] or clinical[9–12] azole-resistant *C albicans* isolates. However, few of these new observations have been confirmed by genetic studies because *C albicans* is difficult to study experimentally due to its asexual diploid nature and variant genetic code.

The calcineurin pathway is involved in the development of azole resistance in *C albicans*[13–15]. Calcineurin is a Ca^{2+} calmodulin-dependent serine/threonine phosphatase consisting of a catalytic subunit A (encoded by CNA1) and a regulatory subunit B (encoded by CNB1)[16]. The phosphatase activity of calcineurin is activated when calcineurin binds calmodulin in the presence of calcium ions. Activated calcineurin regulates downstream gene expression via transcription factors such as Crz1p[17].

In our previous study, we found that *RTA2*, *CaIPF14030,* and *MXR1* were involved in the calcineurin pathway. These three genes were overexpressed in the experimentally induced azole-resistant *C albicans* strain DSF28[18]. The *rta2* and *ipf14030* null mutants from *C albicans* were constructed along with deletions of *CDR1*, *CDR2,* and *CaMDR1*[18]. The disruption of *RTA2* increased the susceptibility of *C albicans* to azoles, whereas the disruption of *CaIPF14030* did not influence the sensitivity of *C albicans* to azoles[18]. Bioinformatic analysis also revealed that the promoters of both the *RTA2* and the *CaIPF14030* genes contained the calcineurin-dependent responsive element (CDRE) sequence, which is controlled by either calcineurin or Crz1p[17, 18]. However, the function of *CaIPF14030* was unknown. In the present study, we con-

* To whom correspondence should be addressed.
E-mail jiaxm@tongji.edu.cn (Xin-ming JIA);
jgu@smmu.edu.cn (Jun GU)
Received 2010-08-17 Accepted 2010-12-31

structed the *ipf14030* null mutant from the *C albicans* wild-type strain to investigate the role of *CaIPF14030* during the development of azole resistance in *C albicans*.

Materials and methods

Antifungal agents

Fluconazole was from Pfizer Inc (New York, NY, USA). Ketoconazole and econazole were purchased from Sigma (St Louis, MO, USA). Itraconazole was a gift from Prof Chao-mei LIU, and voriconazole was a gift from Prof Wan-nian ZHANG from the Second Military Medical University, Shanghai, China.

Candida albicans strains and culture media

Candida albicans strains used in this study are listed in Table 1; they were cultured in YPD medium or SC medium lacking uridine, methionine and cysteine.

RNA isolation and quantitative RT-PCR

All primer sequences are listed in Table 2. RNA isolation, cDNA synthesis, and PCR amplification were performed as described previously[18]. Triplicate independent quantitative RT-PCRs were performed using the LightCycler System (Roche Diagnostics, Mannheim, Germany). Gene expression levels relative to the calibrator were expressed as $2^{-\Delta\Delta CT}$.

Table 2. Primers used in this study.

Name*	Sequence**
Primers used in quantitative RT-PCR	
18 S FWD	GTGCCAGCAGCCGCGGTA
18 S RV	TGGACCGGCCAGCCAAGC
IPF14030 FWD	CTTCCTGTACCTGTTGTGATTC
IPF14030 RV	TCTTCCAAGAAAACTGCTGATG
Primers used in disruption of *IPF14030* gene	
IPF14030up FWD	ccgctcgagACCAACCAGATTCCCCTTC
IPF14030up RV	ctgacggatccgagtcCACTCCAATGGAAACTAGGC
IPF14030down FWD	gactcggatccgtcagGAAGCGAATTTTGCTCTTGG
IPF14030down RV	ggaattccatatgGTTCCCATTACCACGAACTC
Primers used for amplifying *IPF14030* ORF	
IPF14030 FWD	ccggatccACACTAGAACATGTTCATTATT
IPF14030 RV	atgcctgcagCATCTGTCAGTTGTGCTT
Primers used for amplifying hybridization probe of *IPF14030* gene	
IPF14030up FWD	TGGCAACAAATATTAATCCCCG
IPF14030up RV	GTTCAAAATCAAGCCCAATGTG

* FWD, forward; RV, reverse
** Restriction sites are in lower case

Construction of mutant strains

All primer sequences are listed in Table 2. Construction of plasmid pUC-IPF14030-URA3 was performed as described previously[18]. Briefly, the fragment containing the 5′ and 3′ ends of the *CaIPF14030* gene for homologous recombination was obtained according to the Fusion PCR method. The 4-kb hisG-URA3-hisG fragment was from the p5921 plasmid[19]. The two fragments were subsequently cloned into plasmid pUCm-t (Sangon, Shanghai, China). The *Xho*I-digested fragment of pUC-IPF14030-URA3 was transformed into the *ura3* mutant strain (RM1000) by standard methods[20]. The hybridization probe primers are listed in Table 2. Southern blot analysis was used to confirm the absence of the *CaIPF14030* gene.

Overexpression of *CaIPF14030* in *ipf14030* mutants

The *CaIPF14030* ORF was amplified by PCR with Pyrobest polymerase (TaKaRa, Dalian, China). The *BamH* I/*Pst* I-digested PCR fragment was ligated into pCaExp[21] to obtain recom-

Table 1. *C albicans* strains used in this study.

Strain	Parental strain	Genotype	Reference
CAF2-1	SC5314	*ura3Δ::imm434/URA3*	[19]
DSY2091	CAF4-2	*cnaΔ::hisG/cnaΔ::hisG::URA3::hisG*	[17]
DSY2115	DSY2101	*cnaΔ::hisG/cnaΔ::hisG; LEU2::CNA::URA3*	[13]
DSY2195	DSY2188	*crz1Δ::hisG/crz1Δ::hisG::URA3::hisG*	[17]
MKY268	MKY59	*crz1Δ::hisG/crz1Δ::hisG LEU2::CRZ1/URA3*	[17]
DSY1024	CAF4-2	*cdr1Δ::hisG/cdr1Δ::hisG cdr2Δ::hisG/cdr2Δ::hisG camdr1Δ::hisG/camdr1Δ::hisG flu1Δ::hisG/flu1Δ::hisG-URA3-hisG*	[32]
RM1000	RM100	*ura3Δ::imm^{434}/ura3Δ::imm^{434}, his1Δ::HisG/his1Δ::HisG, iro1Δ::imm^{434}/iro1Δ::imm^{434}*	[33]
MZP10	RM1000	*RM1000* ipf14030Δ::hisG-URA3-hisG/IPF14030*	This study
MZP11	MZP10	*RM1000* ipf14030Δ::hisG/IPF14030*	This study
MZP100	MZP11	*RM1000* ipf14030Δ::hisG/ipf14030Δ::hisG-URA3-hisG*	This study
MZP101	MZP100	*RM1000* ipf14030Δ::hisG/ipf14030Δ::hisG*	This study
Exp-14030	MZP101	*RM1000* ipf14030Δ::hisG/ipf14030Δ::hisG RP10/rp10Δ::pExpIPF14030-URA3*	This study
Exp-MZP	MZP101	*RM1000* ipf14030Δ::hisG/ipf14030Δ::hisG RP10/rp10Δ::pCaExp-URA3*	This study
Exp-RM	RM1000	*RM1000* RP10/rp10Δ::pCaExp-URA3*	This study

* RM1000 background.

binant plasmid pEXP-IPF14030. DNA sequencing confirmed that the sequence of the insert was identical to the *CaIPF14030* sequence reported in the Candida Genome Database (http://www.candidagenome.org/). The *ipf14030* mutant (MZP101) was transformed with the *Stu* I-digested and linearized pEXP-IPF14030 plasmid and selected on SC medium lacking uridine, methionine and cysteine.

Susceptibility testing

The sensitivities of the mutant strains to azoles were determined by testing the strains on agar plates containing different concentrations of azoles (fluconazole, ketoconazole, econazole, itraconazole, and voriconazole). Five microliters of ten-fold serial dilutions of each yeast culture (OD_{600}=1.0) were spotted on plates of the appropriate medium and then incubated at 30 °C for the indicated time.

Measurement of intracellular ATP levels

C albicans strains were diluted to 1×10^8 or 1×10^7 cells/mL in YPD broth. A total of 100 μL of cell suspension was mixed completely with the same volume of BacTiter-Glo reagent (Promega Corporation, Madison, WI, USA) and incubated for 10 min at room temperature. Luminescent signals were measured with a TD 20/20 luminometer (Turner Biosystem, Sunnyvale, CA, USA) with a 1 s integration time per sample. A control tube without cells was used to obtain a value for background luminescence. The signal-to-noise ratio (S/N) was calculated as follows: [mean of signal - mean of background]/standard deviation of background. A standard curve for ATP increments from 10 pmol/L to 1 μmol/L was constructed. Signals represented the mean of three separate experiments. The ATP content was calculated from the standard curve.

Statistical analysis

Experiments were performed at least three times. Data are presented as mean±standard deviations, and data were analyzed using Student's *t* test where indicated.

Results

CaIPF14030 up-regulation by Ca^{2+} in a calcineurin-dependent manner

Bioinformatic analysis revealed that the *CaIPF14030* promoter contains the CDRE sequence, which can be controlled by either calcineurin or Crz1p[17]. In our study, expression levels of *CaIPF14030* were examined by quantitative RT-PCR in wild-type (CAF2-1), *cna*Δ/Δ mutant (DSY2091), *crz1*Δ/Δ mutant (DSY2195), *CNA* revertant (DSY2115) and *CRZ1* revertant (MKY268) strains after exposure to 200 mmol/L $CaCl_2$ for 2 h (Figure 1A). *CaIPF14030* was up-regulated by 6.51 fold in the CAF2-1 strain (Figure 1A). Depletion of *CNA* or *CRZ1* inhibited the effects of $CaCl_2$ on *CaIPF14030* up-regulation by 1.53 fold in the DSY2091 strain and by 0.96 fold in the DSY2195 strain (Figure 1A). However, reintroduction of *CNA* or *CRZ1* in the respective null mutant strains restored the effect of 200 mmol/L $CaCl_2$ on *CaIPF14030* up-regulation. There was a 3.62-fold change in the DSY2115 strain and a 3.19-fold change in the MKY268 strain (Figure 1A). Taken together, these data demonstrate that *CaIPF14030* is up-regulated by Ca^{2+} in a calcineurin-dependent manner.

CaIPF14030 is overexpressed during the stepwise acquisition of azole resistance in DSY1024

It has been well documented that calcium can activate the calcineurin pathway and modulate azole activity in *C albicans*[22, 23]. Because the *CaIPF14030* gene of *C albicans* is up-regulated by Ca^{2+} in a calcineurin-dependent manner, we investigated the dynamic expression of *CaIPF14030* in the DSF7, DSF14, DSF21, and DSF28 strains obtained in our previous study[18]. As shown in Figure 1B, the *CaIPF14030* gene was overexpressed in the DSF7, DSF14, DSF21, and DSF28 strains. These results are similar to those found for other known resistance-related genes such as *ERG11*, *CDR1*, and *CaMDR1*[4, 24]. These data suggest that *CaIPF14030* is involved in the development of azole resistance in *C albicans*.

Disruption and ectopic overexpression of the *CaIPF14030* gene in *C albicans*

To investigate the role of *CaIPF14030* during the development

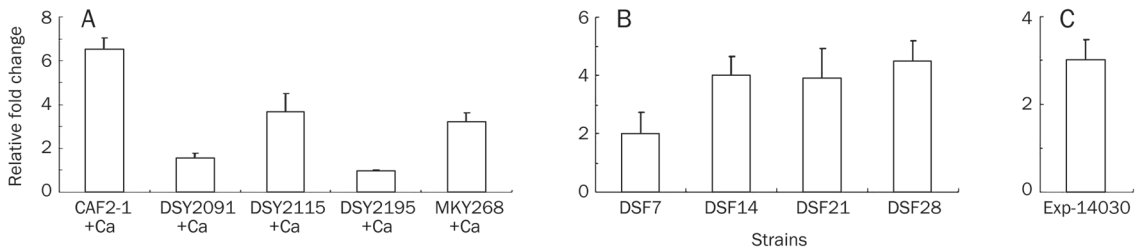

Figure 1. (A) Expression of *CaIPF14030* was examined by quantitative RT-PCR in wild-type (CAF2-1), *cna*Δ/Δ mutant (DSY2091), *CNA* revertant (DSY2115), *crz1*Δ/Δ mutant (DSY2195), and *CRZ1* revertant (MKY268) strains in the presence of 200 mmol/L $CaCl_2$. The corresponding strains in the absence of $CaCl_2$ were used as controls. (B) Expression of *CaIPF14030* was examined by quantitative RT-PCR in DSF7, DSF14, DSF21, and DSF28 strains obtained in our previous study[18] and compared to DSY1024. (C) Expression of *CaIPF14030* in the Exp-14030 strain (MZP101 carrying pCaEXP-IPF14030) was compared to the Exp-RM strain (RM1000 carrying pCaEXP). Strains were cultured in SC medium lacking methionine, cysteine, and uridine for 16 h before harvesting for quantitative RT-PCR analysis. Data are represented as mean±SD.

of azole resistance in *C albicans*, two alleles of *CaIPF14030* were sequentially disrupted in the RM1000 strain using the URA-blaster method and 5-FOA selection. This yielded the following strains: Ura$^+$ *ipf14030/IPF14030* (MZP10), Ura$^-$ *ipf14030/IPF14030* (MZP11), Ura$^+$ *ipf14030/ipf14030* (MZP100), and Ura$^-$ *ipf14030/ipf14030* (MZP101) (Table 1). The strategy to disrupt both copies of *CaIPF14030* is depicted in Figure 2A and 2B. Southern blot analysis of DNA from the constructed strains revealed that the recombination patterns were as expected (Figure 2C). To further characterize the generated mutants, RM1000 and MZP101 growth curves were obtained. They showed identical growth rates.

To investigate whether other deletions were introduced into the *C albicans* genome, the *CaIPF14030* ORF was placed under

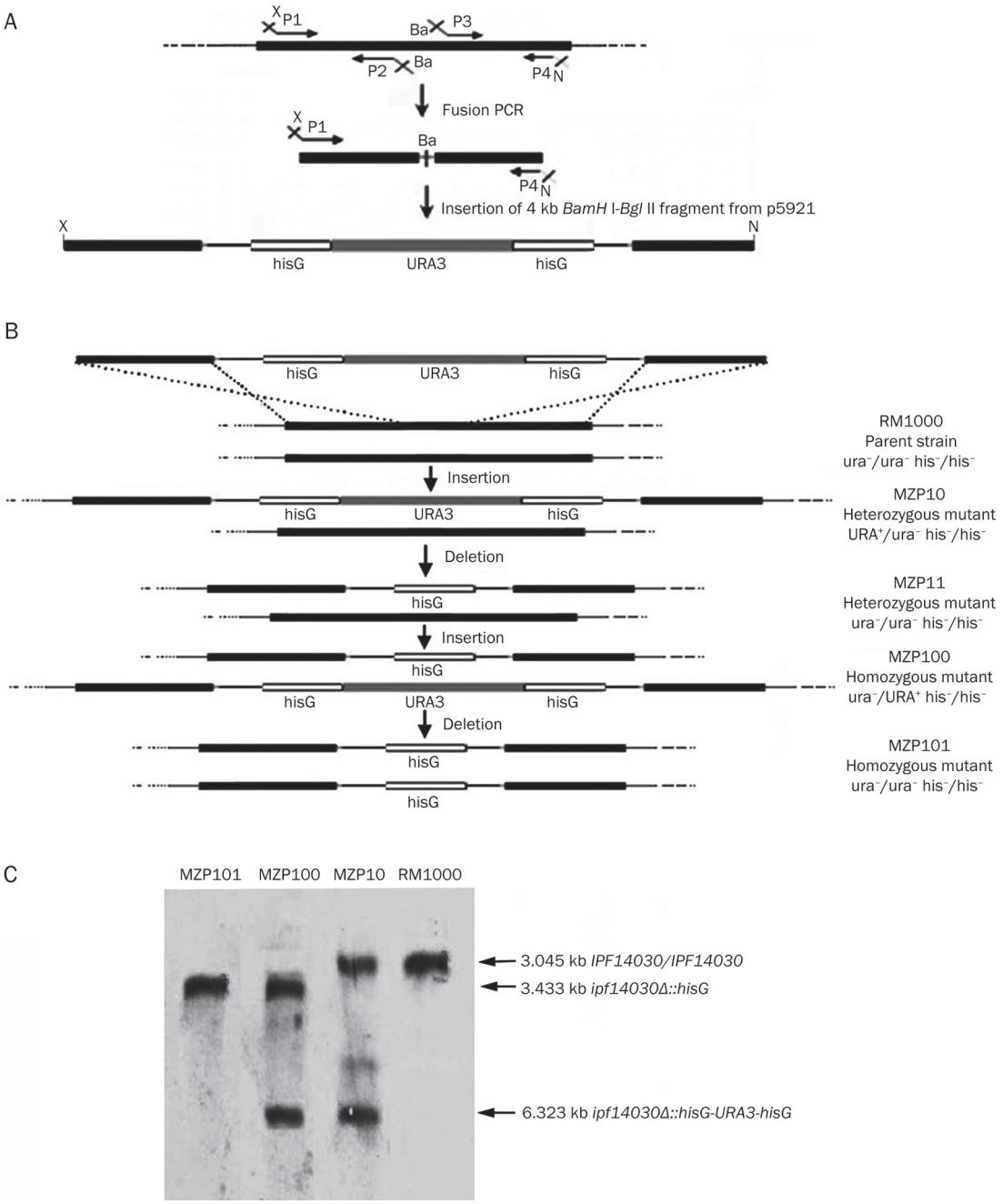

Figure 2. Schematic representation of the plasmid construction and disruption of *CaIPF14030* using the *URA3* selection marker. (A) Diagrammatic representation of the plasmid construction of pUC-IPF14030-URA3 containing *hisG-URA3-hisG* with flanking portions on either side for homologous recombination. Ba: *BamH* I, X: *Xho* I, N: *Nde* I. (B) Sequential targeted disruption of the two *CaIPF14030* alleles in *C albicans* with the disruption cassette. Strain designation is shown on the right. (C) Southern blot analysis of the genomic DNA digested with *Kpn* I and *Sac* I. The exact size and genotype of the expected hybridizing DNA fragment are indicated on the right. The hybridization probe was a 0.528-kb PCR fragment from -432 to 96 of the *CaIPF14030* gene amplified by Pyrobest polymerase (TaKaRa, Dalian, China) from genomic DNA extracted from RM1000.

the control of the MET3 promoter in the pCaEXP vector, and it was successfully integrated into the *ipf14030*Δ/Δ mutant (MZP101) at the RP10 locus as determined by PCR (data not shown). Ectopic overexpression of *CaIPF14030* in the Exp-14030 strain was confirmed by quantitative RT-PCR with *CaIPF14030* expression in the parental strain (RM1000) carrying empty vector pCaEXP, which served as a control (Figure 1C). The growth rates of the RM1000 and Exp-14030 strains were similar, suggesting that there were no other gene disruptions that affected the growth of the strains.

Disruption or ectopic overexpression of *CaIPF14030* does not affect the sensitivity of *C albicans* to azoles

Because the *CaIPF14030* gene was overexpressed during the stepwise acquisition of azole resistance in DSY1024, a drug susceptibility assay was performed to determine whether *CaIPF14030* is associated with enhanced azole resistance in *C albicans*. Spot assay results demonstrated that neither disruption nor ectopic overexpression of *CaIPF14030* affected the sensitivity of *C albicans* to the azoles, including fluconazole, ketoconazole, econazole, itraconazole, and voriconazole (Figure 3A, 3B). Taken together, these data support the hypothesis that *CaIPF14030* does not play an important role in the development of azole resistance in *C albicans*.

CaIPF14030 negatively controls the intracellular ATP content of *C albicans*

It has been well documented that lower intracellular ATP levels are found in *C albicans* strains that are azole resistant or have been treated by azoles[25, 26]. Because overexpression of *CaIPF14030* occurred during the development of azole resistance in *C albicans*, intracellular ATP concentrations were measured in the following strains: wild-type (RM1000), *ipf14030*Δ/Δ mutant (MZP101) and ectopically over-expressed (Exp-14030). As shown in Figure 4, the level of intracellular ATP in the MZP101 strain was significantly higher than that in the RM1000 strain ($P<0.01$), whereas the level of intracellular ATP in the Exp-14030 strain was significantly lower than that in the RM1000 strain ($P<0.01$). These results suggest that *CaIPF14030* plays a critical role in the generation of intracellular ATP during the development of azole resistance in *C albicans*.

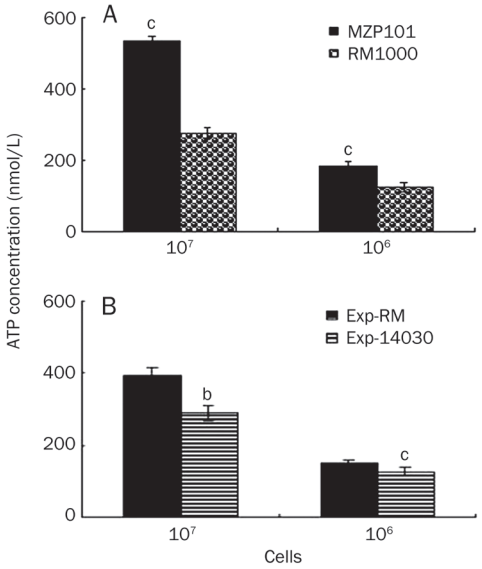

Figure 4. Intracellular ATP content in the wild-type (RM1000), RM1000 carrying pCaEXP (Exp-RM), *ipf14030* mutant (MZP101) and MZP101 carrying pCaEXP-IPF14030 (Exp-14030) strains. ATP levels represent the mean±standard deviation for three independent experiments. $^bP<0.05$ when compared to the control strains (RM1000 or Exp-RM); $^cP<0.01$ when compared to the control strains (RM1000 or Exp-RM).

Discussion

Bioinformatic analysis have revealed that the *CaIPF14030* promoter contains a CDRE sequence, which can be controlled by either calcineurin or Crz1p[17]. The expression levels of *CaIPF14030* were examined by quantitative RT-PCR in the wild-type (CAF2-1), *cna*Δ/Δ mutant (DSY2091), *crz1*Δ/Δ mutant (DSY2195), *CNA* revertant (DSY2115) and *CRZ1* revertant (MKY268) strains after exposure to 200 mmol/L $CaCl_2$.

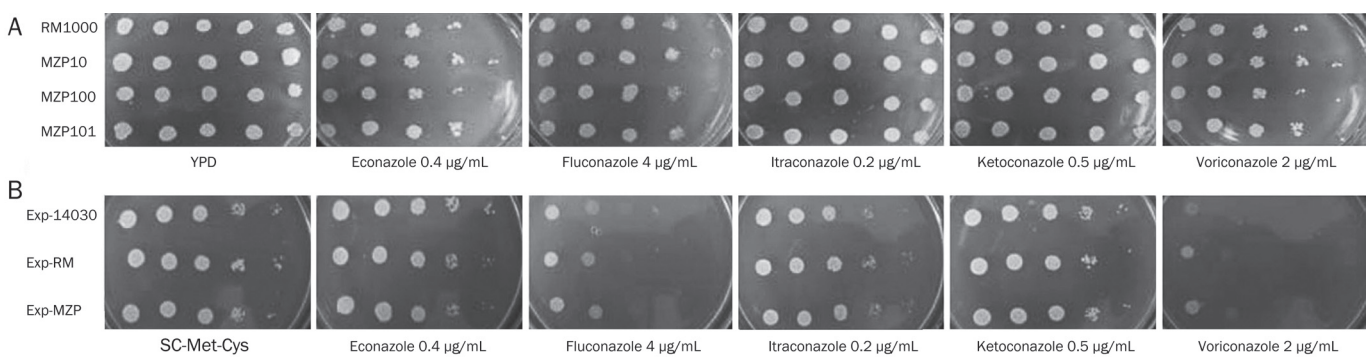

Figure 3. Drug susceptibility profiles of *C albicans* strains (Table 1) determined by spot assays. (A) The *ipf14030* heterozygous and homozygous mutant strains from RM1000 were spotted on YPD agar plates supplemented with 0.0025% uridine with or without different antifungal agents at the indicated concentrations. Plates were incubated for 48 h at 30°C. (B) The *ipf14030* mutant strains (MZP101) carrying pCaEXP or pCaEXP-IPF14030 and the parental strain (RM1000) carrying pCaEXP were spotted on SC medium plates lacking methionine, cysteine, and uridine with or without drugs. Plates were incubated for 72 h at 30 °C.

CaIPF14030 was up-regulated by Ca^{2+} in a calcineurin-dependent manner. It is well documented that calcium can activate the calcineurin pathway and modulate azole activity in *C albicans*[22, 23]. In addition, the dynamic expression of *CaIPF14030* was investigated in the DSF7, DSF14, DSF21, and DSF28 strains obtained in our previous study [18]. The *CaIPF14030* gene shows a steady overexpression state in the DSF7, DSF14, DSF21, and DSF28 strains. These results are similar to those involving other known resistance-related genes such as *ERG11*, *CDR1*, and *CaMDR1*[4, 24]. Taken together, these data suggest that *CaIPF14030* is involved in the development of azole resistance in *C albicans*.

Both copies of *CaIPF14030* were successfully disrupted, and the role of *CaIPF14030* during the development of azole resistance was investigated. A drug susceptibility assay demonstrated that the disruption or ectopic overexpression of *CaIPF14030* did not affect the sensitivity of the tested *C albicans* strains to azoles. Therefore, these data support the hypothesis that *CaIPF14030* does not play an important role in the development of azole resistance in *C albicans*. Recent studies have shown that lower intracellular ATP levels were observed in *C albicans* strains that were azole-resistant or had been treated with azoles[25, 26]. Our data showed that disruption of *CaIPF14030* significantly increased intracellular ATP content, whereas ectopic overexpression of *CaIPF14030* significantly decreased intracellular ATP content. Therefore, *CaIPF14030* may play a critical role in regulating intracellular ATP levels during the development of azole resistance in *C albicans*. Further analysis is required to elucidate the precise relationship between the generation of intracellular ATP that is negatively controlled by *CaIPF14030* and the lower intracellular ATP levels in *C albicans* strains that are azole resistant or have been treated with azoles.

It has been previously reported that there was a strong correlation between azole susceptibility and intracellular ATP levels in *C albicans*[27]. It has also been documented that several peptides have synergistic activity against *C albicans* when combined with fluconazole due to inhibition of production and release of intracellular ATP[28-30]. Because *CaIPF14030* plays a critical role in regulating intracellular ATP levels, the protein encoded by *CaIPF14030* may be targeted by the inhibitors of intracellular ATP. Further studies must be performed to unravel the function of *CaIPF14030* in *C albicans*.

A BLAST search of the *C albicans* genome (available at http://www.genolist.pasteur.fr/CandidaDB/) revealed that the *CaIPF14030* gene (also known as orf19.851) encoded a putative polypeptide of 839 amino acids with a calculated molecular mass of 97.2 kDa. The SOSUI[31] program predicted that the protein encoded by *CaIPF14030* was an integral membrane protein with one membrane-spanning segment. There are two *CaIPF14030* homologs (Mnn4p and YJR061Wp) in the *S cerevisiae* genome database (available at http://www.yeastgenome.org/) that have 30%–37% identity and 44%–55% similarity with the *C albicans* protein. Mnn4p has been shown to be a positive regulator of mannosylphosphate transferase, and it is involved in mannosylphosphorylation of N-linked oligosaccharides. Expression of *MNN4* increases in late-logarithmic and stationary growth phases[32, 33]. It has been shown that YJR061W is a putative membrane protein involved in glycosylation, and it has been shown to be repressed by Rim101p[34, 35]. Further studies are needed to verify whether *CaIPF14030* is involved in mannosylphosphorylation or glycosylation.

Our data show that *CaIPF14030* is up-regulated by Ca^{2+} in a calcineurin-dependent manner as well as during the stepwise acquisition of azole resistance in *C albicans*. Disruption or ectopic overexpression of *CaIPF14030* did not affect the sensitivity of *C albicans* to azoles, although disruption of *CaIPF14030* significantly increased intracellular ATP content, and ectopic overexpression significantly decreased intracellular ATP content. In conclusion, our findings suggest that *CaIPF14030* plays a critical role in the generation of intracellular ATP during the development of azole resistance in *C albicans*.

Acknowledgements

We are grateful to Prof D SANGLARD for the gift of the CAF2-1, DSY2091, DSY2115, DSY2195, MKY268, and DSY1024 strains and to W A FONZI for plasmid p5921. We also thank J PLA for kindly providing the *C albicans* strain RM1000 and P E SUDBERY for plasmid pCaExp. This work was supported by the National Natural Science Foundation of China (No 30900055, 30872276, and 30972650).

Author contribution

Xin-ming JIA and Jun GU designed the experiments; Xin-ming JIA performed the experiments and wrote the paper; and Jundong ZHANG, Ying WANG, Yuan-ying JIANG, and Hongyue TAN critically read the manuscript.

References

1 Richardson MD. Changing patterns and trends in systemic fungal infections. J Antimicrob Chemother 2005; 56: i5–i11.
2 Garber G. An overview of fungal infections. Drugs 2001; 61: 1–12.
3 Prasad R, De Wergifosse P, Goffeau A, Balzi E. Molecular cloning and characterization of a novel gene of *Candida albicans*, CDR1, conferring multiple resistance to drugs and antifungals. Curr Genet 1995; 27: 320–9.
4 Sanglard D, Kuchler K, Ischer F, Pagani JL, Monod M, Bille J. Mechanisms of resistance to azole antifungal agents in *Candida albicans* isolates from AIDS patients involve specific multidrug transporters. Antimicrob Agents Chemother 1995; 39: 2378–86.
5 White TC. Increased mRNA levels of ERG16, CDR, and MDR1 correlate with increases in azole resistance in *Candida albicans* isolates from a patient infected with human immunodeficiency virus. Antimicrob Agents Chemother 1997; 41: 1482–7.
6 Prasad R, Kapoor K. Multidrug resistance in yeast *Candida*. Int Rev Cytol 2005; 242: 215–48.
7 Barker KS, Crisp S, Wiederhold N, Lewis RE, Bareither B, Eckstein J, *et al*. Genome-wide expression profiling reveals genes associated with amphotericin B and fluconazole resistance in experimentally induced antifungal resistant isolates of *Candida albicans*. J Antimicrob Chemother 2004; 54: 376–85.
8 Cowen LE, Nantel A, Whiteway MS, Thomas DY, Tessier DC, Kohn LM, *et al*. Population genomics of drug resistance in *Candida albicans*. Proc Natl Acad Sci U S A 2002; 99: 9284–9.

9 Rogers PD, Barker KS. Genome-wide expression profile analysis reveals coordinately regulated genes associated with stepwise acquisition of azole resistance in *Candida albicans* clinical isolates. Antimicrob Agents Chemother 2003; 47: 1220–7.
10 Xu Z, Zhang LX, Zhang JD, Cao YB, Yu YY, Wang DJ, *et al*. cDNA microarray analysis of differential gene expression and regulation in clinically drug-resistant isolates of *Candida albicans* from bone marrow transplanted patients. Int J Med Microbiol 2006; 296: 421–34.
11 Hooshdaran MZ, Barker KS, Hilliard GM, Kusch H, Morschhauser J, Rogers PD. Proteomic analysis of azole resistance in *Candida albicans* clinical isolates. Antimicrob Agents Chemother 2004; 48: 2733–5.
12 Kusch H, Biswas K, Schwanfelder S, Engelmann S, Rogers PD, Hecker M, *et al*. A proteomic approach to understanding the development of multidrug-resistant *Candida albicans* strains. Mol Genet Genomics 2004; 271: 554–65.
13 Sanglard D, Ischer F, Marchetti O, Entenza J, Bille J. Calcineurin A of *Candida albicans*: involvement in antifungal tolerance, cell morphogenesis and virulence. Mol Microbiol 2003; 48: 959–76.
14 Cannon RD, Lamping E, Holmes AR, Niimi K, Tanabe K, Niimi M, *et al*. *Candida albicans* drug resistance another way to cope with stress. Microbiology 2007; 153: 3211–7.
15 Akins RA. An update on antifungal targets and mechanisms of resistance in *Candida albicans*. Med Mycol 2005; 43: 285–318.
16 Aramburu J, Rao A, Klee CB. Calcineurin: from structure to function. Curr Top Cell Regul 2000; 36: 237–95.
17 Karababa M, Valentino E, Pardini G, Coste AT, Bille J, Sanglard D. CRZ1, a target of the calcineurin pathway in *Candida albicans*. Mol Microbiol 2006; 59: 1429–51.
18 Jia XM, Ma ZP, Jia Y, Gao PH, Zhang JD, Wang Y, *et al*. RTA2, a novel gene involved in azole resistance in *Candida albicans*. Biochem Biophys Res Commun 2008; 373: 631–6.
19 Fonzi WA, Irwin MY. Isogenic strain construction and gene mapping in *Candida albicans*. Genetics 1993; 134: 717–28.
20 Sanglard D, Ischer F, Monod M, Bille J. Susceptibilities of *Candida albicans* multidrug transporter mutants to various antifungal agents and other metabolic inhibitors. Antimicrob Agents Chemother 1996; 40: 2300–5.
21 Care RS, Trevethick J, Binley KM, Sudbery PE. The MET3 promoter: a new tool for *Candida albicans* molecular genetics. Mol Microbiol 1999; 34: 792–8.
22 Cruz MC, Goldstein AL, Blankenship JR, Del Poeta M, Davis D, Cardenas ME, *et al*. Calcineurin is essential for survival during membrane stress in *Candida albicans*. Embo J 2002; 21: 546–59.
23 Steinbach WJ, Reedy JL, Cramer RA Jr, Perfect JR, Heitman J. Harnessing calcineurin as a novel anti-infective agent against invasive fungal infections. Nat Rev Microbiol 2007; 5: 418–30.
24 Calvet HM, Yeaman MR, Filler SG. Reversible fluconazole resistance in *Candida albicans*: a potential *in vitro* model. Antimicrob Agents Chemother 1997; 41: 535–9.
25 Xu Y, Wang Y, Yan L, Liang RM, Tang RJ, Gao PH, *et al*. Proteomic analysis reveals a synergistic mechanism of fluconazole and berberine against fluconazole-resistant *Candida albicans*: endogenous ros augmentation. J Proteome Res 2009; 8: 5296–304.
26 Zheng C, Yan Z, Liu W, Jiang L. Identification and characterization of a functional *Candida albicans* homolog of the *Saccharomyces cerevisiae* TC089 gene. FEMS Yeast Res 2007; 7: 558–68.
27 Kretschmar M, Nichterlein T, Kuntz P, Hof H. Rapid detection of susceptibility to fluconazole in *Candida species* by a bioluminescence assay of intracellular ATP. Diagn Microbiol Infect Dis 1996; 25: 117–21.
28 Lupetti A, Paulusma-Annema A, Welling MM, Dogterom-Ballering H, Brouwer C, Senesi S, *et al*. Synergistic activity of the N-terminal peptide of human lactoferrin and fluconazole against *Candida* species. Antimicrob Agents Chemother 2003; 47: 262–7.
29 Kuipers ME, De Vries HG, Eikelboom MC, Meijer DKF, Swart PJ. Synergistic fungistatic effects of lactoferrin in combination with antifungal drugs against clinical *Candida isolates*. Antimicrob Agents Chemother 1999; 43: 2635–41.
30 Kavanagh K, Dowd S. Histatins: antimicrobial peptides with therapeutic potential. J Pharm Pharmacol 2004; 56: 285–89.
31 Hirokawa T, Boon-Chieng S, Mitaku S. SOSUI: classification and secondary structure prediction system for membrane proteins. Bioinformatics 1998; 14: 378–9.
32 Odani T, Shimma Y, Tanaka A, Jigami Y. Cloning and analysis of the MNN4 gene required for phosphorylation of N-linked oligosaccharides in *Saccharomyces cerevisiae*. Glycobiology 1996; 6: 805–10.
33 Odani T, Shimma Y, Wang XH, Jigami Y. Mannosylphosphate transfer to cell wall mannan is regulated by the transcriptional level of the MNN4 gene in *Saccharomyces cerevisiae*. FEBS Lett 1997; 420: 186–90.
34 Lamb TM, Mitchell AP. The transcription factor Rim101p governs ion tolerance and cell differentiation by direct repression of the regulatory genes NRG1 and SMP1 in *Saccharomyces cerevisiae*. Mol Cell Biol 2003; 23: 677–86.
35 Conde R, Pablo G, Cueva R, Larriba G. Screening for new yeast mutants affected in mannosylphosphorylation of cell wall mannoproteins. Yeast 2003; 20: 1189–211.

Acta Pharmacologica Sinica (2011) 31: 519–527
 1671-4083/11 $32.00
www.nature.com/aps

Original Article

Apoptosis induced by genipin in human leukemia K562 cells: involvement of c-Jun N-terminal kinase in G_2/M arrest

Qian FENG#, Hou-li CAO#, Wei XU, Xiao-rong LI, Yan-qin REN, Lin-fang DU*

Key Laboratory of Bio-resources and Eco-environment of the Ministry of Education, College of Science, Sichuan University, Chengdu 610064, China

Aim: To investigate the effect of genipin on apoptosis in human leukemia K562 cells *in vitro* and elucidate the underlying mechanisms.
Methods: The effect of genipin on K562 cell viability was measured using trypan blue dye exclusion and cell counting. Morphological changes were detected using phase-contrast microscopy. Apoptosis was analyzed using DNA ladder, propidium iodide (PI)-labeled flow cytometry (FCM) and Hoechst 33258 staining. The influence of genipin on cell cycle distribution was determined using PI staining. Caspase 3 activity was analyzed to detect apoptosis at different time points. Protein levels of phospho-c-Jun, phosphor-c-Jun N-terminal kinase (p-JNK), phosphor-p38, Fas-L, p63, and Bax and the release of cytochrome *c* were detected using Western blot analysis.
Results: Genipin reduced the viability of K562 cells with an IC_{50} value of approximately 250 μmol/L. Genipin 200–400 μmol/L induced formation of typical apoptotic bodies and DNA fragmentation. Additionally, genipin 400 μmol/L significantly increased the caspase 3 activity from 8–24 h and arrested the cells in the G_2/M phase. After stimulation with genipin 500 μmol/L, the levels of p-JNK, p-c-Jun, Fas-L, Bax, and cytochrome *c* were remarkably upregulated, but there were no obvious changes of p-p38. Genipin 200–500 μmol/L significantly upregulated the Fas-L expression and downregulated p63 expression. Dicoumarol 100 μmol/L, a JNK1/2 inhibitor, markedly suppressed the formation of apoptotic bodies and JNK activation induced by genipin 400 μmol/L.
Conclusion: These results suggest that genipin inhibits the proliferation of K562 cells and induces apoptosis through the activation of JNK and induction of the Fas ligand.

Keywords: genipin; apoptosis; K562 cells; p-JNK; cell cycle; Fas-L; Bax; cytochrome *c*; p63; dicoumarol

Acta Pharmacologica Sinica (2011) 32: 519–527; doi: 10.1038/aps.2010.158; published online 14 Mar 2010

Introduction

Genipin (Figure 1), an iridoid compound, is an aglycone derived from geniposide. It is the major active ingredient of *Gardenia jasminoides* Ellis fruit, which has long been used in traditional Chinese medicine[1, 2]. Genipin has a molecular weight of 226 and a white crystalline structure. It is soluble in ethanol and ethyl acetate and slightly soluble in water. It also has a low cytotoxicity[2]. Pharmacokinetic studies suggested that geniposide is hydrolyzed into genipin by β-*D*-glucosidases in the intestine and liver[3]. It is genipin, not geniposide, which functions as the main bioactive compound and exhibits the pharmacological activities of the gardenia[4]. Genipin is used to prepare blue colorants in the food industry and as a crosslinking reagent for biological tissue fixation[5].

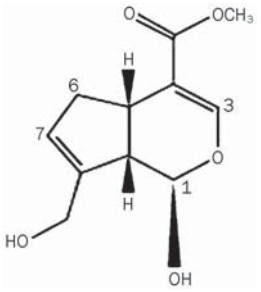

Figure 1. Chemical structure of genipin.

Additionally, genipin has also been shown to possess various pharmacological actions such as anti-inflammatory[2, 6], antiangiogenic[7], antithrombotic[8], anti-diabetic[9], and antioxidative[10] properties, the inhibition of NO production[2] and the protection of neurotrophic activities[11]. Genipin inhibits endothelial exocytosis in human umbilical vein endothelial

# These two authors contributed equally to this work.
* To whom correspondence should be addressed.
E-mail dulinfang@scu.edu.cn
Received 2010-03-18 Accepted 2010-08-12

cells (HUVECs), suppresses vascular and endothelial cell inflammatory activation, and may target acute inflammatory events[12]. Notably, genipin has been shown to induce dose-dependent apoptosis in FaO rat hepatoma cells, human hepatocarcinoma Hep3B cells[13] and PC3 human prostate cancer cells[14]. However, whether genipin shows a potential effect on human leukemia K562 cells and the cellular signaling pathway involved in this potential effect have not been well elucidated.

Stress-activated protein kinase/c-Jun NH_2-terminal kinase (SAPK/$JNK_{1/2}$), a member of the mitogen-activated protein kinase (MAPK) family, is highly activated in response to a variety of stress signals including chemotherapy drugs, tumor necrosis factor, hyperosmotic stress and ultraviolet irradiation. Its activation is most frequently associated with the induction of apoptosis[15–17]. Activated JNK specifically catalyzes the phosphorylation of c-Jun on its N-terminal transactivation domain at Ser63 and Ser73. Phosphorylation of c-Jun, a major target of JNK, is a signal of JNK activation[18]. The death domain-containing receptor Fas and its ligand Fas-L have mainly been studied with respect to their ability to induce apoptosis. JNK/Fas mediation of the apoptotic pathway has been reported in previous studies of genipin[19]. In the present study, we investigated the effect of genipin on apoptosis in human leukemia K562 cells and elucidated the molecular mechanism of cell apoptosis. The results showed that genipin induced apoptosis in K562 cells via blockage of cell cycle progression at the G_2/M phase and the subsequent progression into apoptosis through a multi-signaling pathway.

Materials and methods

Materials

The human leukemia cell line K562 was kindly provided by Professor Sheng-fu LI (Laboratory of Transplant Engineering and Immunology, West China Hospital, Sichuan University, Chengdu, China). Genipin (98%, Figure 1) was purchased from Haikang Biotechnology Co, Ltd (Chengdu, China) and dissolved in distilled water (13.1 mg/mL, pH 7.4). The solution of genipin was filtered with Millipore filtration and stored at -20 °C. Triton X-100, Tris base, SDS, acrylamide, bisacrylamide, ammonium persulfate and TEMED were from Amresco Co (Solon, OH, USA). RPMI-1640 medium was from Gibco Co (Langley, USA). Fetal bovine serum (FBS) was from HyClone Co (Beijing, China). Antibodies against p63, β-actin, Bax and cytochrome *c* were from Cell Signaling Technology Co (Boston, USA). Phosphorylated antibodies (anti-phosphor-JNK, anti-phosphor-c-Jun, and anti-phosphor-p38) were purchased from Cell Signaling Technology Co (Boston, USA). The antibody against Fas-L was from Millipore Co (Billerica, USA). The 0.25% Trypsin/EDTA solution, penicillin and streptomycin were from Beijing Solarbio Science & Technology Co, Ltd (Beijing, China). Peroxidase-conjugated AffiniPure goat anti-rabbit and goat anti-mouse immunoglobulin were from ZSGB-BIO Co, Ltd (China). Dicoumarol (a JNK inhibitor) was purchased from NICPBP (Beijing, China). PVDF paper and the enhanced chemiluminescence (ECL) Western blot detection system were purchased from Millipore Co (Billerica, USA). Trypan blue was from Sigma Co (USA). The Apoptosis DNA Ladder Detection Kit and the Caspase 3 Activity Assay Kit were from the Beyotime Institute of Biotechnology Co (Nanjing, China). The Apoptotic Body/Nuclear DNA Staining Kit was from Bio Basic Inc (Toronto, Canada). All stock solutions were stored at 4 or -20 °C. All other chemicals were of analytical grade.

Cell culture

K562 cells were cultured in RPMI-1640 medium with 10% (*v/v*) heat-inactivated FBS, 100 U/mL penicillin and 100 μg/mL streptomycin in humidified atmosphere at 37 °C with 5% CO_2. Cells were seeded at a density of 5×10^4 in 100-mm Petri dishes and incubated for 6 h before drug treatment. Various concentrations of genipin were added to each well. Experiments were performed in triplicate.

Cell viability assays

Cell viability was determined by direct cell counting. K562 cells were cultured in 24-well plates at a density of 2×10^4 cells/well for 6 h and then incubated with various concentrations of genipin (100, 200, 300, 400, and 500 μmol/L) for 24 h. The cells were then stained with trypan blue dye and counted with a hemocytometer. The result was expressed as a percentage relative to the control, and the IC_{50} values were calculated.

Morphological observation of cells

After being cultured at 37 °C for 6 h in 100-mm Petri dishes, K562 cells were treated with various concentrations of genipin (0, 200, 300, and 400 μmol/L) for 24 h. K562 cells were observed with a phase-contrast microscope (Leica DMIRB, Germany).

Analysis of DNA fragmentation

After incubation with the designated concentrations of genipin (200, 300, 400, and 500 μmol/L) for 24 h, 1×10^6 K562 cells were collected. Genomic DNA was extracted from untreated and genipin-treated cells using the Apoptosis Ladder Detection Kit. The DNA was then electrophoresed in a 1.0% agarose gel and visualized by ethidium bromide (EB) staining. The gel was photographed under ultraviolet light.

Caspase 3 activity assay

Caspase 3 activity in cytosolic extracts was determined using a spectrophotometric assay as described by Song *et al*[20]. Briefly, supernatants from cell lysates treated with 400 μmol/L genipin for different amounts of time were incubated at 37 °C with Ac-DEVE-MCA, a fluorogenic substrate of caspase 3. Cleavage of the substrate was monitored at 405 nm. Data were normalized for the protein content of each supernatant and expressed as the relative value compared to the untreated group (time 0 h).

Flow cytometric analysis of the cell cycle and apoptosis

To further measure the apoptosis induction activity of genipin, K562 cells were incubated for 24 h in 6-well plates with geni-

pin. Cells were then harvested, washed twice with ice-cold phosphate-buffered saline (PBS) and fixed with 70% ethanol at 4 °C. Before the samples were analyzed the DNA was stained on ice with 200 μL of cold (4 °C) propidium iodine (PI) for 10 min in the dark. DNA-bound PI fluorescence was measured using a 15 mW air-cooled argon ion laser at 488 nm as the excitation source and an EPICS ELITE ESP flow cytometer (Beckman Coulter, USA). Analysis of the cell cycle was performed with Coulter Elite 4.5 Multicycle software. Ten thousand events were recorded for each sample[21].

Electrophoresis and immunoblotting

K562 cells were treated for 24 h with different concentrations of genipin (200, 300, 400, and 500 μmol/L). The cells were then harvested and washed with PBS. Whole cell lysates were obtained using cell lysis solution [250 mmol/L NaCl, 50 mmol/L Tris-HCl (pH 7.4), 0.1% SDS, 1% Triton X-100, 1 mmol/L EDTA, 50 mmol/L NaF, and 1 mmol/L PMSF], followed by centrifugation (12 000×*g*, 30 min). Protein samples were heated at 95 °C for 5 min, normalized to a total of 100 μg per lane, resolved by SDS-PAGE, transferred onto PVDF membranes (Millipore) by electroblotting, and probed with antibodies against phosphor-JNK, phosphor-c-Jun, phosphor-p38, p63, Bax, Fas-L, and cytochrome *c*. Primary antibodies were detected with goat anti-rabbit antibody conjugated to horseradish peroxidase using enhanced chemiluminescence with the Immobilon™ Western Chemiluminescent HRP Western blotting detection system (Millipore). Photographs were taken with the ChemiDoc XRS automatic photomicrograph system (Bio-RAD, USA) and analyzed using Quantity One software.

Analysis of cytochrome *c* release

K562 cells were collected by centrifugation at 300×*g* for 5 min at 4 °C and lysed with cell lysis solution for the mitochondrial cytochrome *c* release assay. Samples were then centrifuged at 12 000×*g* at 4 °C for 30 min. Supernatants containing the cytosolic proteins were recovered and analyzed using Western blotting.

Hoechst 33258 staining

Nuclear fragmentation of K562 cells treated with 400 μmol/L genipin was visualized by Hoechst 33258 staining following the use of the Apoptotic body/Nuclear DNA Staining Kit (Canada). Briefly, K562 cells were cultured in 6-well plates for 6 h and then co-incubated for 1 h with 100 μmol/L dicoumarol, an inhibitor of JNK activation[22], before treatment with 400 μmol/L genipin. After treatment for 24 h, the cells were washed with PBS, fixed in 10% formaldehyde solution for 5 min at room temperature and resuspended in 50 μL of PBS before deposition on cover slips. The adhered cells were incubated with Hoechst 33258 for 20 min at room temperature. Cover slips were rinsed with PBS and imaged by fluorescence microscopy (Nikon Eclipse ET2000-E, Japan). Three replicate wells were analyzed for each treatment by the quantitative and qualitative examination of three random fields in each well. Cell viability was calculated from the number of viable cells excluding apoptotic nuclei *vs* the total number of nuclei in each well.

Statistical analysis

Data were presented as the mean±SD and were representative of three independent experiments. Statistical differences were evaluated using the Student's *t*-test.

Results

Effect of genipin on cell viability

The effect of genipin on cell viability was evaluated by the trypan blue dye exclusion method; cells were counted with a hemocytometer. A significant decrease in viable cells and total cell number was detected after treatment with genipin for 24 h. Cell viability decreased to 22.75% of the control after treatment with genipin 500 μmol/L (Figure 2). The IC_{50} of genipin in K562 cells was approximately 250 μmol/L. Genipin showed dose-dependent cytotoxic and antiproliferative effects on K562 cells.

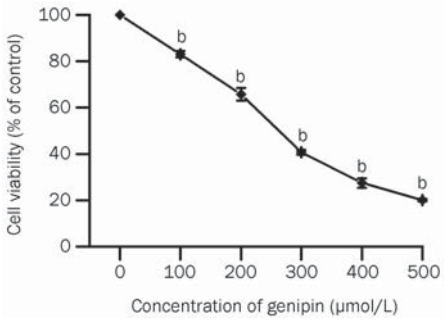

Figure 2. Effect of genipin on cell viability in K562 cells. Cells were treated *in vitro* for 24 h with various concentrations of genipin (0, 100, 200, 300, 400, and 500 μmol/L). Cell viability was determined by cell counting. Data are the mean±SD of three independent experiments. $^bP<0.05$ *vs* control.

Morphological changes in genipin-treated K562 cells

To better clarify the changes in cell morphology induced by genipin, K562 cells were exposed to the indicated concentrations of genipin for 24 h and then observed under a microscope. As shown in Figure 3, characteristic morphological changes were observed in K562 cells. Control K562 cells had normal features with round and homogeneous nuclei (Figure 3A). Significant morphological changes were observed in the cells after treatment with genipin. Cells exhibited the characteristic features of apoptosis such as cell shrinkage, membrane blebbing, and the appearance of apoptotic bodies (Figure 3B–3D, arrows). Genipin was found to inhibit the growth of K562 cells and increase the number of apoptotic cells in a dose-dependent manner. The exposure of K562 cells to 400 μmol/L genipin resulted in the most obvious apoptotic phenomena.

DNA fragmentation

An important feature of apoptosis is the fragmentation of

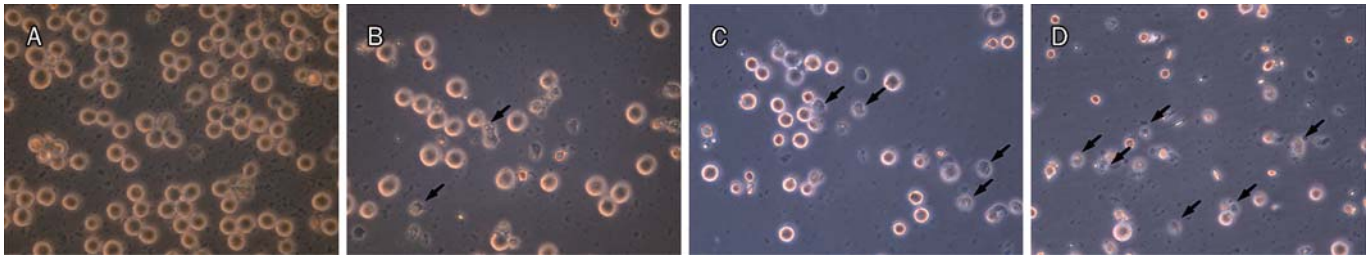

Figure 3. Morphological changes in K562 cells when treated for 24 h with different concentrations of genipin. The cells were observed under a microscope (phase-contrast microscopic view). (A) Control; (B) K562 cells treated with 200 μmol/L genipin; (C) K562 cells treated with 300 μmol/L genipin; (D) K562 cells treated with 400 μmol/L genipin. Apoptotic cells are shown with arrows, 400× magnification.

genomic DNA into integer multiples of 180-200 bp, which results in a characteristic ladder upon agarose gel electrophoresis. Experiments showed that the DNA of K562 cells presented typical ladder-like pattern after treatment with genipin at the indicated concentration (Figure 4). Genipin induced apoptosis in K562 cells.

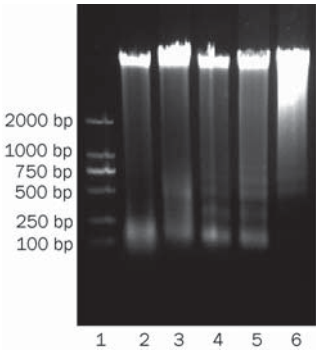

Figure 4. K562 cells were cultured for 24 h in the presence or absence of the indicated concentration of genipin. DNA was isolated and visualized on a 1.0% agarose gel stained with ethidium bromide. Lane 1, DL2000 Marker; lane 2, control; lane 3, 200 μmol/L; lane 4, 300 μmol/L; lane 5, 400 μmol/L; lane 6, 500 μmol/L.

Involvement of caspase 3 in genipin-induced apoptosis

We examined whether apoptosis is induced in genipin-treated K562 cells and when the cells become apoptotic. We measured the activity of caspase 3, the critical mediator of apoptosis, in cytosolic extracts using Ac-DEVD-MCA as its fluorogenic substrate. Genipin significantly activated caspase 3 after 6 h of treatment; the trend increased slightly near 24 h (Figure 5). Caspase 3 activity increased within 24 h in a time-dependent manner in K562 cells treated with 400 μmol/L genipin.

Effect of genipin on apoptosis and the induction of G_2/M cell cycle arrest in K562 cells

Apoptosis and cell cycle distribution were examined at the indicated concentration of genipin. The flow cytometry results shown in Figures 6A–6C demonstrated that the population of apoptotic cells (propidium iodide-positive cells) gradually increased to 17.9% and 27.6% (4- and 7-fold) when the cells were treated with 200 and 400 μmol/L genipin, respectively; the increase in the control group was 4.1%. A dramatic hypodiploid (sub-G_1) population was seen with 400 μmol/L genipin and is shown in Figure 6D. The results suggested that genipin could induce the apoptosis of K562 cells in a dose-dependent manner.

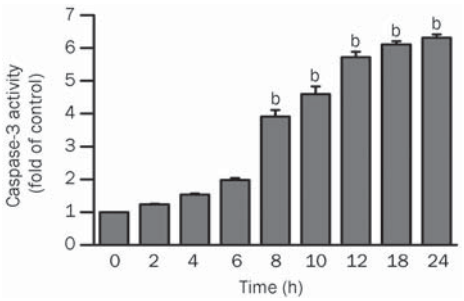

Figure 5. Activation of caspase 3 in K562 cells treated with 400 μmol/L genipin. Enzymatic activity is represented as $\Delta A_{405\ nm}$ per min per mg protein. Data are mean±SD of three independent experiments. $^bP<0.05$ *vs* control.

Cell cycle distribution was analyzed by comparing the percentage of cells in the G_0/G_1, S, and G_2/M populations between the control group and cells treated with genipin for 24 h (Figure 6E and Table 1) without taking into consideration the apoptotic cell (sub G_0/G_1) population. In the control cells, the G_2/M population represented 24.1% of the total number of viable cells. After 24 h of treatment with 200 μmol/L and 400

Table 1. Effect of genipin on cell cycle distribution in K562 cells. The cells in G_0/G_1, S and G_2/M phase was shown in the form. Data are expressed as mean±SD of 3 independent experiments.

Cell cycle distribution	Concentration of genipin (24 h)		
	Control	200 μmol/L	400 μmol/L
% G_0/G_1	38.3±1.6	33.2±2.2	30±0.2
% S	37.6±5.3	35.4±1.8	28.4±2.4
% G_2/M	24.0±6.8	31.5±0.3	41.7±2.6

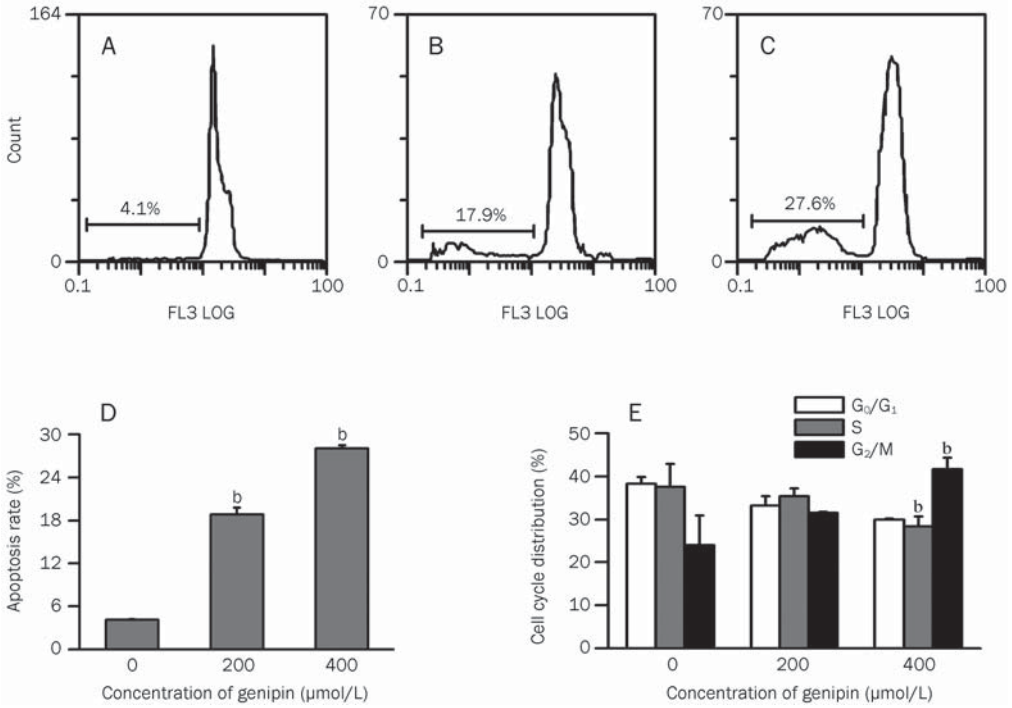

Figure 6. Effect of genipin on the sub-G_1 population and cell cycle distribution in K562 cells. K562 cells were incubated for 24 h in the absence (A) or presence of (B) 200 μmol/L and (C) 400 μmol/L genipin. Cells were then collected, stained with propidium iodide and analyzed by flow cytometry. The percentage of apoptotic cells is shown in each chart, and the apoptosis rate (D) and cell cycle distribution (E) are shown in the histogram. The histogram was obtained using Origin Version 8.0 software. Data are the mean±SD of 3 independent experiments. $^bP<0.05$ *vs* control.

μmol/L genipin, the G_2/M population increased to 31.5% and 41.7% (near 1.5- and 2-fold) of the total viable cells, respectively. This change was accompanied by a decrease in the G_1 and S populations (Table 1). Moreover, it occurred in a dose-dependent manner. Treatment with genipin significantly altered the cell cycle profile and increased the number of apoptotic cells, demonstrating that the decrease in cell viability is due to an induction in cell apoptosis and is related to cell cycle arrest. These findings support the conclusions that the induction of cell death is due to apoptosis and that genipin arrests K562 cells at the G_2/M phase.

Activation of JNK and phosphor-c-Jun expression in genipin-treated K562 cells

To elucidate the signaling pathways involved in the genipin-induced apoptosis of K562 cells, we evaluated the expression of phosphor-JNK and phosphor-c-Jun, a target of JNK, by using Western blotting. JNK has three isoforms (JNK_1, JNK_2, and JNK_3) with splicing variants that are either p46 or p54 in size[23]. Obvious p-JNK and p-c-Jun bands were detected. The results showed that the protein levels of p-JNK and p-c-Jun were increased in a dose-dependent manner; they were dramatically increased after treatment with 500 μmol/L genipin in comparison to the control (Figure 7A, 7B). The protein level

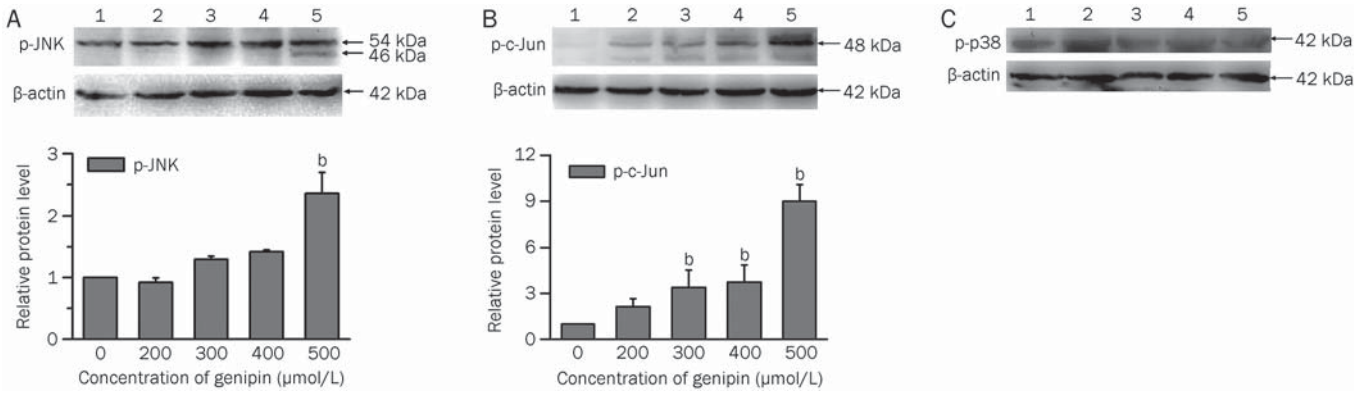

Figure 7. Effect of genipin on phospho-JNK (A), phospho-c-Jun (B) and phospho-p38 (C) activation in K562 cells. K562 cells were treated for 24 h with the indicated concentrations of genipin. The cells were harvested and lysed. Total protein (100 μg per lane) was loaded on the SDS gel, electrophoresed, transferred to PVDF membranes, and probed with antibodies against p-JNK, p-c-Jun and p-p38. Lane 1, control; lane 2, 200 μmol/L; lane 3, 300 μmol/L; lane 4, 400 μmol/L; lane 5, 500 μmol/L. Histograms indicated the changes in p-JNK and p-c-Jun expression as compared to the control. Relative protein levels (fold of the control) were obtained using Quantity One software. Histograms were obtained using Origin Vision 8.0 software. Data are the mean±SD of three independent experiments. $^bP<0.05$ *vs* control.

of p-p38, another stress kinase and member of MAPK family, did not change significantly in the K562 cells exposed to genipin (Figure 7C).

Fas-L and p63 expression in genipin-treated K562 cells

To further confirm that apoptosis was induced by genipin through the death-receptor pathway, Fas-L and p63, two signaling proteins in the apoptotic pathways, were detected by Western blot analysis. The expression of death-receptor Fas-L was induced by genipin in a concentration-dependent manner (Figure 8). Because K562 cells lack functional p53[24], the expression of p63 in genipin-treated K562 cells was investigated. Genipin downregulated the expression of p63 (Figure 8). p63 in general and one of its specific isoforms, ΔNp63α, are overexpressed in a variety of squamous cell cancers. However, their expression is downregulated in apoptotic cells[25]. These results demonstrated that the genipin-induced apoptosis is accompanied by the up-regulation of Fas-L and the downregulation of p63 in K562 cells.

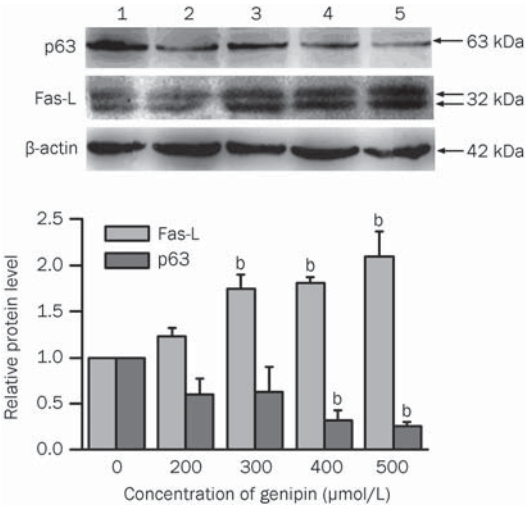

Figure 8. Effect of genipin on Fas-L and p63 expression in K562 cells. K562 cells were treated for 24 h with the indicated concentration of genipin. The Western blot was analyzed using antibodies against Fas-L and p63. Lane 1, control; lane 2, 200 μmol/L; lane 3, 300 μmol/L; lane 4, 400 μmol/L; lane 5, 500 μmol/L. The histogram indicated the changes in Fas-L and p63 expression as compared to the control. The mean densities were obtained using Quantity One software. The histogram was obtained using Origin Vision 8.0 software. Data are the mean±SD of three independent experiments. $^bP<0.05$ *vs* control.

Increase in Bax expression and cytochrome *c* release after genipin treatment

To clarify whether the mitochondria-dependent pathway is involved in genipin-induced apoptosis, the expression of Bax and the efflux of cytochrome *c* into the cytosol were examined in genipin-treated K562 cells using Western blotting. As shown in Figure 9, accumulation of the Bax protein was observed and cytochrome *c* content increased significantly in

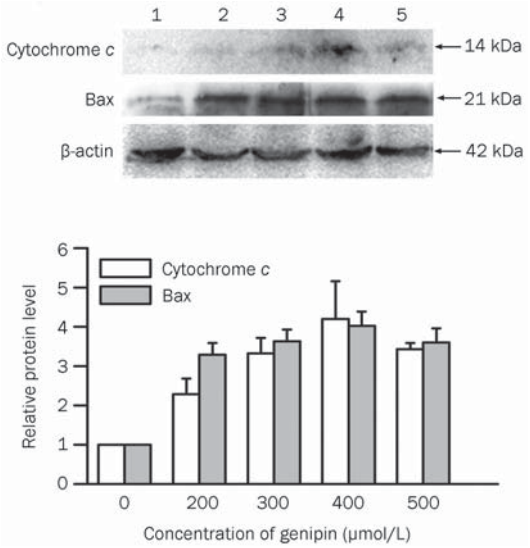

Figure 9. Genipin induced Bax expression and cytochrome *c* release into the cytosol of K562 cells. K562 cells were treated for 24 h with the indicated concentrations of genipin. The Western blot was analyzed using antibodies against Bax and cytochrome *c*. Lane 1, control; lane 2, 200 μmol/L; lane 3, 300 μmol/L; lane 4, 400 μmol/L; lane 5, 500 μmol/L. The histogram indicated the changes in cytochrome *c* release into the cytosol and Bax expression as compared to the control. The mean densities were obtained using Quantity One software. The histogram was obtained using Origin Vision 8.0 software. Three independent experiments were conducted and revealed similar patterns of changes. Data are the mean±SD of three independent experiments. $^bP<0.05$ *vs* control.

the cytosol of genipin-treated K562 cells. These results showed that genipin-induced apoptosis resulted in cytochrome *c* release from the mitochondria into the cytosol in K562 cells.

Activation of JNK in genipin-induced apoptosis

As shown in Figure 7, the activation of JNK was involved in genipin-induced apoptosis in K562 cells. To clarify the role of JNK activation, we tested the effect of dicoumarol, a JNK inhibitor[22], on genipin-induced apoptosis and JNK activation. Nuclear fragmentation in K562 cells treated for 24 h with 400 μmol/L genipin was determined by Hoechst 33258 staining (Figures 10E and 10F). Apoptotic bodies containing nuclear fragments were found only in genipin-treated cells; the nuclear envelope appeared lytic and the cytoplasm had shrunk (Figures 10E and 10F). In contrast, cells cultured with dicoumarol only (Figures 10C and 10D) or with genipin and dicoumarol (Figures 10G and 10H) showed normal cell nuclei morphology as in the control (Figures 10A and 10B). These results showed that dicoumarol markedly suppressed the formation of apoptotic bodies and inhibited genipin-induced JNK activation. Additionally, the results of cell viability analyses in Figure 10I revealed that genipin-induced apoptosis was effectively inhibited by the addition of a JNK inhibitor. Taken together, these results indicated that the JNK signaling pathway mediated the genipin-induced apoptosis in K562 cells.

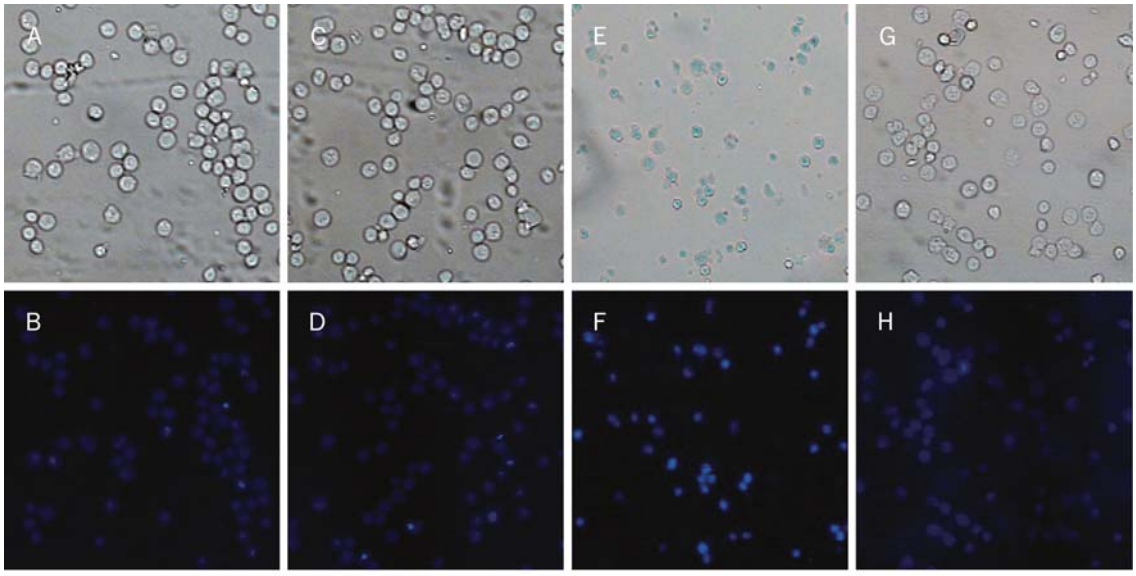

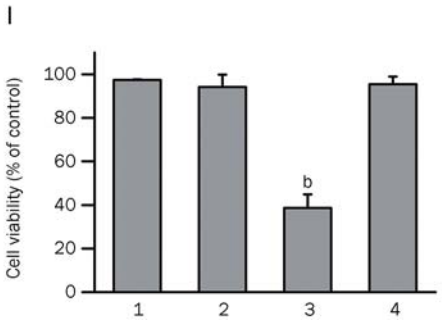

Figure 10. Effect of a JNK inhibitor on genipin-induced apoptosis. K562 cells were treated for 24 h with vehicle or 400 μmol/L genipin in the absence or presence of the JNK1/2 inhibitor dicoumarol (100 μmol/L). Morphological changes in K562 cells treated with 400 for 24 h were observed by Hoechst 33258 staining and fluorescence microscopy. Fragmented or condensed nuclei indicative of apoptosis could be observed in the genipin-treated groups (E, F). However, the dicoumarol-treated cells (C, D) and the dicoumarol and genipin-treated cells (G, H) showed normal cell nuclei morphology as observed in untreated cells (A, B). (400×magnification). Cell viability of each group is shown in the histogram (I), which was obtained using Origin Version 8.0 software. 1, control; 2, dicoumarol-treated cells; 3, genipin-treated cells; 4, dicoumarol and genipin-treated cells. Three independent experiments were conducted and revealed similar patterns of changes. Mean±SD. n=3. $^bP<0.05$ *vs* control.

Discussion

In recent years, genipin has been found to display potent anticancer effects. Genipin has been reported to induce apoptosis in FaO rat hepatoma cells, human hepatocarcinoma Hep3B cells and PC3 human prostate cancer cells[13, 14]. However, the exact mechanism of genipin-induced apoptosis has not yet to be determined. The present study demonstrates that genipin, a plant-derived iridoid, induces apoptosis in human K562 leukemia cells in a dose-dependent manner involving the activation of JNK/Fas-L signaling and G_2/M arrest.

Apoptosis is characterized by specific morphological changes such as condensation of chromatin, nuclear fragmentation, blebbing of the plasma membrane, and the presence of apoptotic bodies[26]. We observed the typical characteristics of apoptosis in genipin-treated K562 cells using phase-contrast microscopy (Figure 3) and fluorescence microscopy (Figure 10). DNA fragmentation, a hallmark of apoptosis, was demonstrated by fragments ranging in size from 180 to 200 bp (Figure 4). Inhibition of cell viability (Figure 2) and the formation of a sub-G_1 peak of apoptosis (Figure 6) were observed in a dose-dependent manner. These results demonstrated that the death of K562 cells induced by genipin was due to apoptosis. Caspase 3, one of the crucial mediators of apoptosis, is an executioner caspase that can be activated by a mitochondrial pathway or a death receptor pathway[27]. Activation of caspase 3 was observed in genipin-treated cells and increased dramatically after 6 h of incubation (Figure 5).

Perturbation of the progression of the cell cycle is a signal that can trigger apoptotic cell death[28]. Several studies have reported that various cytotoxic drugs can induce G_2/M phase arrest. As shown in Figure 6, genipin induced the dose-dependent accumulation of cells in the G_2/M phase of the cell cycle with subsequent accumulation in the sub-G_1 phase suggesting the sequential events of cell cycle arrest followed by apoptosis. Innocente *et al*[29] reported that p53 arrested the cells at the G_2/M phase. However, we determined by Western blot that K562 cells were deficient in functional p53 (data not shown), which was consistent with the results of Lubbert *et al*[24]. Mutation or dysfunction of p53 is found in more than half of all human cancers. However, p63, a transcription factor homologous to p53, was found to be gradually reduced in a dose-dependent manner in our study (Figure 8). p63 has a critical physiological function. There is evidence that p63 in general and its specific ΔNp63α isoform are overexpressed in a variety of squamous cell cancers and in other types of cancers and could act as oncogenes[25, 30, 31]. Stravopodis *et al*[32] reported the dose-dependent attenuation of p63 expression in RT4 cells at the mRNA level in doxorubicin-induced apoptosis. This result

suggested that p63 might regulate apoptosis in genipin-treated K562 cells.

The prolonged and persistent activation of JNK and c-Jun induce apoptotic cell death. Previous studies have shown upregulation of JNK activation in FaO rat hepatoma cells and human hepatocarcinoma Hep3B cells with genipin-induced apoptosis[13]. It has also been reported that JNK plays an important role in IQDMA-mediated G_2/M arrest and apoptosis of K562 cancer cells[33]. Although JNK and p38 MAPKs are collectively termed stress-activated protein kinases and are activated by a variety of stress-related stimuli and chemotherapy drugs[15, 16], there was no obvious change in p-p38 (Figure 7C) in our studies. Kim *et al*[13] reported that the phosphorylation of JNK was clearly detectable in genipin-treated FaO cells, whereas MEK1/2 and p38 MAPKs were not activated after genipin treatment. Here, genipin dose-dependently upregulated the phosphorylation levels of JNK in K562 cells (Figure 7A). The effect of JNK was supported by dose-dependent phosphorylation of c-Jun, a substrate of JNK (Figure 7B). Furthermore, the involvement of JNK activation was confirmed by the use of dicoumarol (a JNK inhibitor)[22] (Figure 10). These results suggest that the genipin-induced apoptosis in K562 cells occurs through the JNK activation pathway.

The Fas/Fas-L pathway is an important cellular pathway regulating the induction of apoptosis in a variety of cell types. JNK has been found to contribute to death receptor apoptotic signaling via c-Jun/AP-1, which leads to the transcriptional activation of Fas-L[19]. Peng *et al*[34] suggested that JNK/Fas plays a pivotal role in $(Ac)_5$GP-induced apoptosis. In the present study, the expression of Fas-L in genipin-treated K562 cells was found to increase dose-dependently (Figure 8), suggesting that genipin triggered Fas-L signaling following JNK activation and induced the death receptor apoptotic pathway in K562 cells. Mundt *et al*[35] suggested that the ΔNp63α isoform of p63 negatively regulated genes encoding Fas. Thus, p63 downregulation may regulate Fas/Fas-L activation. These results indicate that the activation of Fas-L might be attributed to both JNK activation and p63 downregulation in genipin-treated K562 cells; Fas-L is then able to activate caspases to induce apoptosis.

Bax is a member of Bcl-2 family and also plays a crucial role in apoptosis as a proapoptotic protein. Accumulation of the Bax protein was observed (Figure 9) and cytochrome *c* content was significantly increased in the cytosol of genipin-treated K562 cells suggesting that genipin-induced apoptosis also occurs through the mitochondrial apoptotic pathway. It has been reported that genipin induces apoptotic cell death in PC3 cells via JNK-dependent activation of the mitochondrial pathway[14]. Several experiments also revealed that activation of the JNK pathway can also cause cytochrome *c* release from the mitochondria to the cytosol and that apoptotic stimuli fail to release cytochrome *c* in JNK null cells[36]. Additionally, the ΔNp63α isoform repressed apoptosis-related genes of the mitochondrial apoptotic pathway[35].

In conclusion, a signaling pathway associated with genipin-induced apoptosis in K562 cells was preliminarily examined in the present study. Treatment of K562 cells with genipin resulted in G_2/M phase cell cycle arrest and cell apoptosis in a dose-dependent manner. Additionally, the activation of JNK was shown to play a crucial role in genipin-induced apoptosis in K562 cells. Downregulation of p63 may result in both Fas-L activation and cytochrome *c* release, which are related to the death receptor pathway and mitochondrial apoptotic pathway, respectively. These changes lead to caspase 3 activation and the ultimate induction of apoptosis in K562 cells. Further studies will be performed on the specific apoptotic signaling pathways in genipin-induced apoptosis in K562 cells. Taken together, our research provided important insights into the anticancer activity of genipin.

Acknowledgements

This study was supported by the grants from the Key Technologies R&D Program of Sichuan Province (2008SG0025), the Program for New Century Excellent Talents in University (NCET-04-0861) and Sichuan University Research Grant 985. We thank Dr Yong-sheng LIU for kindly providing the electron microscope, Yong-qiu MAO for providing the flow cytometer and assistance, and Sheng-fu LI for providing K562 cells.

Author contribution

Qian FENG, Hou-li CAO, and Lin-fang DU designed the research; Qian FENG, Hou-li CAO, Wei XU, Xiao-rong LI, and Yan-qin REN performed the research; Qian FENG, Hou-li CAO, and Lin-fang DU contributed new analytical reagents and analyzed the data; Qian FENG and Lin-fang DU wrote the paper.

References

1 Tseng TH, Chu CY, Huang JM, Shiow SJ, Wang CJ. Crocetin protects against damage in rat primary hepatocytes. Cancer Lett 1995; 97: 61–7.
2 Koo HJ, Song YS, Kim HJ, Lee YH, Hong SM, Kim SJ, *et al*. Anti-inflammatory effects of genipin, an active principle of gardenia. Eur J Pharmacol 2004; 495: 201–8.
3 Akao T, Kobashi K, Aburada M. Enzymic studies on the animal and intestinal bacterial metabolism of geniposide. Biol Pharm Bull 1994; 17: 1573–6.
4 Zheng HZ, Dong ZH, Yu J. Modern research and application of Chinese Traditional Medicine, vol 4. Beijing, China: Academy Press; 2000. p 3166–72.
5 Hou YC, Tsai SY, Lai PY, Chen YS, Chao PD. Metabolism and pharmacokinetics of genipin and geniposide in rats. Food Chem Toxicol 2008; 46: 2764–9.
6 Koo HJ, Lim KH, Jung HJ, Park EH. Anti-inflammatory evaluation of gardenia extract, geniposide and genipin. J Ethnopharmacol 2006; 103: 496–500.
7 Park EH, Joo MH, Kim SH, Lim CJ. Antiangiogenic activity of *Gardenia jasminoides*. Fruit Phytother Res 2003; 17: 961–2.
8 Suzuki Y, Kondo K, Ikeda Y, Umemura K. Antithrombotic effect of geniposide and genipin in the mouse thrombosis model. Planta Med 2001; 67: 807–10.
9 Zhang CY, Parton LE, Ye CP, Krauss S, Shen R, Lin CT, *et al*. Genipin inhibits ucp2-mediated proton leak and acutely reverses obesity- and

high glucose-induced beta cell dysfunction in isolated pancreatic islets. Cell Metab 2006; 3: 417–27.
10 Okada K, Shoda J, Kano M, Suzuki S, Ohtake N, Yamamoto M, *et al*. Inchinkoto, a herbal medicine, and its ingredients dually exert Mrp2/MRP2-mediated choleresis and Nrf2-mediated antioxidative action in rat livers. Am J Physiol Gastrointest Liver Physiol 2007; 292: G1450–63.
11 Yamazaki M, Chiba K. Genipin exhibits neurotrophic effects through a common signaling pathway in nitric oxide synthase-expressing cells. Eur J Pharmacol 2008; 581: 255–61.
12 Wang GF, Wu SY, Rao JJ, Lü L, Xu W, Pang JX, *et al*. Genipin inhibits endothelial exocytosis via nitric oxide in cultured human umbilical vein endothelial cells. Acta Pharmacol Sin 2009; 30: 589–96.
13 Kim BC, Kim HG, Lee SA, Lim S, Park EH, Kim SJ, *et al*. Genipin-induced apoptosis in hepatoma cells is mediated by reactive oxygen species/c-Jun NH_2-terminal kinase-dependent activation of mitochondrial pathway. Biochem Pharmacol 2005; 70: 1398–407.
14 Hong HY, Kim BC. Mixed lineage kinase 3 connects reactive oxygen species to c-Jun NH2-terminal kinase-induced mitochondrial apoptosis in genipin-treated PC3 human prostate cancer cells. Biochem Biophys Res Commun 2007; 362: 307−12.
15 Johnson GL, Lapadat R. Mitogen-activated protein kinase pathways mediated by ERK, JNK, and p38 protein kinases. Science 2002; 298: 1911–2.
16 Yu JH, Wang HJ, Li XR, Tashiro S, Ikejima T. Protein tyrosine kinase, JNK, and ERK involvement in pseudolaric acid B-induced apoptosis of human breast cancer MCF-7 cells. Acta Pharmacol Sin 2008; 29: 1069−76.
17 Lei XY, Yao SQ, Huang ZX, Liu LJ, Zhong M, Zhu BY, *et al*. Apoptosis induced by diallyl disulfide in human breast cancer cell line MCF-7. Acta Pharmacol Sin 2008; 29: 1233−9.
18 Kennedy NJ, Davis RJ. Role of JNK in tumor development. Cell Cycle 2003; 2: 199–201.
19 Luo J, Sun Y, Lin H, Qian Y, Li Z, Leonard SS, *et al*. Activation of JNK by vanadate induces a Fas-associated death domain (FADD)-dependent death of cerebellar granule progenitors *in vitro*. J Biol Chem 2003; 278: 4542–51.
20 Song JQ, Teng X, Cai Y, Tang CS, Qi YF. Activation of Akt/GSK-3beta signaling pathway is involved in intermedin(1–53) protection against myocardial apoptosis by ischemia/reperfusion. Apoptosis 2009; 14: 1299–307.
21 Li Z, Liu Y, Zhao X, Pan X, Yin R, Huang C, *et al*. Honokiol, a natural therapeutic candidate, induces apoptosis and inhibits angiogenesis of ovarian tumor cells. Eur J Obstet Gynecol Reprod Biol 2008; 140: 95–102.
22 Seanor KL, Cross JV, Nguyen SM, Yan M, Templeton DJ. Reactive quinones differentially regulate SAPK/JNK and p38/mHOG stress kinases. Antioxid Redox Signal 2003; 5: 103–13.
23 Barr RK, Bogoyevitch MA. The c-Jun N-terminal protein kinase family of mitogen-activated protein kinase (JNK/MAPKs). Int J Biochem Cell Biol 2001; 33: 1047–63.
24 Lubbert M, Miller CW, Crawford L, Koeffler HP. p53 in chronic myelogenous leukemia. Study of mechanisms of differential expression. J Exp Med 1988; 167: 873–86.
25 Hu H, Xia SH, Li AD, Xu X, Cai Y, Han YL, *et al*. Elevated expression of p63 protein in human esophageal squamous cell carcinomas. Int J Cancer 2002; 102: 580-3.
26 Reed JC. Apoptosis-targeted therapies for cancer. Cancer Cell 2003; 3: 17–22.
27 Wolf BB, Green DR. Suicidal tendencies: apoptotic cell death by caspase family proteinases. J Biol Chem 1999; 274: 20049–52.
28 Wang CL, Ng TB, Yuan F, Liu ZK, Liu F. Induction of apoptosis in human leukemia K562 cells by cyclic lipopeptide from *Bacillus subtilis* natto T-2. Peptides 2007; 28: 1344–50.
29 Innocente SA, Abrahamson JL, Cogswell JP, LeeJM. p53 regulates a G_2 checkpoint through cyclin B1. Proc Natl Acad Sci USA 1999; 96: 2147–52.
30 Massion PP, Taflan PM, Jamshedur Rahman SM, Yildiz P, Shyr Y, Edgerton ME, *et al*. Significance of p63 amplification and overexpression in lung cancer development and prognosis. Cancer Res 2003; 63: 7113–21.
31 Pruneri G, Fabris S, Dell'Orto P, Biasi MO, Valentini S, Del Curto B, *et al*. The transactivating isoforms of p63 are overexpressed in high-grade follicular lymphomas independent of the occurrence of p63 gene amplification. J Pathol 2005; 206: 337−45.
32 Stravopodis DJ, Karkoulis PK, Konstantakou EG, Melachroinou S, Lampidonis AD, Anastasiou D, *et al*. Grade-dependent effects on cell cycle progression and apoptosis in response to doxorubicin in human bladder cancer cell lines. Int J Oncol 2009; 34: 137–60.
33 Yang SH, Chien CM, Lu CM, Chen YL, Chang LS, Lin SR. Involvement of c-Jun N-terminal kinase in G_2/M arrest and FasL-mediated apoptosis induced by a novel indoloquinoline derivative, IQDMA, in K562 cells. Leuk Res 2007; 31: 1413–20.
34 Peng CH, Tseng TH, Huang CN, Hsu SP, Wang CJ. Apoptosis induced by penta-acetyl geniposide in C6 glioma cells is associated with JNK activation and Fas ligand induction. Toxicol Appl Pharmacol 2005; 202: 172–9.
35 Mundt HM, Stremmel W, Melino G, Krammer PH, Schilling T, Müller M. Dominant negative (DeltaN) p63alpha induced drug resistance in hepatocellular carcinoma by interference with apoptosis signaling pathways. Biochem Biophys Res Commun 2010; 396: 335–41.
36 Tournier C, Hess P, Yang DD, Xu J, Turner TK, Nimnual A, *et al*. Requirement of JNK for stress-induced activation of the cytochrome *c*-mediated death pathway. Science 2000; 288: 870–4.

Acta Pharmacologica Sinica (2011) 32: 528–536
 1671-4083/11 $32.00
www.nature.com/aps

Original Article

Silencing Prx1 and/or Prx5 sensitizes human esophageal cancer cells to ionizing radiation and increases apoptosis via intracellular ROS accumulation

Mai-cang GAO[1, #], Xiao-di JIA[2, #], Qi-fei WU[3], Yan CHENG[1], Fen-rong CHEN[1], Jun ZHANG[1, *]

[1]*Department of Gastroenterology, the Second Affiliated Hospital, Xi'an Jiaotong University, Xi'an 710045, China;* [2]*Department of Key Laboratory of Environment and Genes Related to Diseases (Ministry of Education), Xi'an Jiaotong University, Xi'an 710061, China;* [3]*Department of Hepatobiliary Surgery, the First Affiliated Hospital, Xi'an Jiaotong University, Xi'an 710061, China*

Aim: To investigate whether down-regulation of peroxiredoxin 1 (Prx1) and/or peroxiredoxin 5 (Prx5) sensitizes human esophageal cancer cells to ionizing radiation (IR).
Methods: Human esophageal carcinoma cell lines Eca-109 and TE-1 were used. Prx mRNA expression profiles in Eca-109 and TE-1 cells were determined using RT-PCR. Two highly expressed isoforms of Prxs, Prx1 and Prx5, were silenced by RNA interference (RNAi). Following IR, intracellular reactive oxygen species (ROS) and apoptosis were measured using flow cytometry, the activities of catalase, superoxide dismutase and glutathione peroxidase were measured, and the radiosensitizing effect of RNAi was observed. Tumor xenograft model was also used to examine the radiosensitizing effect of RNAi *in vivo*.
Results: Down-regulation of Prx1 and/or Prx5 by RNAi does not alter the activities of catalase, superoxide dismutase and glutathione peroxidase, but made human tumor cells more sensitive to IR-induced apoptosis both *in vitro* and *in vivo*. When the two isoforms were decreased simultaneously, intracellular ROS and apoptosis significantly increased after IR.
Conclusion: Silencing Prx1 and/or Prx5 by RNAi sensitizes human Eca-109 and TE-1 cells to IR, and the intracellular ROS accumulation may contribute to the radiosensitizing effect of the RNAi.

Keywords: ionizing radiation; peroxiredoxin; radiosensitivity; RNA interference; esophageal cancer; cell cycle distribution; antioxidant enzymes; reactive oxygen species

Acta Pharmacologica Sinica (2011) 32: 528–536; doi: 10.1038/aps.2010.235

Introduction

Over the past three decades, esophageal squamous cell carcinoma remains the dominant histological type of esophageal cancer in Europe and Asia. Despite technological advances in cancer therapies, the overall 5-year survival rate of this malignancy has remained at about 10% since 1980s[1]. Approximately 50%−70% of all cancer patients received radiotherapy during their treatment. However, except for those with very early-stage disease, radiation has had little impact on long-term survival[2]. Epidemiological data strongly suggest that the integration of radiation therapy into multimodal management approaches improves the outcome of therapy for esophageal cancer, but clinical radiation resistance continues to be a major problem[3].

We hypothesize that this resistance is due, in part, to altered levels of antioxidant enzymes. It is well known that the therapeutic effect of ionizing radiation (IR) is damage of DNA and proteins caused by radiation and IR-induced intracellular reactive oxygen species (ROS). Among the antitumor effects of IR, ROS are crucial for cell survival[4, 5]. The enhanced constitutive oxidative stress renders tumor cells highly dependent on endogenous antioxidants, such as catalase (CAT), glutathione peroxidase (GPx), Cu/Zn-superoxide dismutase (SOD), Mn-SOD, and peroxiredoxins (Prxs). These endogenous antioxidants protect tumor cells from continuous intracellular ROS injury.

Among intracellular antioxidant defense enzymes, Prxs have been recently characterized as a group of thiol-containing proteins with efficient antioxidant capacity, and have been

# The two authors contributed equally to this work.
* To whom correspondence should be addressed.
E-mail Jun3z@163.com
Received 2010-08-14 Accepted 2010-11-20

proved to play a critical role in peroxide detoxification[6, 7]. Altogether six distinct Prx isoforms have been identified in mammalian tissues, and elevated expression of different Prx isoforms has been documented in numerous malignancies[8–11]. Furthermore, silencing of Prx expression is currently used to enhance the radiotherapy effect in the cells of breast cancer, lung carcinoma, intestinal cancer and colon cancer[12].

A comparative proteomic analysis showed that the expression of Prx1, increased in human esophageal squamous cell carcinoma tissues as compared with adjacent normal tissues[9]. However, the Prx expression profile is not clear, as well as the relationship between Prx expression and human esophageal squamous cell radiosensitivity.

Therefore, we conducted the present study to get a clear picture of Prx expression. Meanwhile, we explored the influence of Prxs on the radiosensitivity of two human esophageal cancer cell lines, namely, Eca-109 and TE-1.

Materials and methods

Cell culture

Human esophageal carcinoma cell lines Eca-109 and TE-1 were obtained from Cell Bank, Chinese Academy of Sciences (Shanghai, China). The cell lines were cultivated at 37 °C in complete Dulbecco's modified Eagle's medium (DMEM, Invitrogen, USA) supplemented with 10% fetal calf serum (FCS, Gibco, USA), and 100 units/mL penicillin G, 100 mg/mL streptomycin sulfate, in a humidified atmosphere consisting of 95% air and 5% CO_2.

Animals

Male BALB/c nude mice (4-6 weeks old) were used. All mice were handled according to the Guidelines for the Care and Use of Laboratory Animals. This study was approved by the Institutional Animal Care and Use Committee of Xi'an Jiaotong University, Xi'an, China.

Irradiation

For the investigation of radiosensitivity, IR was performed at a fixed dose rate of 0.262 Gy/min and a focus-surface distance of 100 cm from a linear accelerator (ELEKTA, Britain) located in the First Affiliated Hospital, School of Medicine, Xi'an Jiaotong University, Xi'an, China.

Profiling of Prx mRNA expression

Total RNA was isolated from cultured Eca-109 and TE-1 cells using RNAfast200 Kit (Fastagen Biotech, Shanghai, China), and first strand cDNA was synthesized from the total RNA (2 μg) using random hexamer primers and RevertAid™ First Strand cDNA Synthesis Kit (Fermentas, USA); both kits were used according to the manufacturer's instructions. Quantitative real-time PCR was performed using SYBR Premix Ex Taq™ (Takara, Japan). Amplification and detection were performed using the ABI PRISM 7300 Sequence Detection System starting with 2 μL of cDNA. Profiling of Prx mRNA expression was detected by real-time PCR. The primer pairs (listed in Table 1) were synthesized by Sangon Biotech Co, Ltd (Shanghai, China). Real-time PCR was performed following the method taken by Thomas *et al*[13]. Beta-actin was used as an internal control.

Table 1. Upstream and downstream oligonucleotide primers used to determine gene expression using real-time PCR.

Gene	Forward/ reverse	Primers sequence (5'→3')	Product size (bp)
Prx1	Forward	5′-CGGGCCTCTAGATCACTTCT-3′	200
	Reverse	5′-TATGTCTTCAGGAAATGCTA-3′	
Prx2	Forward	5′-TTCAAGCTTATGGCCTTCCG-3′	190
	Reverse	5′-TCTAGACTAATTGTGTTTGG-3′	
Prx3	Forward	5′-AACAGCACACCGTAGTCTCG-3′	144
	Reverse	5′-AGTTGTCGCAGTCTCAGTGG-3′	
Prx4	Forward	5′-CGCTGGCTTGGAAATCTTCG-3′	196
	Reverse	5′-GCTTCTGCTGCCGCTACTG-3′	
Prx5	Forward	5′-ATCAGCCAGGAGCCGAACC-3′	330
	Reverse	5′-GTCCGCAGTTTCAGCAGAGC-3′	
Prx6	Forward	5′-GGCAAGATGGTCCTCAACAC-3′	157
	Reverse	5′-GGGAGACTCATGGGGCATTC-3′	
β-actin	Forward	5′-ATCGTGCGTGTGACATTAAGGAG-3′	178
	Reverse	5′-AGGAAGGAAGGCTGGAAGAGTG-3′	

Prx, peroxiredoxin.

Prx1 small interfering RNA (siRNA) transfection

RNA interference (RNAi) of Prx1 was performed using siRNA duplexes chemically synthesized by GenePharma Co, Ltd (Shanghai, China). The sense strand nucleotide sequence for Prx1 siRNA was 5′-CUGGAAACCUGGCAGUGAUTT-3′, and the anti-sense sequence was 5′-AUCACUGCCAGGUUUCCA-GTT-3′. The negative control siRNA (siNeg) sense sequence was 5′-UUCUCCGAACGUGUCACGUTT-3′, while the anti-sense sequence was 5′-ACGUGACACGUUCGGAGAATT-3′. The siRNA duplexes were introduced into the cells using Lipofectamine 2000 (Invitrogen, USA) according to the manufacturer's guidelines, and Prx1 knock-down was evaluated by Western blotting with antibodies to Prx1.

Prx5 small hairpin RNA (shRNA) transfection and isolation of clones stably expressing Prx5 shRNA

Prx5 specific shRNA (PGPU6/Neo-Prx5) and control shRNA vector (PGPU6/Neo-shNC) were purchased from Genepharma (Shanghai, China). The targeted sequence of PGPU6/Neo-Prx5 was GGAATCGACG-TCTCAAGAGGT, and the targeted sequence of the negative control PGPU6/Neo-shNC was GTTCTCCGAACGTGTCACGT. Eca-109 and TE-1 cells grown on 24-well plates were transfected either with PGPU6/Neo-Prx5 or negative control plasmid. Transfection was performed using Lipofectamine 2000. The cells were incubated at 37 °C in 5% CO_2 overnight, and then DMEM plus 10% FCS was added. After another 12-h incubation the cells were replated at 1/10−1/40 dilution onto the 6-well plates. Selection with G418 (500 μg/mL) started on the next day and the process lasted for 2 weeks. Eca-109 and TE-1 clones with stably

decreased expression of Prx5 as well as the control clones were obtained for further study. Prx5 knock-down was evaluated by Western blotting with antibodies to Prx5.

Western blot analysis

The protein expression of Prxs in Eca-109 and TE-1 cells were examined by Western blotting 72 h post transfection. The cells were washed twice in phosphate buffered saline (PBS), lysed in ice-cold radioimmune precipitation (RIPA) buffer, and then centrifuged for 10 min at 4 °C. Supernatant was collected and protein concentrations were determined and adjusted to 2 mg/mL using the Bio-Rad kit (Bio-Rad Laboratories, Hercules, CA, USA). Cell lysates were mixed with 3×Laemmli buffer and heated for 5 min at 95 °C. They were then resolved by SDS-PAGE (8% or 10% polyacrylamide gels), and transferred to polyvinylidene difluoride membranes (Immobilon^{TM}; Millipore Corp, Bedford, MA, USA) by electroblotting. The membranes were blotted with 10% nonfat milk, washed in Tris-buffered saline (TBS) Tween and incubated with primary rabbit polyclonal antibodies overnight at 4 °C. Washed with TBS Tween again, they were incubated with secondary antibody solution (horseradish peroxidase conjugated IgG) for 60 min at room temperature. The membranes were washed again, and then fluorescence detection was conducted using the enhanced chemiluminescence detection system (Amersham Pharmacia Biotech, Piscataway, NJ, USA). The following primary antibodies were used at dilutions: anti-Prx1, 1:1000; anti-Prx2, 1:1000; anti-Prx5, 1:1000; anti-β-actin, 1:800; secondary antibodies were used at dilutions of 1:5000. Protein loading equivalence was assessed by the expression of β-actin.

Measurement of enzymatic activities of CAT, GPx, Cu/Zn-SOD and Mn-SOD after RNAi

Eca-109 and TE-1 cells, according to the way they were treated, were divided respectively into 7 groups as follows: Blank group; Prx1 siNeg group, cells transfected with negative control siRNA; Prx1 siRNA group, cells transfected with Prx1 siRNA; Prx5 shNeg group, cells stably expressing a non-targeted control shRNA; Prx5 shRNA group, cells stably expressing Prx5 shRNA; Combined negative group (Prx5 shNeg and Prx1 siNeg), cells stably expressing a non-targeted control shRNA and transfected with Prx1 siNeg; Combined group (Prx5 shRNA and Prx1 siRNA), cells stably expressing Prx5 shRNA and transfected with Prx1 siRNA. With Eca-109 and TE-1 cells, we got altogether 14 cell groups. After transfection, cells were grown on T-25 flasks for 48 h at 37 °C. Before IR, cell lysates were centrifuged at 12 000×*g* for 10 min at 4 °C and the supernatant was collected for measuring the activities of CAT, GPx, Cu/Zn-SOD and Mn-SOD, respectively by a Catalase Analysis Kit, a Cellular Glutathione Peroxidase Assay Kit, and Cu/Zn-SOD and Mn-SOD Assay Kit with WST-1 (Beytime Institute of Biotechnology, China). The measurements were performed according to the manufacturer's instructions as well as those described earlier[14-16]. Protein content was determined by using a BCA protein assay kit (Beytime Institute of Biotechnology, China).

Colony-forming assay

The division of cell groups was as described above. Cells were cultured in plastic flasks; 48 h after transfection, the flasks were irradiated with indicated dose of X-rays (0, 2, 4, 6, 8, 10, 15 and 20 Gy). After IR, cells were immediately trypsinized, diluted, counted and seeded in dishes with a diameter of 60 mm at various cell densities. Three replicates were set at each radiation dose of each group. After 2 weeks of incubation, cell colonies were stained with crystal violet dissolved in methanol. The colonies containing more than 50 cells were counted. The plating efficiency (PE) of each group was calculated by PE = (colony number/inoculating cell number)×100%. The survival fraction of each group was corrected by SF=PE (irradiated group)/PE (unirradiated group) × 100%. A dose-survival curve was obtained for each experiment and used for calculating the radiobiological parameters. The cell-survival curve was fitted using SPSS 13.0 software according to the multi-target single-hit model. The equation of $SF = 1-(1-e^{-D/D0})^N$ was applied to calculate the cellular radiosensitivity (mean lethal dose, D0), the capacity for sublethal damage repair (quasithreshold dose, Dq), the dose for 37% survival (D37), the extrapolationnumber (N) and the survival fraction (SF) after irradiation at a dose of 10 Gy (SF10).

Measurement of intracellular ROS

The division of cell groups was the same to that mentioned above. Forty-eight hours after transfection, cells were irradiated with 10 Gy of X-rays, and intracellular ROS were detected using the cell-permeable probe DCFH-DA (Invitrogen) dissolved in high quality anhydrous dimethylsulfoxide (DMSO). Three replicates were set at each observation point of each group. The cells were treated with either DCFH-DA (final concentration of 5 μmol/L) or non-oxidizable control (final concentration of 1 μmol/L) probe at 0 h, 1 h, and 3 h after IR, and then incubated in 5% CO_2 at 37 °C. After 30 min, the cells were collected by trypsinization and washed with cold phosphate buffered saline (PBS) 3 times. Then they were resuspended in cold PBS at a concentration of 1×10^6 cells/mL, and fluorescence was detected by flow cytometry.

Apoptosis analysis

The division of cell groups was as described above. Six replicates were set at each group. Cells were irradiated with 10 Gy of X-rays 48 h after transfection. The cells were collected by trypsinization 24 h post IR, washed twice with cold PBS, and then resuspended in 1×binding buffer at a concentration of 1×10^6 cells/mL. These mixtures (100 μL) were then transferred to 1.5 mL eppendorf tubes respectively and 5 μL of fluorescein-conjugated Annexin V (Annexin V-FITC) and 10 μL of propidium iodide (PI) (Pharmingen, San Diego, CA, USA) were added to each tube. The cells were gently vortexed and incubated for 15 min under room temperature in the dark. Then, 400 μL of binding buffer was added to each tube. Flow cytometry was performed within 1 h. Apoptosis was determined by the percentage of cells stained positively by Annexin V-FITC and PI. Multiparameter cytometric measurements

were performed using the minimum of 10 000 events for each sample. The data were analyzed with LYSIS II software (Becton Dickinson, Buccinasco, Mi, Italy).

Tumor xenograft experiments

Eca-109 cells were chosen for *in vivo* test. Twenty-five nude mice were divided into 5 groups (5 in each group) as follows: Blank group (implanted with control Eca-109 cells), Prx1 siRNA group (implanted with control Eca-109 cells and later transfected with Prx1 siRNA), Prx5 shRNA group (implanted with Eca-109 cells stably expressing Prx5 shRNA), Combined group (implanted with Eca-109 cells stably expressing Prx5 shRNA and later transfected with Prx1 siRNA), and Combined Neg group (implanted with Eca-109 cells stably expressing a non-targeted control Prx5 shRNA and later transfected with Prx1 siNeg). The *in vivo* treatment was performed in the following steps. First, 2×10^5 of each type of Eca-109 cells (those stably expressing Prx5 shRNA, those stably expressing a non-targeted control shRNA, and control cells) were suspended in 200 μL of PBS and injected subcutaneously into the upper hind leg of each mouse in the corresponding group. Second, 7 days after implantation, the tumor reached 4−5 mm in diameter, and intratumoral injections were conducted: Prx1 siRNA (0.5 mg/kg) in the Prx1 siRNA group and Combined group, and Prx1 siNeg (0.5 mg/kg) in the Combined Neg group. The siRNA was mixed with 50 μL Lipofectamine 2000 and proper volume of Opti-MEM medium (Life Technologies, USA) to the final volume of 100 μL[17]. The same volumes of the mixture without siRNA were injected in the mice in Blank group and Prx5 shRNA group. Forty-eight hours following intratumoral injection, IR was performed in all the groups. Tumor sizes were measured by a caliper every three days and the volumes were estimated using the following formula: tumor volume = 0.5×(tumor length)×(tumor width)^2. Thirty-one days later, all the mice were sacrificed.

Statistical analysis

Statistical analysis was performed with SPSS 13.0 for Windows (Scientific Packages for Social Sciences, Chicago, IL, USA) and the results were statistically evaluated by one-way analysis of variance. The difference was considered statistically significant when $P<0.05$.

Results

High expression of Prx1 and Prx5 in Eca-109 and TE-1 cells

The mRNA expression profiles of Prxs in cell lines Eca-109 and TE-1 were analyzed by real-time PCR assay, calculating the relative gene expression by normalizing the results with β-actin mRNA expression. The β-actin normalized mRNA levels of six different Prx isoforms in both Eca-109 and TE-1 cells were shown in Figure 1A and 1B. Among the six Prx isoforms, Prx4 expression was the lowest. Prx1 and Prx5 expressions were significantly higher than Prx2, Prx3, Prx4 and Prx6 expressions in both cell lines ($P<0.05$, $P<0.05$). Results of representative immunodetection of Prxs (Prx1, Prx2 and Prx5) were in accordance with their mRNA expressions in Eca-109 and TE-1 cells (Figure 1C).

Down-regulation of Prx1 and Prx5 by RNAi

Based on the profiles of Prx mRNA expression in Eca-109 and TE-1 cells, the protein expressions of Prx1 and Prx5 were silenced using siRNA and shRNA, respectively. Clones of Eca-109 and TE-1 cells stably expressing Prx5 shRNA or a non-targeted control shRNA were successfully established. The representative results of immunodetection of Prx1 and Prx5 in different cell groups of Eca-109 and TE-1 were shown in Figure 2. Protein loading equivalence of Prx1 and Prx5 was assessed by the protein expression of β-actin. It was shown that Prx1 and/or Prx5 were efficiently silenced by Prx1 siRNA and/or Prx5 shRNA in both Eca-109 and TE-1 cells.

Radiosensitivity of Eca-109 and TE-1 cells with down-regulated Prx1 and/or Prx5

As mentioned in Materials and methods, Eca-109 and TE-1 cells were divided respectively into 7 groups, *ie*, altogether 14 cell groups. For detection of cell radiosensitivity, a total of 24 replicates were set for each group of cells. Forty-eight hours after transfection, the replicates of each cell group were irradiated with different doses (0, 2, 4, 6, 8, 10, 15 and 20 Gy), respectively. After 14-d incubation, clonogenic survival of

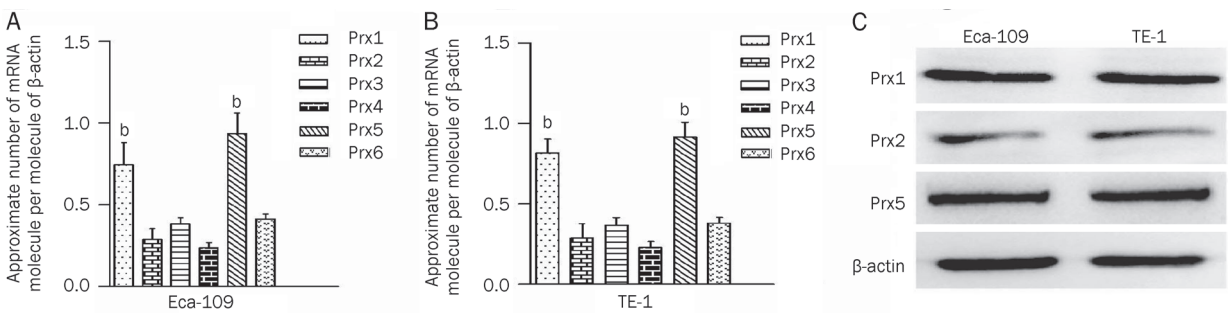

Figure 1. The expression profiles of Prxs in cell lines Eca-109 and TE-1. The mRNA expression levels of six different Prx isoforms were detected by real-time PCR assay; the mRNA levels for Prxs were normalized by the mRNA level of β-actin. (A) The mRNA expression profiles of Prxs in Eca-109. Prx1 and Prx5 are relatively highly expressed ($^bP<0.05$ *vs* Prx2, Prx3, Prx4 and Prx6). (B) The mRNA expression profiles of Prxs in TE-1 cells. Prx1 and Prx5 are relatively highly expressed ($^bP<0.05$ *vs* Prx2, Prx3, Prx4 and Prx6). (C) Representative Western blot analysis of Prxs (Prx1, Prx2 and Prx5) in Eca-109 and TE-1 cells. The results were in accordance with their mRNA expressions in Eca-109 and TE-1 cells.

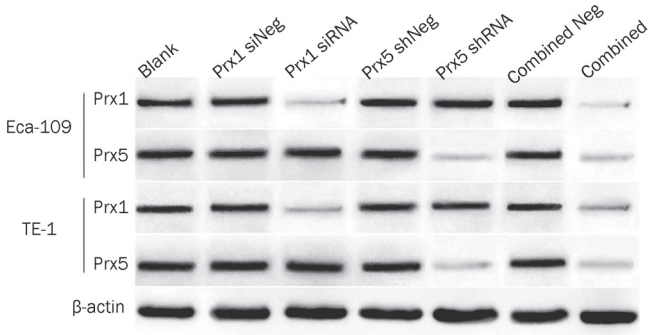

Figure 2. The protein expressions of Prx1 and/or Prx5 in different cell groups 72 h post transfection. The protein expressions of Prx1 and/or Prx5 decreased in Prx1 siRNA group, Prx5 shRNA group and Combined group, compared with those in Blank group, Prx1 siNeg group, Prx5 shNeg group and Combined Neg group.

each group was assessed. The cell-survival curve was fitted according to the multi-target single-hit model (Figure 3A, 3B). As the curves for the control groups are similar, we adopt only that of Blank group to represent the cell survival of all the 4

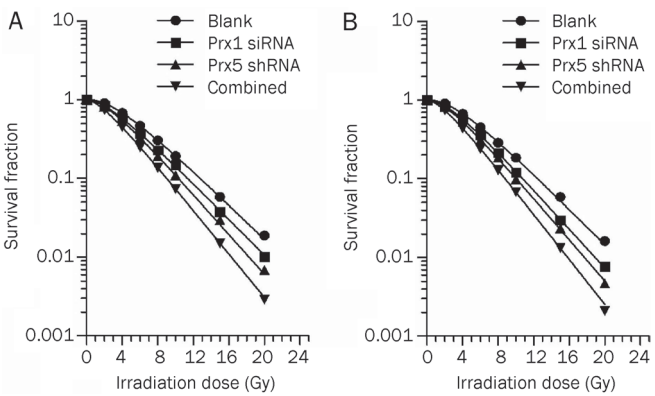

Figure 3. Clonogenic survival of Eca-109 cells (A) and TE-1 cells (B) 14 d post IR. All the cell groups received 0–20 Gy of IR 48 h after transfection, and cloning formation was detected by 14 d after irradiation.

control groups. Relative biological parameters for different cell groups are shown in Table 2. It was found that D0, Dq and D37 of Prx1 siRNA group, Prx5 shRNA group and combined group in both Eca-109 and TE-1 cells were remarkably lower than those in control groups, which suggested that the cells were insensitive to low dose of radiation. While with 10 Gy of radiation, the survival fraction (SF) of the cells decreased obviously in all groups. As shown in Table 2, SF10 was significantly lower in Prx1 siRNA group, Prx5 shRNA group and Combined group as compared to the control groups (P<0.05).

Influence of Prx1 and/or Prx5 down-regulation on the activities of other antioxidant enzymes

With Prx1 and/or Prx5 was down-regulated by RNAi, the activities of other antioxidant enzymes (CAT, GPx, Cu/Zn-SOD and Mn-SOD) were detected before IR by enzyme-linked immunosorbent assay, and the results are shown in Table 3. No remarkable change of the activities of the enzymes was found in the treated groups and the control groups (P>0.05).

Increase of tumor cell intracellular ROS by RNAi *in vitro*

The results showed that intracellular ROS increased significantly in all cell groups 1 h after 10 Gy of radiation, especially in Prx1 siRNA group, Prx5 shRNA group and Combined group (Figure 4A & 4B). No significant difference in ROS levels was observed among the control groups (so the data are not shown). Figure 4C shows that, compared with that in Blank group, the ROS levels were higher in the cells transfected with Prx1 siRNA and/or Prx5 shRNA (P<0.05) at the three observation points, namely, 0 h, 1 h and 3 h. The ROS levels reached the peak at 1 h, while decreased notably at 3 h.

Increase of IR-induced apoptosis rates of Eca-109 and TE-1 cells by RNAi *in vitro*

IR-induced apoptosis in each group was analyzed by flow cytometry 24 h after 10 Gy of radiation (Figure 5A & 5B). The results showed an increase in IR-induced apoptosis rates when Prx1 and/or Prx5 were decreased by RNAi. Furthermore, in cells where both Prx1 and Prx5 were decreased (Combined

Table 2. Relative biological parameters of different cell groups after calculated by multi-target single-hit model.

Cell groups	Eca-109					TE-1				
	D0	Dq	D37	N	SF10	D0	Dq	D37	N	SF10
Blank	4.0160	3.6314	7.6475	2.4700	0.1925	3.8023	3.6185	7.4208	2.5901	0.1851
Prx1 siNeg	4.0241	3.7038	7.7279	2.5103	0.1961	3.8609	3.6938	7.5548	2.6031	0.1903
Prx1 siRNA	3.7722	2.6614	6.4336	2.0250	0.1448	3.5474	2.7842	6.2956	2.1710	0.1190
Prx5 shNeg	4.0568	3.6203	7.6771	2.4410	0.1899	3.8125	3.6179	7.4373	2.5793	0.1877
Prx5 shRNA	3.4188	2.5202	5.9390	2.0901	0.1089	3.2594	2.5101	5.7696	2.1601	0.0978
Combined Neg	3.9761	3.7102	7.6863	2.5424	0.1881	3.7864	3.6331	7.4195	2.6104	0.1839
Combined	3.1456	1.8314	4.9770	1.7902	0.0733	3.0395	1.8552	4.8947	1.8411	0.0675

D0: mean lethal dose; Dq: quasithreshold dose; D37: dose for 37% survival; N: the extrapolation number; SF10: the survival fraction (SF) after irradiation at a dose of 10 Gy.

Table 3. The enzymatic activities of other antioxidant enzymes of different cell groups 48 h after RNAi.

Cell lines	Enzymatic activity	Blank	Prx1 siNeg	Prx1 siRNA	Prx5 shNeg	Prx5 shRNA	Combined Neg	Combined
Eca-109	CAT	33.70±0.70	32.60±2.61	34.23±2.01	33.01±2.20	32.90±2.60	31.77±1.90	33.87±1.31
	GPx	1.88±0.29	1.74±0.57	1.63±0.34	1.59±0.29	1.84±0.38	1.37±0.30	1.78±0.34
	Mn-SOD	4.48±0.79	4.24±0.52	3.98±0.60	4.48±0.21	4.38±0.18	4.12±0.44	3.66±0.27
	Cu/Zn-SOD	2.94±0.47	3.23±0.51	2.05±0.49	2.87±0.59	2.70±0.55	2.13±0.52	2.64±0.22
TE-1	CAT	33.63±2.94	33.33±3.73	31.43±2.00	32.87±2.06	33.90±1.30	34.03±2.34	33.23±2.39
	GPx	1.92±0.66	1.86±0.54	1.57±0.25	1.75±0.20	1.94±0.62	1.67±0.25	1.97±0.76
	Mn-SOD	4.78±0.23	4.00±0.64	4.39±0.20	4.03±0.09	4.45±0.45	3.99±0.42	3.82±0.35
	Cu/Zn-SOD	3.06±0.50	3.08±0.44	3.01±0.71	3.19±0.31	2.84±0.62	2.92±0.33	2.38±0.16

Abbreviations are: CAT, catalase; SOD, Mn- and Cu/Zn- superoxide dismutase; GPx, glutathione peroxidase.
*SOD: U/mg protein; CAT, μmol/L H_2O_2 per min per mg protein; GPx: μmol/L NADPH per min per mg protein.

group), apoptosis rate was higher than that in cells where Prx1 or Prx5 was decreased alone (P<0.05, P<0.05 and P<0.05). No significant difference in apoptosis rate was observed among control groups.

Enhancement of tumor radiosensitivity by RNAi *in vivo*

A tumor xenograft model was used to examine the radiosensitizing effect of Prx1 siRNA and Prx5 shRNA *in vivo*. The tumors in mice grew to final volume between 273 and 1915 mm^3 thirty-one days after implantation. The growth of tumor was delayed by RNAi and IR in Prx1 siRNA group (930.40±267.70 mm^3), Prx5 shRNA group (680.20±240.55 mm^3) and Combined group (364.00±90.77 mm^3), compared to Blank group (1537.20 ± 347.90 mm^3) and Combined negative group (1455.80 ± 294.91 mm^3) (P<0.05, P<0.05 and P<0.05). It is found that the tumor growth in Combined group was more significantly inhibited than that in either Prx1 siRNA group or the Prx5 shRNA group (P<0.05, Figure 6).

Discussion

We have found in this study that only two Prx isoforms (Prx1 and Prx5) are highly expressed in Eca-109 and TE-1 cells, and silencing Prx1 and/or Prx5 sensitizes esophageal cancer cells to IR through accumulation of intracellular ROS. This is the report on the Prx expression profiles in esophageal cancer cells and the influence of Prx1 and Prx5 expressions on the radiosensitivity of esophageal cancer cells.

ROS are usually a side product of general metabolism. Intracellular ROS can be induced by IR and serve as major mediators of radiation damage[18]. When ROS generation exceeds the cellular antioxidant defenses, cell damage ensues[19, 20]. In the present study, we find that Prx1 and/or Prx5 knock-down through RNAi, together with the IR treatment after the transfection, lead to significant elevation of the levels of intracellular ROS and the cell apoptosis rates. Thus, increased intracellular ROS could be, in part, due to the lower Prx1 and/or Prx5 levels in tumor cells. This assumption is

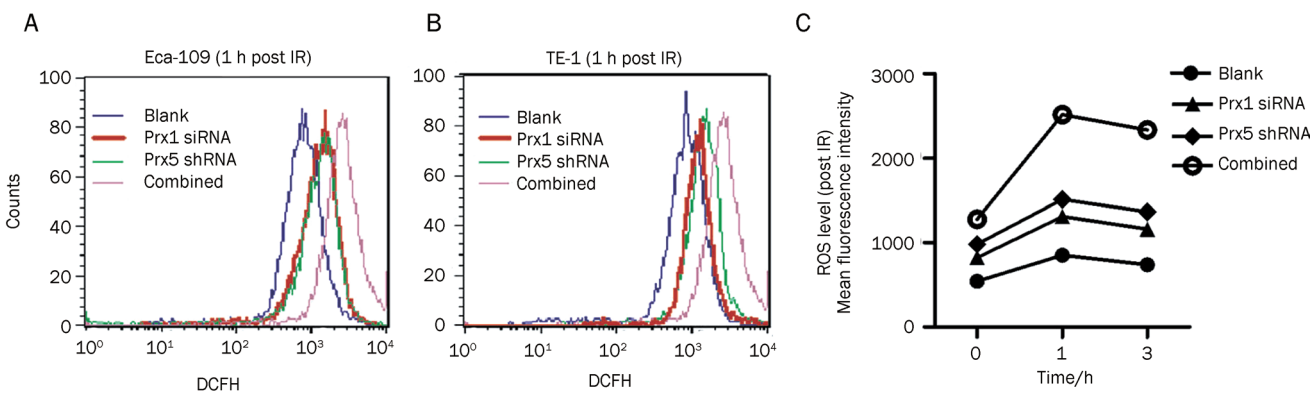

Figure 4. Change of intracellular ROS post transfection and 10 Gy of IR *in vitro*. The levels of ROS were determined using the dye DCFH-DA. Flow cytometric histograms show a broad unimodal distribution of DCF fluorescence in different cell groups. Increase in the ROS levels is indicated as a shift in the histograms. (A) Increased intracellular ROS in Eca-109 cells. (B) Increased intracellular ROS in TE-1 cells. As shown in (A) and (B), ROS increase significantly in all cell groups 1 h post IR. The levels of ROS are higher in the cells transfected with Prx1 siRNA and/or Prx5 shRNA, P<0.05 *vs* Blank group. (C) The change of intracellular ROS levels at different observation points. The ROS levels are higher in the cells transfected with Prx1 siRNA and/or Prx5 shRNA at the three observation points (P<0.05 *vs* Blank group), particularly in the cells transfected with both Prx1 siRNA and Prx5 siRNA (P<0.05 *vs* Prx1 siRNA and Prx5 shRNA groups).

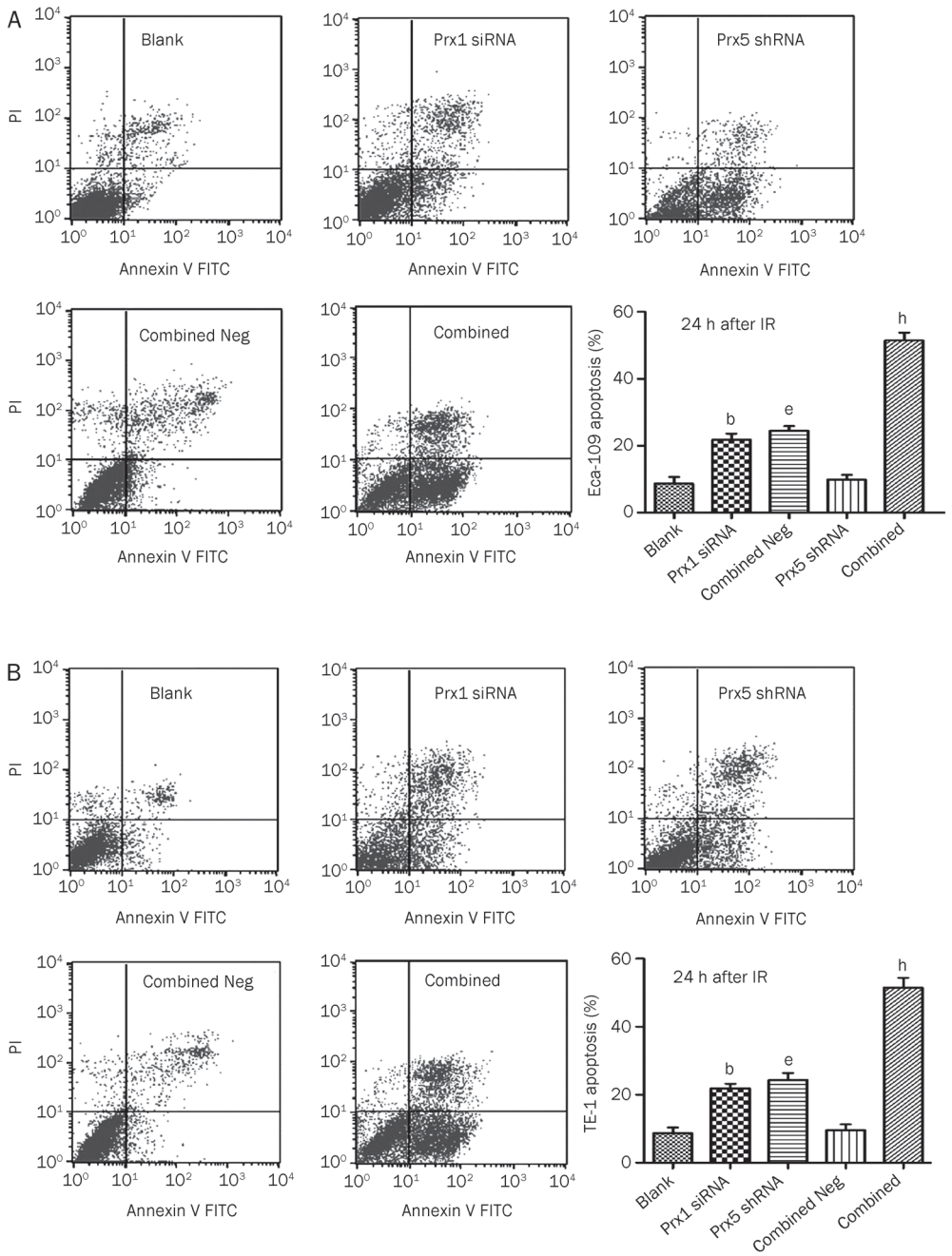

Figure 5. Change of tumor cell apotosis after transfection and 10 Gy of IR *in vitro*. The cells were exposed to 10 Gy of IR 48 h post transfection. IR-induced apoptosis in each group was analyzed by flow cytometry 24 h after IR. (A) Representative flow cytometry profiles of Eca-109 cell groups. It is shown that knockdown of Prx1 and/or Prx5 increased apoptosis. (B) Representative flow cytometry profiles of TE-1 cell groups. It is shown that knockdown of Prx1 and/or Prx5 increased apoptosis. All the data are means±SEM. n=3. $^{b}P<0.05$ *vs* Blank and Combined groups; $^{e}P<0.05$ *vs* Blank and Combined groups; $^{h}P<0.05$ *vs* Blank, Prx1 siRNA, Prx5 shRNA, and Combined Neg groups.

also supported by some studies[21–23]. Furthermore, the more Prx isoforms that are silenced, the more intracellular ROS remained unscavenged in the tumor cells and the more tumor cells die post IR. After IR, the dose-survival curves of Eca-109 or TE-1 cells in Prx1 siRNA and/or Prx5 shRNA groups exhibit a narrower shoulder and a greater slope rate, indicating decreased quasi-threshold dose (Dq) and mean lethal dose (D0), respectively, that suggests that the radiosensitivity of the cells has increased. In our further investigation of the potential radiosensitizing effects of Prx1 siRNA and Prx5 shRNA *in vivo*, we have achieved similar results. So, our findings show that down-regulation of Prx1 and Prx5 can enhance the radiosensitivity of Eca-109 and TE-1 cells.

The enzymatic activity of other primary antioxidant enzymes (CAT, GPx, Cu/Zn-SOD, and Mn-SOD) in the cancer cells has not changed when Prx1 and/or Prx5 are inhibited. In another word, decreasing Prx1 and/or Prx5 does not alter the activities of the enzymes. This suggests that other antioxidant enzymes will not compensate for the loss of Prx1 and/or Prx5. All our findings indicate that tumor cell radiosensitivity is influenced by altered levels of Prxs, and Prx1 and Prx5 play a critical role in regulating intracellular ROS.

In addition to the protective role of Prx1 and Prx5 as peroxidase, evidence has indicated other mechanisms of them involved in protecting cells from radiation-induced death. It is reported that Prx1 plays a negative role in apoptosis signal-

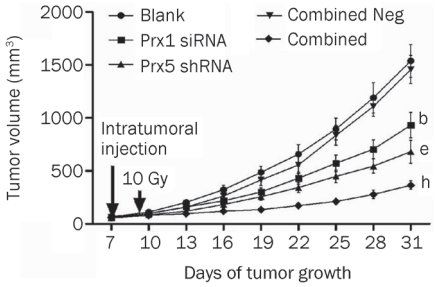

Figure 6. Tumor growth post transfection and IR *in vivo*. The long black arrow indicates intratumoral injection of Prx1 siRNA in Prx1 siRNA group and Combined group, and Prx1 siNeg in Combined Neg group. The short black arrow indicates 10 Gy of IR 48 h after the injection. Each point on a curve represents the mean and standard deviation of tumor mass from the 5 mice at each measuring point. It can be seen that the final tumor growth was delayed in Prx1 siRNA group ($^{b}P<0.05$ *vs* Blank, Prx5 shRNA, and Combined groups), Prx5 shRNA group ($^{e}P<0.05$ *vs* Blank, Prx1 siRNA, and Combined groups) and Combined group, ($^{h}P<0.05$ *vs* Blank, Combined Neg, Prx1 siRNA, and Prx5 shRNA groups).

regulating kinase 1 (ASK1)-induced apoptosis. ASK1 is a mitogen-activated protein kinase (MAPK) kinase kinase which phosphorylates c-Jun N-terminal kinase (c-JNK) and p38 MAPK, and elicits apoptotic response[24]. ASK1 activity is regulated in multiple ways, one of which is through interaction with Prx1. The overexpression of Prx1 inhibits the activation of ASK1, and results in the inhibition of downstream signaling cascades such as the mitogen-activated protein kinase kinase 3/6 (MKK3/6), p38 and c-JNK pathway[25]. Moreover, overexpression of Prx1 could directly suppress IR–induced c-JNK activation and cell apoptosis through interaction with the glutathione *S*-transferase π (GSTπ)-JNK complex[26]. While, in Prx1 knock-down cells, ASK1, p38, and c-JNK are quickly activated, leading to cell apoptosis in response to H_2O_2[25]. The cell cycle phase also determines a cell's relative radiosensitivity, with cells being most radiosensitive in the G_2-M phase, less sensitive in the G_1 phase, and least sensitive during the latter part of the S phase[27]. It has been shown that Prx1 expression is associated with cell cycle phase distribution. After IR, cell cycle phases are redistributed to radiosensitive phases in Prx1 knock-down cells, that is, G_2-M checkpoint arrested, more cells blocked in G_2 phase, and higher ratio of G_2/G_1 observed[21]. In the presence of excess peroxide, the cysteine residue of Prxs is found to be hyperoxidized to the sulfinic acid or to the sulfonic acid to form complex oligomeric structures[28], this hyperoxidized Prx toroids are reported to exhibit a chaperone-like function protecting mammalian cells from hydrogen peroxide-induced apoptosis[29, 30]. A recent study demonstrated that the hyperoxidation of the active-site cysteine of Prx to cysteine sulfonic acid enhanced its molecular chaperone activity[31].

Prx5 has been proved to have a broad range of functions that the expression of the redox-negative Prx5 mainly affects the mitochondrial pathway of apoptosis, and the impairment of the Prx5 enzymatic function also affects transmembrane potential and calcium loading capacity of mitochondria, as well as mitochondrial morphology[32]. For as yet unknown reasons, Prx5 is insensitive to hyperoxidation. To date, there has been no investigation of the chaperone activity of the Prx5. It is expected that these functions of Prx1 and Prx5 do not necessarily depend on peroxidase activity. Additionally, decreasing the expression of Prx1 and/or Prx5 in Eca-109 and TE-1 cells could also abrogate such functions, and, in turn, contribute to increased radiosensitivity.

Conclusion

Silencing Prx1 and/or Prx5 by RNAi can sensitize human esophageal cancer cells Eca-109 and TE-1 cells to IR, and the resulting intracellular ROS accumulation may contribute to the radiosensitizing effect of the RNAi. The results of this study suggest that inactivation of Prx1 and Prx5 may be a promising approach to improving the radiotherapy outcome of esophageal cancer.

Acknowledgments

This study was supported by a grant from Clinical Disciplines' Key Project of Ministry of Health of China (No 2007-353).

Author contribution

Prof Jun ZHANG designed the research and revised the manuscript; Mai-cang GAO, Xiao-di JIA and Qi-fei WU conducted the research, analyzed the data and wrote the paper; Yan CHENG and Fen-rong CHEN helped with part of the research.

References

1 Ekman S, Dreilich M, Lennartsson J, Wallner B, Brattström D, Sundbom M, *et al*. Esophageal cancer: current and emerging therapy modalities. Expert Rev Anticancer Ther 2008; 8: 1433–48.
2 Herskovic A, Martz K, al-Sarraf M, Leichman L, Brindle J, Vaitkevicius V, *et al*. Combined chemotherapy and radiotherapy compared with radiotherapy alone in patients with cancer of the esophagus. N Engl J Med 1992; 326: 1593–8.
3 Gebski V, Burmeister B, Smithers BM, Foo K, Zalcberg J, Simes J. Survival benefits from neoadjuvant chemoradiotherapy or chemotherapy in esophageal carcinoma: a meta-analysis. Lancet Oncol 2007; 8: 226–34.
4 Leach JK, Van Tuyle G, Lin PS, Schmidt-Ullrich R, Mikkelsen RB. Ionizing radiation-induced, mitochondria-dependent generation of reactive oxygen/nitrogen. Cancer Res 2001; 61: 3894–901.
5 Diehn M, Cho RW, Lobo NA, Kalisky T, Dorie MJ, Kulp AN, *et al*. Association of reactive oxygen species levels and radioresistance in cancer stem cells. Nature 2009; 458: 780–3.
6 Kinnula VL, Lehtonen S, Sormunen R, Kaarteenaho-Wiik R, Kang SW, Rhee SG, *et al*. Overexpression of peroxiredoxins I, II, III, V, and VI in malignant mesothelioma. J Pathol 2002; 196: 316–23.
7 Kang SW, Rhee SG, Chang TS, Jeong W, Choi MH. 2-Cys peroxiredoxin function in intracellular signal transduction: therapeutic implications. Trends Mol Med 2005; 11: 571–8.
8 Karihtala P, Mäntyniemi A, Kang SW, Kinnula VL, Soini Y. Peroxiredoxins in breast carcinoma. Clin Cancer Res 2003; 9: 3418–24.
9 Qi Y, Chiu JF, Wang L, Kwong DL, He QY. Comparative proteomic analysis of esophageal squamous cell carcinoma. Proteomics 2005; 5: 2960–71.
10 Ai J, Tan Y, Ying W, Hong Y, Liu S, Wu M, *et al*. Proteome analysis

of hepatocellular carcinoma by laser capture microdissection. Proteomics 2006; 6: 538–46.
11 Cheng Y, Zhang J, Li Y, Wang Y, Gong J. Proteome analysis of human gastric cardia adenocarcinoma by laser capture microdissection. BMC Cancer 2007; 7: 191.
12 Zhang B, Wang Y, Su YP. Peroxiredoxins, a novel target in cancer radiotherapy. Cancer Lett 2009; 286: 154–60.
13 Thomas S, Muralidharan A, Shah GV. Knock-down of calcitonin receptor expression induces apoptosis and growth arrest of prostate cancer cells. Int J Oncol 2007; 31: 1425–37.
14 He Z, Sun X, Mei G, Yu S, Li N. Nonclassical secretion of human catalase on the surface of CHO cells is more efficient than classical secretion. Cell Biol Int 2008; 32: 367–73.
15 An R, Dong C, Lei Y, Han L, Li P, Chen J, *et al*. PrP mutants with different numbers of octarepeat sequences are more susceptible to the oxidative stress. Sci China C Life Sci 2008; 51: 630–9.
16 Siafakas AR, Wright LC, Sorrell TC, Djordjevic JT. Lipid rafts in *Cryptococcus neoformans* concentrate the virulence determinants phospholipase B1 and Cu/Zn superoxide dismutase. Eukaryot Cell 2006; 5: 488–98.
17 Liu TG, Yin JQ, Shang BY, Min Z, He HW, Jiang JM, *et al*. Silencing of hdm2 oncogene by siRNA inhibits p53-dependent human breast cancer. Cancer Gene Ther 2004; 11: 748–56.
18 Mikkelsen RB, Wardman P. Biological chemistry of reactive oxygen and nitrogen and radiation-induced signal transduction mechanisms. Oncogene 2003; 22: 5734–54.
19 Gamaley IA, Klyubin IV. Roles of reactive oxygen species: Signaling and regulation of cellular functions. Int Rev Cytol 1999; 188: 203–55.
20 Cerutti PA. Prooxidant states and tumor promotion. Science 1985; 227: 375–81.
21 Zhang B, Su Y, Ai G, Wang Y, Wang T, Wang F. Involvement of peroxiredoxin I in protecting cells from radiation-induced death. J Radiat Res 2005; 46: 305–12.
22 Chen WC, McBride WH, Iwamoto KS, Barber CL, Wang CC, Oh YT, *et al*. Induction of radioprotective peroxiredoxin-I by ionizing irradiation. J Neurosci Res 2002; 70: 794–8.
23 Chen MF, Lee KD, Yeh CH, Chen WC, Huang WS, Chin CC, *et al*. Role of peroxiredoxin I in rectal cancer and related to p53 status. Int J Radiat Oncol Biol Phys 2010; 78: 868–78.
24 Tobiume K, Matsuzawa A, Takahashi T, Nishitoh H, Morita K, Takeda K, *et al*. ASK1 is required for sustained activations of JNK/p38 MAP kinases and apoptosis. EMBO Rep 2001; 2: 222–8.
25 Kim SY, Kim TJ, Lee KY. A novel function of peroxiredoxin 1 (Prx-1) in apoptosis signal-regulating kinase 1 (ASK1)-mediated signaling pathway. FEBS Lett 2008; 582: 1913–8.
26 Kim YJ, Lee WS, Ip C, Chae HZ, Park EM, Park YM. Prx1 suppresses radiation-induced c-Jun NH_2-terminal kinase signaling in lung cancer cells through interaction with the glutathione S-transferase Pi/c-Jun NH2-terminal kinase complex. Cancer Res 2006; 66: 7136–42.
27 Pawlik TM, Keyomarsi K. Role of cell cycle in mediating sensitivity to radiotherapy. Int J Radiat Oncol Biol Phys 2004; 59: 928–42.
28 Seo JH, Lim JC, Lee DY, Kim KS, Piszczek G, Nam HW, *et al*. Novel protective mechanism against irreversible hyperoxidation of peroxiredoxin: Nα-terminal acetylation of human peroxiredoxin II. J Biol Chem 2009; 284: 13455–65.
29 Moon JC, Hah YS, Kim WY, Jung BG, Jang HH, Lee JR, *et al*. Oxidative stress-dependent structural and functional switching of a human 2-Cys peroxiredoxin isotype II that enhances HeLa cell resistance to H_2O_2-induced cell death. J Biol Chem 2005; 280: 28775–84.
30 Lee W, Choi KS, Riddell J, Ip C, Ghosh D, Park JH, *et al*. Human peroxiredoxin 1 and 2 are not duplicate proteins: the unique presence of Cys83 in Prx1 underscores the structural and functional differences between Prx1 and Prx2. J Biol Chem 2007; 282: 22011–22.
31 Lim JC, Choi HI, Park YS, Nam HW, Woo HA, Kwon KS, *et al*. Irreversible oxidation of the active-site cysteine of peroxiredoxin to cysteine sulfonic acid for enhanced molecular chaperone activity. J Biol Chem 2008; 283: 28873–80.
32 Kropotov A, Gogvadze V, Shupliakov O, Tomilin N, Serikov VB, Tomilin NV, *et al*. Peroxiredoxin V is essential for protection against apoptosis in human lung carcinoma cells. Exp Cell Res 2006; 312: 2806–15.

Acta Pharmacologica Sinica (2011) 32: 537–542
 1671-4083/11 $32.00
www.nature.com/aps

Original Article

A comparison of androgen deprivation therapy versus surgical castration for patients with advanced prostatic carcinoma

Yu-hsiang LIN[1, #], Chien-lun CHEN[1, 2, #], Chen-pang HOU[1], Phei-lang CHANG[1, 2], Ke-hung TSUI[1, 2, *]

[1]*Department of Urology, Division of Geriatric Urology, Chang Gung Memorial Hospital and Chang Gung University College of Medicine, Taoyuan, Taiwan, China;* [2]*Bioinformation Center, Chang Gung Memorial Hospital-Linko, Chang Gung University, Taoyuan, Taiwan, China*

Aim: To examine the outcomes of patients with advanced prostate carcinoma who underwent medical or surgical castration.
Methods: A hundred twenty one consecutive cases of patients with advanced prostate carcinoma who underwent medical or surgical castration between 2001 and 2006 were retrospectively reviewed. Associations between clinical outcomes and prognostic scoring factors were determined based on the Reijke study. In the surgical and medical castration groups, the impact on the prostate-specific antigen (PSA) normalization rate, the rebound rate and the disease-free survival rate were evaluated. The mean follow-up was 36.1 months.
Results: In the initial 12 months, there were no statistical differences in the PSA normalization rate and the PSA rebound rate between the two groups. However, the PSA rebound rate after the 12th month (20.90% *vs* 40.74%, P=0.0175) and the 18th month PSA normalization rate (59.70% *vs* 37.04%, P=0.0217) differed significantly between the two groups, and these differences were maintained to the end of the study. When comparing patients grouped according to Reijke prognosis scores, there was no difference between medical and surgical castration for the good prognosis group. However, among the patients given a poor prognosis, surgical castration was superior in terms of the PSA normalization rate, the PSA rebound rate, the tumor progression-free survival rate (P<0.001) and the overall survival rate (P<0.001).
Conclusion: Advanced prostate carcinoma patients with poor pretreatment prognosis scores should undergo surgical castration rather than medical castration for better PSA rebound rates and overall survival.

Keywords: androgen; surgical castration; prostate neoplasm; metastasis; prognosis; medical castration; prostate-specific antigen; luteinizing hormone-releasing hormone (LHRH)

Acta Pharmacologica Sinica (2011) 32: 537–542; doi: 10.1038/aps.2010.236; published online 14 Mar 2011

Introduction

Prostate carcinoma is the most common nonskin malignancy among men. Age is acknowledged as one of the risk factors for prostate carcinoma. With prostate-specific antigen (PSA)-based screening and postoperative follow-up being widely used[1–3], the incidence of prostate carcinoma has increased. Androgen deprivation therapy (ADT) is a well-established treatment for advanced and metastatic prostate carcinoma, which began with Huggins's observations on advanced and metastatic prostate carcinoma[4]. Although ADT improves survival for undergoing hormone therapy, biochemical recurrence after ADT remains a long-term problem to be solved. The optimal time to initiate hormone therapy for patients with a regular PSA follow-up is still under investigation[3, 5, 6]. As the modern pharmaceutical industry advanced, a luteinizing hormone–releasing hormone (LHRH) agonist with monthly dosing became available. From that point on, surgical castration was largely replaced by medical castration with an LHRH agonist to reduce the psychological impact of orchiectomy to the patients and to preserve reversibility[7, 8]. Then, maximal androgen blockade (MAB) was proposed to address the androgens of adrenal origin[9]. Many trials followed comparing MAB and monotherapy[10–12]. However, because of the high cost of LHRH agonist and the limited medical reimbursement system, surgical castration has again become more prevalent[13, 14]. There are several reports comparing the castration level and the sustainability of surgical and medical castration[7, 15, 16]. However, there are few reports comparing the prognosis between these two groups.

# The two authors contributed equally to this work.
* To whom correspondence should be addressed.
E-mail khtsui@yahoo.com
Received 2010-07-17 Accepted 2010-12-31

In this study, we compared the clinical effectiveness of surgical and medical castration with respect to patient outcomes. We also identified clinical outcomes and PSA response features that predicted favorable treatment outcomes for prostate carcinoma after ADT.

Materials and methods

Patient selection

After obtaining institutional review board approval for a retrospective study of the medical records from January 2001 to March 2006, we identified all patients who had advanced prostate carcinoma. Patients with localized prostate carcinoma received definitive therapy, such as radical surgery or radiotherapy. Patients whose clinical staging was greater than tumor stage T3, T4, or metastatic disease, received hormone therapy. In this study, we included these patients receiving hormone therapy but excluded patients on radiotherapy or chemotherapy for prostate carcinoma. However, there were some patients on palliative radiotherapy for spinal or other bone metastases.

The exclusion criteria for this study were concurrent malignancy, previous surgical, radiotherapy or hormonal therapy for prostate carcinoma, poor renal and hepatic function, and a life expectancy of less than 3 months. All of the patients enrolled had a baseline PSA test, chest X-ray films, pelvic magnetic resonance imaging, and whole-body bone scans as baseline data.

From January 2001 to March 2006, we identified 121 patients with advanced prostate carcinoma (defined as stage III or stage IV carcinoma) with complete medical records. MAB included either surgical castration plus antiandrogen therapy with cyproterone (100 mg twice daily), flutamide (250 mg three times per day), or bicalutamide (50 mg daily) or medical castration consisting of LHRH agonist hormone therapy (goserelin 3.6 mg monthly or leuprorelin 14 mg monthly) plus antiandrogen therapy. The patients who received medical castration received antiandrogen 2 weeks in advance for testosterone flare-up prevention[17]. All of the prostate tumors were pathologically staged according to the 1997 TNM classification.

Reijke[18] developed a prognostic scoring system for patients with advanced prostate carcinoma receiving hormone therapy. The prognostic scoring system is characterized by (a) >5 sites of bone metastasis, (b) hydronephrosis, (c) pain requiring analgesics, and (d) alkaline phosphatase >2 times the upper limit of the normal range. A prognostic score is determined by counting the parameters present and obtaining a five-level score (0–4 points). Collapsing the prognostic score, we divided patients into subgroups according to their prognostic score: the good prognosis group (scores 0 and 1) and the poor prognosis group (scores 2, 3, and 4). We further divided the surgical castration (group 1) and medical castration (group 2) patients into good and poor prognostic groups based on Reijke's classification. The four groups were defined as the following: (1) G1g: surgical castration with a good prognosis score, (2) G1p: surgical castration with a poor prognosis score, (3) G2g: medical castration with a good prognosis score, and (4) G2p: medical castration with a poor prognosis score. We evaluated these enrollment criteria in association with subsequent disease progression and treatment patterns to clarify the most appropriate therapy for metastatic prostate carcinoma. After initiating the hormone therapy, patients were monitored regularly with a PSA checkup every 3 months.

Statistical analysis

SPSS 15.0 for Windows [SPSS INC., CHICAGO, IL60616] was used to analyze the collected data. The PSA normalization rate and the PSA rebound rate were examined using the Chi-squared test. The tumor progression–free survival rate and the overall survival rate were calculated using the Kaplan-Meier method.

Results

We identified 121 patients with complete medical records. There were 67 patients in group 1 (surgical castration) and 54 patients in group 2 (medical castration). Table 1 shows the patient distribution and prostate carcinoma characteristics (initial PSA, Gleason score, tumor staging, and metastasis). The bone metastasis rate was higher in the medical castration group, and it reached statistical significance. However, in Reijke's criteria with four independent prognosis factors for advanced prostate carcinoma, there was no difference between these two groups.

The cancer-specific survival rates for patients within group 1 and 2 differed significantly (P<0.001) (Figure 1). Patients in the surgical castration group demonstrated better survival than the medical castration group.

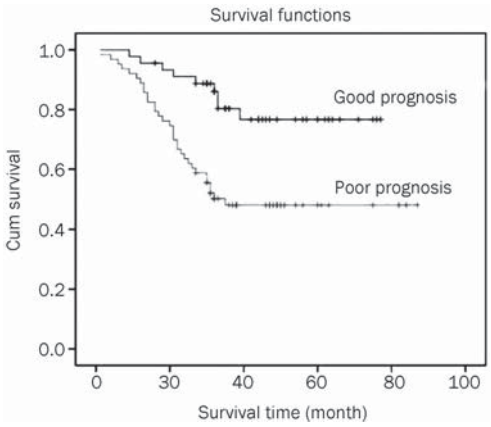

Figure 1. Cancer-specific survival based on overall good and poor prognosis groups.

PSA normalization rate

The PSA normalization rates by study group are shown in Table 2. We defined the PSA normalization rate as the percentage of patients with a PSA level returning to normal (<4 ng/mL) and staying normal. The PSA normalization

Table 1. Patient characteristics of the advanced prostate cancer.

	Group 1: Orchiectomy + Anti-androgen	Group 2: LHRH Agonist + Anti-androgen	*P* value
Number	67	54	
Age (mean)	74.13 (59–89)	72.94 (50–88)	0.3676
Initial PSA level (median)	202.82 (2.56–13851.20)	297.72 (19.14–7422.83)	0.3234
Gleason score			
2–6	9	2	
7	13	10	
7–10	45	42	
TNM stage			
Stage III	17.91% (12/67)	5.56% (3/54)	
Stage IV	82.09% (55/67)	94.44% (51/54)	0.0763
Metastasis			
Bone metastasis	58.21% (39/67)	81.48% (44/54)	0.0109
Lung metastasis	1	3	
Liver metastasis	0	3	
Reijke prognosis criteria			
Good	45 (67.16%)	34 (62.96%)	0.7714
Poor	22 (32.84%)	20 (37.04%)	
Anti-androgen			
Steroid	56.9%	37.25%	
Non-steroid	43.1%	62.75%	

Table 2. Match comparison of patients undergoing ADT at PSA normalization rate.

	Group 1	Group 2	*P*-value	Group 1g	Group 2g	*P*-value	Group 1p	Group 2p	*P*-value
3 month	55.22% (37/67)	44.44% (24/54)	0.3192	55.56% (25/45)	47.06% (16/34)	0.6024	54.55% (12/22)	40.00% (8/20)	0.3743
6 month	71.64% (48/67)	53.70% (29/54)	0.0645	75.56% (34/45)	58.82% (20/34)	0.1806	63.64% (14/22)	45.00% (9/20)	0.3521
9 month	68.66% (46/67)	55.56% (30/54)	0.1960	75.56% (34/45)	55.88% (19/34)	0.1094	54.55% (12/22)	55.00% (11/20)	1
12 month	62.69% (42/67)	42.59% (23/54)	0.0434	71.11% (32/45)	47.06% (16/34)	0.0530	45.45% (10/22)	35.00% (7/20)	0.5403
15 month	61.19% (41/67)	42.59% (23/54)	0.0637	66.67% (30/45)	47.06% (16/34)	0.1281	50.00% (11/22)	35.00% (7/20)	0.3665
18 month	59.70% (40/67)	37.04% (20/54)	0.0217	66.67% (30/45)	47.06% (16/34)	0.1281	45.45% (10/22)	20.00% (4/20)	0.0375
21 month	61.19% (41/67)	35.19% (19/54)	0.0078	64.44% (29/45)	44.12% (15/34)	0.1159	54.55% (12/22)	20.00% (4/20)	0.0289
24 month	55.22% (37/67)	31.48% (17/54)	0.0152	64.44% (29/45)	41.17% (14/34)	0.0676	36.36% (8/22)	15.00% (3/20)	0.0465

PSA normalization is defined as PSA level <4 ng/mL

Group 1: Orchiectomy+anti-androgen. Group 2: LHRH agonist+anti-androgen. G1g: surgical castration group with good prognosis score. G1p: surgical castration group with poor prognosis score. G2g: medical castration group with good prognosis score. G2p: medical castration group with poor prognosis score.

rate peaked in the 6th and 9th months in the surgical and the medical castration group, respectively. The PSA normalization rate then decreased with time; in the 18th month, there was a difference between these two groups (P=0.0217). When

we further divided groups 1 and 2 into four subgroups by Reijke's[19] prognostic factors, patients with good prognosis scores, regardless of the castration method, showed no significant difference in PSA normalization during the 2 years of follow-up (P=0.0676). However, in the poor prognosis patient group, patients in the surgical castration group (G1p) had significantly better PSA normalization rates than those in the medical castration group (G2p) (P=0.0465). This difference, which occurred after the 18th month, remained to the end of the study.

PSA rebound rate

After ADT, follow-up was performed every 3 months for the first 2 years. The first detected PSA increase after steady state for all available PSA measurements at least 3 months apart were analyzed for PSA rebound. PSA rebound was defined as a PSA level ≥4 ng/mL or greater than the previous measurement. Table 3 summarizes the PSA rebound rate. The PSA rebound rate was lower in group 1 (surgical castration) than group 2 (medical castration); the significant difference occurred 12 months after castration (P=0.0175). In the good prognosis group, there was no significant difference in the PSA rebound rate between surgical and medical castration until the 21st month. In contrast, in the poor prognosis group, the PSA rebound rate was significantly lower in group 1 (surgical castration) after 15 months than in group 2 (medical castration) (P=0.0286).

Tumor progression-free survival rate

After stratifying the patients in groups 1 and 2 according to the Reijke scoring system, the cancer survival for patients within the four prognostic groups (G1g, G1p, G2g, and G2p) was analyzed. Tumor progression was defined as any one of the following situations: (1) PSA rebound, (2) increased prognosis score, (3) death, (4) imaging or clinical evidence of tumor progression. In the good prognosis group, the curves of tumor progression–free survival were similar between surgical and medical castration (P=0.001). However, in the poor prognosis group, patients in the surgical castration (G1p) group survived significantly longer than those in the medical castration group (G2p) (P<0.001, Figure 2).

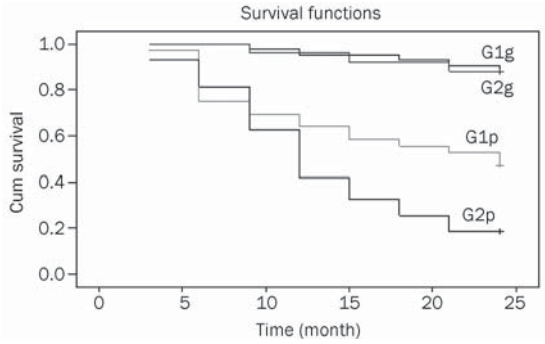

Figure 2. Tumor progression–free survival rate by group.

Overall survival rate

The overall survival of patients in the four groups is shown in Figure 3. The overall survival rate in the good prognosis group did not differ significantly by castration method. However, among patients with a poor prognosis, those in the surgical castration group survived significantly longer than patients in the medical castration group (P<0.001).

Discussion

The concept of treating metastatic prostate carcinoma started with Huggins's observation in 1941[4]. After that, hormone

Table 3. Match comparison of patients undergoing ADT at PSA rebounding rate.

	Group 1	Group 2	*P*-value	Group 1g	Group 2g	*P*-value	Group 1p	Group 2p	*P*-value
6 month	8.96% (6/67)	12.96% (7/54)	0.6800	4.44% (2/45)	8.82% (3/34)	0.7435	18.18% (4/22)	15.00% (3/20)	1
9 month	16.42% (11/67)	27.78% (15/54)	0.1971	13.33% (6/45)	29.41% (10/34)	0.1394	22.72% (5/22)	25.00% (5/20)	1
12 month	20.90% (14/67)	40.74% (22/54)	0.0175	17.78% (8/45)	35.29% (12/34)	0.1307	27.27% (6/22)	50.00% (10/20)	0.2040
15 month	22.39% (15/67)	48.15% (26/54)	0.0054	20.00% (9/45)	41.18% (14/34)	0.0717	27.27% (6/22)	65.00% (12/20)	0.0286
18 month	23.88% (16/67)	53.70% (29/54)	0.0014	22.22% (10/45)	44.12% (15/34)	0.0676	27.27% (6/22)	70.00% (14/20)	0.0124
21 month	23.88% (16/67)	57.41% (31/54)	0.0004	22.22% (10/45)	47.06% (16/34)	0.0371	27.27% (6/22)	75.00% (15/20)	0.0048
24 month	25.37% (17/67)	57.41% (31/54)	0.0007	22.22% (10/45)	47.06% (16/34)	0.0371	31.82% (7/22)	75.00% (15/20)	0.0068

PSA rebound was defined as that PSA level become higher than the previous checked data.

Group 1: Orchiectomy+anti-androgen; Group 2: LHRH agonist+anti-androgen; G1g: surgical castration group with good prognosis score; G1p: surgical castration group with poor prognosis score; G2g: medical castration group with good prognosis score; G2p: medical castration group with poor prognosis score.

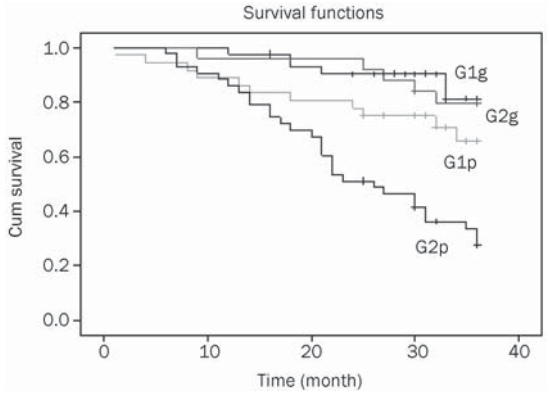

Figure 3. The overall survival rates by group.

therapy became the mainstay of treatment for men with advanced and metastatic prostate carcinoma. The initial regimen of androgen deprivation therapy included bilateral orchiectomy, estrogen therapy, or both. However, these therapies had a greatly negative impact on quality of life, not to mention the occurrence of lethal cardiac events[20, 21]. The discovery of synthetic luteinizing hormone–releasing hormone agonists reduced the cardiac toxicity and the other side effects of androgen deprivation therapy. Then, in 1983 Labrie *et al*[9] conducted a new trial for the total elimination of androgen from both the testes and adrenal glands. They reported a small series of patients with advanced prostate carcinoma managed with an LHRH analogue combined with an oral antiandrogen. The results showed an impressive improvement in survival rate, and this success led to numerous studies exploring this concept. In addition, with the longer duration of LHRH dosage intervals and the reduced negative impact to patients' self-image and cosmetic appearance[7, 8], LHRH agonist therapy became more popular than surgical castration[22, 23].

Because medical castration is reversible and has less of a psychiatric impact than surgical castration, several new trials have been conducted in different clinical situations. These trials showed that patients with localized prostate carcinoma received no benefit from primary androgen deprivation therapy[24, 25]; on the contrary, patients with metastatic prostate carcinoma showed a survival benefit with androgen deprivation therapy[26, 27]. Additionally, these trials provided evidence supporting androgen deprivation therapy for a survival benefit among patients who underwent radical prostatectomy with positive lymph node resection[28, 29] and among those with locally advanced prostate carcinoma after radiotherapy[30, 31].

The medical insurance system has become more prevalent and influential in recent decades. Medical expenses surge with administration of more new drugs and the use of new and delicate medical instruments. Restriction of medical expenses became inevitable and is an important factor in physicians' decision-making processes. As a result, the number of surgical castrations increased again[13, 14]. This study provides evidence supporting surgical castration rather than medical castration with LHRH, especially among patients with poor prognoses. We also showed that there was little survival benefit among patients with good prognosis scores, regardless of the method of castration. In Samson's analysis of patients with complete androgen blockade or monotherapy with LHRH, they also concluded that there was no survival benefit between complete androgen blockade and monotherapy with LHRH in patients with a good prognosis[10]. As a result, in the poor prognosis group (>5 sites of bone metastasis, hydronephrosis, pain requiring analgesics, alkaline phosphatase >2 times the upper limit of the normal range), bilateral orchiectomy should be performed for a better survival benefit. The reason why surgical castration is superior to medical castration with LHRH is not clear. According to Morgentaler's saturation model, prostate carcinoma requires a fairly low testosterone concentration for the carcinoma to flourish[32]. There are some studies indicating that LHRH therapy does not achieve as low of a testosterone level as does bilateral orchiectomy[33–36]. This might be one of the reasons why surgical castration had better outcomes for advanced prostate carcinoma, especially in the poor prognosis group. Another reason that might explain this difference is the sustainability of testosterone suppression. Bilateral orchiectomy would definitely cease the production of testosterone. Owing to different pharmacokinetics from person to person, the LHRH agonist might not be able to remain effective for one full month in every single person. Then, during readministration of the LHRH agonist, testosterone flares up and this causes so-called acute-on-chronic responses[36]. In our present study, antiandrogen was used in the medical castration group, but repeated flare-up episodes might also lead to a poor result.

In this study, ADT for the treatment of advanced prostate carcinoma improved tumor progression-free survival and biochemical failure rates after 12 months for patients in the surgical castration group. When we compared Reijke scores among the patients, surgical castration for patients with poor prognostic scores resulted in better disease-free survival and PSA normalization rates. The survival advantage suggests that surgical castration is beneficial in patients with poor prognosis scores, although further studies are needed to identify which patients would derive the most benefit from hormone therapy, particularly when balanced against the potential adverse cardiovascular effects of long-term ADT.

Acknowledgements

This study was supported by research grants from Chang Gung Memorial Hospital (No CMRPD-170471 and CMRPD-160131) and the National Science Council, Taiwan, China (No 97-2320-B-182-023-MY3 and 98-2314-B-182-042-MY3).

Author contribution

Ke-hung TSUI designed research; Ke-hung TSUI, Phei-lang CHANG performed research; Yu-hsiang LIN and Chien-lun CHEN contributed new analytical tools and reagents; Chen Pang HOU analyzed data; Yu-hsiang LIN wrote the paper.

References

1 Stamey T, Yang N, Hay A, McNeal J, Freiha F, Redwine E. Prostate-specific antigen as a serum marker for adenocarcinoma of the prostate. N Engl J Med 1987; 317: 909–16.
2 Wang MC, Valenzuela LA, Murphy GP, Chu TM. Purification of a human prostate specific antigen. Invest Urol 1979; 17: 159–63.
3 Loblaw DA, Virgo KS, Nam R, Somerfield MR, Ben-Josef E, Mendelson DS, *et al*. Initial hormonal management of androgen-sensitive metastatic, recurrent, or progressive prostate cancer: 2007 Update of an American Society of Clinical Oncology Practice Guideline. J Clin Oncol 2007; 25: 1596–605.
4 Huggins C, Hodges CV. Studies on prostatic cancer: I. The effect of castration, of estrogen and of androgen injection on serum phosphatases in metastatic carcinoma of the prostate. Cancer Res 1941; 1: 293–7.
5 Studer UE, Collette L, Whelan P, Albrecht W, Casselman J, de Reijke T, *et al.* Using PSA to guide timing of androgen deprivation in patients with T0-4 N0-2 M0 prostate cancer not suitable for local curative treatment (EORTC 30891). Eur Urol 2008; 53: 941–9.
6 Studer UE, Whelan P, Albrecht W, Casselman J, de Reijke T, Hauri D, *et al.* Immediate or deferred androgen deprivation for patients with prostate cancer not suitable for local treatment with curative intent: European Organisation for Research and Treatment of Cancer (EORTC) Trial 30891. J Clin Oncol 2006; 24: 1868–76.
7 Anderson J, Abrahamsson PA, Crawford D, Miller K, Tombal B. Management of advanced prostate cancer: can we improve on androgen deprivation therapy? BJU Int 2008; 101: 1497–501.
8 Saylor PJ, Smith MR. Metabolic complications of androgen deprivation therapy for prostate cancer. J Urol 2009; 181: 1998–2006.
9 Labrie F, Dupont A, Belanger A, Lacoursiere Y, Raynaud JP, Husson JM, *et al.* New approach in the treatment of prostate cancer: complete instead of partial withdrawal of androgens. The Prostate 1983; 4: 579–94.
10 Samson DJ, Seidenfeld J, Schmitt B, Hasselblad V, Albertsen PC, Bennett CL, *et al*. Systematic review and meta-analysis of monotherapy compared with combined androgen blockade for patients with advanced prostate carcinoma. Cancer 2002; 95: 361–76.
11 Eisenberger MA, Blumenstein BA, Crawford ED, Miller G, McLeod DG, Loehrer PJ, *et al.* Bilateral orchiectomy with or without flutamide for metastatic prostate cancer. N Engl J Med 1998; 339: 1036–42.
12 Loblaw DA, Mendelson DS, Talcott JA, Virgo KS, Somerfield MR, Ben-Josef E, *et al*. American Society of Clinical Oncology recommendations for the initial hormonal management of androgen-sensitive metastatic, recurrent, or progressive prostate cancer. J Clin Oncol 2004; 22: 2927–41.
13 Weight CJ, Klein EA, Jones JS. Androgen deprivation falls as orchiectomy rates rise after changes in reimbursement in the US medicare population. Cancer 2008; 112: 2195–201.
14 Chodak GW. Is the increase in orchiectomy for prostate cancer patients appropriate? Cancer 2008; 112: 2106–7.
15 Morote J, Esquena S, Abascal JM, Trilla E, Cecchini L, Raventós CX, *et al.* Failure to maintain a suppressed level of serum testosterone during long-acting depot luteinizing hormone-releasing hormone agonist therapy in patients with advanced prostate cancer. Urol Int 2006; 77: 135–8.
16 Kaisary AV, Tyrrell CJ, Peeling WB, Griffiths K. Comparison of LHRH analogue (Zoladex) with orchiectomy in patients with metastatic prostatic carcinoma. Br J Urol 1991; 67: 502–8.
17 Bubley GJ. Is the flare phenomenon clinically significant? Urology 2001; 58: 5–9.
18 de Reijke T, Derobert E. Prognostic factor analysis in patients with advanced prostate cancer treated by castration plus anandron or placebo: a final update. Eur Urol 2002; 42: 139–46.
19 Studer UE, Whelan P, Albrecht W, Casselman J, de Reijke T, Hauri D, *et al*. Immediate or deferred androgen deprivation for patients with prostate cancer not suitable for local treatment with curative intent: European Organisation for Research and Treatment of Cancer (EORTC) Trial 30891. J Clin Oncol 2006; 24: 1868–76.
20 Chuang CK, Chu SH, Chiang YJ, Chun-Te Wu M, Lin MH, Wei TY, *et al.* Tolerability assessment of maximal androgen blockade with 50 mg daily of bicalutamide and castration in patients with advanced prostate cancer. Chang Gung Med J 2002; 25: 577–82.
21 Albertsen P. Androgen deprivation in prostate cancer–step by step. N Engl J Med 2009; 360: 2572–4.
22 Shahinian VB, Kuo YF, Freeman JL, Orihuela E, Goodwin JS. Increasing use of gonadotropin-releasing hormone agonists for the treatment of localized prostate carcinoma. Cancer 2005; 103: 1615–24.
23 Barry MJ, Delorenzo MA, Walker-Corkery ES, Lucas FL, Wennberg DC. The rising prevalence of androgen deprivation among older American men since the advent of prostate-specific antigen testing: a population-based cohort study. BJU Int 2006; 98: 973–8.
24 Wong YN, Freedland SJ, Egleston B, Vapiwala N, Uzzo R, Armstrong K. The role of primary androgen deprivation therapy in localized prostate cancer. Eur Urol 2009; 56: 609–16.
25 Lu-Yao GL, Albertsen PC, Moore DF, Shih W, Lin Y, DiPaola RS, *et al.* Survival following primary androgen deprivation therapy among men with localized prostate cancer. JAMA 2008; 300: 173–81.
26 Diblasio CJ, Malcolm JB, Hammett J, Wan JY, Aleman MA, Patterson AL, *et al.* Survival outcomes in men receiving androgen-deprivation therapy as primary or salvage treatment for localized or advanced prostate cancer: 20-year single-centre experience. BJU Int 2009; 104: 1208–14.
27 Keating NL, O'Malley AJ, McNaughton-Collins M, Oh WK, Smith MR. Use of androgen deprivation therapy for metastatic prostate cancer in older men. BJU Int 2008; 101: 1077–83.
28 Messing EM, Manola J, Yao J, Kiernan M, Crawford D, Wilding G, *et al.* Immediate versus deferred androgen deprivation treatment in patients with node-positive prostate cancer after radical prostatectomy and pelvic lymphadenectomy. Lancet Oncol 2006; 7: 472–9.
29 Messing EM, Manola J, Sarosdy M, Wilding G, Crawford ED, Trump D. Immediate hormonal therapy compared with observation after radical prostatectomy and pelvic lymphadenectomy in men with node-positive prostate cancer. N Engl J Med 1999; 341: 1781–8.
30 Bolla M, Gonzalez D, Warde P, Dubois JB, Mirimanoff RO, Storme G, *et al.* Improved survival in patients with locally advanced prostate cancer treated with radiotherapy and goserelin. N Engl J Med 1997; 337: 295–300.
31 D'Amico AV, Manola J, Loffredo M, Renshaw AA, DellaCroce A, Kantoff PW. 6-Month androgen suppression plus radiation therapy *vs* radiation therapy alone for patients with clinically localized prostate cancer: a randomized controlled trial. JAMA 2004; 292: 821–7.
32 Morgentaler A, Traish AM. Shifting the paradigm of testosterone and prostate cancer: the saturation model and the limits of androgen-dependent growth. Eur Urol 2009; 55: 310–20.
33 Oefelein MG, Cornum R. Failure to achieve castrate levels of testosterone during luteinizing hormone releasing hormone agonist therapy: the case for monitoring serum testosterone and a treatment decision algorithm. J Urol 2000; 164: 726–9.
34 Yri OE, Bjoro T, Fossa SD. Failure to achieve castration levels in patients using leuprolide acetate in locally advanced prostate cancer. Eur Urol 2006; 49: 54–8; discussion 58.
35 Tombal B. The importance of testosterone control in prostate cancer. Eur Urol Suppl 2007; 6: 834–9.
36 Tombal B, Berges R. How good do current lhrh agonists control testosterone? Can this be improved with Eligard®? Eur Urol Suppl 2005; 4: 30–6.